NuSTAR calibration facility and multilayer reference database

Optic response model comparison to NuSTAR on-ground calibration data

Thesis submitted for the degree of philosophiae doctor
Author: Nicolai F. Brejnholt
Supervisor: Finn E. Christensen
Submitted: December 31, 2011

DTU Space
National Space Institute

DTU Space
National Space Institute
Technical University of Denmark

Juliane Maries Vej 30
DK - 2100 Copenhagen
Tel (+45) 3532 5700
Fax (+45) 3536 2475

Author email: nicolai@space.dtu.dk
Supervisor email: finn@space.dtu.dk

Dedicated to karaoke, ninja frogs and white trash Tuesdays.

Resumé

Røntgenastronomien tog for alvor fat i at løse universets højenergigåder for tolv år siden med opsendelsen af to røntgenobservatorier, XMM-Newton (ESA) og Chandra (NASA). Begge missioner benytter tyndfilmsbelægninger til at opnå fokusering af såkaldt blød røntgenstråling med energier op til 15 keV. I 2012 opsender NASA Nuclear Spectroscopic Telescope ARray (NuSTAR). NuSTAR lover på lignende vis at skyde en ny guldalder i gang indenfor røntgenastronomien ved at muliggøre fokusering af hård røntgenstråling på op til 80 keV. Denne evne hviler på udviklingen af multilagstyndfilmsbelægninger bestående af op til 291 lag af ned til 25 Å tykkelse.

I denne afhandling beskrives etableringen af en referencedatabase for NuSTAR multilagene. Databasen skal benyttes til at anslå nødvendige observationstider, idet en præcis angivelse af teleskopets effektive areal, og dermed antallet af indsamlede fotoner som funktion af tid, afhænger af multilaget. Ydermere vil kendskab til det effektive areal give astronomer bedre mulighed for at udrede detaljer fra de indsamlede data.

Databasen blev opbygget ved at kortlægge deponeringen af tyndfilmsbelægningen, samt ved måling af vidneprøver fra tyndfilmsbelægningerne installeret i NuSTAR-optikken. Databasen blev efterfølgende valideret ved simulering af en realistisk geometrisk repræsentation af NuSTAR-optikken og en sammenligning med målinger foretaget på den egentlige optik. Disse målinger blev udført på et til formålet opført hårdt røntgenstrålingsanlæg. Design og kvalifikation af anlægget indgik som en integreret del af afhandlingen.

Afhandlingen har kortlagt NuSTAR tyndfilmsbelægningen. Ved brug af referencedatabasen og et simuleringsværktøj er et optimistisk skøn på NuSTAR-optikkens effektive areal blevet foretaget. Skønnet ligger væsentligt under det effektive areal, der var forventet fra NuSTAR designet, men over det konservative skøn foretaget på baggrund af kalibreringsdata. Yderligere udvikling af simuleringsværktøjet er nødvendig for til fulde at udnytte den etablerede referencedatabase.

Abstract

The Nuclear Spectroscopic Telescope ARray (NuSTAR) is a NASA Small Explorer mission carrying the first focusing hard X-ray telescope ($5 - 80\,keV$) to orbit. NuSTAR is slated for launch in 2012. Through a leap in sensitivity, the realization of focusing optics holds promise of heralding in a golden age for hard X-ray astronomy similar to the one introduced by XMM-Newton (ESA) and Chandra (NASA) in the soft X-ray range ($0.1 - 15\,keV$) twelve years earlier. The leap in sensitivity over a broad energy range is achieved using depth-graded multilayer coatings.

In order to predict and interpret the optic response for both on- and off-axis NuSTAR observations, detailed knowledge of the as-coated multilayer is required. The purpose of this thesis is to establish a multilayer reference database. As an integral part of this effort, a hard X-ray calibration facility was designed and constructed.

Each of the nearly five thousand substrates installed in the NuSTAR optics are coated with a unique multilayer. The uniqueness derives from multilayer deposition induced non-uniformities and run-to-run variations. As mapping the multilayer of each substrate is not feasible, this thesis presents a detailed study of the coating uniformity and run-to-run variations. The uniformity of multilayers deposited on representative flight spare substrates is mapped out as a function of deposition chamber location. The uniformity map describes the relative deposition for a given chamber location compared to a witness sample. A similar witness sample was included in all flight coating runs. From the flight witness samples, the multilayer run-to-run variations are determined. Combining the uniformity map with the witness multilayer provides an estimate of the as-coated multilayer for all substrates mounted in the optics. To couple the as-coated multilayer to the actual optics, ray tracing is carried out in a detailed geometric model of the optic, including in-situ measured figure error for the mounted substrates. The effective area as a function of energy estimated from ray tracing is compared to NuSTAR on-ground calibration data. The on-ground calibration and flight witness sample investigations were carried out at a hard X-ray facility constructed for the same purpose.

This thesis established the NuSTAR multilayer reference database and found that it provides a good description of the as-coated multilayers of the NuSTAR optics. A thorough quantitative study of the NuSTAR effective area requires the utilized ray tracing tool to mature further. Currently, the effective area estimated from the multilayer reference database represents an optimistic upper limit. Along with a conservative estimate derived from on-ground calibration data, the expected effective area of NuSTAR has been constrained. The multilayer reference database estimates the effective area to be on average 10% higher than the NuSTAR level 4 requirements.

Contents

List of Figures

List of Tables

List of acronyms and abbreviations

AFM	Atomic Force Microscopy ... 89
Ar	Argon ... 7
C	Carbon ... 12
C1	Cathode 1
C2	Cathode 2
C3	Cathode 3
C4	Cathode 4
Caltech	California Institute of Technology ... 89
CCD	Charge-Coupled Device ... 8
CEN	Center for Electron Nanoscopy ... 87
CU	Columbia University Astrophysics Laboratory ... 53
Cu	Copper ... 20
DTU	DTU Space, Technical University of Denmark ... 12
EAG	Evans Analytical Group ... 71
EDS	X-ray Energy Dispersive Spectroscopy ... 87
ESA	European Space Agency
FFT	Fast Fourier Transform ... 81
FIB	Focused Ion Beam ... 72
FM0	Flight Module 0 ... 12
FM1	Flight Module 1 ... 15
FM2	Flight Module 2
Ge	Germanium ... 54
HEFT	High Energy Focusing Telescope ... 45
IDL	Interactive Data Language ... 1
IMD	IDL software package
LLNL	Lawrence Livermoore National Laboratories ... 71
LVDT	Linear Variable Differential Transformer ... 89
MT_RAYOR	Ray tracing tool developed at DTU
NASA	National Aeronautics & Space Administration
NuSIM	Official NuSTAR simulator
NuSTAR	Nuclear Spectroscopic Telescope ARray ... 1
ORM	Optic Response Model ... 17
PSF	Point Spread Function ... 89
PSD	Power Spectral Density ... 89

Pt	Platinum	3
RaMCaF	Rainwater Memorial Calibration Facility	13
RXO	Reflective X-ray Optics	19
Si	Silicon	12
SiC	Silicon Carbide	12
TEM	Transmission Electron Microscopy	8
UCB	University of California, Berkley	105
W	Tungsten	12

Preface

This thesis is submitted in fulfillment of the Ph.D. degree at DTU Space, National Space Institute (Technical University of Denmark, DTU). The thesis concludes more than three years of work on the development of the Nuclear Spectroscopic Telescope ARray (NuSTAR), a NASA Small Explorer mission scheduled for launch in early 2012.

The primary contribution to the NuSTAR project was a nearly two-year term spent at the Columbia University Astrophysics Laboratory (CU) in New York City, working to design, construct and eventually run the Rainwater Memorial Calibration Facility (RaMCaF) for X-ray optic calibration. RaMCaF was instrumental in several NuSTAR prototype tests and carried out the on-ground calibration of the two flight modules in March 2011. Following the conclusion of the on-ground calibration campaign RaMCaF was reconfigured to acquire multilayer witness data. The bulk of this data set, along with select parts of the optics calibration data, is analyzed in this thesis.

The work carried out at RaMCaF prior to and during calibration is summarized in a peer reviewed article [1] and a conference proceedings paper [2] available from Appendix A. In addition to this, an unpublished report and a number of safety manuals are also available from Appendix A. These were authored as part of the CU Environmental Health and Safety application for operating a high-power X-ray source at RaMCaF. Approval was given without remarks on account of a comprehensive Geant4 [3] simulation and an extensive, custom-designed safety interlock system described in the report.

The above-mentioned articles and reports are provided as documentation for the majority of the Ph.D. work carried out at RaMCaF. The thesis focuses on constructing a multilayer reference database for the Optic Response Model (ORM). The database contains two separate data sets. One is a uniformity mapping of the multilayer coating laid down on individual NuSTAR mirror substrates. The uniformity campaign was carried out at DTU immediately following the flight coating campaign. The second database component is a library of multilayer coated witness sample data. Each sample witnessed a flight coating. These samples were measured at RaMCaF following the NuSTAR on-ground calibration. The witness sample campaign was concluded in December 2011, and as such the data set presented here is representative, but not complete. The complete data set will be presented in a paper under preparation. The abstract is available in Appendix A.

Before approaching either data set, Chapter 1 introduces the motivation for the database and general concepts relating to the investigations carried out in this thesis, including the NuSTAR design. Chapter 2 constructs the uniformity map, while Chapter 3 details the witness sample campaign and results. Following this, Chapter 4 explores an approach to improve and expand on the results from Chapter 3. Finally, Chapter 5 brings the preceding chapters together by comparing NuSTAR on-ground calibration data to results from a ray tracing tool utilizing the multilayer reference database.

An up-to-date version of the database and related documents are accessible online from the DTU NuSTAR website. Throughout the electronic version of this thesis referenced repositories are accessible via hyperlink. This is used extensively in the appendices. In print the hyperlink address will not display. In these cases, refer to `http://www.nustar.space.dtu.dk`

Acknowledgements

I would like to thank my supervisor Finn E. Christensen for the opportunity to work on the NuSTAR project and for his guidance during my Ph.D.. A special thanks also goes to Professor Charles J. Hailey from CU for his support as I took on the responsibilities and challenges that came with constructing the NuSTAR calibration facility in New York. I could not have imagined a more exciting way to spend the past three years.

I would further like to extend a thank you to my colleagues in New York and Copenhagen for the stimulating environment they created, both during the lengthy NuSTAR schedule crunch, and in the brief interludes of relative calm. Special mention goes to Melania D. Nynka, for being part of the original tunnel rat team, Todd A. Decker, Kenneth L. Blaedel and Gordon C. Tajiri, for being shining beacons of excellence to a young engineer, and finally, Mette Friis, Joanna F. Levinsen, Peter Krohne-Nielsen, Philip Brown, Niels Jørgen S. Westergaard and Desiree D. M. Ferreira for their advice and assistance during the final month of the thesis work.

Chapter 1

Introduction

Abstract - *In this chapter, the motivation and general concepts relevant to the thesis are presented. Basic principles of multilayers, multilayer deposition, X-ray telescopes and TEM are laid out, and the NuSTAR design is introduced.*

The intention of the following chapter is not to provide a rigorous treatment of the theory, but merely to present terms and nomenclature used throughout the thesis. This includes an introduction to the details of the Nuclear Spectroscopic Telescope ARray (NuSTAR). For an in-depth treatment of the theory the reader is referred to several excellent choices in the literature, e.g. [4, 5, 6, 7] and references therein.

Note that throughout the thesis, Interactive Data Language (IDL) is used for data reduction, analysis and visualization. Multilayer reflectivity is calculated using a sub-routine of the IMD software package developed for IDL to model the optical properties of multilayer films [8].

1.1 Multilayers

At the very core of the X-ray investigations carried out in this thesis three broadly known concepts, namely Snell's law [6], the Fresnel equations [5] and Bragg's law [9], are found. Snell's law shows the relationship between grazing incidence angle (α_i) and refracted grazing angle (α_{i+1}) off an interface. The Fresnel equations relate these angles to the subsequent specular reflectivity ($r_{i,i+1}$) and transmission ($t_{i,i+1}$) coefficients of the interface, enabling the reflectivity r_{slab} of a thin slab of material to be calculated. Both Snell and the Fresnels are described in Figure 1.1. For a thin slab of material, i.e. a single interface with $i = 1$, the refractive indices are given by $n_0 = 1$ (vacuum) and $n_1 \equiv 1 - \delta_1 + i\beta_1$. δ_1 and β_1 describe the scattering and absorption properties of the material. In the X-ray region, the real part of n_1 is slightly less than 1. An important implication of this is that for $\alpha_i \leq \alpha_c$, Snell's law shows that total external reflection occurs. α_c is called the critical angle. Assuming $\beta_1 << 1$, the critical angle is given by $\alpha_c = \sqrt{2\delta}$. This assumption is valid for X-rays and demonstrates a close relationship between electron density for the reflecting material, and derived critical angle.

Bragg's law is shown in Fig. 1.2 and given by

$$n\lambda = 2dsin(\theta_I) \tag{1.1}$$

Equation 1.1 describes the interaction of an X-ray with a periodic lattice, or set of planes, making it essential to understanding the response of multilayer structures. Bragg's law gives rise to distinct "Bragg peaks" in reflectivity when $\alpha_i = \theta_I$. As shown below this can be exploited in graded multilayers to achieve higher reflectivity over a broad angular (or energy) range at the cost of peak reflectivity.

Evolving the theory to describe the specular reflectivity response of a full multilayer structure, such as the one shown in Fig. 1.3, involves several steps. The first of these is to assume that the transmitted wave encounters a second interface, giving rise to yet another reflected and transmitted wave. To calculate the combined response of a multilayer with an arbitrary number of interfaces

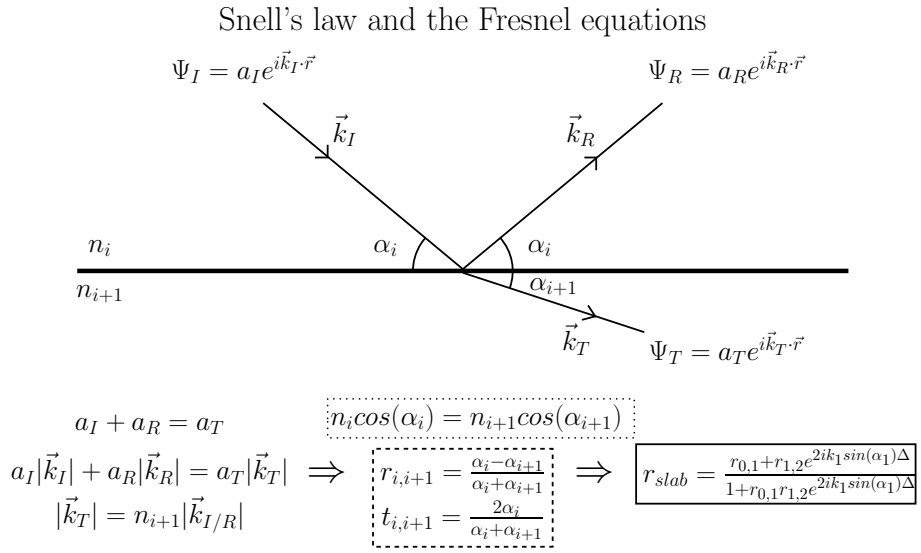

Figure 1.1: Snell's law (dotted frame) and the Fresnel equations (dashed frame) are derived from requiring continuity for Ψ and its derivative at the interface between two materials with refractive index n_i and n_{i+1} and (for Fresnel) assuming small α_i. Taking the results from Snell and Fresnel one can show that the reflectivity of a thin slab of material is given by r_{slab} (framed).

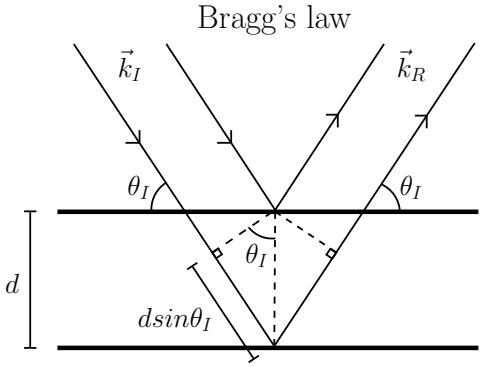

Figure 1.2: Bragg's law describes the condition for constructive interference from a set of planes, or equivalently, a periodic lattice with interplanar spacing d. X-rays with wavevector $\vec{k_I}$ are specularly reflected and interfere constructively if the path length difference is an integer multiple of the wavelength λ. Under this condition the incidence angle θ_I is termed the Bragg angle.

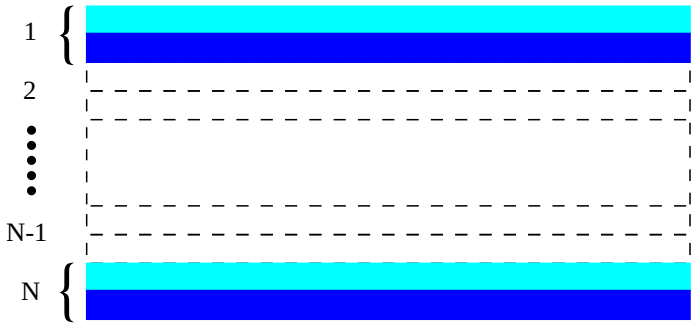

Figure 1.3: Shows a multilayer with N bilayers. Each bilayer consists of a low electron density material on top of a high electron density material. A high electron density contrast improves reflectivity from the bilayer.

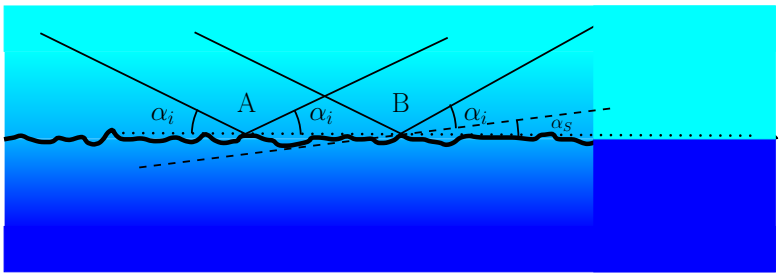

Figure 1.4: Most interfaces are not sharply defined as the ones indicated in Fig. 1.3, and on the right side of this figure. Instead, they have imperfections caused by interfacial diffusion and/or roughness. These are indicated in the left side of the figure. The dotted line is parallel to the surface element A, which in turn is parallel to the idealized sharp interface. The surface element B is parallel to the dashed line. While specular reflection occurs in both elements the rough interface cause surface element B to reflect in a non-specular direction. The diffuse, or graded, interface cause a reduction in the reflectivity dependent on the graded interface width.

and material combinations either a matrix [10] or (the more prevalent) recursive [11] method is used. IMD implements the latter method.

Fresnel assumes sharp interfaces. Real interfaces exhibit imperfections such as interfacial diffusion and roughness, as indicated in Fig. 1.4. The imperfect interfaces modify the reflectivity coefficients. To take this into account IMD implements Stearns interface profile functions [12] and Névot-Croce coefficients [13]. The most poignant result is that the modifications of the specular reflectivity can be described by the interface profile width, commonly referred to as the micro-roughness, without knowledge of the specific nature of the interface imperfections. This suffice for the X-ray investigations carried out in this thesis, however, additional study is required to describe the details of X-ray scattering. Brief mention of efforts on modeling the NuSTAR X-ray scattering is made in Chapter 5.

It is clear from the above that the details of the reflectivity as a function of angle (or energy) is determined by the physical parameters of the multilayer such as material combinations, heavy-to-light material ratio (Γ), number of bilayers (N), micro-roughness (σ) and bilayer thickness (d, commonly referred to as the d-spacing), including any grading of d as a function of N. Figure 1.5 summarizes the evolution of the reflectivity from a thin slab of Platinum (Pt) to one of the NuSTAR flight multilayer coatings discussed in Sec. 1.5. Bragg peaks are apparent from the simple and simple graded multilayers while individual peaks overlap in the flight multilayer response. The oscillations visible between Bragg peaks are due to constructive and destructive interference of the waves reflected from the top and bottom interface(s). A total of $N-2$ oscillations occur and are referred to as Kiessig fringes [14].

As hinted above the specular reflectivity of a multilayer structure can be expressed as a function of energy E or grazing incidence angle α_i. This is illustrated in Fig. 1.6 where reflectivity is given as a function of energy and angle for a multilayer structure with a constant d-spacing (cst-d, Fig.

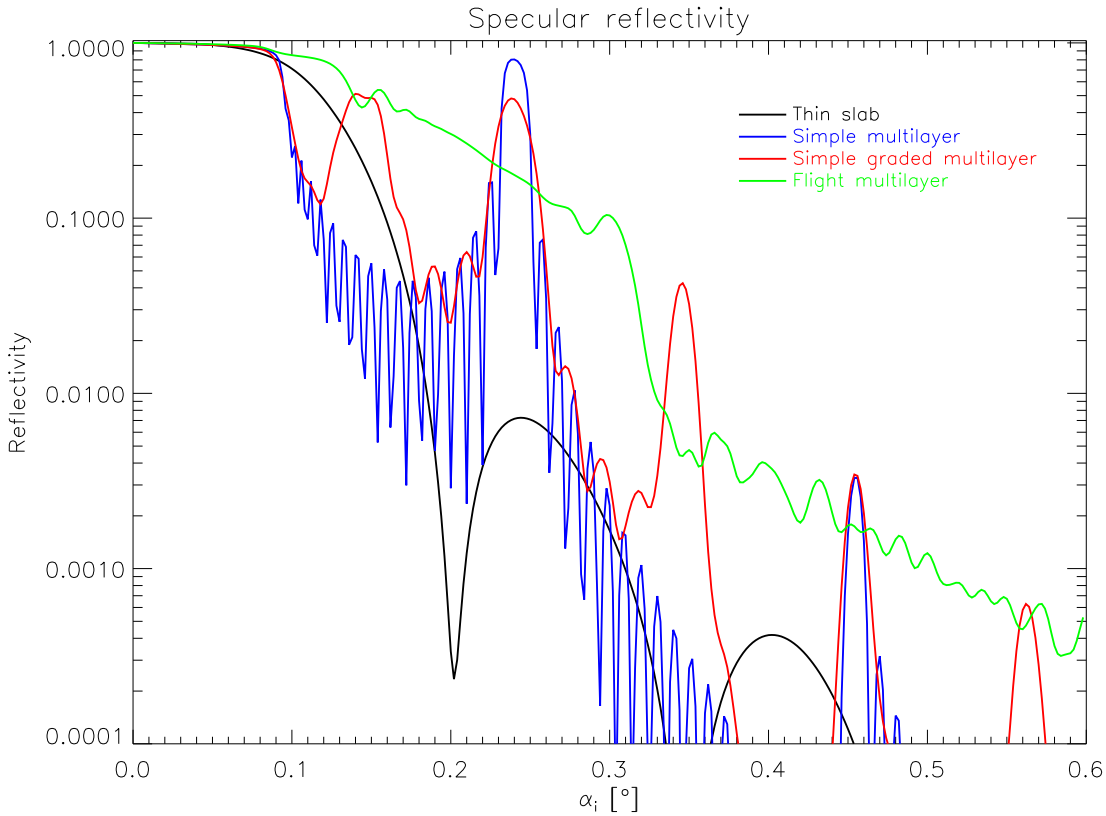

Figure 1.5: Reflectivity evolution at 50 keV from a thin slab of Pt (black, $d = 100$ Å) to a simple multilayer (blue, $N = 20$, $d = 40$ Å, $\Gamma = 0.55$) and a simple graded multilayer (red, $N = 20$, first ten bilayers $d = 40$ Å, $\Gamma = 0.55$, remaining bilayers $d = 80$ Å, $\Gamma = 0.55$) is shown along with reflectivity from a graded flight multilayer (green, NuSTAR recipe 1, refer to Sec. 1.5).

1.6a) and graded d-spacing (Fig. 1.6b). The plots illustrate the relationship and comparability between measurements taken at a fixed energy (Chapter 2) and those with fixed angle (Chapter 3). The relationship between the two types of measurements is expressed through the wavevector transfer Q given by

$$Q \equiv 2|\vec{k}|sin(\alpha_i) \tag{1.2}$$

where the wavevector $|\vec{k}|$ is

$$|\vec{k}| = \frac{E}{\hbar c} \tag{1.3}$$

A further point to note from Fig. 1.6 is that similar to α_c in angle space a critical energy E_c exists for a given incidence angle below which total external reflection occurs.

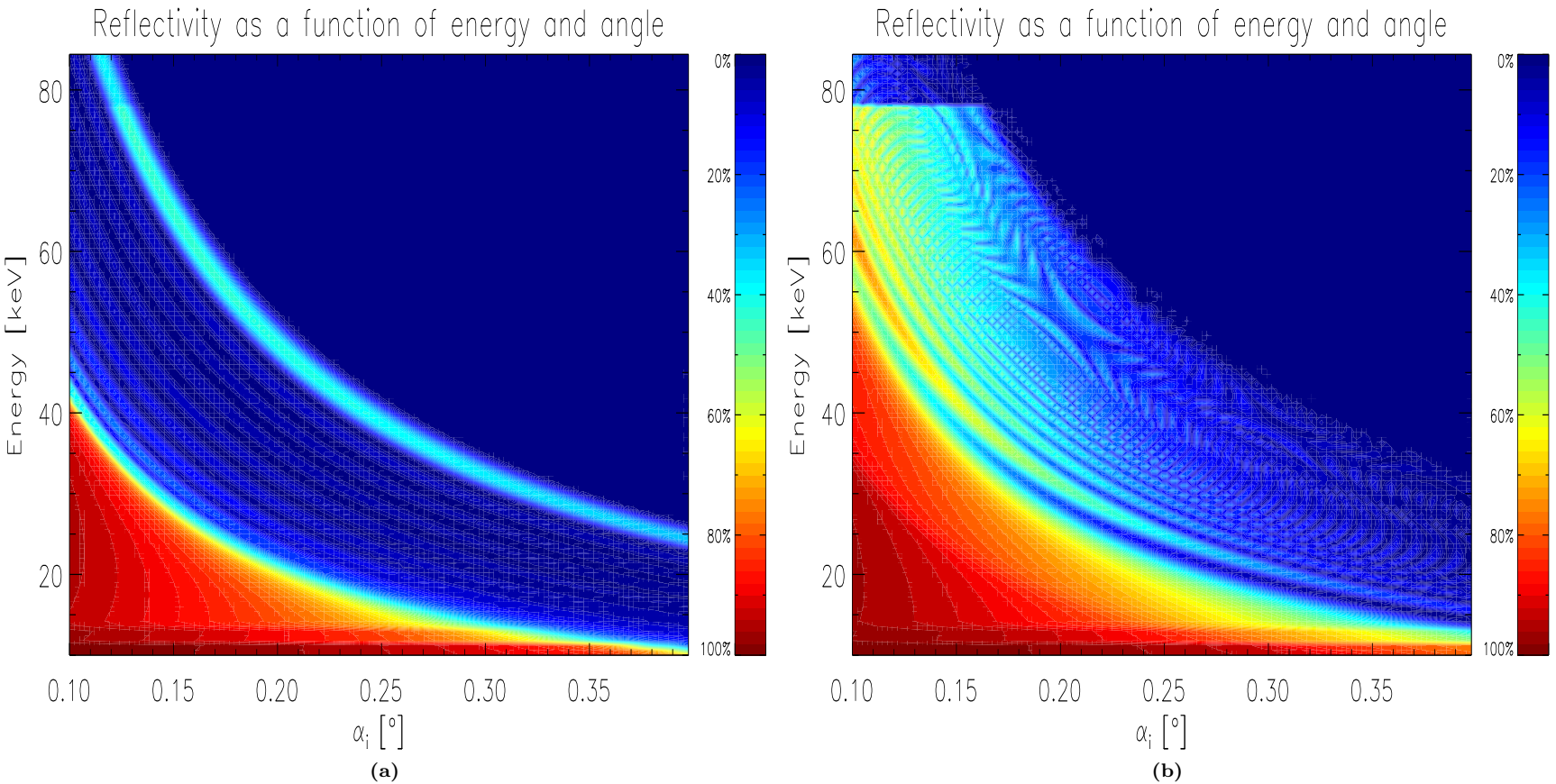

Figure 1.6: Reflectivity as a function of energy and angle for two multilayer structures (a) A cst-d multilayer ($N = 10, d = 40$ Å, $\Gamma = 0.45$). Kiessig fringes and the first order Bragg peak are clearly visible beyond the total external reflection region (b) A graded d-spacing multilayer (NuSTAR flight recipe 1, refer to Sec. 1.5). The benefit of the graded multilayer structure is obvious from the much broader region with reflectivity above 20% owing to the overlapping Bragg peaks. Further note the cutoff at 78.4 keV caused by the Pt K-edge absorption. The feature is also present in (a).

1.2 Multilayer deposition

A number of methods exist for depositing multilayers [15]. Sputter deposition was used for NuSTAR, the principle of which is illustrated in Fig. 1.7. An inert gas atmosphere, in the present case Argon (Ar), is established in a vacuum chamber. By applying a high voltage over the target an Ar plasma is created containing positively charged ions. To increase the ionization of the plasma, without having to increase the high voltage level, the cathode is magnetic, trapping electrons near the target where they collide with the plasma. As the ions accelerate towards the planar magnetron cathode, they impact the target, sputtering target material onto the substrate. The deposition rate of the basic setup shown in Fig. 1.7 is determined by the distance (solid angle of substrate seen from target), the cathode geometry and power setting (ion speed when impinging on target and ionization efficiency) and the Ar pressure. For a simple treatment of the deposition rate the angular distribution of the sputtered material can be assumed to follow an ejection law [16]

$$P(\xi) \propto \frac{cos(\xi)}{\alpha_e^2 + (1-\alpha_e^2)cos^2(\xi)} \tag{1.4}$$

in which the ejected particles favor the forward direction, $\xi = 0°$, as indicated by the Fig. 1.7 inset. α_e determines the shape of the distribution depending on the target power settings and material type. The influence of the Ar pressure is complicated by the fact that a higher pressure will increase the number of ions impinging on the target, but will also result in the target atoms having a higher likelihood of encountering the gas on its flight to the substrate, lowering the deposition rate and increasing the micro-roughness. This effect is most pronounced for the light material in the multilayer due to the relative heaviness of the Ar atoms. Equation 1.4 does not take any of these effects into account. It further assumes sputtered particles stick to the substrate, i.e. no resputtering of material. As discussed in Chapter 4 this assumption does not hold at the heavy-on-light interface. However, for the rudimentary modeling carried out in Chapter 2, only relative values are sought after, so the simplification suffice.

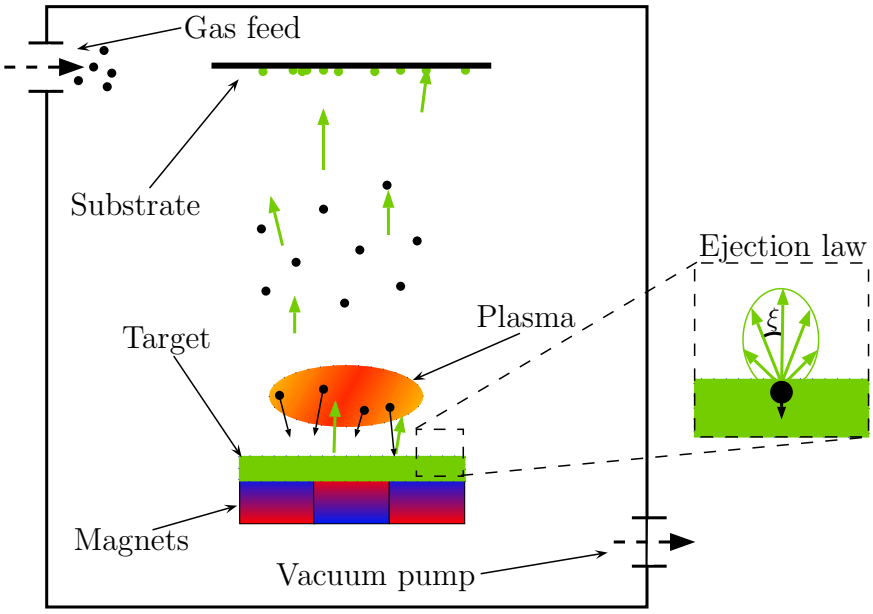

Figure 1.7: A vacuum chamber is filled with a low pressure inert gas atmosphere and a negative high voltage is applied over a target of the sputtering material. As the high voltage ionizes the gas a plasma forms in front of the target. The positive ions are propelled into the target, sputtering material onto the substrate. The magnets capture the electrons near the target, increasing the ionization efficiency. The inset indicates an angular dependency of sputtered material flux. The flux magnitude is given by the length of the vectors which trace out an ellipsoid. The forward direction, $\xi = 0°$, sees the highest flux.

1.3 Transmission Electron Microscopy

In addition to "traditional" specular reflectivity measurements, Transmission Electron Microscopy (TEM) investigations of the multilayers were also carried out. TEM improve on the resolution limit δ imposed on visible-light microscopy through the lower wavelength of electrons. δ of an imaging system is given by Rayleigh's criterion

$$\delta = 1.22\frac{f\lambda}{D_l} \tag{1.5}$$

where f and D_l are the focal length and diameter of the lens, respectively, while λ is the electron wavelength. TEM equipment commonly operate at $> 100\,keV$. TEM resolution is limited by lens abberations rather than δ, yet still achieves Ångström-level resolving power. Figure 1.8 outlines a standard TEM. An electron gun produces a stream of electrons that are condensed by consecutive lenses onto the specimen. Electron lenses are usually made up of an array of electromagnetic coils. Manipulating microscope parameters is done through changing coil current. The first condenser lens acts to define the general spot size range while the second tunes the size of the exposed specimen area. Exposed specimen area ranges from hundreds of microns down to tens of nanometers. Prior to hitting the specimen the beam is often collimated to reduce spherical abberations, and an objective lens ensures parallel illumination. Another objective lens collects the specimen-modulated beam and images it to a system of magnifying lenses. Degree of magnification can be greater than 10^6. The image is displayed on a viewing screen, commonly a Charge-Coupled Device (CCD) camera. The objective aperture allows for selecting either "bright-field" or "dark-field" imaging. Simplified the former is contrast imaging between low density, or equivalently thin, and high density, or thick, areas on the specimen, created by electron absorption (amplitude modulation) in the media. Through this individual layers of a multilayer stack can be imaged directly. It is termed bright-field as areas with no specimen in the beam path appear bright. Conversely, dark-field images are dark where no contributions from specimen interaction can be found.

The contrast imaging simplification assumes that phase effects can be ignored. This breaks down as the magnification increases or the interaction volume decreases. The phase-contrast induced details are included in high-resolution TEM to achieve sub-Ångström resolution. It is

also present in the images discussed in Chapter 4. For these it is important to keep in mind that the observed lattice fringes are not direct images of crystal planes, but may provide insights on orientation and lattice spacing d_{hkl} of the crystalline material. Specifically, from knowing the lattice constant a of a given material the Miller indices (hkl) of imaged planes can be found through

$$d_{hkl} = \frac{a}{\sqrt{h^2 + k^2 + l^2}} \tag{1.6}$$

To image the multilayer edge-on, cross-sectional TEM is carried out. Cross-sectional TEM specimens are prepared by cleaving the sample and subsequently thinning it using mechanical grinding. Further thinning is carried out by polishing and/or by focused ion beam milling. These techniques are sciences unto themselves and will not be presented here, but the interested reader is referred to [17]. It will suffice to mention that specimens must be thinned sufficiently to be transparent to electrons. In the relevant cases this means thicknesses less than $100\,nm$.

It is important to note that unlike optical microscopy, TEM has a relatively broad depth of field. The broad depth of field results in TEM images representing a two-dimensional projection of atomic details averaged over the specimen thickness. This is known as the projection-limitation and must be kept in mind when interpreting images.

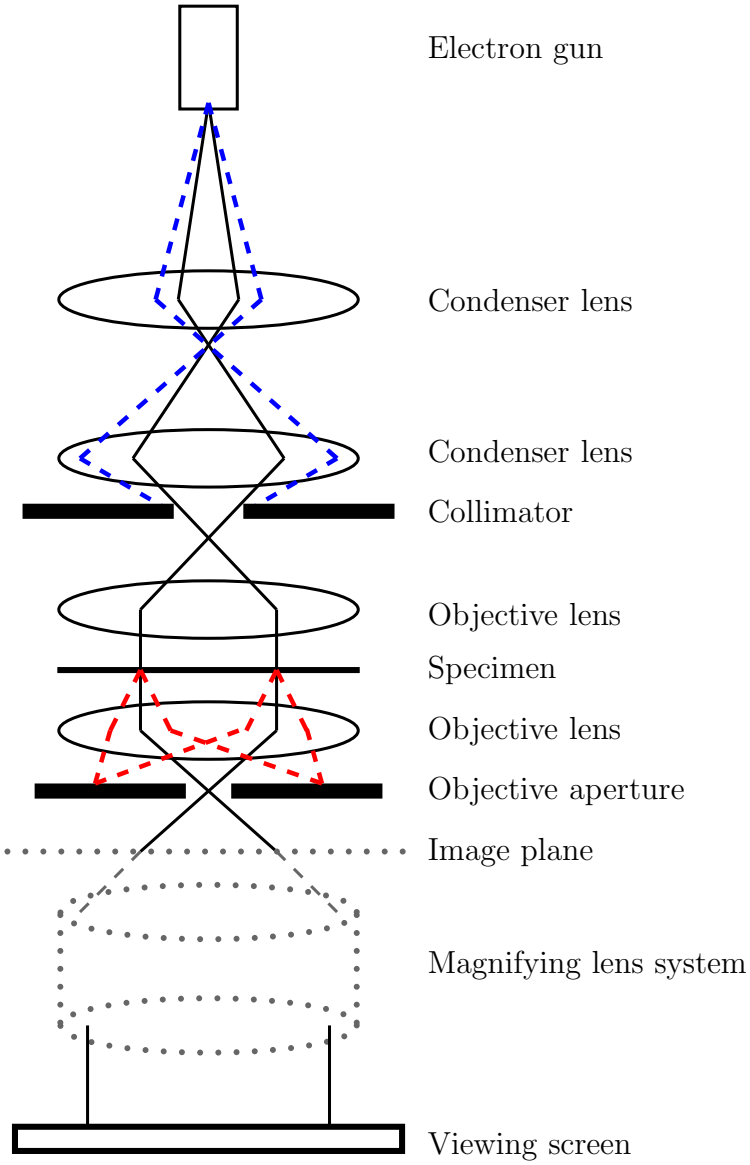

Figure 1.8: Sketch of a TEM column. Electrons are injected from the gun (dashed blue) and condensed through two lenses. A collimator limits stray electrons and spherical aberrations by reducing the beam size (black). Electrons diffracted by periodic structure in the specimen (dashed red) are blocked by the objective aperture in TEM mode, but can be viewed if details on the crystalline composition are sought after. The remainder of the column consists of a magnifying lens system and concludes with a viewing screen.

1.4 X-ray telescopes

The Wolter-I design, illustrated in Fig. 1.9, is one of the most prevalent methods for satisfying the Abbe sine condition in X-ray telescopes with incident paraxial rays [18, 19, 20, 21, 22]. The design forms an image through a double-reflection off a parabola followed by a confocal and coaxial hyperboloid surface. Far away from the vertices both the parabola and hyperbola are well-described by straight segments. This makes a conical approximation to the substrate shape sufficient, provided that the substrate length is much smaller than the focal length. The conical approximation significantly reduces the requirements on forming the substrates that make up the reflectors. Both a single and a double reflection are indicated in Fig. 1.9. The Abbe sine condition is only fulfilled for double reflection. In a telescope the single reflection may occur if the incidence angle is too large (or equivalently, the hyperbola substrate is too short) which could ensue from a divergent source at finite distance. Finite source distance caveats are important in the context of the NuSTAR on-ground calibration.

As seen in Sec. 1.1 a thin slab or a more complicated multilayer can provide substrates with significant reflectivity in the X-ray range, but a further strength of the Wolter-I design is that nesting reflectors is relatively straightforward, as illustrated in Sec. 1.5. Nesting is necessary as shallow α_i limit the entrance aperture of each substrate significantly making collecting area a prime commodity.

For specular reflections under grazing incidence, it is clear that a telescope will have a long focal length f. For a Wolter-I design f is approximately given by

$$f \approx \frac{r_i}{4\alpha_i} \tag{1.7}$$

where r_i describes the distance from the intersection between the paraboloid and the hyperboloid to the optical axis (refer to Fig. 1.9). r_i should not be confused with the reflectivity coefficient $r_{i,i+1}$. For future reference it is relevant to note that while Eq. 1.7 is valid for a source at infinite, the thin lens formula

$$\frac{1}{S} + \frac{1}{f_s} = \frac{1}{f} \tag{1.8}$$

must be used for finite source distance S to determine the actual focal length f_s of the telescope.

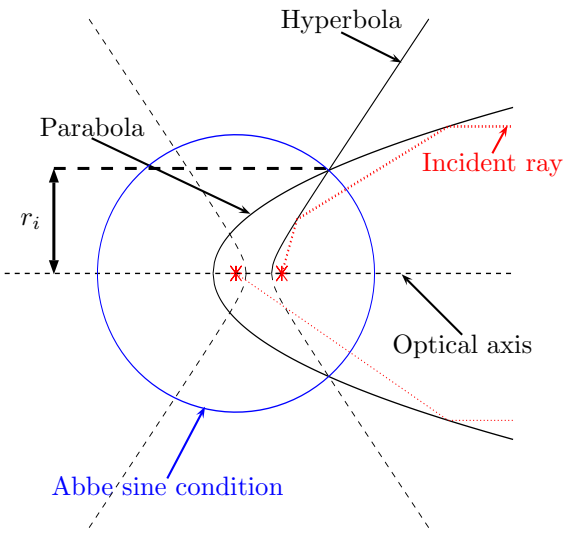

Figure 1.9: Demonstrates the Wolter-I design with a parabola and hyperbola arranged such that they are confocal and coaxial. The geometry ensures that the parabola and hyperbola intersections nearly describe a circle thus approximately fulfilling the Abbe sine condition, allowing the design to act as an imaging lens.

1.5 The Nuclear Spectroscopic Telescope Array

NuSTAR will carry two Wolter-I optics and is set for launch to a low-inclination Earth orbit in early 2012 on a Pegasus rocket. The two near-identical optics onboard NuSTAR promises significant improvements in sensitivity compared to present-day instruments and will focus X-rays up to an unprecedented 80 keV using graded multilayer coatings. This section briefly describes the optics in the context of the concepts introduced in Sec. 1.1 and 1.4. For additional details the reader is referred to several published papers [23, 24, 25, 26, 27, 1, 2, 28, 29, 30] and references therein.

1.5.1 The NuSTAR coatings

While past space missions have provided focusing in the soft X-ray range, NuSTAR is the first to bring focusing to the hard X-ray region. This is due entirely to the graded multilayer coating applied to the substrates at DTU Space, Technical University of Denmark (DTU). The telescope design includes ten distinct multilayer recipes, seven of which consists of Pt, and Carbon (C) and the remaining three composed of Tungsten (W) and Silicon (Si), bilayers. For all recipes the d-spacing progress following

$$d_i = \frac{a}{(b+i)^c} \qquad i = 1 \ldots N \tag{1.9}$$

with

$$a = d_{min} \cdot (b+N)^c \qquad b = \frac{(1 - N \cdot k)}{k-1} \qquad k = \frac{d_{min}}{d_{max}}^{\frac{1}{c}}$$

where d_{min} and d_{max} is the d-spacing of the bottom and top layer, respectively, and c controls the slope between these extreme values over the N layers. Table 1.1 outlines the ten design recipes and also includes Γ and projected σ values. The table further includes "recipe 0" utilizing Silicon Carbide (SiC) in place of C. This was the intended flight recipe 1 through the production of the final pre-flight optic, Flight Module 0 (FM0). X-ray studies showed a build-up in micro-roughness towards the top of the stack and increased non-specular reflectivity (diffuse scattering, refer to [31]), significantly deteriorating optic performance. As a result, the design recipes were re-optimized using Pt/C. However, as all studies on adhesion strength of the multilayer had been carried out on Pt/SiC coatings, it was deemed appropriate to keep the original recipe for the highest mechanical

stress layer, namely layer 1. Internal studies later showed there to be no distinguishable difference in adhesion strength between the two multilayer recipes. For the original design recipes refer to [25]. The studies leading to the recipe change, and the updated recipes themselves, are described in [28].

The coating was deposited using collimated magnetron sputtering. The coating chamber allows up to thirty-five NuSTAR substrates to be coated in a single run, depending on r_i (or equivalently, width) of the substrates in question [32]. As a multitude of effects perturb the intended multilayer period and structure, each flight coating run included a commercially available flat single-crystal Si wafer. Initially, these witness samples served as quality assurance through in-house specular reflectivity measurements at $8\,keV$. Later, they were part of an in-depth investigation of the as-coated multilayer structure at the Rainwater Memorial Calibration Facility (RaMCaF) and other facilities. The chamber induced perturbations and detailed investigation of the as-coated multilayers are discussed in Chapter 2 and 3, respectively.

Table 1.1: Overview of the NuSTAR design recipes. Note that the Γ_{top} applies only to the top layer (i.e. $d_{N=1}$ which has the thickness d_{max}). The thicker heavy material improves total external reflectivity efficiency significantly below the critical energy, E_c.

Recipe	Materials	Layer range	α_i range [°]	d_{min} [Å]	d_{max} [Å]	N	c	Γ_{top}	Γ	σ[Å]
0	Pt/SiC	1	0.077	31.7	128.1	150	0.245	0.70	0.45	4.5
1	Pt/C	2-12	0.078-0.087	29	133.7	145	0.245	0.70	0.45	4.5
2	Pt/C	13-24	0.088-0.097	29	131.6	145	0.228	0.70	0.45	4.5
3	Pt/C	25-36	0.098-0.111	29	129.6	145	0.234	0.70	0.45	4.5
4	Pt/C	37-49	0.112-0.127	29	121.8	145	0.214	0.70	0.45	4.5
5	Pt/C	50-62	0.128-0.143	29	109.5	145	0.225	0.70	0.45	4.5
6	Pt/C	63-76	0.145-0.163	29	107.5	145	0.225	0.70	0.45	4.5
7	Pt/C	77-89	0.165-0.184	29	102.8	145	0.212	0.70	0.45	4.5
8	W/Si	90-104	0.186-0.210	25	95.2	291	0.238	0.80	0.38	4.3
9	W/Si	105-118	0.212-0.237	25	83.9	291	0.220	0.80	0.38	4.3
10	W/Si	119-133	0.242-0.270	25	74.5	291	0.190	0.80	0.38	4.3

Figure 1.10: Photo of FM1 mounted in its calibration fixture. Photo credit: Scientific American.

1.5.2 The NuSTAR optics

Assembly of the NuSTAR optics was completed in early 2011 and on-ground calibration was carried out immediately following this. The second full scale module Flight Module 1 (FM1) is depicted in Fig. 1.10 while a schematic end-view is shown in Fig. 1.11. Each optic is comprised of 2376 pieces of multilayer coated glass substrates nested in a Wolter-I conical approximation. There are 133 nested shells with individual substrates spanning 30° (layers $69-133$) or 60° (layers $1-68$). Mounting radii (r_i) range from $54.4\,mm$ to $191\,mm$. The substrates are $225\,mm$ long and $0.21\,mm$ thick. Each substrate is thermally slumped to have a radius of curvature $\pm 1\,mm$ their designated mounting radii. The radius is approximated to reduce number of slumping mandrels required. After slumping and coating, substrates are mounted on graphite spacers placed on the backside of the previous layer. The spacers are precision-machined to provide α_i ranging from 0.077° to 0.27° such that f is $10.15\,m$ (refer to Eq. 1.7). As the spacers are machined in-situ stack-up errors do not occur. The optic design document details all aspects of the optic and includes α_i and r_i for each layer. The document is available from Appendix A.

The on-ground calibration of the NuSTAR optics was carried out at RaMCaF. The finite distance of the X-ray source meant f_s is $10.82\,m$ (refer to Eq. 1.8). In addition to this, with the optic axis aligned to the X-ray source, substrates were illuminated at an angle as much as 0.067° higher than the intended α_i. The higher angle not only influences the multilayer response (refer to Fig. 1.1 and Fig. 1.6), but also results in a significant reduction in contributing substrate area as illustrated in Fig. 1.12. Although the nesting of shells in a NuSTAR optic is not tight enough to cause shadowing (Fig. 1.12b), reflection overshoot (Fig. 1.12c) is significant. To provide a more complete picture of the optic response, individual sections, or subgroups, were therefore calibrated in turn with pseudo-parallel illumination (Fig. 1.12d). In Chapter 5, subgroup data sets are used to assess the results from Chapter 2 and Chapter 3.

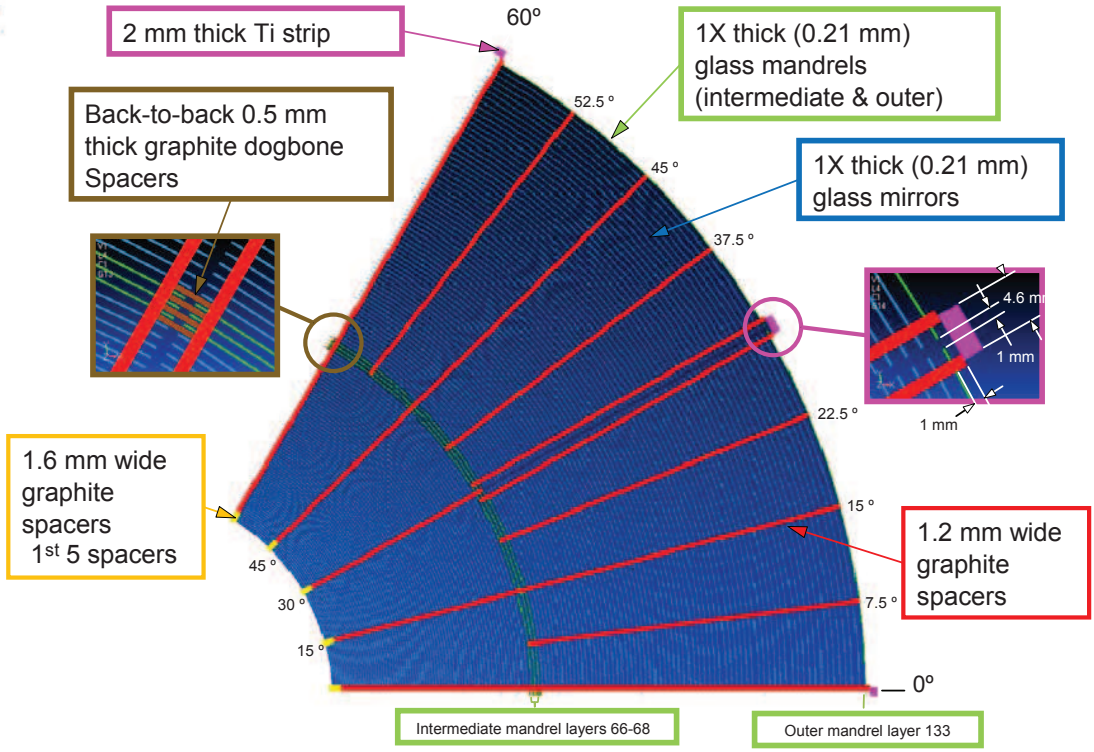

Figure 1.11: A detailed schematic end-view of a 60° section of a NuSTAR optic with emphasis on supporting elements. The precision-machined spacers are shown in red and yellow. The intermediate mandrel (green) indicates where the substrates switch from a 60° span to 30°. The figure is reproduced from the optic design document.

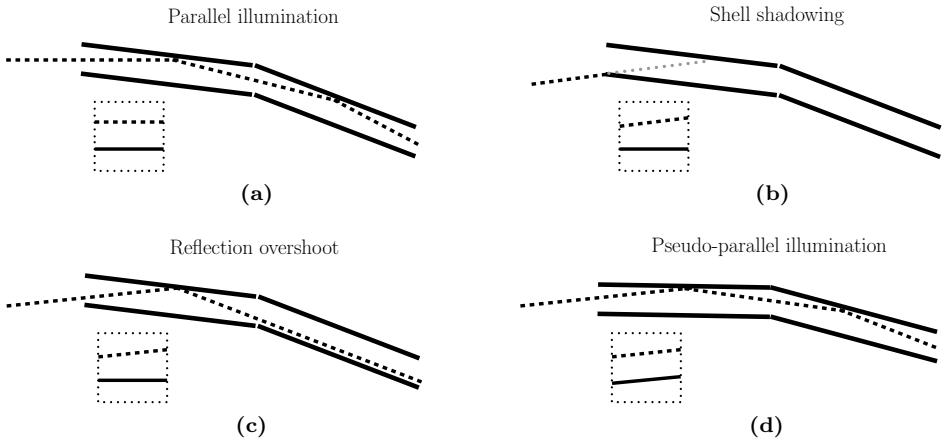

Figure 1.12: Various modes of illumination of a conical approximation Wolter-I design. Dotted square insert indicates relationship between ray (dotted) and optical axis (full line) (a) Parallel illumination is the ideal achieved during observation of sources at infinite (b) For a tightly nested telescope the adjacent inner shell may cause part of the primary shell to be shadowed (c) For specular reflection a higher incidence angle may result in the reflected ray missing the second reflection (d) Pseudo-parallel illumination can be carried out by compensating for the higher incidence angle by rotating the optical axis.

1.6 Thesis motivation

To support the in-orbit calibration of the NuSTAR telescope, a detailed study of the optic response must be carried out on-ground. On-ground calibration is presented with a number of challenges, such as the finite source distance. However, the greater flexibility in singling out sub-selections of the optic for investigation, makes the task of understanding the optic response significantly more manageable.

As discussed in this chapter, the NuSTAR optics are comprised of several thousand unique multilayer coated substrates, each contributing in their own specific way to the overall optic response. These contributions are expected to differ significantly from the intended design as a result of run-to-run variations in the coating deposition. The motivation for this thesis is to produce accurate estimates of the as-coated response from individual substrates through analysis of witness sample coatings. The information derived from the witness samples are coupled to the mounted substrates through a deposition uniformity mapping of the coating chamber. The as-coated multilayer of each substrate acts as an input to the Optic Response Model (ORM), which describes the response of NuSTAR as a function of energy. The improvements to the ORM, or equivalently, the accuracy of the estimated as-coated multilayer, are assessed through comparison with on-ground calibration data.

While the as-coated multilayer response constitutes the single largest contribution to the ORM, several other major components, including a multilayer scattering model and the substrate metrology database, are also required. Their status at the time of writing is presented in Chapter 5, along with the assessment of the current implementation of the as-coated multilayer reference database.

Chapter 2

Uniformity campaign

Abstract - *In this chapter, the multilayer coating process for the NuSTAR optics is presented, and perturbations to the designed multilayer deriving from coating deposition non-uniformity are mapped out as a function of chamber location. Rudimentary modeling to describe the uniformity is carried out, and additional work is suggested. The proposed model is found to agree well with the acquired data.*

Nearly ten thousand substrates were multilayer coated for NuSTAR between May 2009 and February 2011 at the DTU sputtering facility in Copenhagen. The majority of these were installed in prototype, proto-flight (FM0) or flight (FM1 and FM2) optics . The individual substrates carry a unique multilayer owing to run-to-run variations and chamber position during coating. Due to the sheer amount of substrates, it is not feasible to establish the as-coated multilayer for each substrate. Instead, the as-coated multilayers are estimated through two separate campaigns. In the present chapter, the uniformity of the coating as a function of chamber position is mapped out, while the run-to-run variations are established in Chapter 3. The uniformity was mapped in two steps as illustrated within the dashed box in Fig. 2.1 and described in Sec. 2.3.

35% of the W/Si coatings were carried out at a private company, Reflective X-ray Optics (RXO), in New York, to keep up with production schedule. The RXO chamber setup and uniformity data are presented in Sec. 2.1.1 and Sec. 2.3.8, respectively.

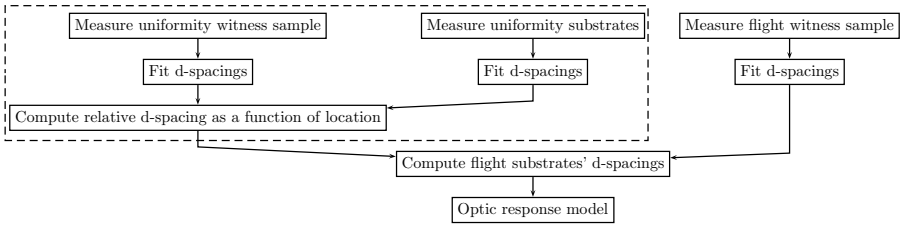

Figure 2.1: Illustration of the necessary steps to estimate the as-coated multilayer on the mounted flight substrates for use in the ORM. This section focuses on the tasks within the dashed box.

2.1 DTU coating facility

The DTU coating chamber consists of a $1\,m$ (diameter) by $1.2\,m$ (height) bell jar and resides within a class 10000 cleanroom. The chamber achieves a vacuum pressure of $10^{-6}\,Torr$ in six hours, including a thermal heating cycle ($120\,°C$ for two hours) and has feeds for adding Ar, or other inert gasses. A schematic top view is shown in Fig. 2.2. A total of four cathodes (C1-C4) can be mounted with sputter targets and up to eighteen slots are available for substrate mounting plates. Each plate mount on a rail circumventing the chamber as shown in the schematic view, allowing the substrates to travel past the cathodes. Only nine mounting plates were used for NuSTAR due to the length of the substrates. Shutters are in place to shield off targets during plasma ignition and when turning off cathodes. The chamber is controlled through custom Visual Basic software. A ceiling mounted crane allows lifting the bell jar top off for access to the mounting plates and targets.

In addition to the hardware mentioned above, the setup also includes a target mask to improve deposition rate uniformity along the vertical height and separator plates mounted in between the substrates to collimate the sputtered material. The separator plates reject material sputtered far outside the forward direction, refer to mounting plate inset in Fig. 2.2. Such plates have been shown to improve micro-roughness at the cost of deposition rate [33, 34]. Note that the separator plates are generally referred to by their bay width s_y, e.g. $100\,mm$ plates imply the bay to be $100\,mm$ wide along the vertical axis. The target mask is a semi-permanent installation while the separator plates are changed according to the diameter of curvature of the mounted substrate, D_{sub}. Masks are designed for each target material type. In addition to this, the widest separator bay for W/Si ($s_y = 120\,mm$) utilizes a unique mask based on past uniformity studies.

The coated material-ratio Γ and d-spacing values are adjusted through cathode power settings and rotational speed, respectively. The motor stepping was calibrated occasionally throughout the coating campaign, primarily to compensate for target wear. Calibration runs are carried out by depositing a cst-d, $N = 10$, coating on a $2 \times 10\,cm^2$ flat Si wafer and measuring it at a rotating Copper (Cu) anode beamline at DTU. The beamline is outlined in Fig. 2.3. Specular reflectivity from the calibration sample is measured at $8\,keV$ as a function of angle and the d-spacing is fitted using IMD. The result is used to determine the deposition rate as a function of rotation speed.

With two light element targets and one heavy installed a Pt/C flight coating run takes twelve hours, largely owing to the low deposition rate of C, while W/Si takes roughly eight hours. Chamber parameters are summarized in Table 2.1. Pt, W and C targets were used for eight runs on average while Si was replaced every fifth run. Up to thirty-five substrates and a Si witness wafer can be coated in a single run. Witness sample specular reflectivity measured over the full NuSTAR energy range is the subject of Chapter 3.

The first layer of Pt/SiC substrates were coated with 32% larger cathodes compared to the standard size used throughout the coating campaign. No detailed investigation of these were carried out. They were decommissioned just prior to starting FM1 coating on account of unreliability.

An overview of the coating campaign carried out is given in Table 2.2 with additional details available from Appendix B

2.1.1 RXO coating facility

RXO coatings are applied with the same sputtering technique used at DTU. The coating geometry is shown in Fig. 2.4. Note the tilt of the mounted substrates. This was done to compensate for lower deposition rate away from the center of the target by decreasing the target-substrate

Table 2.1: Overview of the DTU chamber coating parameters for the NuSTAR flight coatings. The Ar pressure, p_{Ar}, was kept as low as possible to reduce micro-roughness, but high enough that plasma can reignite during coating. This is necessary as the plasma may discharge, refer to Sec. 3.4.2. Note that C4 was not used throughout the coating campaign.

	$P_{C1}[W]$	$P_{C2}[W]$	$P_{C3}[W]$	$P_{C4}[W]$	$p_{Ar}[mTorr]$
Pt/SiC	2500	2500	600	N/A	3.2
Pt/C	1100	1100	150	N/A	2.8
W/Si	900	900	860	N/A	$2.8 - 3.1$

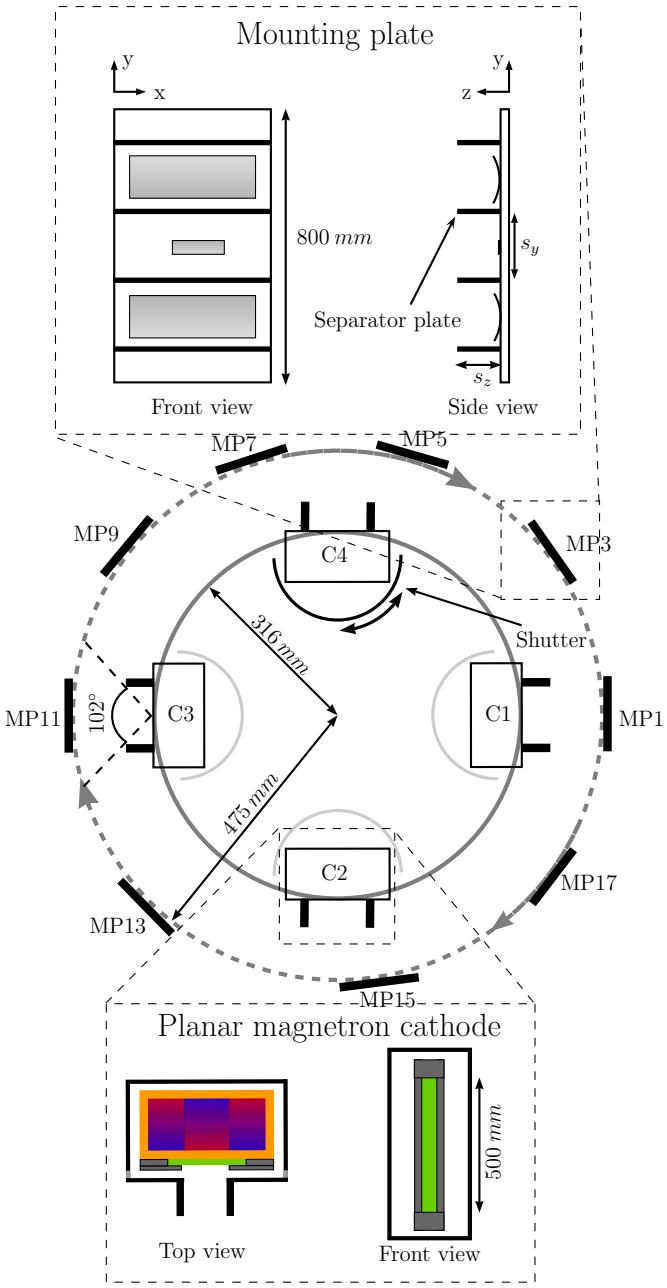

Figure 2.2: Schematic top view of the DTU coating chamber with front and side view of mounting plate 3 (MP3) and a detailed top and front view of the planar magnetron cathodes. MP3 is sketched with two substrates and a witness sample placed in between separator plates. Between three and four items can be mounted depending on separator plates, refer to Table 2.5 (Sec. 2.3). Separator plates for a given coating run is determined based on D_{sub} of the mounted substrates. Nine mounting plates were installed for NuSTAR coatings. The planar magnetron is sketched with the Cu cathode in orange. Three permanent magnets are shown within the cathode which in turn resides within the anode shield. The target is indicated in green. Cathode 1 through Cathode 3 (C1-C3) were used. The heavy material was always installed on C3.

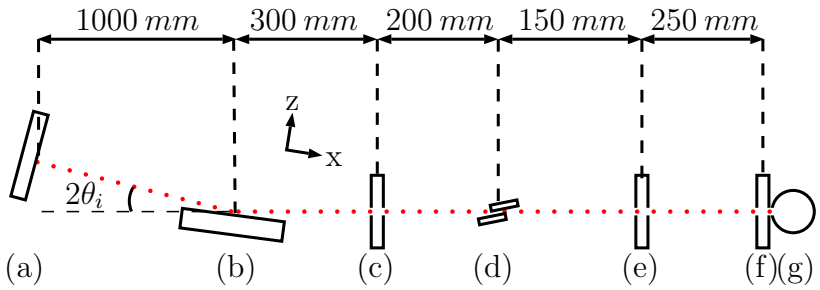

Figure 2.3: Sketch of the DTU 8 keV specular reflectivity beamline. Samples mount at (b) where x, y and z translations as well as yaw and roll motions are available. The detector (a) is a position sensitive gas proportional counter on a yaw stage centered on the sample. This enables θ-2θ scans to be executed, i.e. a scan in which the sample is illuminated at variable θ_i values with the detector located at $2\theta_i$. A slit at (c) defines the pencil beam after collimation through slits at (e) and (f). Pencil beam size is $2 \times 0.1\, mm^2$. The source (g) is a Cu rotating anode producing strong K_α and K_β lines. The 8.048 keV line ($K_{\alpha-1}$) is selected by an asymmetric cut Ge(111) monochromator crystal at (d). Roughly 950 mm of the 1900 mm total length is evacuated to $< 1\, Torr$ to reduce absorption. Refer to [35] for additional details on the beamline.

Table 2.2: Overview of the coating campaign carried out for the NuSTAR flight optics. D_{sub} is the slumped diameter of the substrates, ϕ_{sub} describes the span of the substrates and s_y is the distance between separator plates. Separator plate height is given by s_z (refer to Fig. 2.2). A value of "RXO" for s_y indicates that the coatings were carried out at the RXO coating facility introduced in Sec. 2.1.1. Separator plates are generally referred to based on their s_y value, i.e. "100 mm plates" indicates $s_y = 100\, mm$.

Optic	Layers	D_{sub} [mm]	ϕ_{sub}[°]	s_y [mm]	s_z [mm]	Materials
FM1	1	108	60	100	50	Pt/SiC
FM1	2-25	108-140	60	100	50	Pt/C
FM1	25-68	140-216	60	120	50	Pt/C
FM1	69-89	216-260	30	90	50	Pt/C
FM1	90-114	264-328	30	RXO	N/A	W/Si
FM1	113-133	324-380	30	120	50	W/Si
FM2	1	108	60	100	50	Pt/SiC
FM2	2-25	108-140	60	100	50	Pt/C
FM2	25-68	140-216	60	120	50	Pt/C
FM2	69-89	216-260	30	90	50	Pt/C
FM2	90-96	264-276	30	RXO	N/A	W/Si
FM2	97-100	280-288	30	90	50	W/Si
FM2	100-104	284-300	30	100	50	W/Si
FM2	104-133	296-380	30	120	50	W/Si

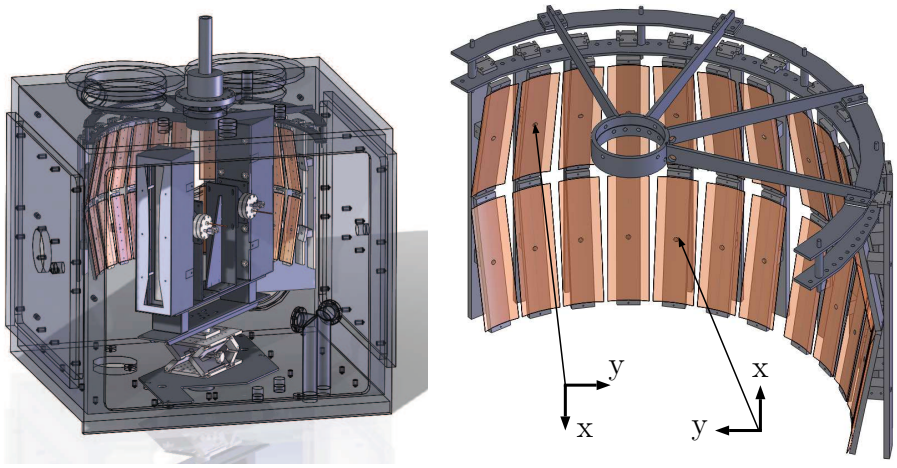

(a) (b)

Figure 2.4: RXO chamber setup (a) View of the RXO chamber in shell coating geometry. Cathodes are visible in the front and back (blue boxes). Targets are mounted vertically with masks to improve coating uniformity (b) Substrate fixture custom-built for NuSTAR. Witness samples were located at height with center top position. Note the inverted substrate coordinate system for the upper and lower rack. This was done to ensure substrates had similar non-uniformity regardless of rack.

distance. Additional details regarding the RXO coating facility can be found in [36]. RXO carried out a limited set of uniformity measurements. The results are presented in Sec. 2.3.

2.2 Coating uniformity

Past studies at DTU have shown significant non-uniformities ($> 15\%$) in the coating as a function of chamber location depending on target features (e.g. magnetic field topography and masks), installed separator plates and vertical placement on mounting plates [33, 34]. In addition to this, the curvature and extent of the substrate as well as the mounting plate rotation are expected to cause deviations from the coating applied to a flat witness sample. A full understanding of these effects will not be pursued here, but a first order quantitative study is carried out. While the measured values could be used at face value in the ORM, it is deemed appropriate to coarsely determine the origin of the non-uniformities. Modeling is secondary to providing an input to the ORM in the present work, but additional investigations are proposed in Sec. 2.4 for in-depth modeling. At the present stage the model is used to fill out gaps in the map caused by missing data points.

It is expected that the primary complication of a comprehensive model derive from the intricacies of the target and by extension deposition rate. In the following a simplistic view of these are assumed and geometrical contributions to the non-uniformity are laid out. In addition to this, it is assumed that the horizontal and vertical uniformity can be treated separately. This is done to simplify comparison to the data presented in Sec. 2.3. As both Γ and micro-roughness are anticipated to have a greater dependency on details not considered here, neither are modeled in this study.

2.2.1 Vertical uniformity

The overall setup of a mounting plate is shown in the inset of Fig. 2.2 with a more detailed view in Fig. 2.5. The figure indicates how the collimation of the target, and through this the coating uniformity, is substrate and separator plate dependent. The collimation at a point P for a setup is tracked through θ_{top} and θ_{bot} given by

$$\theta_{top} = arctan(\frac{\frac{s_y}{2} - y}{s_z - h_{z,x}}) \tag{2.1}$$

and

$$\theta_{bot} = 90 - arctan(\frac{s_z - h_{z,x}}{\frac{s_y}{2} + y}) \tag{2.2}$$

where

$$y = \frac{D_{sub}\sqrt{2 - 2cos(2\phi_i)}}{4} \tag{2.3}$$

and

$$h_{z,x} = \frac{1}{2}D_{sub}(1 - cos(\phi_i)) \tag{2.4}$$

y, $h_{z,x}$, ϕ_i, s_y and s_z are illustrated in Fig. 2.5. Note that for $\phi_i < 0$, $y = -y$. Further note that $-\frac{\phi_{sub}}{2} \leq \phi_i \leq \frac{\phi_{sub}}{2}$ with $\phi_{sub} = 30°$ or $\phi_{sub} = 60°$ depending on the layer, refer to Table 2.2. As an example, Eq. 2.1 and Eq. 2.2 result in the opening angle of the widest substrates (layer 68) being reduced by 18% at the substrate edges, i.e. $\phi_i = \frac{\phi_{sub}}{2}$, compared to the substrate center, $\phi_i = 0$.

Under the assumption that the deposition rate received from individual points on the target follows a simple inverse-square law, Fig. 2.5 indicates that an increase towards the substrate edges, dependent on $h_{z,x}$, can be expected. This is described by the coefficient $T_{z,x}$ given by

$$T_{z,x} = \frac{l_T^2}{(l_T - h_{z,x})^2} \tag{2.5}$$

where l_T is the distance from the target to the substrate mounting plate. For the above given example $T_{x,z}$ yields a 20% deposition rate increase near the substrate edges.

The above considerations could facilitate a straightforward geometric expression for the coating uniformity along the substrate y-axis if not for the complications introduced by target features. A simple model is proposed to accommodate some of these effects. Assuming the ejection law (Eq. 1.4) to be valid along the length of the target, a point P on the substrate would receive maximum deposition rate from the forward ejection direction. Other target locations would contribute following Eq. 1.4, but with $|\xi| > 0$. In other words the ejection law may be expressed seen from P as a "deposition law". This may in turn be evaluated to provide a coefficient T_{dep} for the exposed target efficiency

$$T_{dep} = \int_{\xi_d=\theta_{bot}}^{\theta_{top}} \frac{cos(\xi_d)}{\alpha_d^2 + (1 - \alpha_d^2)cos^2(\xi_d)} d\xi_d \tag{2.6}$$

Similar to α_e in Eq. 1.4, α_d determines the shape of the distribution, while ξ_d is the angle to normal incidence on the substrate mounting plate. T_{dep} describes the exposed target efficiency at P as a function of mounting plate setup through the integration limits. The extent of the target must also be accounted for, i.e. maximum values for θ_{top} and θ_{bot}. These are given by

$$\theta_{T,top} = arctan(\frac{y_{T,top}}{l_T - h_{z,x}}) \tag{2.7}$$

and

$$\theta_{T,bot} = arctan(\frac{y_{T,bot}}{l_T - h_{z,x}}) \tag{2.8}$$

respectively. As shown in Fig. 2.6, $y_{T,bot}$ and $y_{T;top}$ describe the physical extent of the target. α_d is expected to be close to 1 for all relevant material combinations [16], acting as a coarse fitting parameter in this context. Coarse, since it does not account for differences between light and heavy materials, resputtering and Ar induced particle scattering, all of which may in turn be a function of P, owing to magnetic field variations and/or masking artifacts. These shortcomings may at least partially be accounted for by measuring the deposition rate profile T_y of the target. Ideally, this would be described by

$$T_y = \int_{\xi_d=\theta_{T,bot}}^{\theta_{T,top}} \frac{cos(\xi_d)}{\alpha_d^2 + (1 - \alpha_d^2)cos^2(\xi_d)} d\xi_d \tag{2.9}$$

for a given point and α_d. Note that Eq. 2.9 is simply Eq. 2.6 taken over the full extent of the target disregarding the limitations imposed by the separator plates (i.e. θ_{top} and θ_{bot}). As such a measured value of T_y can be used to normalize T_{dep}.

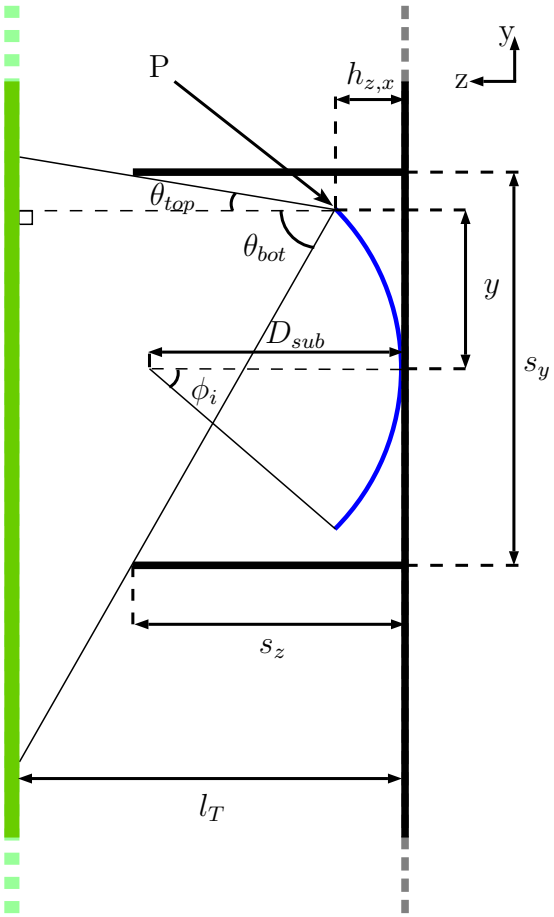

Figure 2.5: Detailed view of substrate (blue) installed between separator plates at a distance l_T from the target (green). Separator plate width (s_z) and height (s_y) cause collimation of the target at a point P expressed through a top and bottom opening angle (θ_{top} and θ_{bot}). P lies y above the vertical center of the substrate in the mounting plate plane (xy). Depending on the specific substrate (defined by D_{sub}) and ϕ_i, P will be $h_{z,x}$ above the mounting plate plane. ϕ_i is shown at its additive inverse to reduce clutter near P.

Changes in T_y caused by target wear are not accounted for. The data set discussed in Chapter 3 imply that target wear leads to $< 2\%$ decrease in deposition rate between consecutive flight coatings. As such it is negligible in the comparably thin coatings deposited for the investigations in this chapter.

2.2.2 Horizontal uniformity

Traditionally, horizontal uniformity is approximated by two line sources equidistant from the horizontal center of the target, corresponding to the "racetrack" created by characteristic electron paths [37]. Here this is simplified and the deposition is assumed to derive from a line drawn down the center of the target. From this the rotation of the mounting plate influences the coated d-spacing through projected footprint $cos\theta_t$ and increased target-substrate distance l_T. From Fig. 2.7 trigonometry shows that

$$\theta_t = arctan(u/r_c) \tag{2.10}$$

and

$$h_{z,y} = \sqrt{u^2 + r_c^2} - r_c \tag{2.11}$$

where r_c is the chamber rail rotational radius and u is the distance from the substrate center to the target normal along the length of the substrate, i.e. $u = 0$ for $\theta_t = 0$. Again assuming

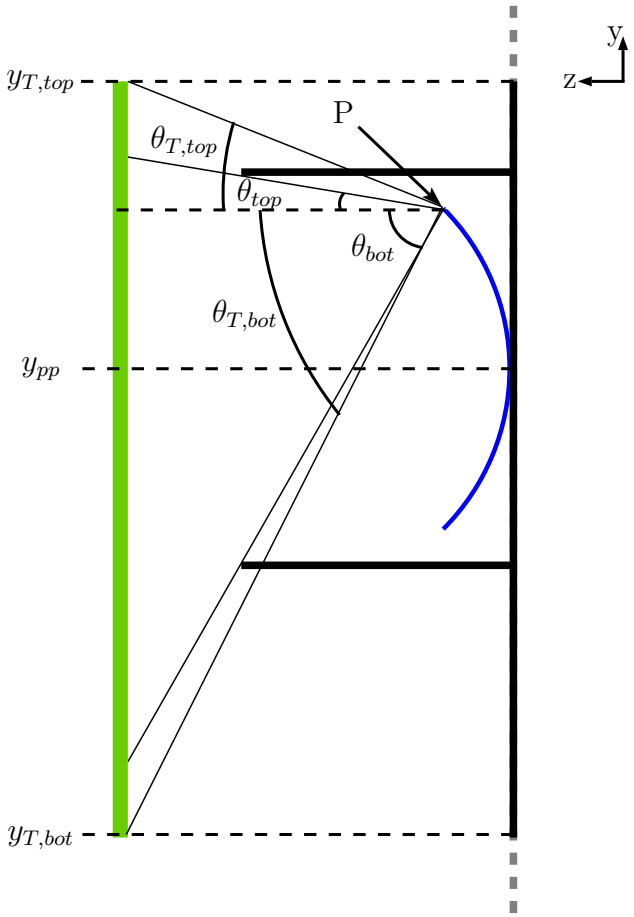

Figure 2.6: Detailed view of substrate (blue) and target opening angles $\theta_{T,top}$ and $\theta_{T,bot}$ as seen from a point P. Depending on the mounting plate setup, and the value of y_{pp}, the target opening angles may be smaller than θ_{top} and θ_{bot}. This must be accounted for in Eq. 2.9. y_{pp} values are given in Table 2.5 (Sec. 2.3).

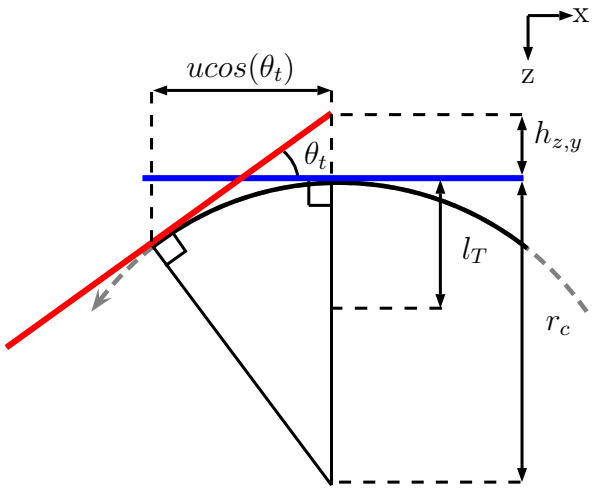

Figure 2.7: Sketch of a substrate (blue) directly across from the target and one rotated (red) on the chamber rail radius r_c such that the target distance is increased to $l_T + h_{z,y}$ and the footprint reduced by $cos(\theta_t)$. The substrate has been assumed flat for illustrative purposes.

the deposition rate to have a straightforward inverse-square law dependency the reduction in the horizontal plane can be expressed through

$$T_x = cos(\theta_t)\frac{l_T^2}{(l_T + h_{z,y})^2} \tag{2.12}$$

For $u = 112.5\,mm$, corresponding to half the length of a NuSTAR substrate, $h_{z,y}$ is approximately $13\,mm$, indicating a 15% reduction in deposition rate. Maximum θ_t is roughly 13° corresponding to a 2.5% smaller footprint at the extreme points of the substrate. A high θ_t could further increase the micro-roughness, but previously mentioned studies [34] indicated that the effect only becomes pronounced at angles higher than 20°.

The chamber is assumed to have complete rotational symmetry, such that all mounting plates experience the same horizontal uniformity. This is not strictly correct on account of the mounting plate placement relative to vertical support rods, for the mounting plate fixtures, as well as the position relative to the cathodes at the beginning and end of a run. The rods follow the mounting plate and are not situated so to cause direct shadowing between substrate and target. For this reason the perturbation is assumed negligible. The relative position to the cathodes should not influence uniformity, but will result in some coatings having a light material laid down first. This has no noticeable impact on specular reflectivity. Steps are taken to ensure the final layer is always Si or C. As discussed in Sec. 2.3.1, differences in uniformity between mounting plates derive primarily from mounting plate fixture slew.

2.3 Coating uniformity campaign

According to the discussion in Sec. 2.2 a multilayer laid down on a flat witness sample in one specific chamber location will not provide an accurate account of the coating deposited on curved substrates distributed throughout the chamber. To investigate this, a two part uniformity campaign was carried out. The priority task was sampling a number of points on twenty cst-d coated spare flight substrates, representing all possible substrate mounting setups and material combinations at DTU. These substrates were coated immediately following the flight coating campaign in March 2011 and provide the minimum required uniformity input to the ORM. The location of the measurement points is illustrated in Fig. 2.8. All data was taken at the $8\,keV$ beamline. Initially data was acquired in nine points only (1-9). An additional eight points (A-H) were measured to improve coverage near the substrate edges. An overview of the uniformity sample set is available in Table 2.3. Note that cracks and broken edges meant that a few substrates were not measured in all points. The missing points are primarily from the second round of measurements, i.e. A-H. Uniformity

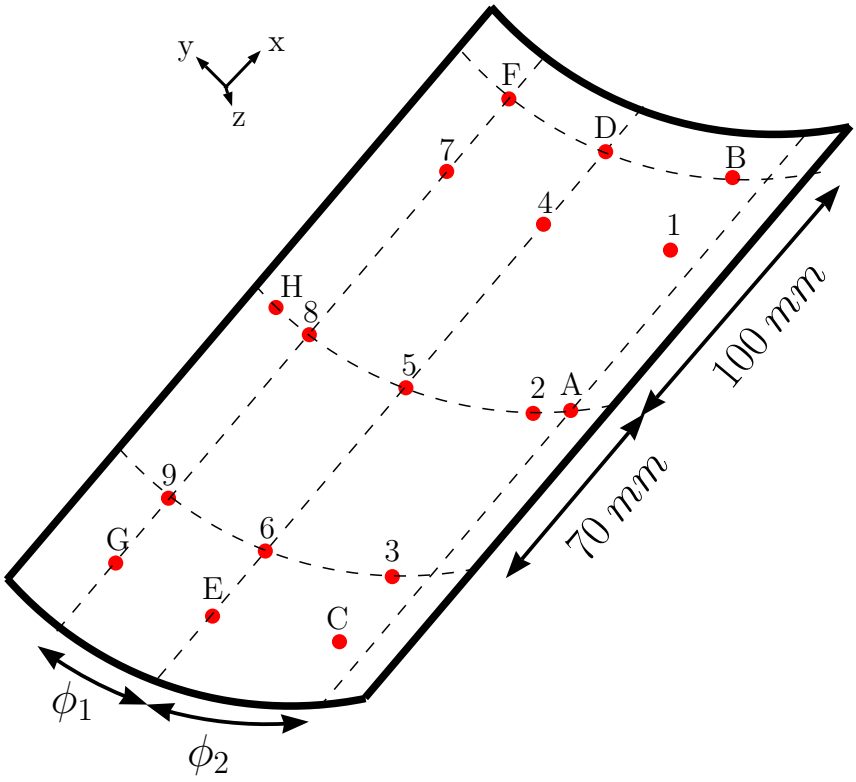

Figure 2.8: Overview of uniformity measurement points on flight substrates. For substrates with $\phi_{sub} = 30°$, $\phi_1 \approx 9.5°$ and $\phi_2 \approx 12.5°$ while for 60° segments $\phi_1 \approx 19°$ and $\phi_2 \approx 25°$. Uncertainty in point location is $\pm 3\,mm$ in both directions.

witness sample details are collected in Table 2.4. Table 2.5 contain additional information about the substrate and witness sample chamber locations with reference to Fig. 2.5 and Fig. 2.6.

The second part of the campaign consisted of establishing how well-understood the uniformity data is from the considerations made in Sec. 2.2. To assist with this an additional five substrates and twenty Si wafers were coated in September and October 2011. An overview of these data can be found in Table 2.6 and Table 2.7. Note that focus is on the 100 mm setup and Pt/C. Section 2.4 propose additional work required to develop the model further.

The entire data set acquired in this campaign is available from Appendix C.

2.3.1 Optic response model input data

A selection of the uniformity data is presented here. Similar plots for the entire data set can be found in Appendix D. The point-wise modification of the coating is available from Appendix C. The point-wise modifications represent the uniformity input to the ORM in Chapter 5. Note that values derived from the proposed model are used in place of missing data points.

Figure 2.9 and Fig. 2.10 show uniformity data acquired with 100 mm and 90 mm plates. The relative thicknesses corresponds to the measured percentage difference from the witness sample multilayer as a function of substrate location. The quoted uncertainty for each point contains contributions from several sources. d-spacing determination at the 8 keV beamline can be done to within ± 0.2 Å. Depending on the d-spacing in question this results in $0.5 - 2\%$ uncertainty. The point location is determined to within $\pm 3\,mm$. The impact of this is model-dependent and difficult to estimate based on discrete points, especially well away from $y = 0$. Based on the considerations in Sec. 2.2.1 it is anticipated to add on average 2% uncertainty, primarily deriving from the change in $h_{z,x}$ along y. The data set further implies an average uncertainty of 2% in deposition rate between mounting plates. The average uncertainty is estimated based on plate position 2, plate 5 (PP2P5) data. Data from two mounting plates per coating run are available from this position, namely the witness sample and a substrate. The difference between plates cannot be explained by a rate

Table 2.3: Overview of the uniformity data set. Plate position describes vertical position of the installed item. Refer to Fig. 2.2, Fig. 2.8 and Table 2.5 for geometry and further details. The substrate naming convention goes: mandrel name (NxxxA or NxxxB), production cycle (yyy), layer (zzz), mirror location (P for hyperbola/upper placement or S for parabola/lower) and span (0 for 60° and 1 or 2 for 30°). It is further worth noting that "xxx" equals D_{sub} in millimeters.

Witness	Substrate	$s_y[mm]$	Plate pos.	Mount. plate	Point
Si5358		120	2	9	5
	N352A539-124S2	120	1	7	123456789ABCDEFGH
	N356A570-125P1	120	2	7	123456789ABDEFGH
	N356B568-125S1	120	3	7	123456789ABCDEGH
Si5359		100	2	5	5
	N352A573-123P2	100	1	3	123456789ACDEGH
	N348B568-123S2	100	2	3	123456789ABCDEFGH
	N356A548-124P2	100	3	3	123456789ACEH
Si5360		90	2	9	5
	N280A500-098S1	90	1	7	123456789ABCDEFGH
	N280B517-098S2	90	2	7	123456789ABCDEFGH
	N284B493-099P2	90	3	7	123456789ABCDEFGH
	N284A516-099S1	90	4	7	123456789ABCDEFGH
Si5372		100	2	5	5
	N184B409-051P0	100	1	3	123456789ABCDEFGH
	N180B384-051S0	100	2	3	123456789ABCDEFGH
	N184B423-052P0	100	3	3	123456789ABCDEFGH
Si5373		90	2	9	5
	N144B420-027P0	90	1	7	123456789ABCDEFGH
	N144B423-027P0	90	2	7	123456789ABCDEFGH
	N144B432-028P0	90	3	7	123456789ABCDEFGH
	N144B428-028S0	90	4	7	123456789ABCDEFGH
Si5374		120	2	13	5
	N184B418-052S0	120	1	11	123456789ABCDEFGH
	N188A432-053P0	120	2	11	123456789ABCDEFGH
	N184B426-053S0	120	3	11	123456789

Table 2.4: Overview of the uniformity witness samples. d-spacing, Γ and micro-roughness were measured at the 8 keV beamline. d is determined to within ±0.2 Å, Γ to ±0.01 and micro-roughness to ±0.2 Å.

Witness	d [Å]	N	Γ	σ[Å]	s_y	Material
Si5358	35.9	10	0.45	3.0	120	W/Si
Si5359	44.7	10	0.43	3.4	100	W/Si
Si5360	44.2	10	0.43	3.3	90	W/Si
Si5372	58.8	10	0.43	3.3	100	Pt/C
Si5373	55.8	10	0.45	3.1	90	Pt/C
Si5374	64.2	10	0.44	3.3	120	Pt/C

Table 2.5: Vertical position y_{pp} of measurement point 5 in relation to bottom edge of the mounting plate for different separator plate setups. Witness samples are always mounted at y_{pp} for plate position 2 (PP2P5), unless otherwise noted. In addition to the values given in the table, it is worth noting that $y_{T,top} = 590\,mm$ and $y_{T,bot} = 90\,mm$.

$s_y[mm]$	Plate pos.	$y_{pp}[mm]$
90	1	480
90	2	390
90	3	300
90	4	210
100	1	470
100	2	370
100	3	270
120	1	460
120	2	340
120	3	220

Table 2.6: Overview of extra data acquired to model chamber non-uniformities. Plate position describes vertical position of the installed item. Refer to Fig. 2.2, Fig. 2.8 and Table 2.5 for geometry and further details. The substrate naming convention goes: mandrel name (NxxxA or NxxxB), production cycle (yyy), layer (zzz), mirror location (P for hyperbola/upper placement or S for parabola/lower) and span (0 for 60° and 1 or 2 for 30°). It is further worth noting that "xxx" equals D_{sub} in millimeters.

Witness	Substrate	$s_y[mm]$	Plate pos.	Mount. plate	Point
Si5449		100	2	5	5
	N136B408-023S0	100	2	1	123456789ABCDEFGH
Si5451		100	2	5	5
	N140A418-024S0	100	2	1	123456789ABCDEFGH
Si5452		100	2	5	5
	N140B418-024S0	100	2	1	123456789ABCDEFGH
Si5480		100	2	3	5
Si5486		100	2	5	5
	N108B432-001P0	100	1	5	123456789ABCDEFGH
	N180B398-050P0	100	3	5	123456789ABCDEFGH

Table 2.7: Overview of coated Si wafers for determining chamber non-uniformities. d-spacing was measured at the 8 keV beamline and determined to within ±0.2 Å.

Witness	d [Å]	N	Γ	s_y	$y_{pp}[mm]$	Mount. plate	Material
Si5449	39.5	10	0.45	100	370	5	Pt/C
Si5451	22.7	10	0.46	100	370	5	Pt/C
Si5452	113.4	10	0.44	100	370	5	Pt/C
Si5475	54.4	10	0.47	100	510	3	Pt/C
Si5476	56.8	10	0.43	100	470	3	Pt/C
Si5477	45.4	10	0.45	100	440	3	Pt/C
Si5478	51.0	10	0.45	100	400	3	Pt/C
Si5480	58.2	10	0.43	100	370	3	Pt/C
Si5482	49.4	10	0.43	100	340	3	Pt/C
Si5483	54.8	10	0.44	100	300	3	Pt/C
Si5484	63.0	10	0.44	100	270	3	Pt/C
Si5485	55.2	10	0.46	100	240	3	Pt/C
Si5486	57.9	10	0.45	100	370	5	Pt/C
Si5487	54.8	10	0.48	N/A	570	7	Pt/C
Si5488	64.0	10	0.46	N/A	520	7	Pt/C
Si5489	67.0	10	0.42	N/A	470	7	Pt/C
Si5490	70.0	10	0.42	N/A	420	7	Pt/C
Si5491	72.0	10	0.42	N/A	370	7	Pt/C
Si5492	74.4	10	0.435	N/A	320	7	Pt/C
Si5493	76.2	10	0.45	N/A	270	7	Pt/C
Si5494	78.0	10	0.47	N/A	220	7	Pt/C
Si5495	76.2	10	0.49	N/A	170	7	Pt/C
Si5496	65.0	10	0.49	N/A	120	7	Pt/C

change over time as all ten bilayers are affected approximately equally. This implies a geometric explanation. There is no correlation between relative chamber mounting plate placement and the observed variation. The lack of correlation implies that differences in target distance caused by plate mounting slew is to blame. The mounting plate is fixed with a slew of a few millimeters and may inadvertently be installed at a slight angle. The combination of mounting errors adds up to 6% uncertainty for points located far from the mounting plate center (e.g. PP1PH), and corresponds well with the observed 2% uncertainty at PP2P5. Finally, a number of points near the substrate edges were mounted poorly at the 8 keV beamline resulting in increased uncertainty in d-spacing determination. Relevant points are indicated with red in the figures. Based on expected values from the model this effect is estimated to add 5% uncertainty.

Relative Γ and micro-roughness values are also included in the ORM input. Available data is discussed in Sec. 2.3.6 and Sec. 2.3.7.

2.3.2 Vertical uniformity: Model verification

To minimize the influence of horizontal uniformity only data from $x = 0$, i.e. points A, 2, 5, 8 and H, is used in the following.

T_y was measured by installing ten Si wafers on a mounting plate with no separator plates. The setup is shown in Fig. 2.11. Refer to Table 2.7 for sample details. The observed deposition rate profile is plotted in Fig. 2.12. The shape is ill-described by Eq. 2.9, regardless of α_d, due to its asymmetry. The asymmetry is fit by adding a gradient to l_T, corresponding to the target being tilted by 2.5° in relation to the mounting plate, and having $\alpha_d = 6$. Such a severe tilt is not reasonable given the relevant mounting uncertainties. This is confirmed in Fig. 2.13, where data from coatings carried out with separator plates installed, is shown. The tilt clearly skews the deposition rate more than it should. T_{dep} is also shown in the figure with $\alpha_d = 1.75$. From this it is concluded that the asymmetric deposition profile is due to intricacies of the target not considered here, chiefly deriving from effects near the target ends. Two likely candidates are poorly designed masks and non-uniform magnetic field topography of the cathode. T_y data is still useful, however, in that it provides normalization to T_{dep} for the relevant opening angles. Normalization was already imposed on the model shown in Fig. 2.13. Similarly, Fig. 2.14 shows the normalized model compared to data from two curved substrates. As can be seen the overall shape of the deposition is well-described. In Fig. 2.15, $T_{z,x}$ (Eq. 2.5) has been added to the model to take into account the change in deposition rate with target distance. All but but one point is now within the error bars, but the fit to N108B432-001P0 data is significantly worse compared to Fig. 2.14. A potential cause could be the high $h_{z,x}$ (low D_{sub}) of this substrate and may indicate that deposition rate is tied to substrate curvature in a more intricate way than considered here. Sampling a broader range of D_{sub} values is required to establish the mechanism.

Fig. 2.16 shows data from all uniformity coating runs taken at $x = 0$ with 100 mm plates and Pt/C coatings. Note that models for all measured substrate diameters are plotted. The seemingly heavy line in the middle separator plate range is due to substrates having nearly the same D_{sub}, refer to Table 2.3 and Table 2.6. Figure 2.17 shows all data taken on W/Si with 90 mm plates. The model has not had T_y imposed, as this was not measured for W/Si. The data indicates that T_y for W/Si would also have a hump near the bottom of the target. The hump would compensate for the model undershoot around 200 mm plate height. That the hump remains makes a strong case for magnetic field topography dominating T_y, as this would not change significantly between materials. Appendix E contains similar plots for all coating geometries.

2.3.3 Horizontal uniformity: Model verification

The rotation of the mounting plate is expected to reduce the d-spacing along the x-axis of the substrate as discussed in Sec. 2.2.2. To eliminate the influence of the substrate curvature on the coated d-spacing, the relative thickness in points 2, 5 and 8 is assumed to be nominal d for the row in question. Doing so effectively replaces PP2P5 as the overall nominal d, as illustrated in Fig. 2.18. The same data are shown in Fig. 2.19 collapsed to a single line. Data from all measured substrates are plotted and a fit to the data is shown. Ideally this would equal Eq. 2.12, but as implied by the inverse-square law, also plotted in Fig. 2.19, T_x unmodified would severely

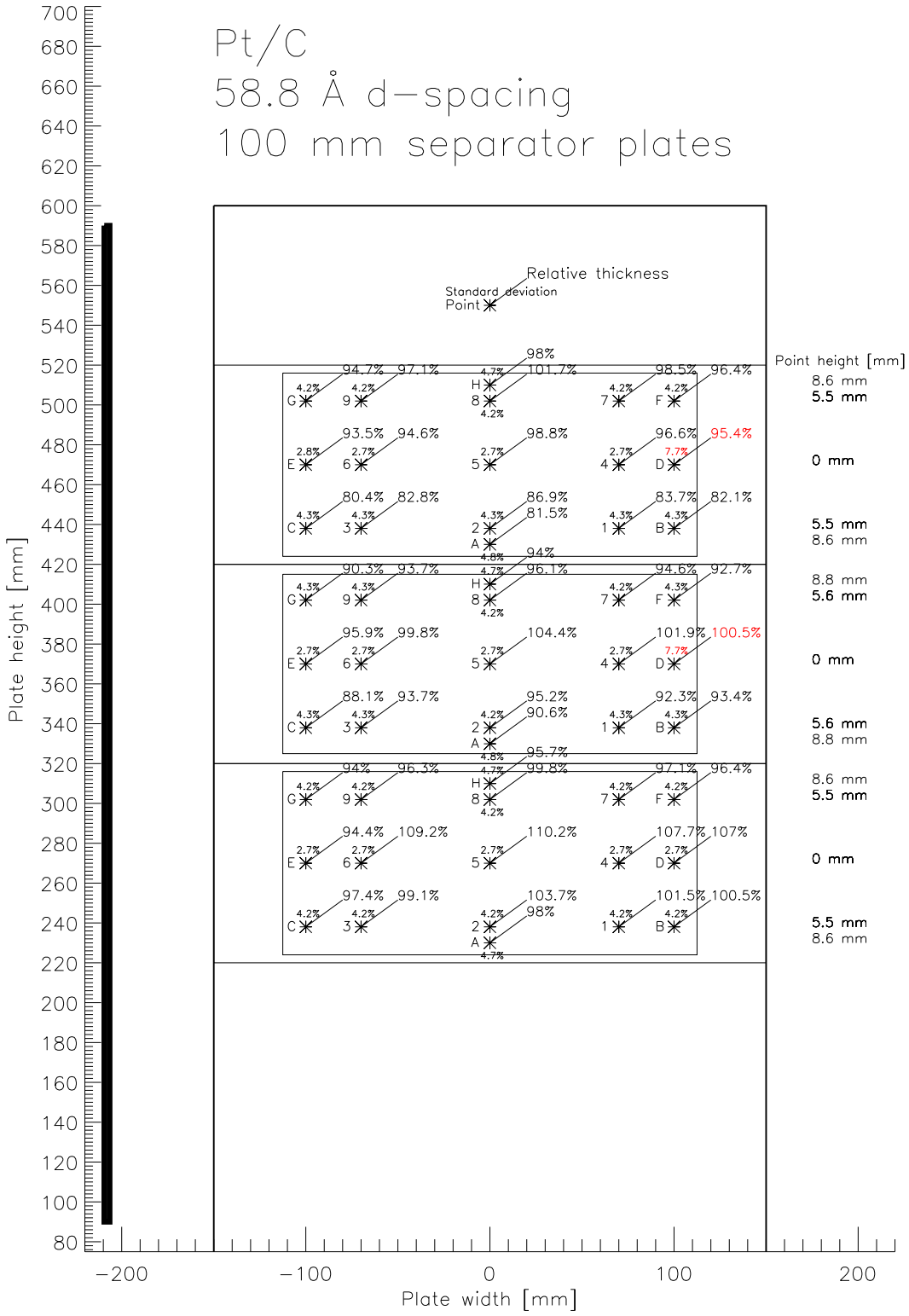

Figure 2.9: Uniformity mapping expressed through relative thickness between location on substrate and witness sample mounted in PP2P5 on different mounting plate. Estimated standard deviation of each point is indicated. Values colored red indicate substrate mounting issue at the 8 keV beamline. Uncertainty in point location is coarsely given by star. The vertical target extent is indicated by thick black line on left side.

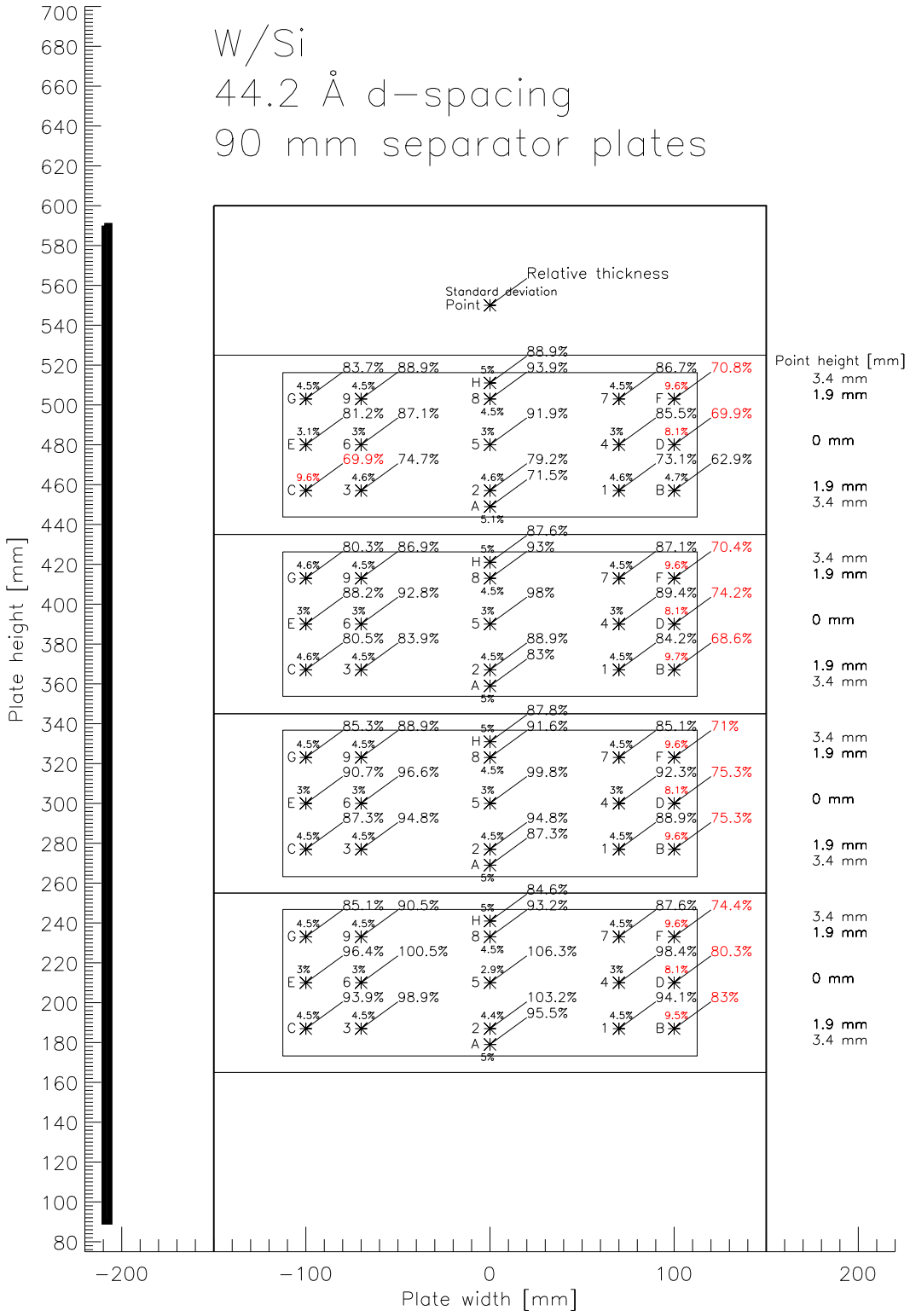

Figure 2.10: Uniformity mapping expressed through relative thickness between location on substrate and witness sample mounted in PP2P5 on different mounting plate. Estimated standard deviation of each point is indicated. Values colored red indicate substrate mounting issue at the $8keV$ beamline. Uncertainty in point location is coarsely given by star. The vertical target extent is indicated by thick black line on left side.

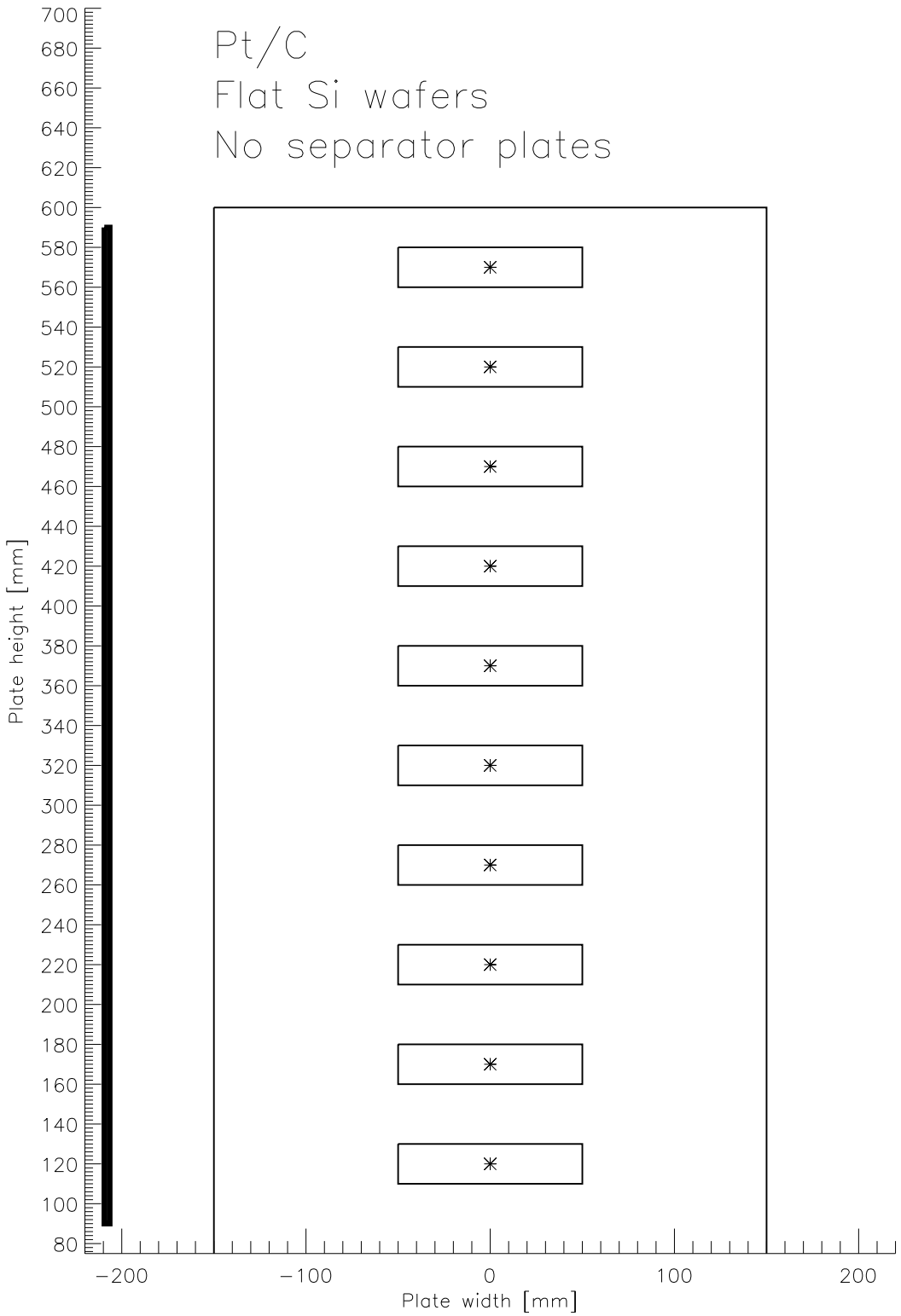

Figure 2.11: Sample setup for determining T_y by measuring coated d-spacing on flat Si wafers. Uncertainty in point location is coarsely given by star. With no separator plates installed the sample is exposed to the full target opening angle. The vertical target extent is indicated by thick black line on left side.

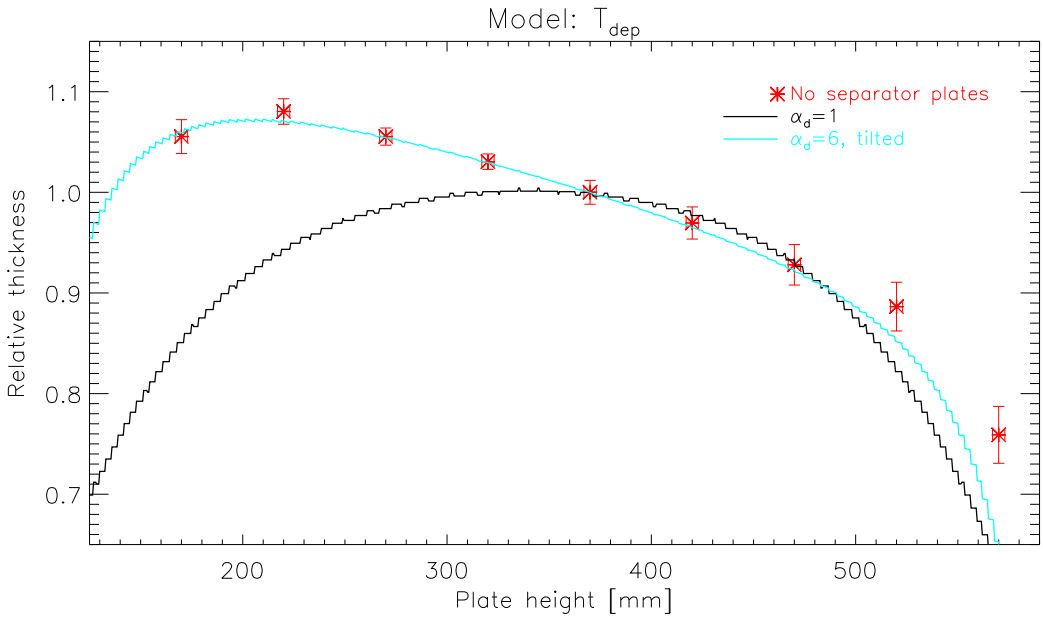

Figure 2.12: Data from ten points along the vertical height of a mounting plate (red) plotted against T_{dep} in two configurations, namely expected α_d value (black) and high α_d value (teal). No separator plates were installed. The high value model further includes a tilt angle of 2.5° between target and mounting plate. Given mounting uncertainties this model is not realistic.

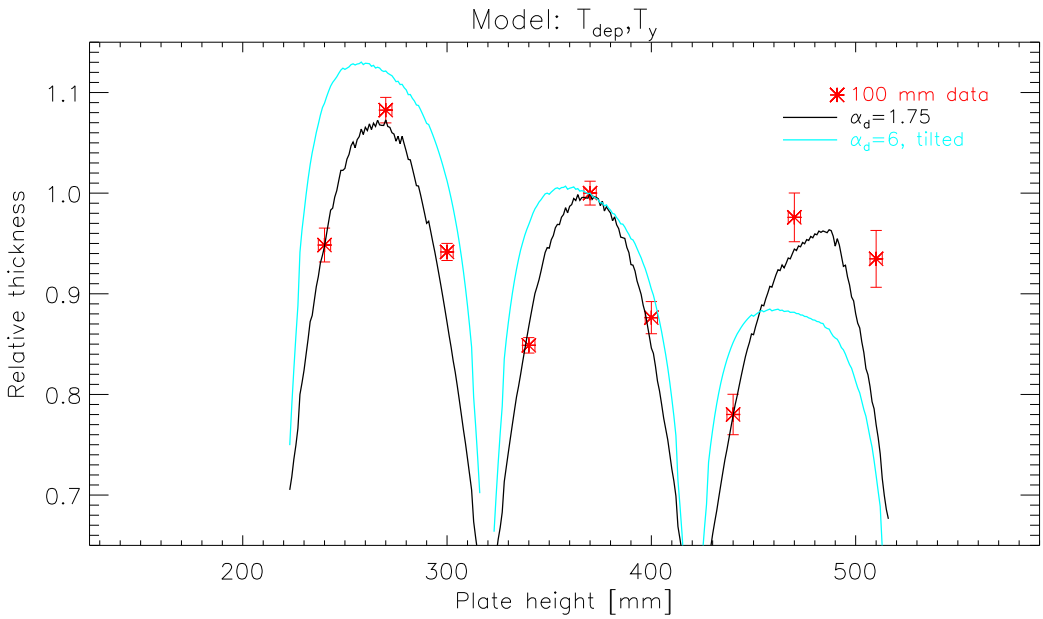

Figure 2.13: Data from nine points along the vertical height of a mounting plate (red) with $100mm$ plates installed. T_{dep} in two configurations is also plotted. The tilted model cannot account for the collimated deposition. $\alpha_d = 1.75$ comes close overall, but displays some discrepancies near the top of the plate. Note that models are plotted to the edge of the separator plates, i.e. beyond the extent of the samples.

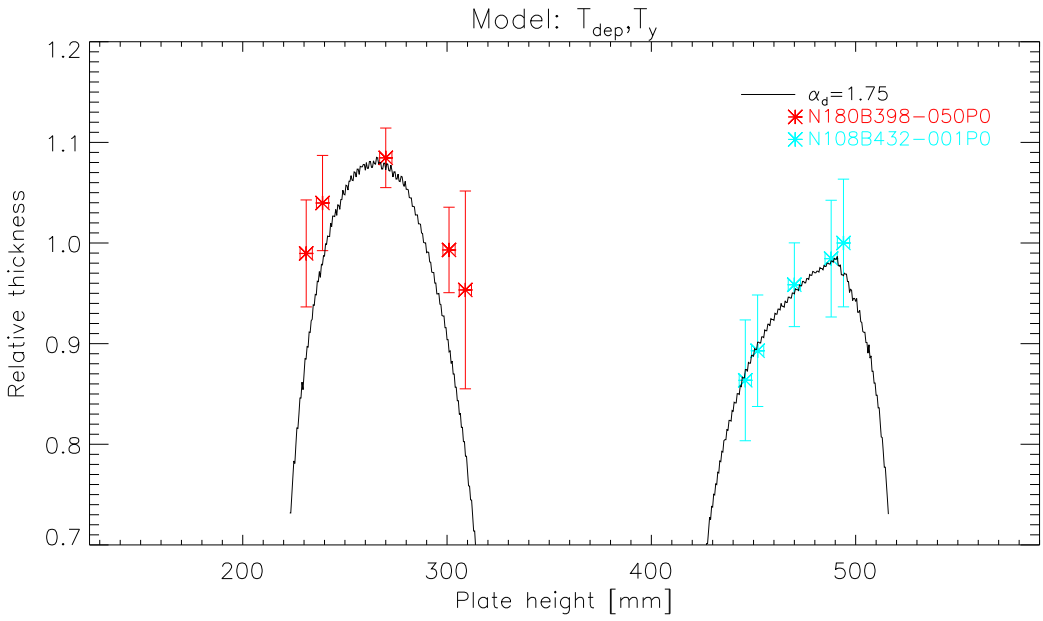

Figure 2.14: Data from curved substrates compared to model. The model has been scaled according to T_y. Note that models are plotted to the edge of the separator plates, i.e. beyond the extent of the substrates.

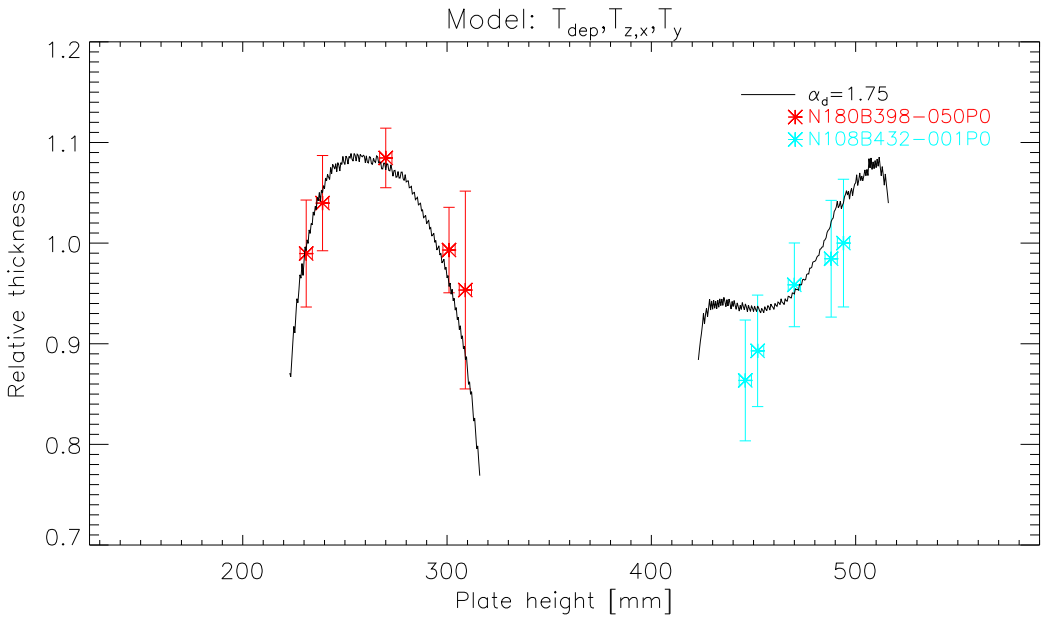

Figure 2.15: Data from curved substrates compared to model. The model has been scaled according to T_y. The model is further modified by $T_{z,x}$ to compensate for the decrease in target-substrate distance with substrate curvature. The low diameter substrate data (teal) indicates that additional effects act as a function of D_{sub}.

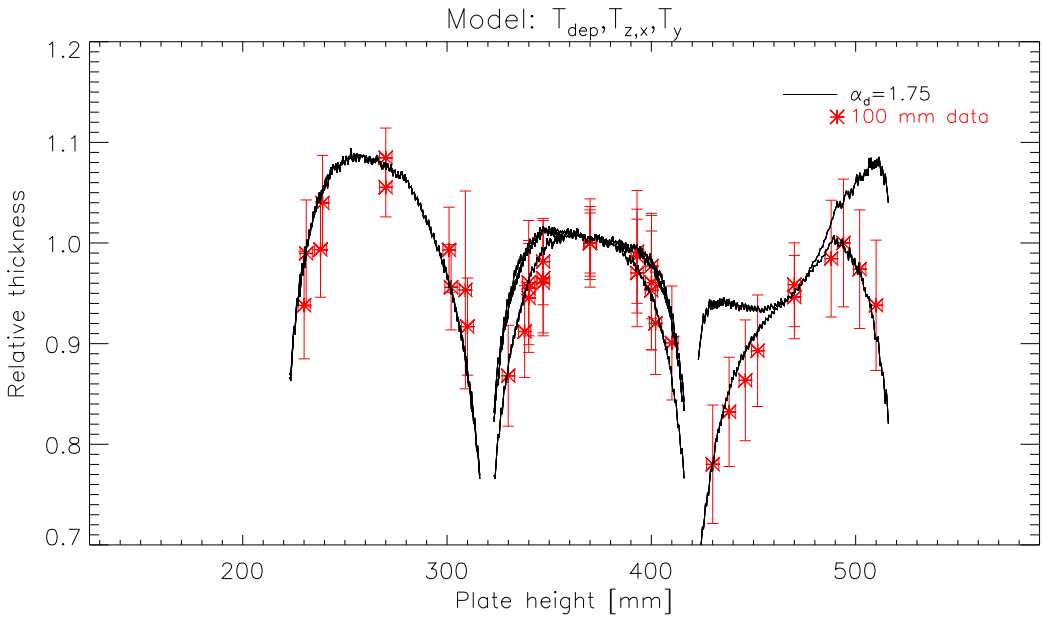

Figure 2.16: Data from all uniformity substrates coated with Pt/C using 100 mm plates compared to model. As the model is dependent on D_{sub} a total of eight models are plotted here, but only the six unique D_{sub} values are discernible.

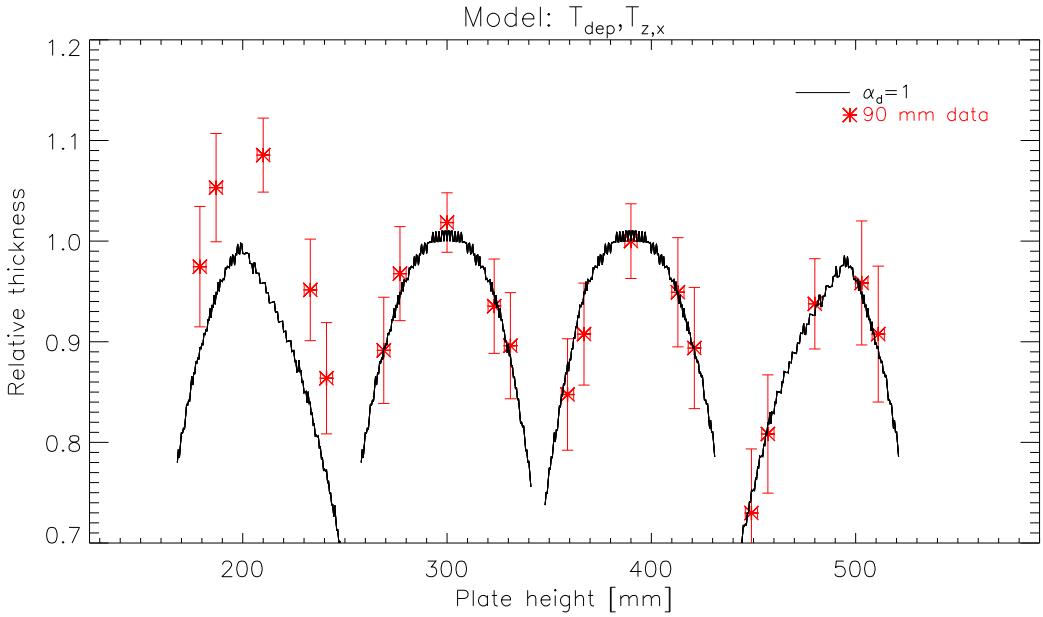

Figure 2.17: Data from all uniformity substrates coated with W/Si using 90 mm plates compared to model. The model is not scaled in relation to T_y as this was not measured for W/Si. The data indicates that the target deposition profile would be similar to the one found for Pt/C. This implies the asymmetry to be caused by the cathode.

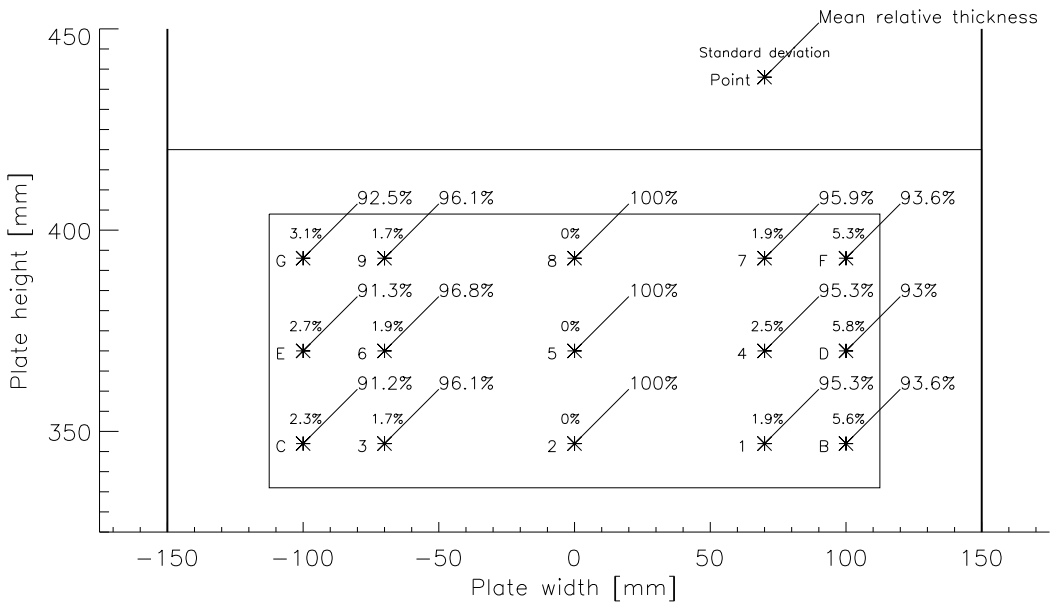

Figure 2.18: Row-wise mean relative thickness compared to the horizontal central point (2, 5 and 8, refer to Fig. 2.8) d in 15 points for the entire uniformity data set, disregarding plate position and coating type. The high standard deviation of in particular points B, D and F are due to mounting issues at the 8 keV beamline. Vertical point location and substrate extent are for illustrative purposes only.

underestimate the relative thickness as a function of rotation. To compensate for this the plotted T_x value is found by scaling $h_{z,y}$ with $\beta_s = 0.43$. A likely candidate for explaining the scaling is the assumption of the target being a one-dimensional line.

2.3.4 Substrate uniformity: Full model verification

Combining the results from Sec. 2.3.2 and Sec. 2.3.3 one may estimate the relative thickness as a function of substrate and mounting plate setup. Examples of this are shown in Fig. 2.20 for Pt/C and Fig. 2.21 for W/Si. Appendix F contain similar plots for all uniformity data. For convenience, Fig. 2.22 and Fig. 2.23 provides an overview of the measured versus modeled relative thicknesses for Pt/C, using 100 mm, and W/Si, using 90 mm, plates. Appendix G contain overview plots for all separator plates. For Pt/C, there is good correspondence with the model across the board, albeit with a slight bias towards model overshoot. For W/Si the lack of T_y shows itself by the model missing in particular the bottommost mounted substrates, as was clearly seen in Fig. 2.17. The missing normalization of T_{dep} bias the data set towards a model undershoot.

2.3.5 Uniformity as a function of d-spacing

The flight coatings consist of graded multilayers and as such it must be established that the non-uniformities are independent of the thickness of the individual bilayers. To reduce the contributions from other sources three substrates with nearly the same curvature were selected and coated in three separate runs with identical mounting plate setup. The mean relative d is illustrated in Figure 2.24. Considering the uncertainties discussed in Sec. 2.3.1, standard deviations given in Fig. 2.24 strongly imply uniformity to be independent of d-spacing. This is assumed to be the case regardless of material combination, plate position and D_{sub}.

2.3.6 Γ uniformity

Based on the flat Si data, listed in Table 2.7, Γ on the uniformity substrates is expected to follow the trend shown in Fig. 2.25. No attempt at modeling these values has been made as it requires

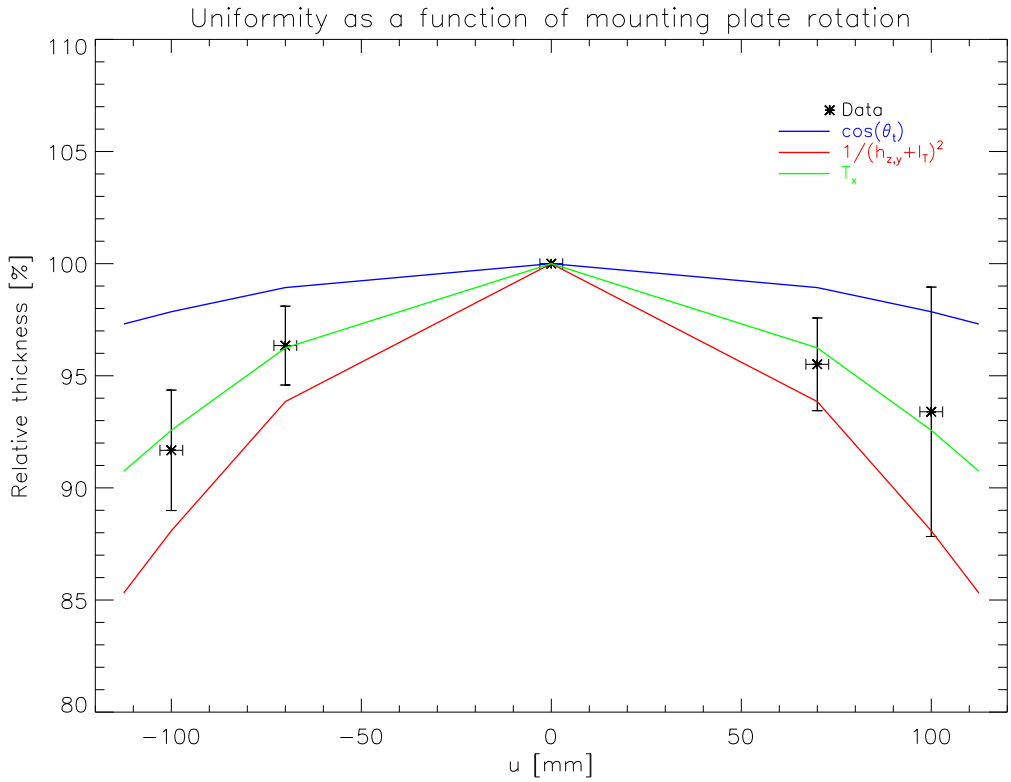

Figure 2.19: Data points showing Fig. 2.18 vertical means compared to a simple cosine (blue) with θ_t given by Eq. 2.10 and the dependency on target distance (red) described by Eq. 2.11. The product of these two contributions, T_x given by Eq. 2.12, is shown (green) with $h_{z,y}$ scaled by $\beta_s = 0.43$.

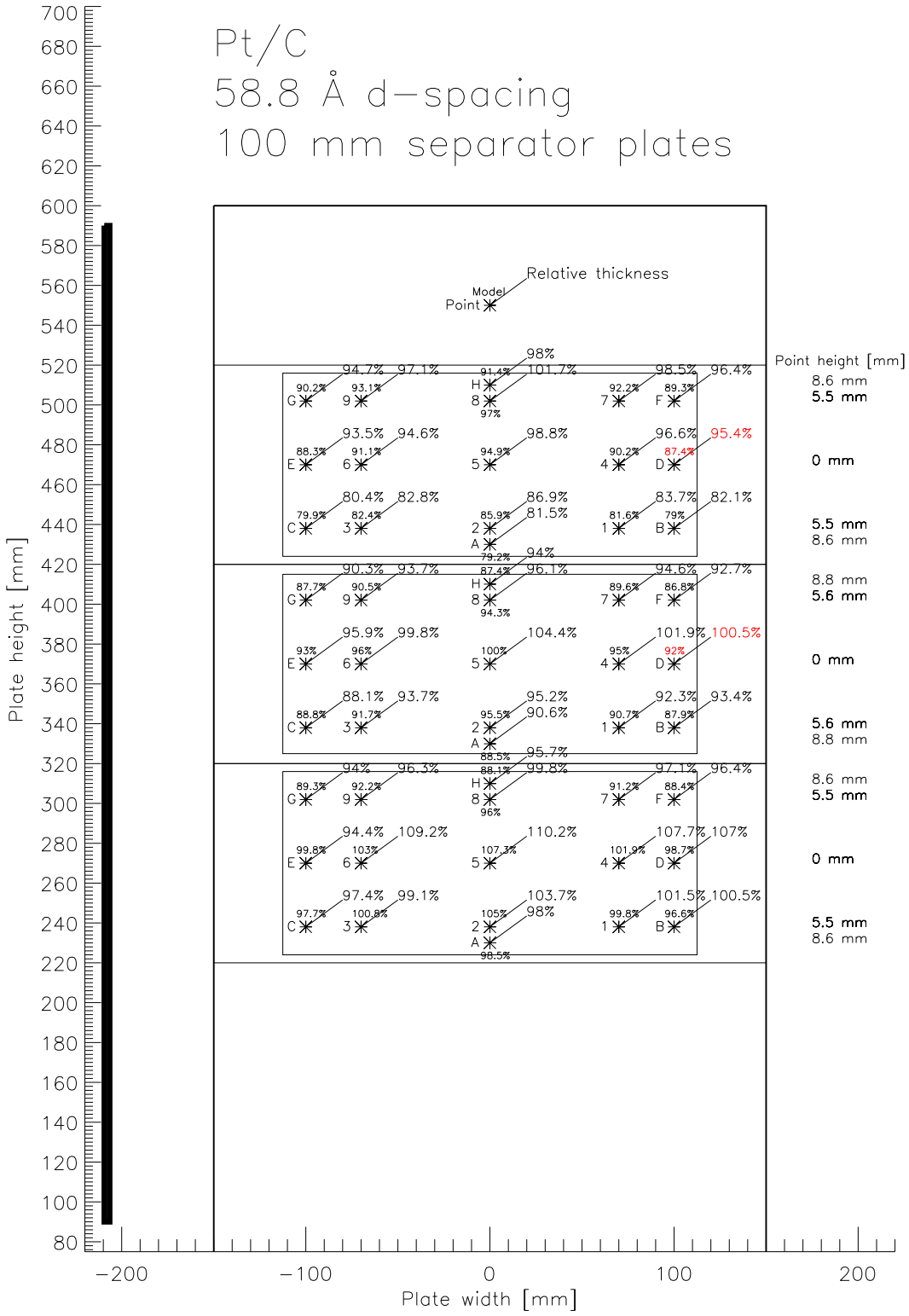

Figure 2.20: Uniformity mapping expressed through relative thickness between substrate location and PP2P5 on same mounting plate for Pt/C. Estimated model value of each point is indicated. Model includes T_x, T_y, $T_{z,x}$ and T_{dep}. Values colored red indicate substrate mounting issue at the $8\,keV$ beamline. Uncertainty in point location is coarsely given by star. The vertical target extent is indicated by thick black line on left side.

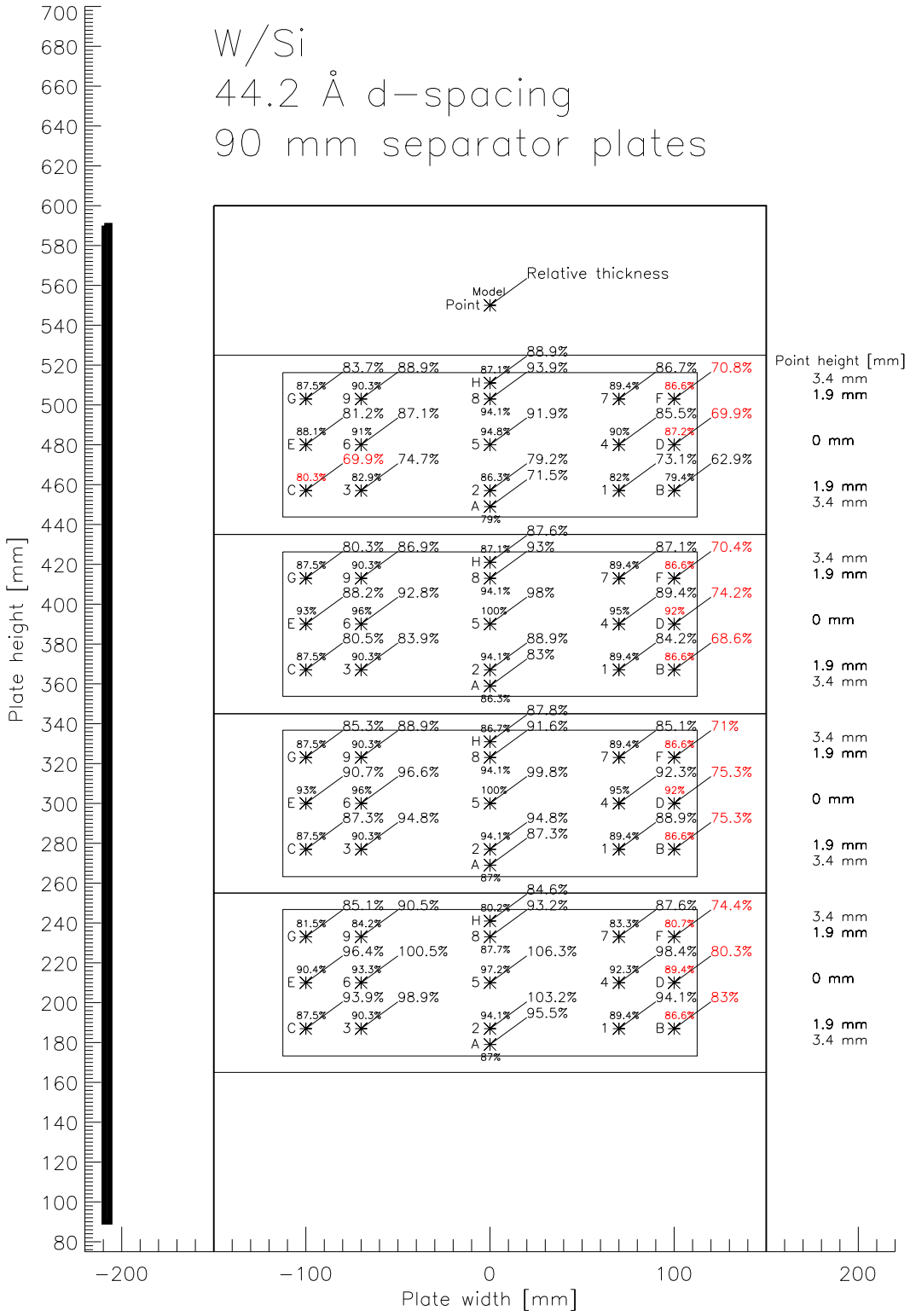

Figure 2.21: Uniformity mapping expressed through relative thickness between substrate location and PP2P5 on same mounting plate for W/Si. Estimated model value of each point is indicated. Model includes T_x, $T_{z,x}$ and T_{dep}. Values colored red indicate substrate mounting issue at the 8 keV beamline. Uncertainty in point location is coarsely given by star. The vertical target extent is indicated by thick black line on left side.

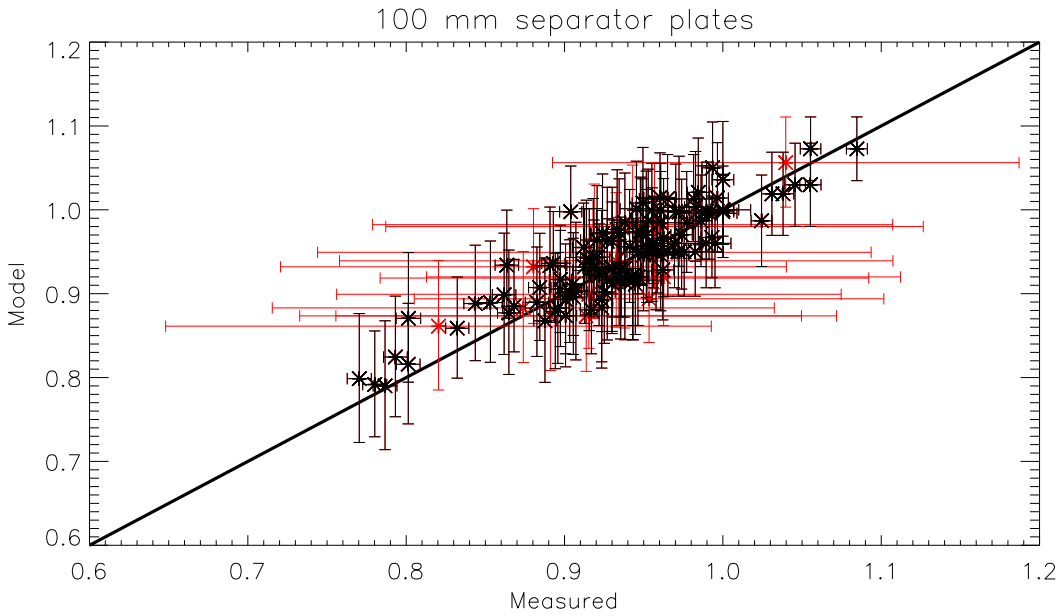

Figure 2.22: Overview of the model fit for all uniformity substrates with Pt/C coated using 100 mm plates. Ideal fit indicated by heavy black line. The data is slightly biased towards a model overshoot. Points colored red indicate substrate mounting issue at the 8 keV beamline.

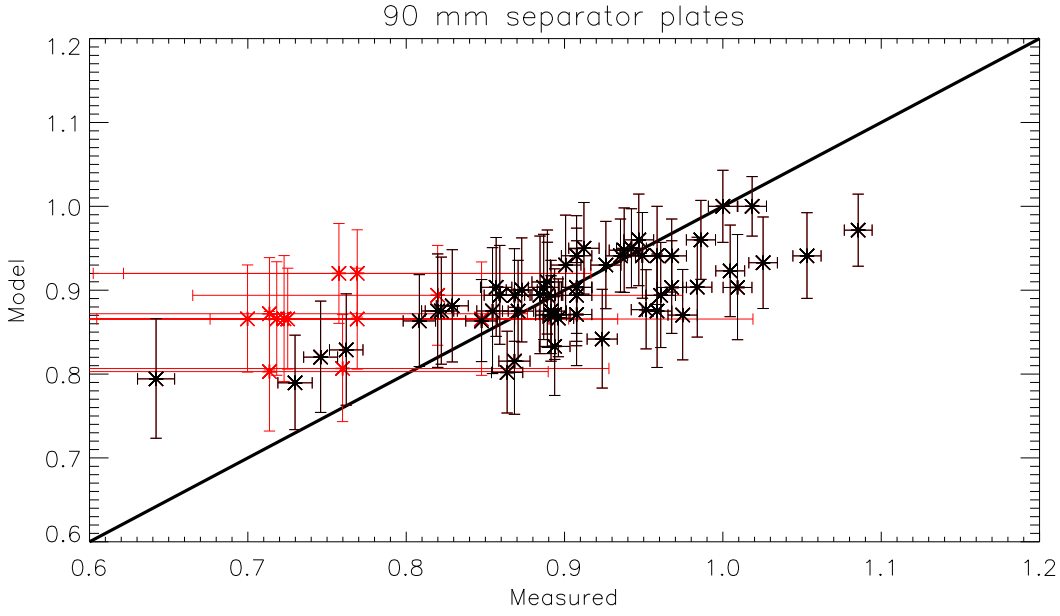

Figure 2.23: Overview of the model fit for all uniformity substrates with W/Si coated using 90 mm plates. Ideal fit indicated by heavy black line. The data is biased towards a model undershoot as T_y was not established. Points colored red indicate substrate mounting issue at the 8 keV beamline.

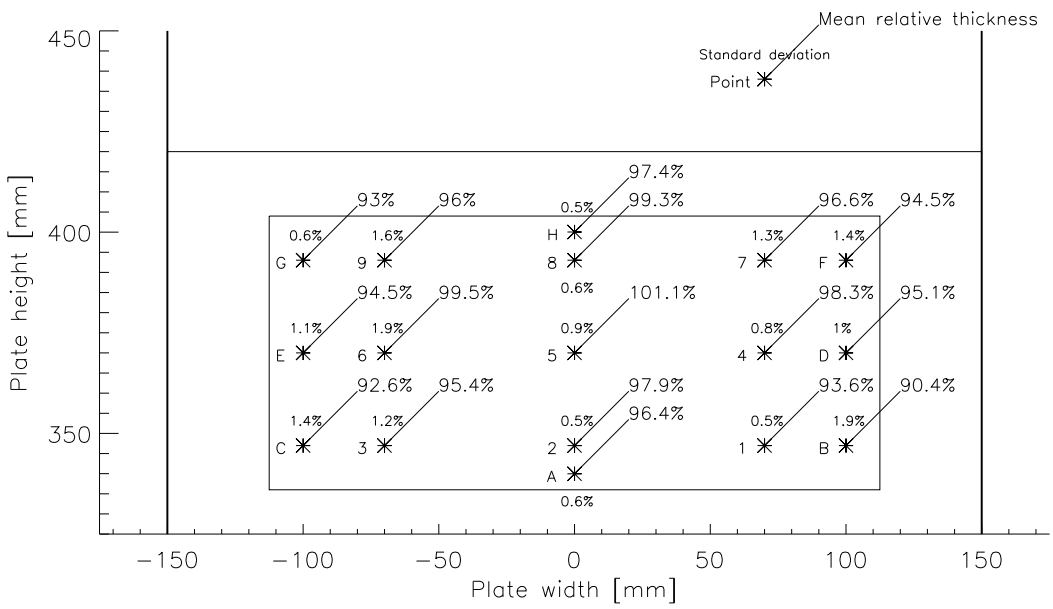

Figure 2.24: Mean relative thickness compared to relevant witness d in 17 points on three spare flight substrates. Three cst-d coating runs were carried out witnessed by Si5449, Si5451 and Si5452, refer to Table 2.7. Mean standard deviation of each point is indicated. Uncertainty in point location is given by star.

establishing the deposition rate of individual targets. It is, however, noted that a tendency for Γ to increase near the separator plates is observed, similar to the clear increase towards the target ends. This corresponds well with expectations as it implies $\alpha_{d,Pt} > \alpha_{d,C}$, or equivalently a more forwardly biased distribution of the Pt deposition rate compared to C. This was found by [38] to be the case. While the tendency towards the target end is still noticeable in Fig. 2.26 for curved substrates, Γ appears to decrease for $|\phi_i| > 0$ within the individual separator bays. The decrease is not surprising as C deposition rate is expected to increase with decreasing target distance, both as a result of the inverse-square law and due to decreased scattering caused by the Ar atmosphere. The latter does not influence the Pt deposition rate, therefore resulting in a net decrease of Γ.

From [38], Γ is expected to behave similarly for both material combinations. However, the W/Si data is more ambiguous compared to Pt/C as shown in Fig. 2.27. In the case of the 120 mm data this is caused by a unique mask arrangement used to improve coating uniformity. While the same overall shape, as observed for Pt/C, is found from 90 mm and 100 mm W/Si data, the decrease in Γ with increasing $|\phi_i|$ is less pronounced. This is due to Si being comparable in mass to Ar and subsequently less effected by the Ar atmosphere compared to C. Note that the Γ increase at low plate height values indicates the increased relative d observed in Sec. 2.3.2 (Fig. 2.17) derives from a higher W deposition rate near the target bottom.

2.3.7 Micro-roughness uniformity

Micro-roughness values of the uniformity data set were found to have no clear dependency on plate height as illustrated in Fig. 2.28 for Pt/C and Fig. 2.29 for W/Si. For W/Si there is a tendency for 120 mm plates to display higher micro-roughness values. The higher values are partially derived from the smaller d-spacing [28] and decreased collimation (higher s_y). However, the dominant effect is the relative σ being skewed due to an unusually low micro-roughness on the witness sample, refer to Table 2.4. Not including these values a reduction of 0.15 Å in micro-roughness with narrower collimation is observed as expected from previous studies [33].

Neither Fig. 2.30 nor Fig. 2.31 data indicates any clear dependency on $h_{z,x}$ for Pt/C and W/Si, respectively.

Nearly all data points indicates a significantly higher micro-roughness compared to the witness

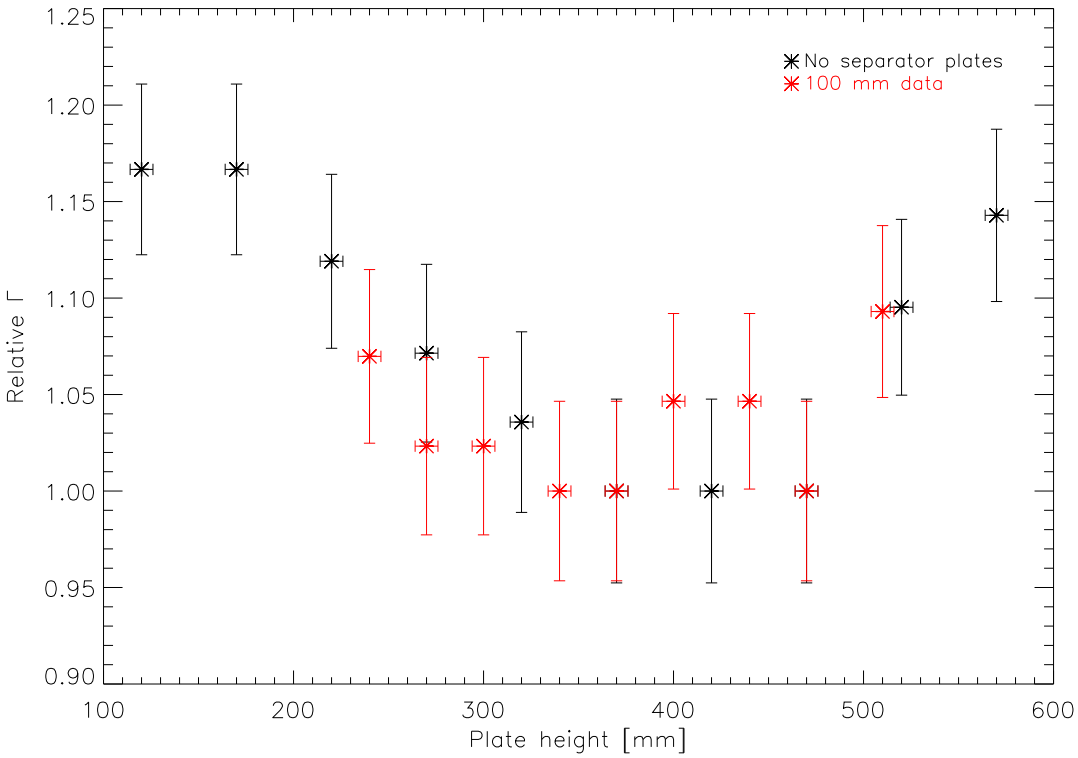

Figure 2.25: Relative Γ as a function of plate height for Pt/C with and without separator plates. See text for discussion.

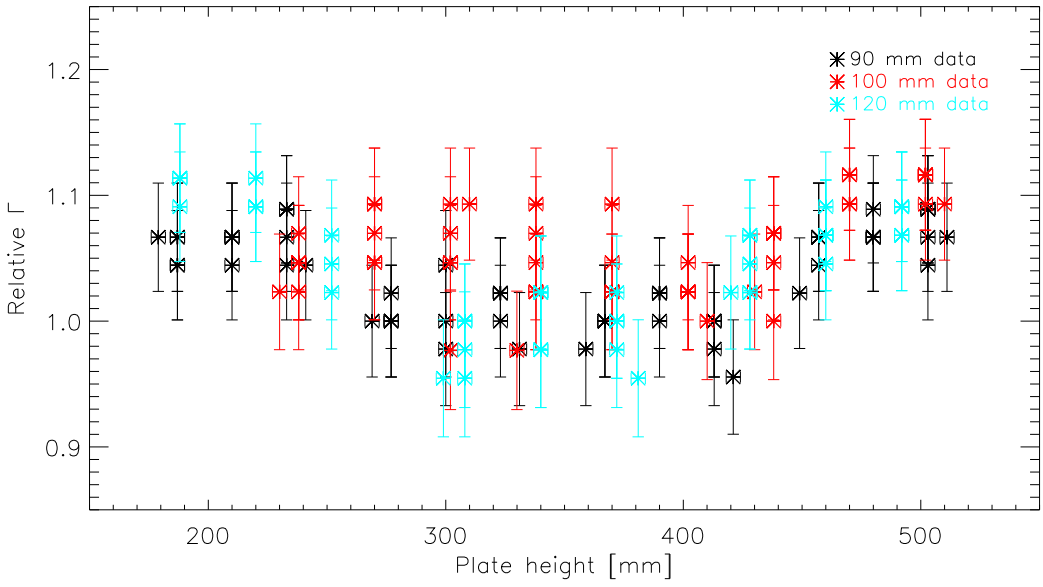

Figure 2.26: Relative Γ as a function of plate height for Pt/C. See text for discussion.

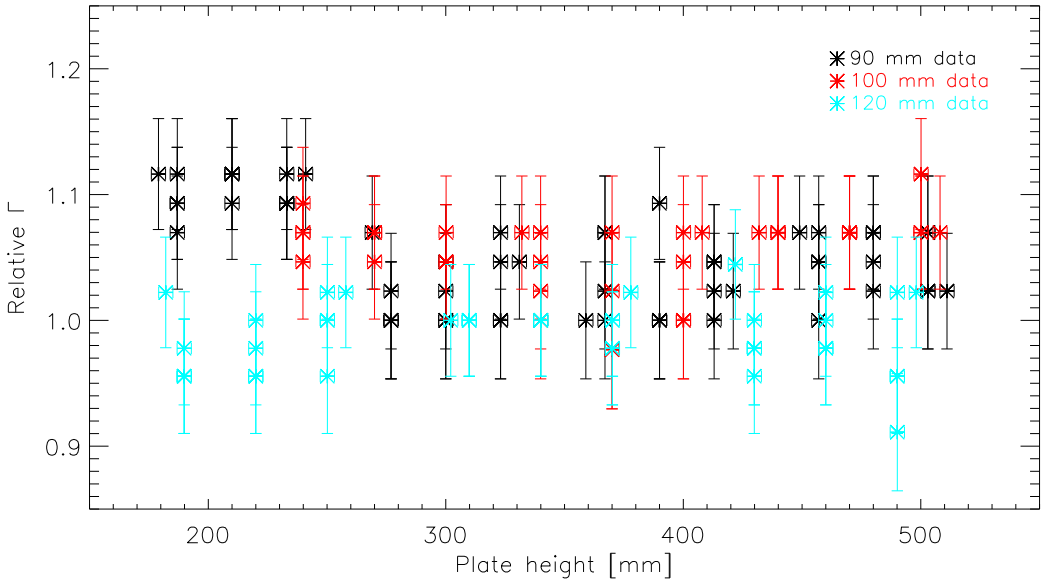

Figure 2.27: Relative Γ as a function of plate height for W/Si. See text for discussion.

samples. The increase in σ has been confirmed for flight coatings measured at RaMCaF and is attributed to the higher initial roughness of the substrate compared to the Si wafer [28]. The adverse effect on the high energy performance of the optics is discussed in Chapter 5.

2.3.8 RXO uniformity

Coating uniformity along the substrate x-axis was measured at RXO on a single substrate from the upper and lower rack. The results are shown in Fig. 2.32. RXO did not keep track of individual substrate mounting position. Therefore the average relative thickness is used in the ORM.

Investigations of the overall uniformity were reported by RXO to have been carried out on High Energy Focusing Telescope (HEFT) substrates prior to the NuSTAR contract being acquired. HEFT is the progenitor of NuSTAR. Refer to [39, 40] and references therein for additional details. Data from HEFT substrates are shown in Fig. 2.33. HEFT substrates were NuSTAR-like, but significantly shorter. They were mounted directly across from the center of the target and not tilted. For this reason the uniformity is closer to unity compared to the NuSTAR case. RXO estimates the differences along y (X in Fig. 2.33) between these results and ones relevant to NuSTAR to be minimal. Potential irregularities derive from the NuSTAR induced remodeling of the chamber geometry, specifically target masks and mounting fixture. It may be assumed that these changes would primarily affect the chambers vertical coating uniformity (i.e. Fig. 2.32) as the rotational symmetry is conserved. Given this, an ad hoc model based on Fig. 2.33 data is defined to describe uniformity along the substrate y-axis. This is given by

$$T_{RXO} = cos(\phi_i/\Xi) + 0.005) \tag{2.13}$$

with $\Xi = 1.5$ for $\phi_{sub} = 30°$ and $\Xi = 3$ for $\phi_{sub} = 60°$. The value of T_{RXO} must be used in conjunction with the results shown in Fig. 2.32 for a given substrate position. Values are exemplified in Fig. 2.34 at the uniformity measurement points used in the DTU uniformity campaign. The RXO uniformity mapping is available from Appendix C.

No data on substrate Γ and micro-roughness uniformity is available from RXO.

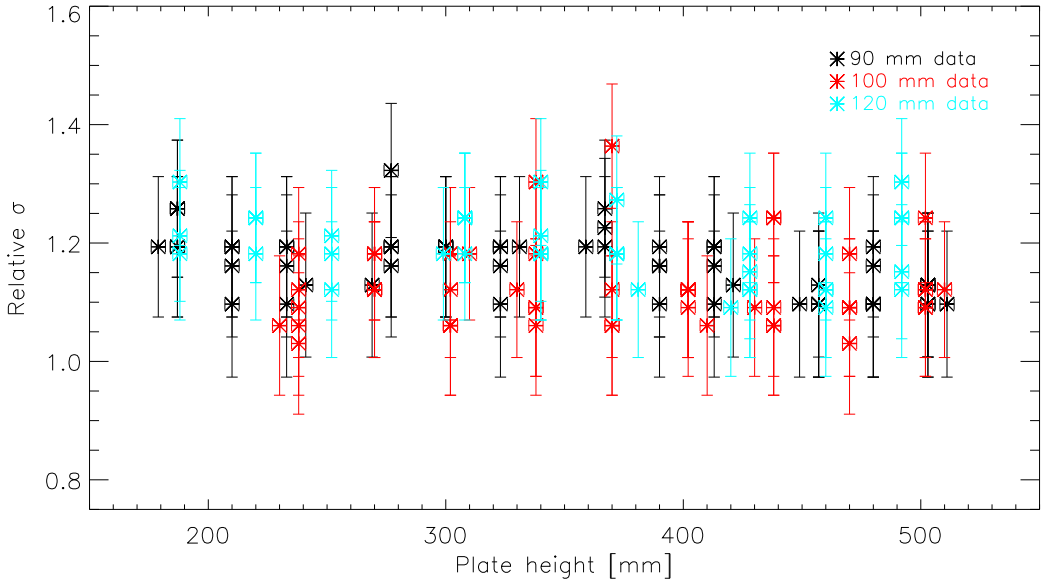

Figure 2.28: Micro-roughness as a function of plate height for Pt/C. See text for discussion.

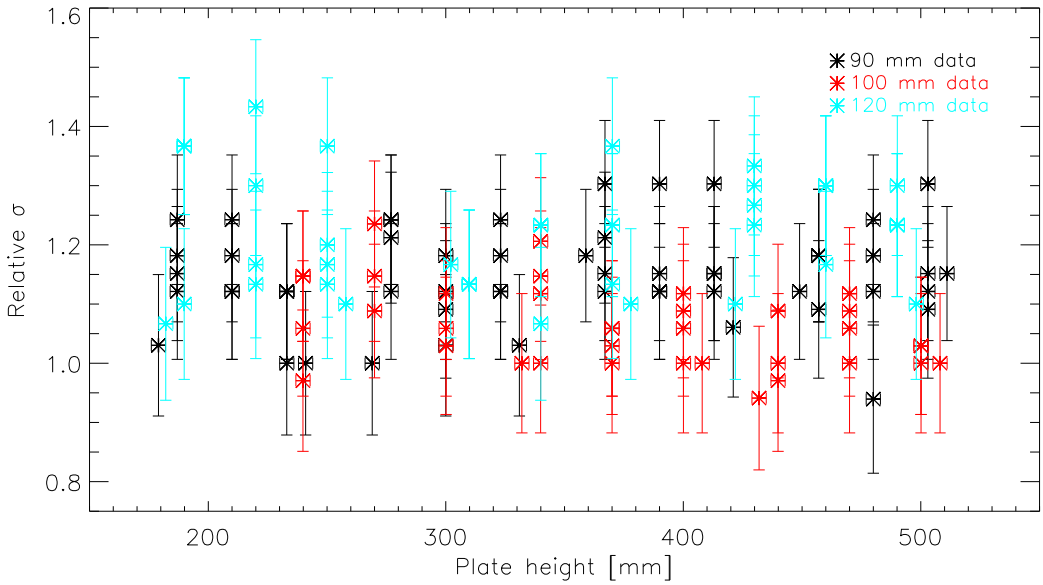

Figure 2.29: Micro-roughness as a function of plate height for W/Si. See text for discussion.

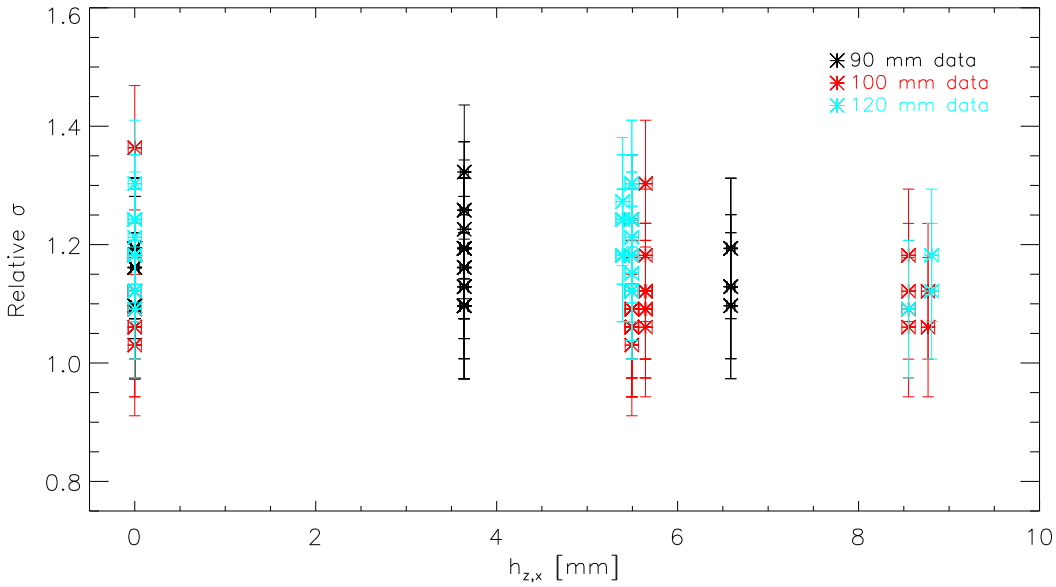

Figure 2.30: Micro-roughness as a function of $h_{z,x}$ for Pt/C. The values appear to have no clear dependency on $h_{z,x}$.

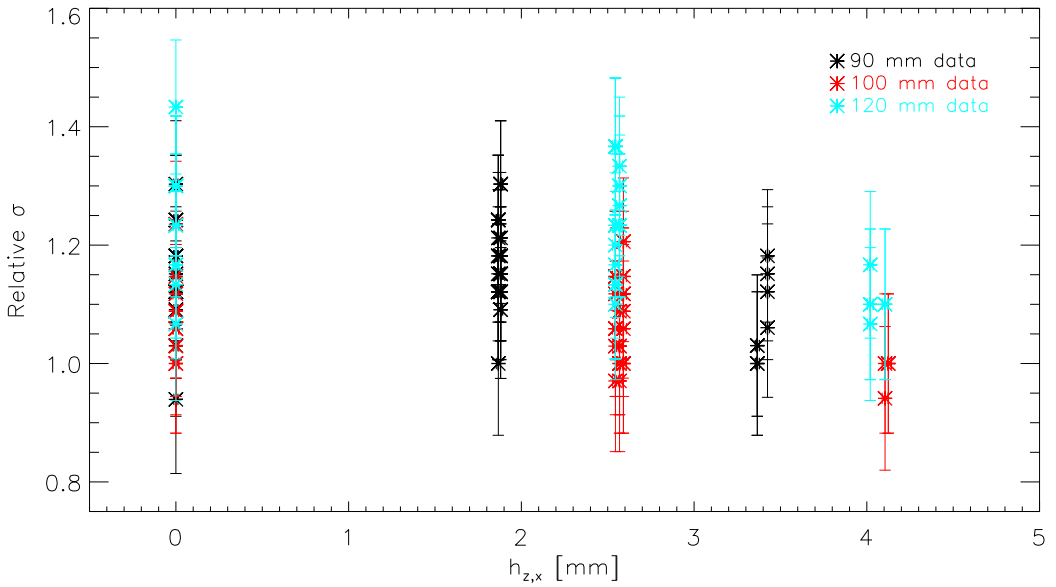

Figure 2.31: Micro-roughness as a function of $h_{z,x}$ for W/Si. The values appear to have no clear dependency on $h_{z,x}$.

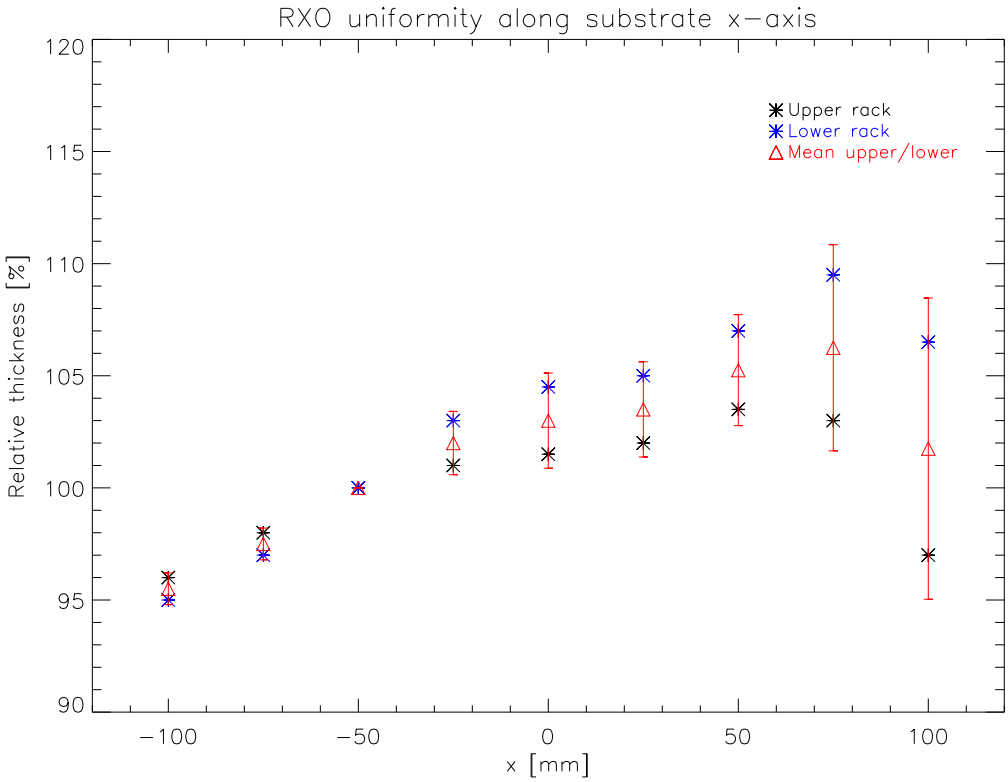

Figure 2.32: RXO coating uniformity along substrate x-axis. Note that this corresponds to vertical mounting in the RXO chamber (Fig. 2.4). Due to lack of substrate positional data the average (red) of the upper (black) and lower (blue) rack uniformity is used.

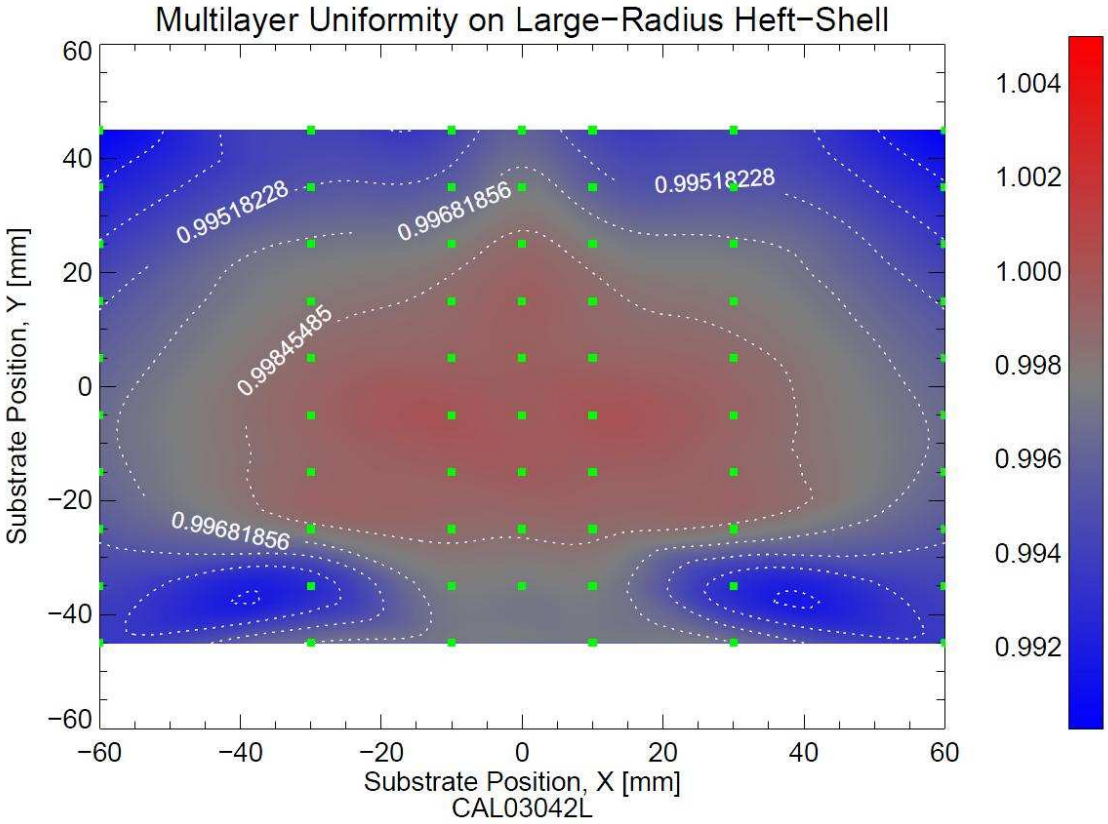

Figure 2.33: Surface contour plot supplied by RXO showing multilayer relative thickness as a function of substrate position. Note that HEFT substrates are 100 mm long, i.e. the coordinate system shown here is reversed compared to the DTU coordinate system (Y→ x, X→ y).

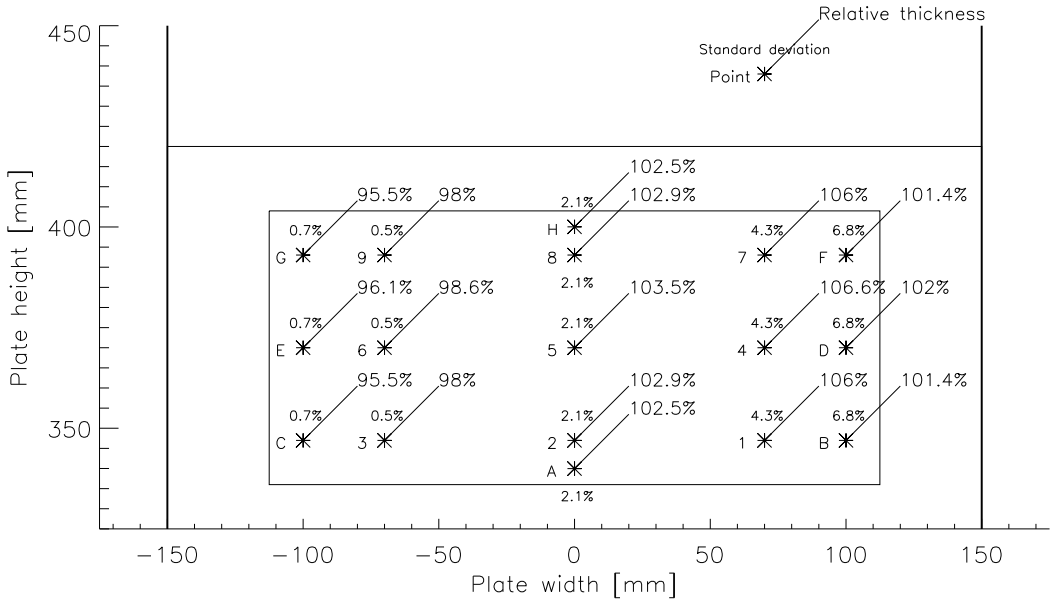

Figure 2.34: RXO substrate uniformity exemplified for the DTU uniformity measurement points, refer to Fig. 2.8.

2.4 Additional work

Section 2.3 has shown that the deposition as a function of chamber location can be modeled relatively well through rudimentary considerations. Several improvements to the model, some requiring additional experimental work, have been identified and are listed in this section along with a brief description of method and goal, when relevant.

The following list focuses on additional experimental work, i.e. coating of additional flat samples and curved substrates, followed by measurements at the $8\,keV$ beamline.

- Measurement of the target profile, T_y, for W/Si should be the immediate priority. T_y is expected to improve the model for all W/Si data. A sample set corresponding to the one described in Table 2.7 should be coated and measured. Care must be taken that masks identical to the flight campaign setup are installed. While $90\,mm$ and $100\,mm$ plates use the same masks, a separate sample set must be acquired for the unique $120\,mm$ mask.

- Measurements of the dependency on target distance, $T_{z,x}$, for both W/Si and Pt/C should be carried out on flat Si wafers. The measurements can be done by offsetting wafers a known distance from the mounting plate surface. Benefits from using flat wafers compared to curved substrates include smaller uncertainties in $h_{z,x}$ determination and ability to test extreme values. Such measurements would also provide additional insights on the Γ and micro-roughness dependency on target distance discussed in Sec. 2.3.6 and Sec. 2.3.7, respectively. Several same-height offsets within a single bay would further allow mapping out $T_{z,x}$ as a function of collimation.

- Measurements of T_y for individual targets should be carried out. Owing to the uncertainties in determining Γ accurately this is best done by depositing a several hundred Ångström thick single layer rather than ten cst-d bilayers. T_y for individual targets is required to model Γ.

- Measurements on additional substrates with regularly spaced D_{sub} values, e.g. every tenth layer, should be carried out. This would enable a more complete model verification.

- Each coating run should include a minimum of two identical mounting plate setups. While repeats double the number of $8\,keV$ measurements required they would assist with reducing the uncertainty in results caused by run-to-run variations. Increasing the number of mounting plates populated with samples would further provide more detailed knowledge of systematic differences in deposition rate from one mounting plate to the next.

- A complete uniformity campaign should be carried out in the RXO chamber. The lack of flight substrate positional data reduces the usefulness of such a campaign. However, the campaign would enable validation or replacement of the currently used HEFT data. The campaign should also map out Γ and micro-roughness non-uniformities.

As a general note to all of the above, greater care should be taken towards mounting samples, be it in the coating chamber or at the $8\,keV$ beamline, so to reduce uncertainties. This was not done initially in fear of inducing systematic differences between uniformity coatings and flight coatings. To this end, cleaning, mounting, coating and cataloging were carried out by the flight coating technicians with no perturbation to their usual routine. Such measures would not be required going forward. The uncertainty induced by the mounting issues at the $8\,keV$ beamline had other causes. Custom substrate fixtures and upgrades to the translation stages would be required to eliminate the problems. Neither were feasible within the time frame and budget of the uniformity campaign.

The simplistic approach taken towards modeling sputter deposition leaves a number of routes open for improvements. A large body of work exists on the subject, see e.g. [16, 15, 38] and references therein. While the physics can be derived from these and implemented in the present work, detailed modeling of the specific DTU (and RXO) coating geometry is required for accurate predictions. The below suggestions focus on improvements to the geometric representation rather than the physics model. The focus reflects that relative, rather than absolute, deposition values are of interest in the suggested work.

- The model should be upgraded to utilize solid angles. This effectively corresponds to combining the horizontal and vertical models into a single one. As part of this upgrade the target should be approximated by two line sources similar to the approach used in [16].
- The model should include a more complete geometric representation of the coating chamber. Among these improvements would be knowing the relative placement of mounting plates with respect to cathodes, including the mask geometry, and more stringently defining the individual targets.
- The model should include attenuation of the light material sputtering flux as a function of Ar pressure and target-to-substrate distance. Attenuation was seen to have a significant influence on in particular C deposition rate in Sec. 2.3.6. The mean free path of sputtered atoms can be estimated to first order based on values given by simulations in [41].

As is discussed in Chapter 5, other tasks relating to the ORM input, especially the implementation and qualification of the complete uniformity map, have greater priority than an upgraded uniformity model. Nonetheless, Chapter 5 indicates that a finely grided uniformity map can improve the ORM. From the work in this chapter, it is clear that a detailed uniformity map can be based on a model given the suggested improvements.

2.5 Results and chapter summary

A map of the coating uniformity as a function of chamber location was constructed. The map describes the relative thickness at up to seventeen points on individual substrates compared to a witness sample. Γ and micro-roughness uniformity were also mapped. Examples of the results were presented in several figures. For convenience, Table 2.8 contains summarized uniformity results.

It was established that substrate micro-roughness is expected to be on average 16% higher compared to witness samples for Pt/C coatings and 14% for W/Si coatings.

Through rudimentary modeling it was shown that a combination of collimation and substrate curvature accounts for the majority of the non-uniformities. The model was used to patch missing data points in the uniformity map. Additional work was suggested to improve on the model.

The NuSTAR ORM input repository contains the complete uniformity map.

Table 2.8: Summary of the relative thickness uniformity found from the uniformity campaign data. $d_{rel,mean}$ is the mean relative thickness and Δd_{rel} the standard deviation. $d_{rel,min}$ and $d_{rel,max}$ describe the extreme values in the data set. While the table values do not take separator plates and chamber location into account, they do provide a straightforward measure for the non-uniformity of the coatings.

Material	$d_{rel,mean}$	Δd_{rel}	$d_{rel,min}$	$d_{rel,max}$
Pt/C	0.966	0.080	0.733	1.170
W/Si	0.871	0.083	0.629	1.094

Chapter 3

Witness campaign

Abstract - *In this chapter, specular reflectivity data acquired from flight witness samples is presented and discussed. The approach to fitting the data is outlined and data set findings discussed. It is found that the as-coated multilayers are not well-described by the design recipes. Improvements to the fitting approach are suggested.*

As shown in Fig. 3.1, the second part of the ORM improvements relate to flight witness samples. The baseline ORM assumes the designed multilayer coating was applied. Modified by the findings in Chapter 2, this is still not representative of the as-coated multilayer. The run-to-run variations observed by the witness samples must also be included.

Ideally, the multilayer response in the entire NuSTAR energy and angular range should be used to probe the layer structure. RaMCaF was therefore suitable for the campaign not least since it was available for the extended time period required following optic calibration in March 2011. The baseline number of samples per day was ten, but due to a vacuum pump failure and reduction in available workforce the average ended up at less than one per day. For this reason the data set presented here is representative, but not complete. The online data repertoires referred to in this chapter's appendices will be updated as the remaining data filter in and is analyzed.

Special mention goes to Marcela Stern, Shuo Zhang, Clio Sleator, Doug Thornhill and Jason Koglin at Columbia University Astrophysics Laboratory (CU) for assisting with the data acquisition in the months following calibration.

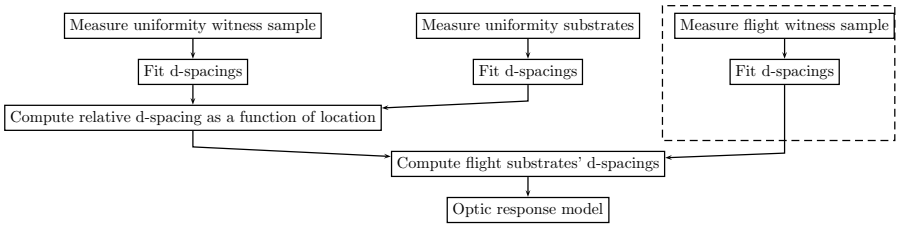

Figure 3.1: Illustration of the necessary steps to estimate the as-coated multilayer on the mounted flight substrates for use in the ORM. This chapter focuses on the tasks within the dashed box.

3.1 RaMCaF

The Rainwater Memorial Calibration Facility (RaMCaF) was constructed in an existing underground tunnel, neighboring the NuSTAR optics' assembly room. The facility was built specifically for the NuSTAR flight optics' on-ground calibration and for prototype and witness sample testing. A hard X-ray continuum up to 100 keV is produced by a high power X-ray tube located 163 m upstream from the optic hutch. Most of the source-optic distance and the 10.82 m optic-focal plane distance is under medium vacuum. When the beam exits the vacuum pipe into the optic hutch its diameter is nearly 0.5 m. For the witness sample campaign the beam is heavily collimated to produce a $0.1 \times 4\ mm^2$ pencil beam. The witness sample setup is sketched in Fig. 3.2. Note that the coordinate system subscript f is to distinguish it from the substrate one used in Chapter 2. Specular reflectivity of the mounted sample is measured at two angles. One angle allows determination of the d-spacing progression all the way down to d_{min} while the other, lower angle, is limited by the K-edge absorption, refer to Fig. 1.6 (Sec. 1.1) and Sec. 3.2.1. Ideally, the lower angle would correspond to the grazing incidence angle of the telescope, α_i, for the relevant recipe (refer to Table 1.1). However, for convenience and due to difficulties aligning the witness samples to the shallowest angles, fixed values were used. The incidence angle is measured using a Micro-Radian T40 autocollimator optical head with a resolution of $< 1''$. The reflected beam is collected within a $15 \times 8\ mm^2$ area in the focal plane by an Ortec High-Purity Germanium (Ge) detector, used throughout the campaign. The detector is well-understood based on an absolute calibration against the RHESSI [42] spare flight detector and a detailed Geant4 [3] model. It has excellent high energy quantum efficiency, but the 5 cm thick Ge crystal is not ideal for low energy measurements with a Bremsstrahlung spectrum due to energy redistribution. For this reason, and on account of a vacuum pump failure, witness sample data will only be analyzed from 15 keV and up. Section 3.3.2 discuss the implications of this.

Additional details regarding the facility can be found in a peer-reviewed article available from Appendix A.

3.1.1 Data acquisition

The data acquisition and processing follows a fairly standard route as illustrated in Fig. 3.3. X-rays are collected by the detector sending a signal to an Amptek DP5 digital pulse processor. The DP5 shapes and histograms the signal. The histogram is read into LabVIEW via Ethernet and written to file along with housekeeping data, such as vacuum pressure and motor positions. The IDL procedures are custom and based on the detector model and DP5 settings. The energy scale is calibrated using the Tungsten K and L lines in the direct beam. Output files contain reflectivity as a function of energy with 1σ error bars.

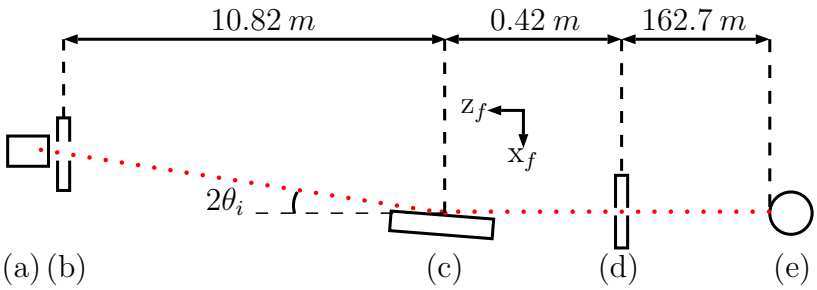

Figure 3.2: Sketch of the RaMCaF witness campaign setup. The Ge detector is located at (a) and allows for translation in x_f. A slit defines a collection area of $15 \times 8\ mm^2$ at (b). Reflectivity data is normalized to the direct beam measured at $\theta_i = 0°$ with the sample mount (c) translated out of the beam path. The sample can be translated in x_f and y_f, as well as moved in yaw, pitch and roll. Only yaw is used to set θ_i, in the witness campaign. A pencil beam is defined at (d) to $0.1 \times 4\ mm^2$. The X-ray source (e) produce continuum radiation up to 100 keV. The 162.2 m of the source-sample distance is pumped down to 0.1 $Torr$. 10 m of the optic-detector distance was at 10 $Torr$ until a vacuum pump failure, causing the full length to be at ambient pressure for the majority of the campaign.

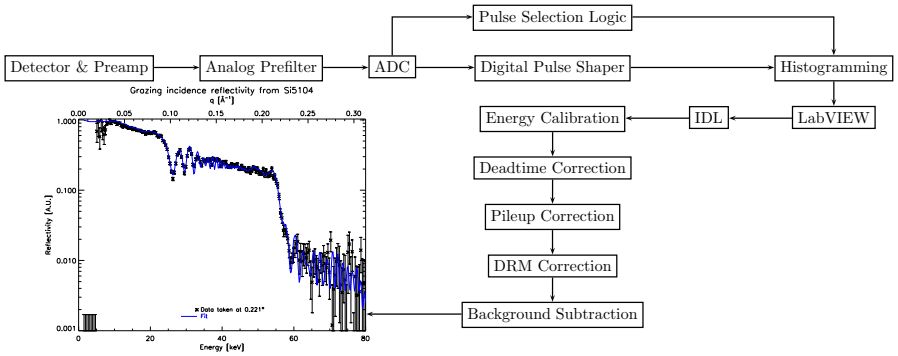

Figure 3.3: Flowchart illustrating the data acquisition and processing. From the detector and preamplifier the signal is fed to a digital pulse processor unit (Amptek DP5). LabVIEW accepts histogrammed data from this unit through an Ethernet port and writes it to file along with motor positions and other housekeeping. From there IDL procedures process the data and outputs a simple text file with reflectivity as a function of energy.

3.2 Witness sample campaign

The entire specular reflectivity data set acquired during the witness sample campaign can be found from Appendix H. Pt/C data was acquired at a nominal θ_i value of 0.22° while for W/Si $\theta_i \approx 0.24°$. Data was also taken at 0.16° and 0.18° for Pt/C and W/Si, respectively.

Tabulated recipe values describing the as-coated multilayer can be found from Appendix I. The as-coated recipes constitute the input to the ORM from the witness campaign. Plots of all available data and the accompanying fits can be found from Appendix J.

3.2.1 Campaign timeline

The extended RaMCaF witness campaign induced several caveats in the data set and ultimately led to the data set being incomplete. The latter was primarily caused by manpower reduction causing a planned three month campaign to last nearly eight months. The campaign will end with the Ge detector being required for NuSTAR flight detector calibration in December 2011. At the time of writing a total of eleven DTU and all forty-five RXO witness samples are not included in the data set. It is expected that data from twenty RXO samples will not be acquired prior to the campaign conclusion. From Chapter 5 findings, the impact of this on the ORM is expected to be limited since RXO as-coated multilayers are indicated to be close to design.

In addition to a number of samples not having been measured, a measurement script error corrupted low angle data from the initial sixty-five witness samples and forty-five samples later a pump failure compromised the low energy count rate. The failure occurred on the optic-detector pipeline, adding an additional 10 m of ambient air to the beamline. When a replacement pump arrived lack of manpower prevented it from being implemented. As a consequence available flux was reduced by roughly 30%, primarily below $20keV$. The increased attenuation effectively created a cutoff at 12 keV. Section 3.3.2 discusses the implications of this. Finally, near the end of the campaign it was found that a combination of smaller than design as-coated minimum d-spacing ($d_{min,ac}$) and a θ_i value occasionally up to 4% lower than nominal, meant $d_{min,ac}$ could not be accurately determined for several W/Si witness samples. This is seen from Bragg's law (Eq. 1.1) in that the highest energy reflected is given by

$$E_{max} = \frac{hc}{2d_{min,ac}sin(\theta_i)} \tag{3.1}$$

where Planck's constant (h) and the speed of light (c) convert the wavelength fulfilling Bragg's law to energy. If E_{max} is above the K-edge of the heavy material, absorption will dominate and no information on d_{min} will be available. Instead, the d_{min} dip will be located at the K-edge. This is extremely unfortunate as $d_{min,ac}$ is a critical parameter in the fitting process, as discussed in Sec. 3.3. To prevent the loss of d_{min} information from occurring the nominal high angle for W/Si was increased to 0.27°. At this angle $d_{min,ac}$ must be less than 19 Å for the K-edge to dominate (down

Table 3.1: Relative values of average recipe parameters compared to design recipes given in Table 1.1.

Recipe	$d_{min,R}$	$d_{max,R}$	c_R	$\Gamma_{top,R}$	Γ_R	σ_R
1	93%	91%	105%	100%	83%	101%
2	97%	101%	114%	101%	100%	98%
3	95%	95%	106%	100%	92%	98%
4	94%	92%	105%	100%	87%	99%
5	92%	89%	105%	98%	91%	96%
6	92%	90%	105%	99%	83%	98%
7	89%	84%	106%	99%	82%	95%
8	96%	100%	101%	101%	99%	97%
9	88%	102%	118%	101%	94%	94%
10	88%	100%	115%	100%	89%	97%

from 21 Å at 0.24°). Note that the lower than intended incidence angle does not imply uncertainty in the angle value. It is an artefact of the alignment procedure and scripts.

3.2.2 Design versus as-coated recipes

The data set shows that design recipes are not descriptive of the as-coated multilayers. One way to illustrate the discrepancies is by finding average as-coated recipes for the witness samples representing a given design recipe. Table 3.1 shows the difference between the as-coated and the design recipe parameters. The average as-coated recipe parameters are given in Table 3.2. Note that recipe 0 and RXO witness samples are not included as no data are available on either at the time of writing.

The following observations are based on Table 3.1.

An overall lower d_{min} should cause d-spacings in general to be lower than design. This is complicated by c being significantly higher than intended, changing the overall bilayer thickness progression. The high c is connected to the quality of the deposition rate calibration discussed in Sec. 3.4.3, and may also tie into the degeneracy issues discussed in Sec. 3.3. The complicated nature of the degeneracies makes conclusions based on the average d-spacing parameters (c, d_{min} and d_{max}) ill-advised. These parameters should only be evaluated on a case-by-case basis.

The generally low values of Γ does not agree well with Γ_{top} being close to nominal in most cases. While the two parameters have been considered decoupled in the present work, they must by definition be coupled, as the rotational speed is constant for one full revolution at a time, and cathode power settings are fixed for the entire run. The implication is that one or both of the parameters have not been determined correctly. Additional comments relating to Γ_{top} determination are given in Sec. 3.3.2.

Micro-roughness is found on average to be lower in W/Si coatings compared to Pt/C due to crystallite growth in the Pt layers. Refer to Chapter 4 for additional details.

Standard deviations of the as-coated parameters are given in Table 3.3. The Δd_{min} value for recipe 5 is high due to a documented operator error during coating. The error was repeated in three consecutive runs and caused significantly lower $d_{min,ac}$. The high uncertainty in recipe 8 values can also be tracked to a limited set of consecutive coatings, but no indications of the cause can be identified from the logs. The variation in Γ is expected to derive from all targets rarely being replaced at the same time. This is supported by recipe 2 $\Delta\Gamma$ being low as all targets were replaced simultaneously for those coatings.

The overall approach to fitting the data and results are discussed in Sec. 3.3 and Sec. 3.4. Chapter 5 illustrates the implications for the ORM deriving from the as-coated multilayers being significantly different from design.

Table 3.2: Average as-coated recipes. The mean values are calculated over the n_w witness samples of a given design recipe (refer to Table 1.1). The number of mounted substrates is given by n_m and χ^2 is the average chi-square of the fits. Note that d_i with $i = 1..6$ describes relative thickness modifications of bilayers one through six. These are applied independent of the overall d-spacing progression. Similarly, Γ_1 and Γ_2 modify Γ for bilayer two and three only. RXO witness samples are not included in the averages.

Recipe	n_w	n_m	χ^2	$d_{min,ac}$[Å]	$d_{max,ac}$[Å]	c_{ac}	$\Gamma_{top,ac}$	Γ_{ac}	σ_{ac}[Å]	d_1	d_2	d_3	d_4	d_5	d_6	Γ_2	Γ_3
1	14	289	1.13	27.0	121.9	0.257	0.70	0.37	4.5	0.98	1.02	0.99	1.00	0.98	1.00	0.49	0.40
2	14	284	0.69	28.2	133.2	0.261	0.71	0.45	4.4	0.99	1.00	1.01	1.00	0.99	1.00	0.49	0.41
3	15	285	0.77	27.4	123.7	0.247	0.70	0.41	4.4	0.98	1.01	1.01	1.00	0.99	1.00	0.50	0.41
4	16	308	0.95	27.3	111.7	0.224	0.70	0.39	4.4	0.98	1.00	1.00	1.00	0.99	1.00	0.50	0.41
5	19	327	0.95	26.6	97.9	0.237	0.69	0.41	4.3	0.99	1.00	1.01	1.01	0.99	1.00	0.48	0.41
6	22	511	0.83	26.8	96.4	0.237	0.70	0.38	4.4	0.98	1.01	0.99	1.00	0.99	1.00	0.49	0.40
7	22	636	0.95	25.7	86.8	0.224	0.69	0.37	4.3	0.98	1.01	1.00	1.00	0.99	1.00	0.48	0.40
8	9	703	1.38	24.1	94.9	0.240	0.80	0.37	4.2	0.99	1.00	1.02	1.03	1.01	1.00	0.41	0.36
9	22	663	1.03	22.1	85.6	0.260	0.81	0.36	4.1	1.01	0.99	1.01	1.01	0.99	1.00	0.41	0.34
10	29	716	0.83	22.0	74.2	0.218	0.80	0.34	4.2	1.01	0.98	1.01	1.01	1.00	1.00	0.40	0.34

Table 3.3: Standard deviation of as-coated recipe parameters for the mean values given in Table 3.2.

Recipe	Δd_{min}	Δd_{max}	Δc	$\Delta\Gamma_{top}$	$\Delta\Gamma$	$\Delta\sigma$
1	4%	7%	3%	1%	15%	7%
2	3%	2%	4%	1%	5%	5%
3	4%	2%	3%	2%	12%	3%
4	3%	4%	3%	1%	10%	3%
5	10%	8%	6%	3%	12%	7%
6	4%	6%	4%	2%	12%	4%
7	6%	8%	4%	2%	10%	4%
8	12%	9%	4%	12%	9%	6%
9	3%	5%	6%	5%	9%	3%
10	3%	6%	4%	6%	12%	5%

3.3 Fitting approach

The main challenge with fitting the data is that individual measurements suffer from the inversion, or phase, problem [43], preventing an unambiguous determination of the multilayer structure. In the following, this is presented in the context of utilized fitting parameters. Caveats in the data and resultant fits are also discussed. A few of the caveats are highlighted for further investigation in Chapter 4 and Chapter 5.

3.3.1 Fitting parameters

Eight parameter types were used to fit the data. To clarify the degeneracy between them it is instructional to review their individual effect. This is done in Fig. 3.4-3.11 for variations on NuSTAR recipe 1 at $\theta_i = 0.22°$. The following observations are made from these eight figures.

The six primary fitting parameters are the ones traditionally used namely d_{min}, d_{max} and c from Eq. 1.9 as well as Γ, Γ_{top} and micro-roughness. The influence of d_{max} and d_{min} are strongest just past total external reflection and at the dip to second order Bragg contributions, respectively. The location of the dip is almost entirely determined by d_{min}. For this reason d_{min} may be found to within ± 0.1 Å. With d_{min} basically fixed c can be used to set the period of the prominent ridges just past total external reflection. d_{max} influence the general level of reflectivity especially in the first few ridges. Unfortunately, its strong degeneracy with Γ_{top} makes it difficult to ascertain if it has been determined accurately. Section 3.3.2 discuss this further. The influence of Γ and micro-roughness is more subtle as it accumulates over all the layers. Both assist in setting the level of the entire first order plateau. Micro-roughness acting on the reflectivity as a function of energy prevents a strong degeneracy between the two. It should be noted that the interface in the present work is assumed to resemble an error function as defined by [12].

The remaining two parameter types are sub-selections of the d-spacing and Γ. The already mentioned ridges consist of summed Bragg peaks from the top bilayers. Their individual relationship is governed by Γ_i and d_i. Note that while d_1 influences the d_{max} bilayer (i.e. the top bilayer), d_i are relative adjustments of the bilayer thickness. Specifically, $d_1 = 1.01$ adds 1% to the top bilayer thickness, but the recipe parameter d_{max} remains unchanged. Conversely, Γ_i replaces the bilayer value of Γ for a given layer. Early observations found that adjusting these values for a number of the topmost bilayers improved the fit. Γ_i, $i = 2, 3$, and d_i, $i = 1...6$, were fit individually. Additional bilayers could have been micro-managed in this manner, but the influence on overall reflectivity structure decreases rapidly with i while the necessary computing power increases. d_i can be interpreted as the influence of a slow deposition rate fluctuation in time. The rapidly increasing d-spacing near the top of the stack results in increased coating time and a more pronounced deposition rate fluctuation. Similarly, Γ_i describes a difference in the deposition rate fluctuation between the heavy and the light materials. TEM investigations were carried out to determine whether these localized d and Γ variations were real or caused by the degeneracy between fitting parameters. The investigations found that d_i adjustments are real and can be substantial. Γ_i was not determined with TEM, but re-fitting witness data with corrected d_i values from the TEM campaign indicates that Γ_i is a degeneracy artifact. The TEM data is presented in Chapter 4. As mentioned Sec. 3.3.2 discuss the problem further with focus on the low energy response.

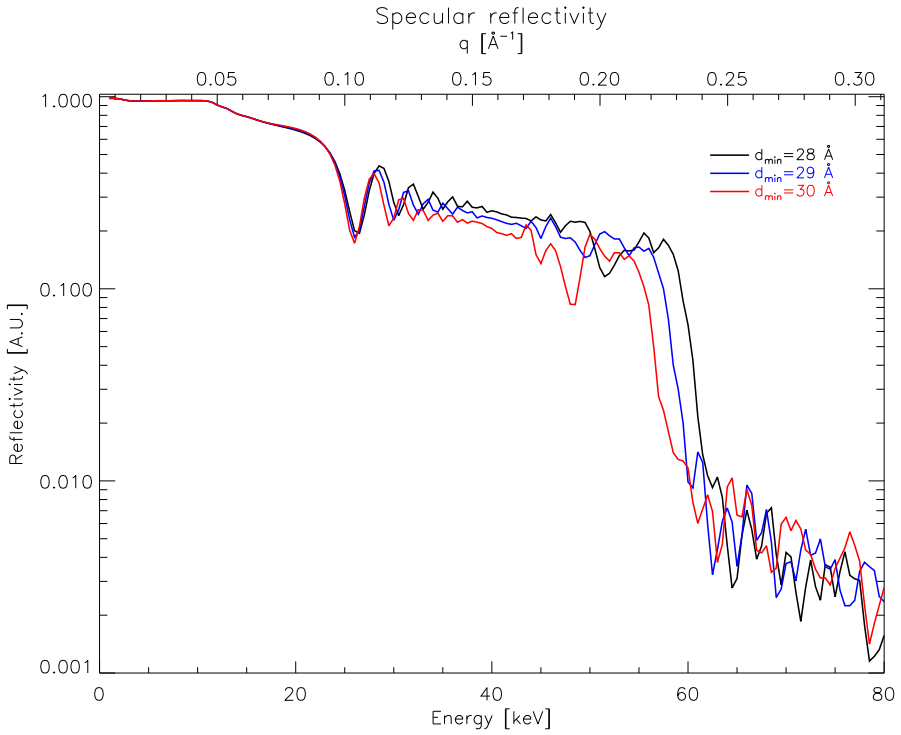

Figure 3.4: d_{min} determines the highest energy of the first order Bragg plateau for a given measurement, refer to Eq. 1.1. This is a unique feature assuming said energy is below the heavy material K-edge, allowing it to be unambiguously determined to within ± 0.1 Å($< 1\%$). d_{min} also influence d-spacing progression through Eq. 1.9 (Sec. 1.5).

Note that the structure variation near $50\,keV$ in all figures is a result of the detailed workings of the multilayer reflections. At the lower NuSTAR incidence angles these effects are not seen.

3.3.2 Low energy response

High uncertainty in the data at low energy increases the difficulty of breaking degeneracy between Γ_{top} and d_{max}. Only a marginal difference in chi-square values was found when favouring modifications of either d_{max} or Γ_{top} in the fitting routine. Both approaches found $d_{min,ac}$ to be off from design values, implying a similar behavior for $d_{max,ac}$. However, Γ_{ac} showed variations from design as well, indicating that $\Gamma_{top,ac} \neq \Gamma_{top}$. While the Γ/Γ_{top} relationship is not complicated by a dependency on c, as is the case for d_{min} and d_{max}, neither Γ nor Γ_{top} are determined unambigiously, contrary to $d_{min,ac}$. For this reason it was decided to favour a $d_{max,ac}$ variation. Table 3.1 reflects the favouring of a d_{max} variation through $d_{max,R}$ in most cases being significantly different from 100%, contrary to $\Gamma_{top,R}$.

The validity of this approach was coarsely confirmed by the high and low angle measurements demonstrating the same overall quality of fit. However, true cross-fitting between angles was not carried out. Figure 3.12 shows an example of the comparison carried out. Data from the $8\,keV$ beamline was also considered. Refer to Appendix J for all such plots. Overall the three data sets agree well on the multilayer period, but level differences in reflectivity are observed, especially from the upper layers and total external reflection. This is expected to be due to the d_i and Γ_i fitting parameters compensating for incorrect values of c, d_{max} and Γ_{top} in ways that imitate the actual multilayer through degeneracy, but does not necessarily represent the true multilayer. At the lower angle discrepancies stand out more. In Chapter 4, a better fit to the low energy response is achieved by establishing the top bilayer thicknesses from TEM images rather than through specular reflectivity. Direct imaging of the top bilayers provides an estimate for d_i, while Γ values cannot be determined with TEM. Refer to Chapter 4 for additional details. Section 3.5 discuss suggested improvements to the fitting approach while Chapter 5 investigates the impact on the ORM.

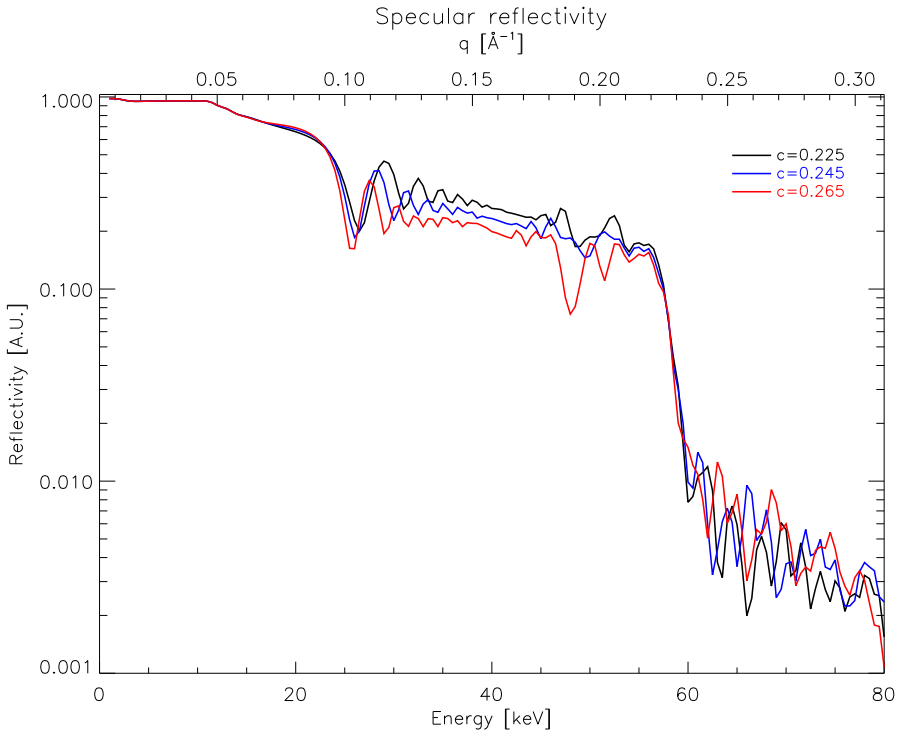

Figure 3.5: c determines d-spacing progression through Eq. 1.9 (Sec. 1.5). It has negligible influence on the d_{min} dip and through this acts to fit the prominent ridges just below total external reflection. The ridges consist of summed Bragg peaks from the top layers. The achieved c value depend primarily on deposition rate calibration and target wear.

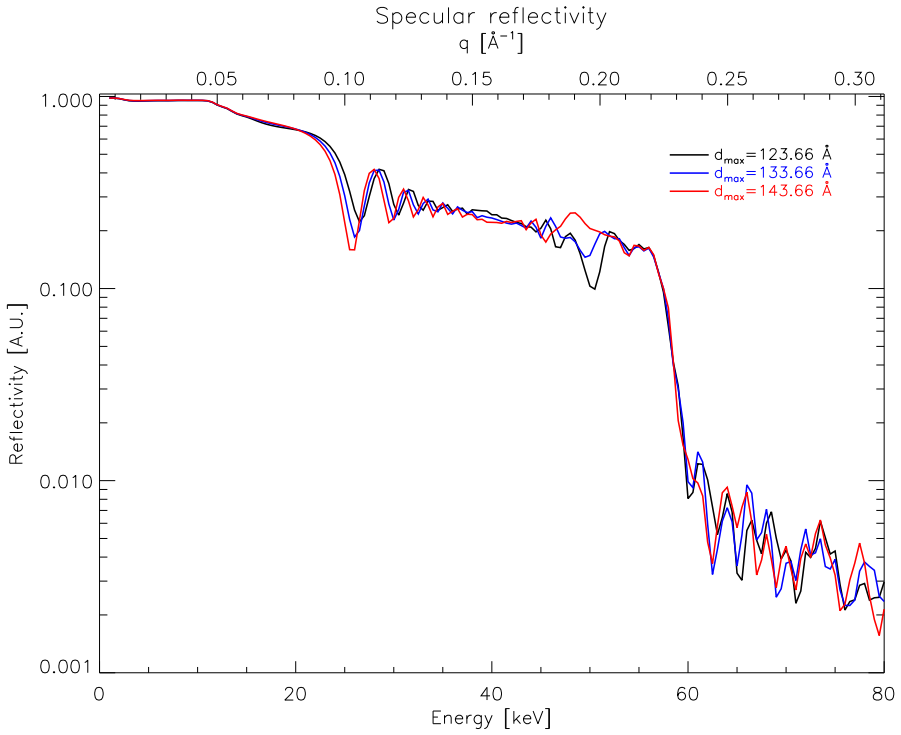

Figure 3.6: d_{max} influence d-spacing progression through Eq. 1.9 (Sec. 1.5). It can be used to fit the overlap between the first Bragg peak and total external reflection without significantly altering the ridge structure period, unlike c. Degeneracy with Γ_{top} is a major obstacle in unambiguously determining the multilayer structure.

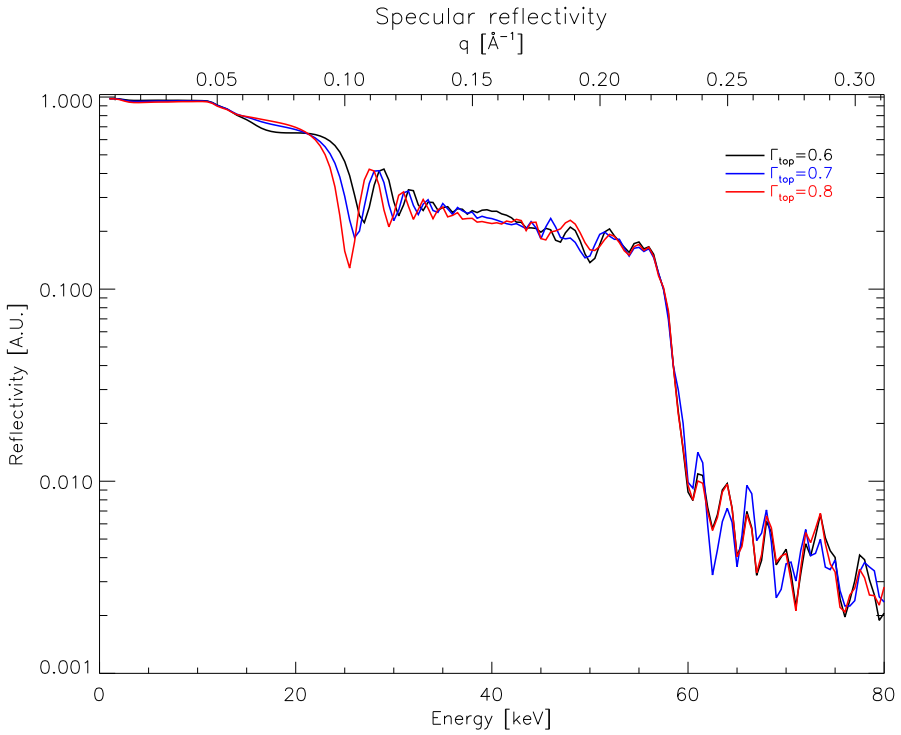

Figure 3.7: Γ_{top} determines the efficiency of total external reflection. This in turn impacts the initial ridges. Data between E_c and the first Bragg peak provides a strong feature for Γ_{top}. Degeneracy with both c and d_{max} is a major obstacle in unambiguously determining the multilayer structure.

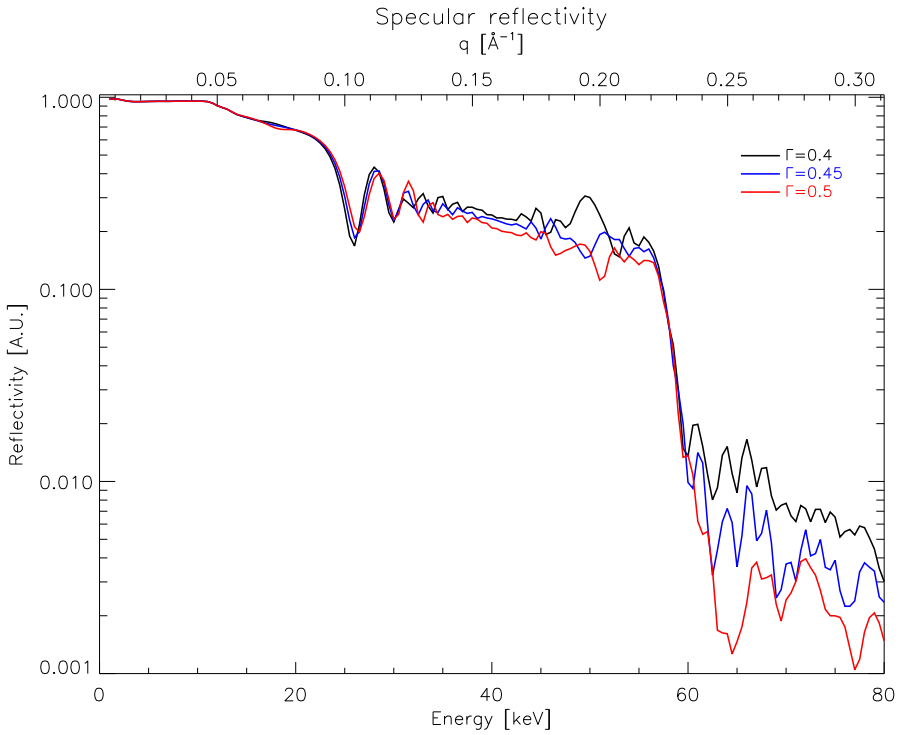

Figure 3.8: Γ determines the reflectivity efficiency from the individual layers and as such influence the overall reflectivity level. Degeneracy with micro-roughness is broken through σ being energy-dependent.

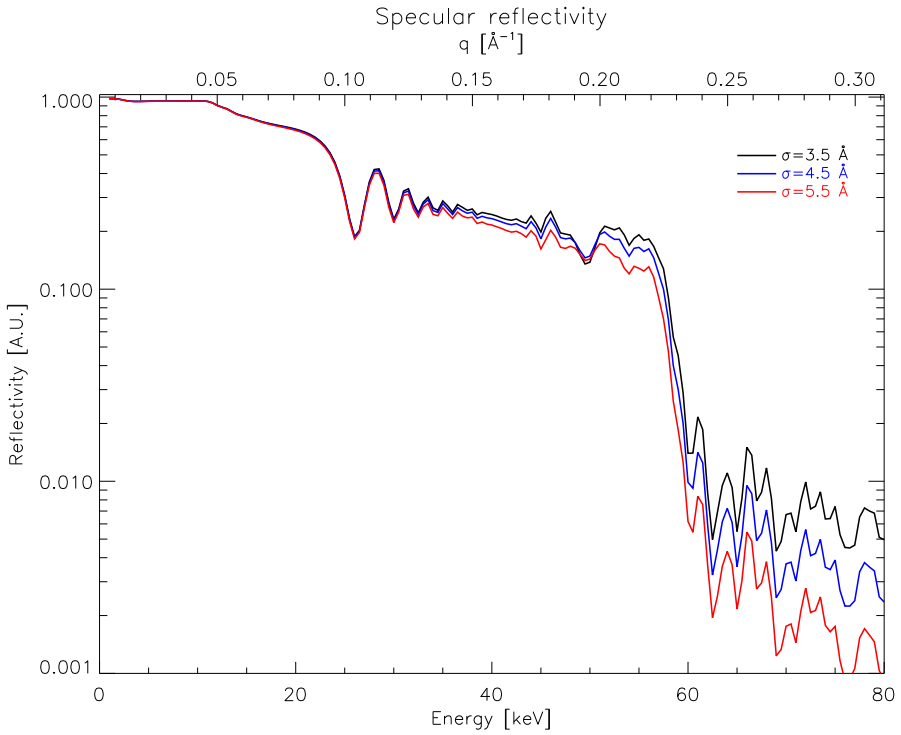

Figure 3.9: Micro-roughness influence the reflectivity efficiency as a function of energy.

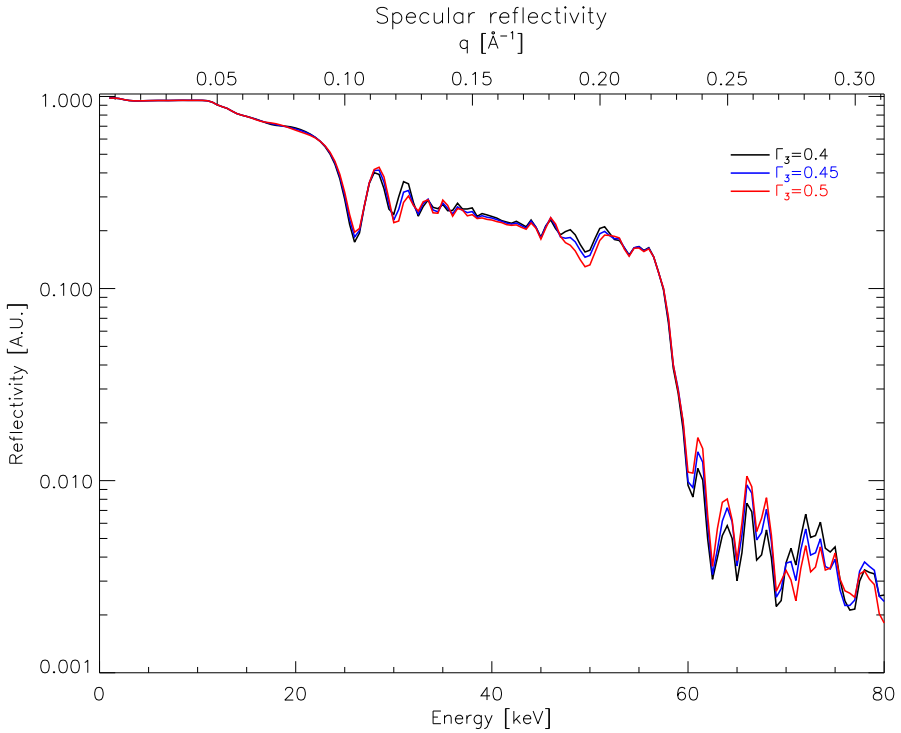

Figure 3.10: Γ_3 determines the reflectivity efficiency of the third Bragg peak. This enables detailed fitting of the relative reflectivity levels in the ridge structure. Γ_2 is also fit. Degeneracy with all parameters except micro-roughness imply that the adjusted values do not represent the actual multilayer structure.

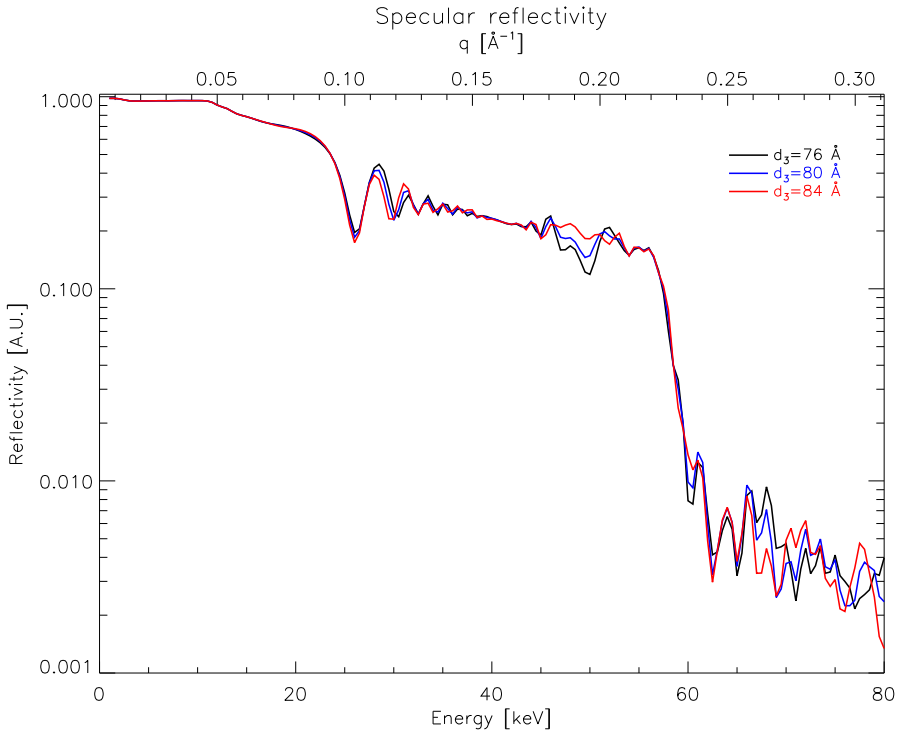

Figure 3.11: d_3 determines the location of the third Bragg peak. This enables detailed fitting of the ridge structure period independent of the power law progression. d_2, d_4, d_5 and d_6 are also fit. Degeneracy with all parameters except micro-roughness implies that the adjusted values may not represent the actual multilayer structure, but TEM images confirm that a variation exists.

Note that bulk density has been assumed for all materials. Early analysis attempted to incorporate a fitting of the density value, but the degeneracy with d_{max} and Γ_{top} prevents a reliable value to be determined. Several studies have shown sputtered material to have lower than bulk density [44, 45, 46]. The effect is effectively rolled into Γ_{top} and Γ through lowered reflectivity efficiency, especially near the critical energy (E_c). This further complicates the interpretation of the low energy response. Chapter 4 briefly discuss determining density from TEM images.

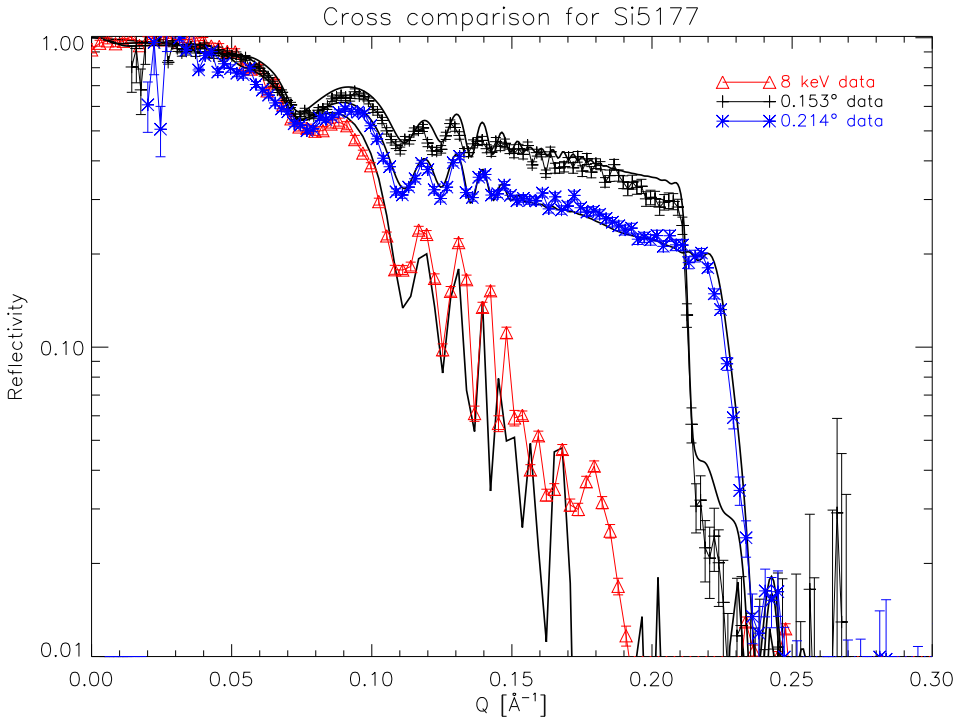

Figure 3.12: Cross-comparison of the three available witness sample data sets against the as-coated multilayer structure derived from fitting the 0.214° data. Although generally good agreement is found there is a tendency for the fit to overestimate response from the initial ridge structure. This tendency becomes more pronounced for the low angle and energy data. The 8 keV data has been offset by $-0.04°$ owing to motor readout error. $\chi^2 = 0.65$ for the 0.214° data.

3.4 Data set findings

Through fitting the data several data and fit artifacts were identified. They are laid out in Sec. 3.4.1-3.4.3.

3.4.1 d_{min} dip

The fits show a general tendency to overestimate reflectivity at the d_{min} dip as shown in Fig. 3.13. This is caused by the finite size of the RaMCaF beam footprint, specifically, due to small variations in d_{min} and θ_i over the illuminated area. The difference in incidence angle is caused by mounting induced wafer figure error. Figure 3.13 shows the effect of a 2%(± 0.5 Å) variation of d_{min} and a θ_i variation of $\pm 0.005°$. The structure of the dip indicates that a combination of the two is required for an accurate fit. This agrees well with Chapter 2 indicating that d_{min} vary on order 1% over the $20 - 40\,mm$ by $4\,mm$ footprint (depending on angle), i.e. too little to explain the full effect, but sufficient to contribute. The figure error required to provide a significant contribution cannot be explained by Si wafer or mounting fixture flatness, as these contribute at the arcsecond level. The implication is that particulate contamination during sample mounting induce the effect. This is supported by the feature being more or less pronounced on a sample-by-sample basis.

3.4.2 Cathode drop-outs

During coating deposition local charge build-up on the target may occur, causing the plasma to discharge through arcing [37]. Before sputtering can continue the plasma has to reignite. While ignition occurs automatically, providing the Ar pressure is high enough, the rotational stage will not pause. Therefore a number of flight coatings exhibit artifacts from these so-called cathode drop-outs. One such is imaged by TEM in Fig. 3.14. The influence on reflectivity can be substantial as indicated by Fig. 3.15. Note that TEM does not necessarily provide an accurate account of the Γ value. This is illustrated in Fig. 3.14 by the fact that only one C cathode dropped out, yet the residual C layer appears to be much less than 50% of its intended thickness. The dip in reflectivity was fit by reducing the affected C layer thickness by 48%. Refer to Chapter 4 for additional details on the TEM campaign.

The drop-outs were monitored by polling all cathodes at the beginning of each bilayer. A limitation in the chamber software prevented continuous monitoring. Lack of continuous monitoring potentially compromises the witness sample data ability to represent the coating applied to the flight substrates. All witness samples were mounted on MP7 (refer to Fig. 2.2, Sec. 2.1). For a drop-out occurring on C2 between one and five minutes pass before the witness sample travels past the affected cathode, depending on the d-spacing and material being coated. The problem is illustrated by witness sample Si5169. The coating log for the Si5169 run indicates that C2 dropped out on bilayer 56. No other drop-outs were recorded. However, both TEM and RaMCaF data show the only drop-out significantly affecting reflectivity occurred at bilayer 123. Table 3.4 provides an overview of the number of recorded and observed drop-outs as well as the afflicted samples. A total of nineteen coating runs have drop-outs. Thirty-eight substrates were mounted in FM1 and 347 in FM2 from these runs. It is stressed that the actual number of drop-outs may be higher.

The lack of continuous monitoring prevents detailed investigation of the impact on individual substrate reflectivity. Instead, Chapter 5 investigates NuSTAR calibration data from subgroups containing a high fraction of potentially affected substrates. It is confirmed that the witness sample does not provide an accurate account of the as-coated multilayer for all substrates when drop-outs occur.

3.4.3 Target wear and calibration

While no detailed investigation of observed target wear and accuracy of deposition rate calibration is carried out some general observations are relevant. A total of fifteen deposition rate calibrations were carried out during the flight coating campaign. The calibrations were unevenly distributed so that up to fifty-one consecutive runs towards the end of the coating campaign (almost all W/Si runs) saw no recalibration while the longest stretch during the first half was twenty. This was done to maximize substrate output towards the end of the coating campaign. On a case-by-case

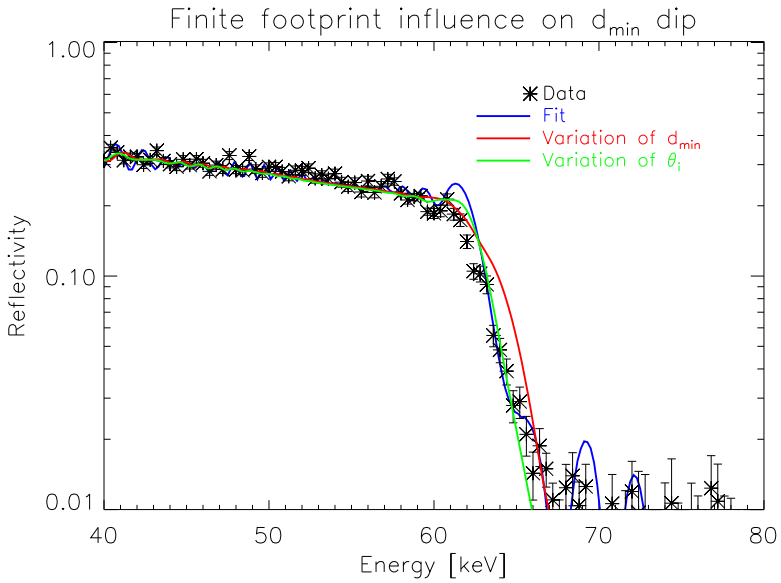

Figure 3.13: Specular reflectivity from Si5216 at RaMCaF. The fit overestimates reflectivity at the d_{min} dip. The peak arises through a variation in d_{min} or θ_i over the pencil beam footprint. The structure at the dip implies that a combination of the two is necessary for an accurate fit. $\chi^2 = 0.58$ for the 0.224° data.

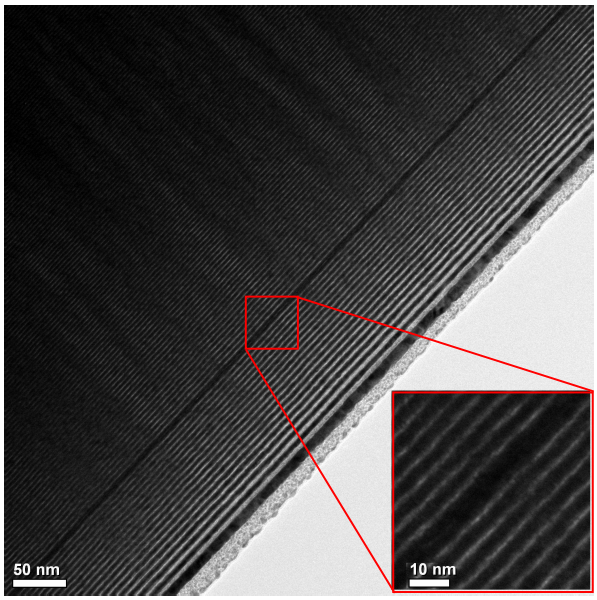

Figure 3.14: TEM image of Si5169. Bright streaks correspond to C layers while dark are Pt. The top of the stack is shown with a cathode drop-out on C2 during coating of bilayer 123. Refer to Chapter 4 for additional details on TEM images.

Table 3.4: Overview of the recorded and observed cathode drop-outs. Recorded drop-outs were parsed from the coating chamber run logs. Observed drop-outs were found from X-ray data. Note that a single coating run may have multiple drop-outs.

	Recorded	Observed
Pt/C	14	7
W/Si	16	15
Samples	Si5167, Si5168, Si5169, Si5181, Si5185, Si5186, Si5202, Si5204, Si5281, Si5282, Si5283, Si5290, Si5318, Si5319, Si5357	Si5167, Si5168, Si5169, Si5181, Si5282, Si5283, Si5289, Si5290, Si5291, Si5314, Si5318, Si5319, Si5320, Si5338, Si5357

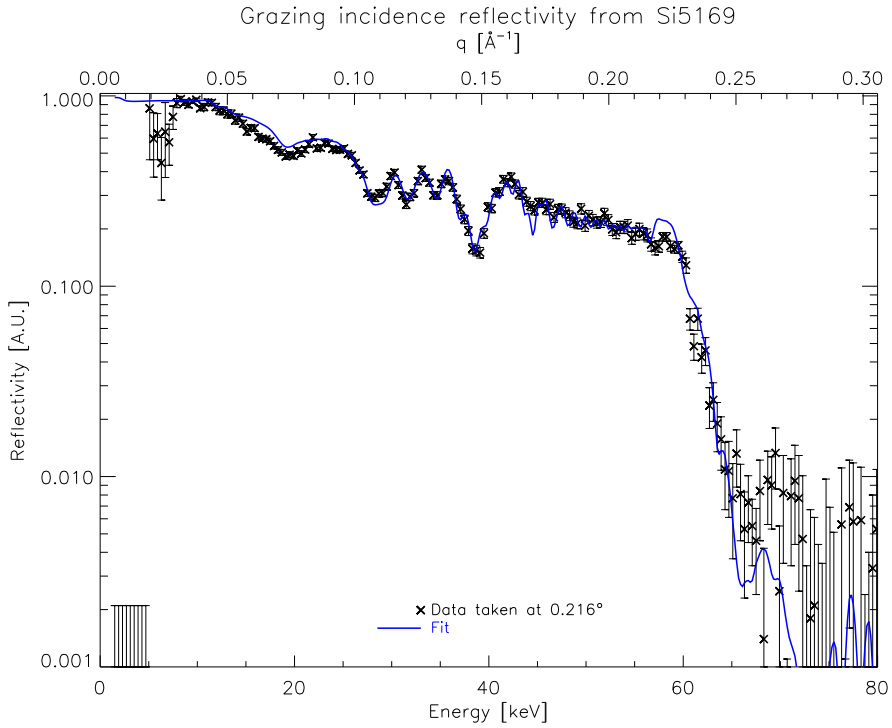

Figure 3.15: Specular reflectivity from Si5169 at RaMCaF. The dip in reflectivity near 40 keV is caused by a C cathode drop-out. The data has been fit by reducing the affected layer thickness by 48 %. $\chi^2 = 0.94$ for the 0.216° data.

basis very few calibrations correctly established the deposition rate. The data set implies the primary reason for this was a failure to correctly scale from the calibration sample d-spacing to the intended d_{min}. On average the recipe minimum d-spacing was missed by 7% in the first run following a calibration. In addition to this, for Pt/C, a $1-2\%$ decrease in deposition rate per run was accumulated from target wear. Target wear is observable in the evolution of $d_{min,ac}$ during periods with no target changes and calibrations. Establishing whether a similar trend exists for W/Si requires a more detailed investigation. Table 3.1 and the evolution of $d_{min,ac}$ for W/Si indicate that it is not the case. The following considerations therefore only apply to Pt/C.

Barring a few operator induced errors, the rail rotational speed was set according to recipe, but with a wrong offset, as observed from $d_{min,ac}$ being smaller than design. From this a generally higher c value was achieved. Estimating $d_{max,ac}$ can be done by compensating for the offset and target wear, e.g. by

$$d_{max,ac} = (0.99)^n \frac{d_{min,cal}}{d_{min}} d_{max} \tag{3.2}$$

In Eq. 3.2 $d_{min,cal}$ is the minimum d-spacing of the most recent coating applied immediately following a calibration run and the pre-factor 0.99 compensates for the deposition rate decrease n runs from said calibration. d_{min} and d_{max} are given by the design recipe. Equation 3.2 predicts $d_{max,ac}$ to within a couple of percent. The accuracy of this prediction relies on a low deposition rate fluctuation and the rotational speed remaining fixed from run-to-run. The rotational speed is only changed after a deposition rate calibration, at which point a new $d_{min,cal}$ must be established.

Equation 3.2 implies that accurate knowledge of $d_{min,cal}$ can significantly improve recipe prediction prior to fitting the specular reflectivity data. It is further worth noting that in the seven cases where a target change was not followed by a calibration, $d_{min,ac}$ reverted to within 2% of $d_{min,cal}$ in all but one instance. Reverting to $d_{min,cal}$ indicates that all new targets have approximately the same deposition rate. The implication of this is that redoing the calibration introduces greater uncertainty on coated $d_{min,ac}$ compared to a target change. This consideration is complicated when only a subset of targets are changed, especially if the Pt target is not one of them.

Even so, the average uncertainty is below the 7% introduced by recalibration.

3.5 Additional work

While the as-coated recipes fit the data well at both RaMCaF angles, Chapter 4 shows that the actual multilayer structure is not necessarily well-described near the top of the stack. Several improvements to the fitting approach are suggested here, most of them breaking the degeneracy by including additional data or coupling existing parameters. The relevance of these improvements is illustrated in Chapter 5 by assessing how well the multilayer response of mounted substrates is modeled by the ORM. While findings are complicated by ORM implementation issues it is indicated that improvements in the low energy fit is recommendable.

- $d_{min,ac}$ provides an in-situ measurement of the deposition per second, as the steps per second (rotational speed) is known from the coating logs. Seeing as the coating logs also contain rotational speeds for the remaining stack, c_{ac} and $d_{max,ac}$ can be estimated independent of the degeneracies plaguing the low energy response. It is important to note, that while $d_{min,ac}$ is determined to better than 1%, $d_{max,ac}$ uncertainty will be on order 5% due to the up to six times thicker d-spacing. This is a minimum uncertainty value assuming negligible deposition rate fluctuation. While Eq. 3.2 illustrates the validity of predicting $d_{max,ac}$ from initial coating conditions for Pt/C, the multilayer estimated from $d_{min,ac}$ and coating logs should only be used as a starting point for the fit to specular reflectivity data.

- Γ_{top} and Γ should be coupled in the fitting process. As this ties the Γ_{top} value to the response of the entire stack it may provide significant leverage for breaking the degeneracy between Γ_{top} and d_{max}.

- True cross-fitting between the high and low angle RaMCaF data should be implemented. While $d_{min,ac}$ may only be determined using the high angle data, adding the low angle data to fit the top bilayer thicknesses can provide a more realistic multilayer fit.

- A more complex interface should be included in the fitting process. The TEM images discussed in Chapter 4 show that assuming both interfaces (heavy-on-light and light-on-heavy) to resemble an error function is a simplification.

- Dedicated measurements should be carried out to establish the as-coated density of the individual materials. While Chapter 4 indicates that density depends on bilayer thickness, merely including, or ruling out, a lower-than-bulk density for the top layers would be helpful in firmly establishing the low energy response. Utilizing several different techniques (such as TEM, specular reflectivity and Rutherford backscattering [46]) is anticipated to be required.

- Scattered intensity in the specular direction should be subtracted from the specular reflectivity data. Subtracting the scattered intensity requires a detailed scattering model, but allows greater detail to be deduced from the data acquired beyond the d_{min} dip. In addition to this, Γ and micro-roughness values can be more accurately determined. The NuSTAR flight coating scattering model has yet to be finalized. Refer to Chapter 5 for additional details.

3.6 Chapter summary

Specular reflectivity data acquired on NuSTAR witness samples were used to determine as-coated recipes. The data were fitted using eight parameters, several of which are heavily degenerate. As-coated recipes were found to differ significantly from design recipes. For several fitting parameters (d_{max}, c and Γ), part of the deviation from design derives from parameter degeneracy. However, $d_{min,ac}$ is not affected by the degeneracy and was found to be on average 8% lower than the intended value. For Pt/C it was found that target wear induces a significant part of the deviation from design. For both Pt/C and W/Si, the main cause for missing design values is a failure to accurately establish the deposition rate from calibration coatings.

From fitting cathode drop-outs using both RaMCaF and TEM data, it was found that the witness sample and the coating log information are not adequate for determining the influence of cathode drop-outs on flight substrate multilayers. As investigating individual substrates is not possible, NuSTAR on-ground calibration data is used in Chapter 5.

A number of improvements were suggested for reducing the effect of parameter degeneracy.

The NuSTAR ORM input repository contains the complete set of as-coated recipes.

Chapter 4

TEM campaign

Abstract - *In this chapter, TEM images acquired from three flight witness samples are discussed. Interface details observed with TEM are presented. Bilayer thicknesses for the witness samples are determined from the acquired images. Specular reflectivity is calculated for the TEM estimated multilayer and compared to Chapter 3 data and fit. Significant improvements to the low energy response is found, and additional work is suggested.*

Previous studies have shown TEM to be helpful in breaking the parameter degeneracy in cst-d and simple graded multilayer coatings [47, 48, 49, 44]. Common to these experiments were the careful control exercised throughout the deposition process and a low number of bilayers. Conversely, the witness samples were coated under transient conditions and span hundreds of graded d bilayers. Owing to the complicated multilayer structure the intention of the TEM campaign is not to meticulously determine individual bilayer thicknesses, but simply to obtain additional information on a representative selection of flight witness coatings. The additional information aids the effort on validating and improving the as-coated recipes discussed in Chapter 3.

TEM images were acquired in California by Evans Analytical Group (EAG), a privately held surface analysis and electron microscopy laboratory. EAG was hired based on their close collaboration with a NuSTAR related group at the Physics Division, Physical and Life Science Directorate, Lawrence Livermoore National Laboratories (LLNL). The campaign was funded by LLNL under Contract DE-AC52-07NA27344 (U.S. Department of Energy). The work was further supported by the LLNL Laboratory Directed Research and Development Program.

4.1 TEM campaign

A JEOL 2010 TEM with an acceleration voltage of $200\,keV$ was used. Images were acquired with a Gatan Multiscan 794 CCD camera. A JEOL 2010 high-resolution pole piece enable a point-to-point resolution of 1.9 Å. Lattice fringes down to 1.4 Å in width can be resolved. Magnifications of up to $500000\times$ were used for image acquisition. The CCD contains 1024×1024 pixels with a pixel size of $24 \times 24\,\mu m^2$. Pixel to Ångström conversion factors $T_{p,r}$ are given in Table 4.1 for the magnifications used.

Additional comments on the magnification are relevant for the discussion in Sec. 4.5. From Table 4.1 $T_{p,r}$ is found to follow a power law given by

$$T_{p,r} = b_r M^{-k_r} \tag{4.1}$$

where M is the magnification and b_r and k_r are constants related to TEM lens settings. Establishing the constants using Table 4.1 shows that $b_1 \neq b_2$ and $k_1 \neq k_2$. Neither constant being fixed for the device implies that a minimum of three M values must be well-known to predict a fourth. In Sec. 4.5 this means that when the nominal $500000\times$ magnification is shown to be off by a given amount, the actual magnification of the nominal $50000\times$ magnification cannot be determined. This prevents in-situ calibration of M to be carried out between degrees of magnification unless at least three separate M values resolve structure that can be used for the in-situ calibration. This is not the case in the present data set.

Table 4.1: Pixel to Ångström conversion factors $T_{p,r}$ for the utilized magnifications. During round one ($r = 1$) Si5117 was measured while round two ($r = 2$) samples were Si5218 and Si5355. Round one took place in February 2011, and round two in August 2011.

M	$T_{p,1}[\text{Å}/pixel]$	$T_{p,2}[\text{Å}/pixel]$
25000×	6.29902...	N/A
50000×	3.03671...	3.07929...
100000×	N/A	1.54560...
250000×	0.60576...	N/A
500000×	0.28291...	0.31496...

Witness samples Si5117 and Si5218 (Pt/C), as well as Si5355 (W/Si) constitute the sample set. Refer to Appendix I for the as-coated recipes found for these samples. In the remainder of the chapter the fragment of the witness sample prepared for TEM will be referred to as the "specimen". Specimen preparation was carried out in stages. The witness wafers were cleaved along the Si(110) face, such that the electron beam enters parallel to the Si[110] axis for a cross-sectional view of the multilayer. The cleaved specimens were thinned to approximately $1\,\mu m$ using Buehler Ecomet III polishing wheels. Following thinning the specimens were mounted to $3.05\,mm$ TEM grids and ion milled using either a Gatan precision ion mill at $4\,kV$ (Si5218 and Si5355) or a FEI Focused Ion Beam (FIB) tool (Si5117). EAG could not provide any additional information on the FIB model or settings. The company's best estimate for specimen thickness was $< 100\,nm$, and a wedge along the length of the specimen could not be ruled out.

The acquired images can be found from Appendix K.

4.2 Data processing

Processing of the bright-field images is carried out using custom IDL software. The general approach for bilayer thickness determination is illustrated in Fig. 4.1 for Si5355. The outlined segment is summed horizontally to provide a one-dimensional contrast intensity curve. Low intensity valleys correspond to high absorption, i.e. Pt or W, while the peaks correspond to C or Si. Peaks and valleys are identified and a simple Gaussian fit to each layer. The transition between materials is arbitrarily defined as the location where intensity has dropped to 30% of the peak to valley value. The arbitrary number illustrates that Γ cannot be unambiguously determined from standard TEM. Inability to determine Γ is due to a number of reasons discussed in Sec. 4.3. It is important to note that the arbitrary number only affects the determination of individual layer thicknesses, not the bilayer thickness.

The Java$^{\text{TM}}$-based image processing and analysis tool ImageJ [50] also deserves mention. ImageJ was used for reading the raw image files supplied by EAG and to carry out the reciprocal space operations in Sec. 4.5.1.

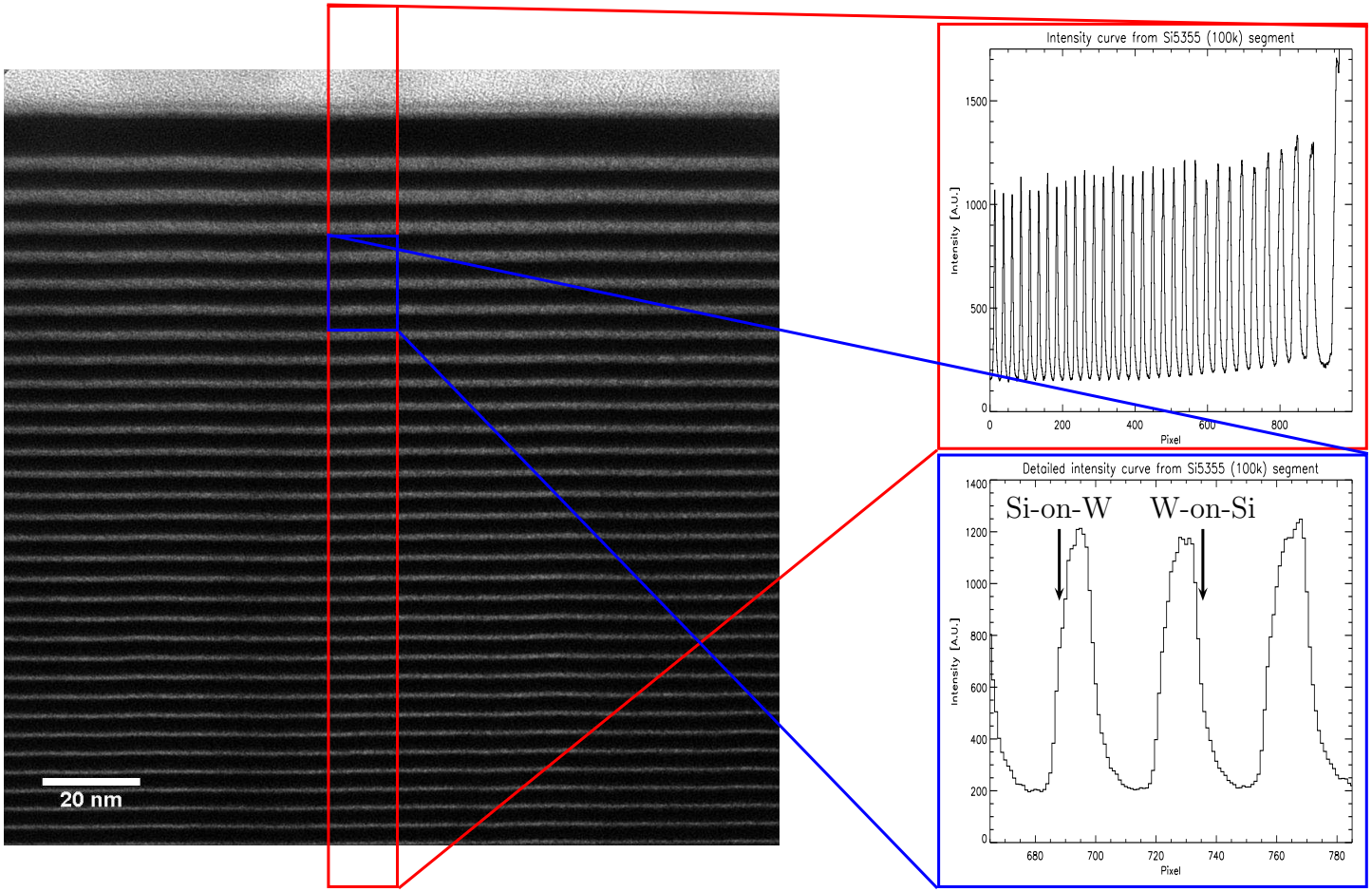

Figure 4.1: TEM image of Si5355. Image is taken at the top of the stack with 100000× magnification. Bright areas correspond to low electron absorption, i.e. low density material, while the opposite is true for dark areas. The top 6 nm of the image shows a low density epoxy capping layer applied during TEM specimen preparation. Contrast intensity curves are shown for the full vertical length of the image (red box) and a limited number of bilayers ($i = 5, 6, 7$) to bring out details of the interfaces (blue box). See text for discussion.

4.3 Interface details

Interface morphology plays a critical role in detailed modeling of non-specular reflectivity from multilayers as discussed by [12, 31]. On its own, standard TEM cannot provide the information required for a comprehensive scattering model [51], but general features of the interface can be deduced for further investigation, e.g. through specular and non-specular X-ray reflectivity studies. It is important to note that care must be taken when comparing interface widths observed from TEM to the micro-roughness found from an X-ray study. Erroneous conclusions may be drawn due to the projection-limitation, i.e. contrast averaging along the thickness of the specimen. The average will depend heavily on the incidence angle of the electron beam. The beam being off by less than one degree is sufficient to blur the interface over a range comparable to the total interface width observed here for a 100 nm thick specimen.

Figure 4.1 shows details of the contrast at bilayers $i = 5, 6, 7$ from Si5355 at 100000× magnification. The nearly linear change of intensity at the Si-on-W interface can be interpreted as a rough interface with some interfacial diffusion, caused by Si bombardment. It is well-approximated by the error function interface profile used for fitting the witness sample data in Chapter 3. The total interface width is implied to be on order 16 Å, corresponding to a micro-roughness σ_{TEM} on order 4 Å [12], which is reasonable compared to the as-coated recipe σ value for Si5355 (3.9Å). At the W-on-Si interface the profile implies a broader diffusion range (22 Å or $\sigma_{TEM} \approx 5.5$ Å) with intensity decreasing as one over pixel distance from the peak. The distance dependence arise from an effect described in [52] where the W-on-Si interface is churned by the energetic bombardment of atoms. A significant fraction of these atoms consists of Ar backscattered from the W target. The energetic Ar atoms not only cause additional diffusion, but also induce resputtering of Si, i.e. Si brought to the surface by the churning is stripped. A similar effect is not observable at the Si-on-W interface as the amount of backscattered Ar is small on account of the lower atomic mass of Si.

Si5218 at 100000× magnification is shown in Fig. 4.2. Details of the contrast at bilayers $i = 4, 5, 6$ are highlighted. Although the interfaces appear to develop similar to W/Si coming off the C intensity peak, the profile quickly changes. At the Pt-on-C interface the change is caused by Pt forming crystallites [44]. The observable influence on contrast is complicated by the projection-limitation and the island nature of the crystallite growth. Conversely, the C-on-Pt interface profile is shaped by the fully formed crystallites. Once the deposited layer is thicker than the protruding crystallites, intensity climbs nearly linearly as seen for W/Si. The net result of this behavior is a broader interface width for Pt/C compared to W/Si.

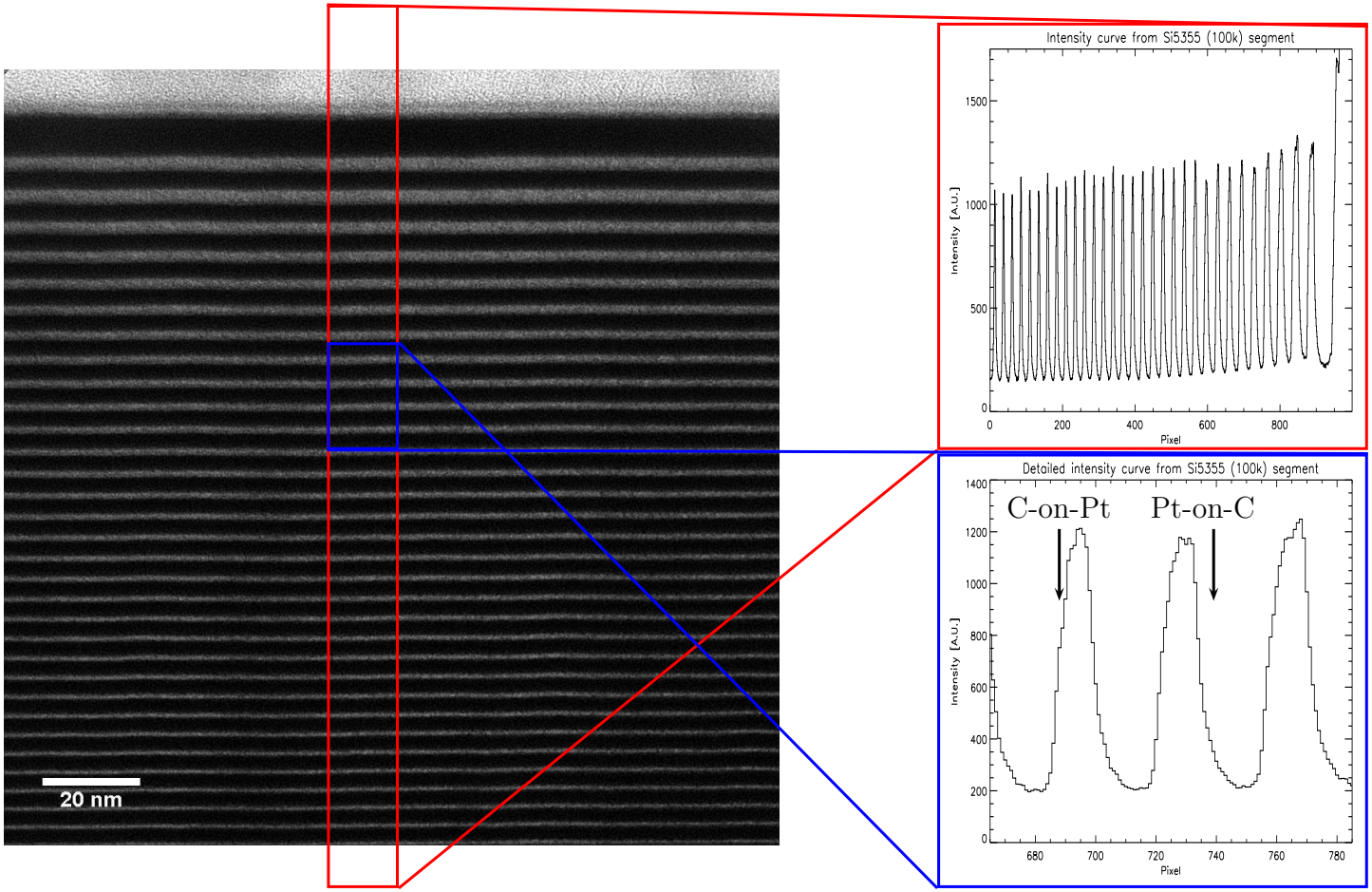

Figure 4.2: TEM image of Si5218. Image is taken at the top of the stack with 100000× magnification. Bright areas correspond to low electron absorption, i.e. low density material, while the opposite is true for dark areas. The top 33 *nm* of the image shows a low density epoxy capping layer applied during TEM specimen preparation. Contrast intensity curves are shown for the full vertical length of the image (red box) and a limited number of bilayers ($i = 4, 5, 6$) to bring out details of the interfaces (blue box). See text for discussion.

The difference in the profile of the two interfaces (i.e. light-on-heavy and heavy-on-light) can be modeled in IMD to potentially improve the fit to specular reflectivity data. A similar study carried out on W/Si multilayers indicated the effect of changing the interface profiles to be negligible [53]. However, it is noted that the interface widths found here are nearly twice that reported by [53]. Owing to the broader interface widths the impact on reflectivity may be great enough for realistic interface profiles to be beneficial for the overall fit. It is important to keep in mind that the estimated interface widths assume the interface profile observed from TEM has not been corrupted by the projection-limitation.

From the above discussion it is clear that the concept of layer transition is vague. The ill-defined transition in turn results in the arbitrary 30% of peak contrast value assumed as the point of transition and the subsequent high inaccuracy of Γ values. In Sec. 4.6 Γ and Γ_{top} are fitted using RaMCaF data.

4.4 Material density

Since the TEM image is essentially a density mapping, it is only natural to assume that information regarding the as-coated density of the layers can be found. As seen from Sec. 4.3 this is complicated by the complex composition of the individual layers, the projection-limitation and specimen wedge. For amorphous materials [48] proposed a method utilizing contrast theory ([7], Chapter 6) for determining as-coated density. The method ties the electron transmittance of the multilayer materials to the observed intensity in a set of TEM images. It is worth noting that the as-coated density in the topmost layers are the most interesting as the main influence of a lower density would be at the critical energy E_c.

As already discussed the Pt layers are made up out of crystallites, and so strictly speaking the proposed method cannot be used for the Pt/C multilayers. From [45] Pt is not expected to differ significantly from bulk density. Figure 4.1 and Fig. 4.2 both show indications of contrast evolving through the stack, i.e. the peak and valley height/depth varies for individual layers. For Pt/C the variation is due to the Pt crystallites and accompanying lattice fringes, while for W/Si it can indicate actual density changes. As only a single image was acquired in each location at a given magnification the method proposed by [48] cannot be tested.

4.5 TEM estimated d-spacings

Estimated d-spacings from all specimens are available from Appendix L. Figure 4.3-4.5 show the estimated d-spacing progression relative to the as-coated recipes. The discussion in the present section and Sec. 4.6 focus on the 50000× magnification data unless otherwise noted. The treatment is exemplified by Si5355 results. Figures similar to the ones shown below are available in Appendix L for Si5117 and Si5218.

The relative d being higher than one for the majority of points in Fig. 4.3-4.5 indicates that TEM claims d-spacings to be greater compared to the as-coated recipes from Chapter 3. However, two indicators point to a scale error M_e in the TEM data. For one, the minimum d-spacing from TEM ($d_{min,TEM}$) is estimated to be several Ångström higher than $d_{min,ac}$. A greater d_{min} is not realistic as $d_{min,ac}$ is unambiguously determined to within ± 0.1 Å from high angle data in Chapter 3. The higher $d_{min,TEM}$ cannot be explained by non-uniformities either, as this would require more than an order of magnitude greater deposition rate change over the witness sample compared to Chapter 2 results. Secondly, estimated d-spacing decreases with increasing magnification. From Eq. 4.1 this is not surprising, as M_e will not be linear.

Both artifacts imply a poorly calibrated magnification. EAG claims the magnification is calibrated to within 5% monthly. This value assumes accurate setting of specimen height during image acquisition. EAG could provide no estimate for specimen height error. Appendix M contain statements from EAG on the subject.

Establishing a more accurate magnification value must be done using in-image references. Two such references are present in the images. As already implied d_{min} is one, as it is known to better than 1% from Chapter 3. The second reference is the highly ordered crystal structure of the Si wafer substrate. The Si wafer approach is discussed in Sec. 4.5.1.

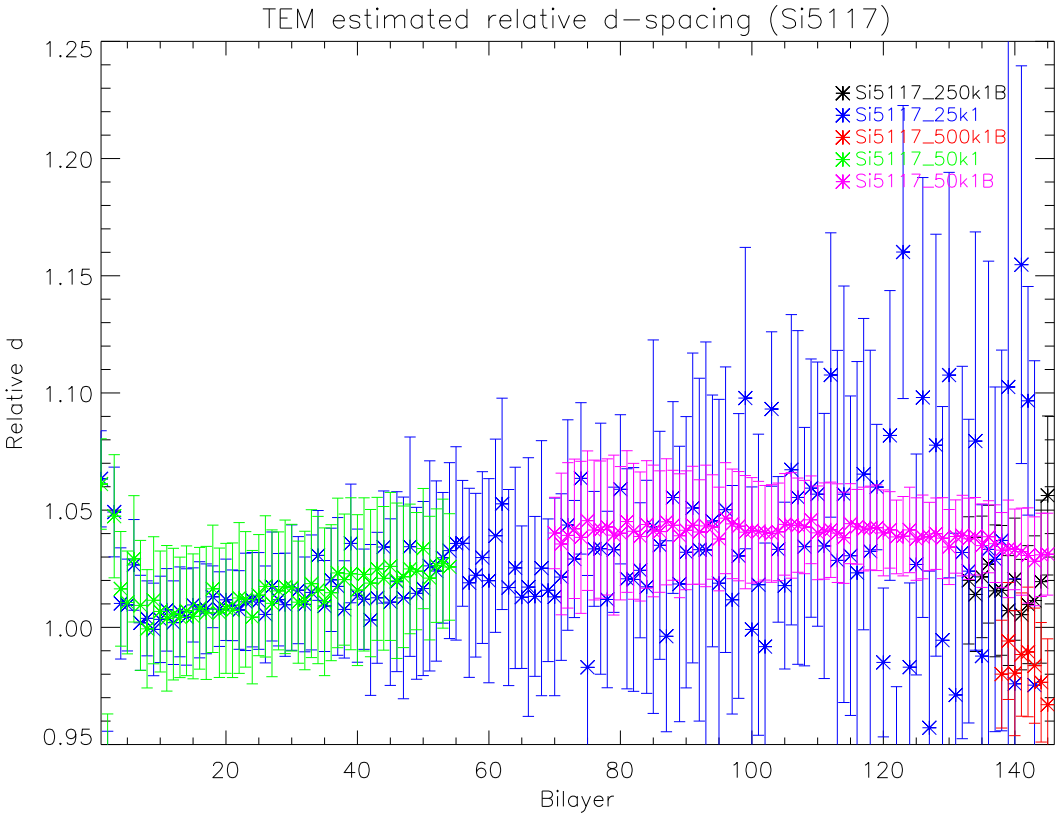

Figure 4.3: Relative d as determined from TEM compared to as-coated recipes for Si5117. All but Si5117_500k1B find thicker bilayers throughout the stack. The unrealistic values in the Si5117_25k1 data are due to the bottom layers not being resolved.

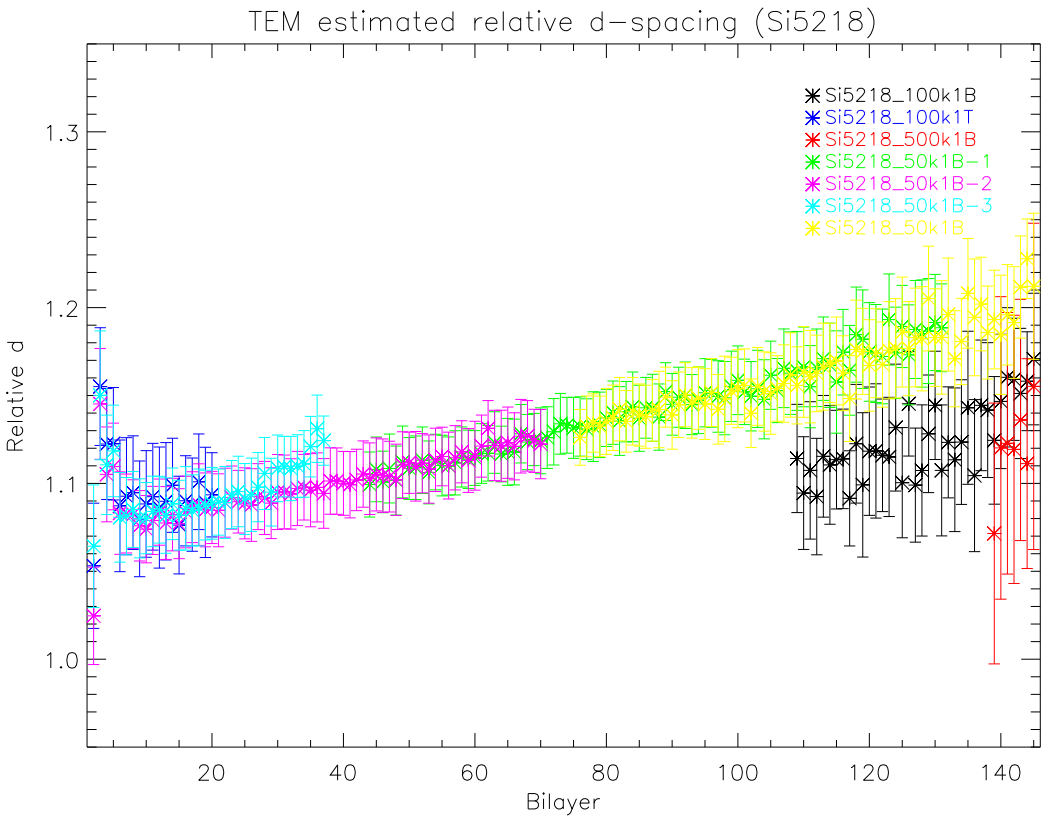

Figure 4.4: Relative d as determined from TEM compared to as-coated recipes for Si5218. The high magnification images deviate significantly from values determined at lower magnification in the same bilayer range. In addition to this, the overall trend of the 50000× images is for the relative d to increase towards the bottom of the stack. Si5218_50k1B-3 indicates this to be a measurement artifact as the increase is not reproduced by the overlapping Si5218_50k1B-2 data.

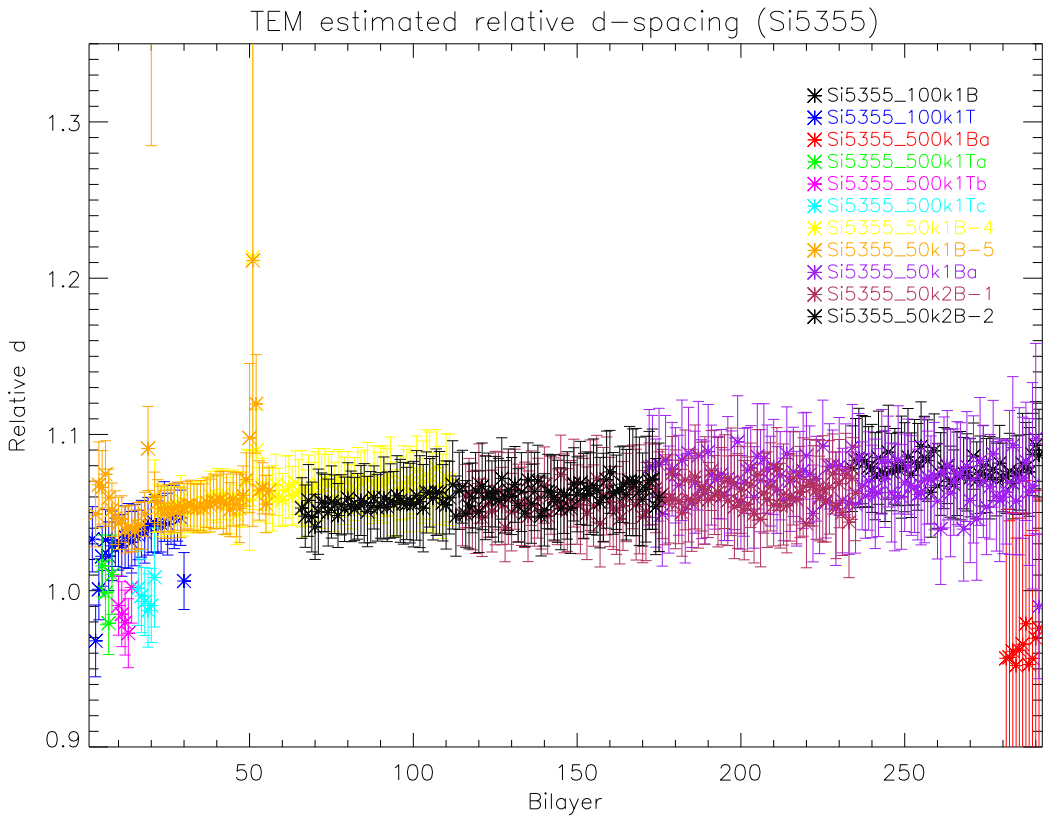

Figure 4.5: Relative d as determined from TEM compared to as-coated recipes for Si5355. All but the 500000× data claim the majority of the bilayers to be thicker viewed by TEM. On average the 50000× data is found to be 6% thicker than as-coated bilayers, but near the top of the stack the relative d decreases. The effect is more easily interpreted in Fig. 4.6 where the proposed scale error M_e has been compensated for. The spikes in Si5355_50k1B-5 data are due to specimen preparation causing cracks parallel to the bilayers. The affected bilayers were replaced by interpolated values in Sec. 4.6 when calculating specular reflectivity.

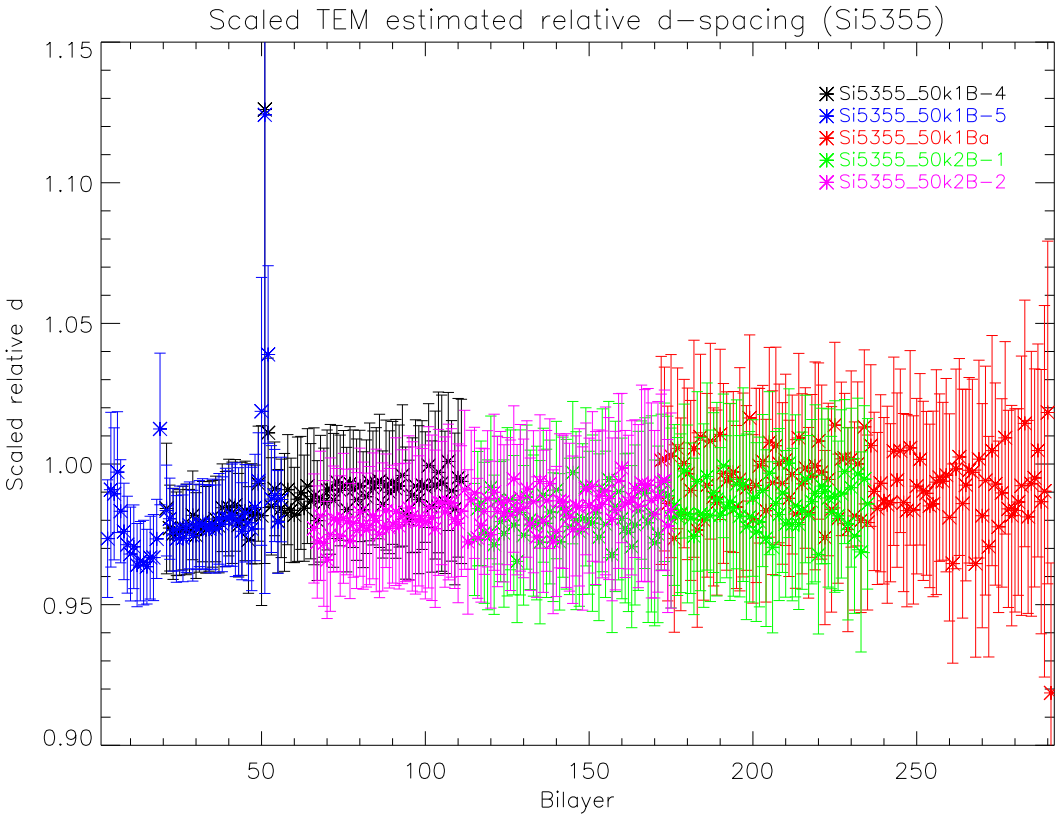

Figure 4.6: Relative d values scaled by M_e from Table 4.2 such that $d_{min,TEM}$ found from 50000× images equals $d_{min,ac}$. The scaled TEM data implies the top bilayer thicknesses to be overestimated by the as-coated recipe. The trend for the relative d to decrease towards the top of the stack indicates that the two data sets disagree regarding the c value. Similarly, the increase in relative d in the final few bilayers imply disagreement on d_i values.

Table 4.2: Overview of the magnification errors M_e at 50000× magnification. M_e is defined through $d_{min,ac} = d_{min,TEM} M_e$. The uncertainty in M_e is derived from $d_{min,ac}$ and $d_{min,TEM}$ uncertainties.

Sample	M_e
Si5117	0.968 ± 0.035
Si5218	0.824 ± 0.021
Si5355	0.928 ± 0.04

Scaling $d_{min,TEM}$ to $d_{min,ac}$ results in the M_e values listed in Table 4.2 at 50000× magnification. It is important to note that while $d_{min,ac}$ is known to better than 1%, $d_{min,TEM}$ uncertainty is markedly higher (3.5% for Si5355). As a result M_e for Si5355 corresponds to the actual magnification being $46400 \times \pm 2000$. The large scale error found in Si5218 images derives from a steady increase in relative d (refer to Fig. 4.4) towards the bottom of the stack. Si5218_50k1B-3 data show a similar trend within a single image. The localized increase is not reproduced in Si5218_501kB-2 acquired in the same region. It is assumed that an additional measurement artifact was introduced in these images. EAG could offer no input regarding a mechanism for the artifact.

Relative d values for Si5355 with the corrected magnification are shown in Fig. 4.6. Including M_e, TEM d-spacings are found to be thinner compared to the as-coated recipe values. A trend for the relative d to drop through the stack is broken near the top. The trend is also seen for Si5117 and Si5218 (refer to Appendix L). The implication is that the two types of measurements disagree on c and d_i values. Section 4.6 fit the TEM estimated d-spacings to RaMCaF witness data finding better agreement for the low energy response.

Table 4.3: Overview of the magnification errors M_e and M_{Si} at 500000× magnification. M_e is defined through $d_{min,ac} = d_{min,TEM} M_e$. The uncertainty in M_e derives from $d_{min,ac}$ and $d_{min,TEM}$ uncertainties. M_{Si} is based on lattice spacings derived from Si lattice fringe patterns. The primary contributor to M_{Si} uncertainty is detector resolution.

Sample	M_e	M_{Si}
Si5117	0.97 ± 0.018	0.91 ± 0.1
Si5355	0.96 ± 0.075	1.01 ± 0.1

4.5.1 Lattice fringe calibration

EAG calibrates their TEM using a MAG*I*CAL^{TM} calibration standard. Details on the calibration standard are available from Appendix M. Briefly stated, the standard allows calibration to better than 1% from 1000× to 1000000× magnification against an intricate arrangement of well-known Si/SiGe layer thicknesses. At any given magnification a layer thickness can be measured and compared to the calibration standard data sheet. The actual magnification is calculated and used to correct the device magnification, giving rise to the variation in $T_{p,r}$ from round one to round 2, refer to Table 4.1. The strength of the calibration approach is that all measured values can be traced back to the lattice spacing of Si{111} in the calibration sample substrate, i.e. a natural constant.

Following a similar approach in-situ calibration may be carried out against the Si wafer substrate. As the structure is only resolved at $>$ 250000× magnification the result is not directly applicable to the 50000× data, refer to Sec. 4.1. However, after scaling the data sets can be compared to establish whether the estimated d-spacings agree.

The bottom of the stack is shown in Fig. 4.7 at 500000× magnification. The Si wafer lattice fringe pattern is clearly distinguishable. Recall that lattice fringes do not directly image the atomic structure, but may provide insights regarding lattice spacing and crystal orientation. The fringes can be interpreted in reciprocal space. For this purpose a two-dimensional Fast Fourier Transform (FFT) is shown in Fig. 4.7. The vertical streaking imply a spread in the lattice fringe spacing caused by detector pixel size. The artifact is only barely discernible in the horizontal direction due to the limited vertical extent of the Si lattice fringes in the real space image. Table 4.3 shows M_e and M_{Si} for Si5117 and Si5355. None of the Si5218 images resolve the Si lattice fringes. In Fig. 4.8 M_{Si} has been used to scale the 500000× relative d values while the 50000× data is scaled by M_e from Table 4.2. Good agreement is found between the two corrected magnifications, confirming the presence of a scale error and the successful correction for it. Carrying out a similar confirmation using Si5117 data carries a large uncertainty as only the top two bilayers are uniquely identified in 500000× images. However, from these two bilayers M_{Si} from Table 4.3 is implied to be too low, i.e. for the corrected magnifications to agree M_{Si} should be 0.98 for Si5117. It is noted that 0.98 is close to M_e and that all values agree within the given uncertainties.

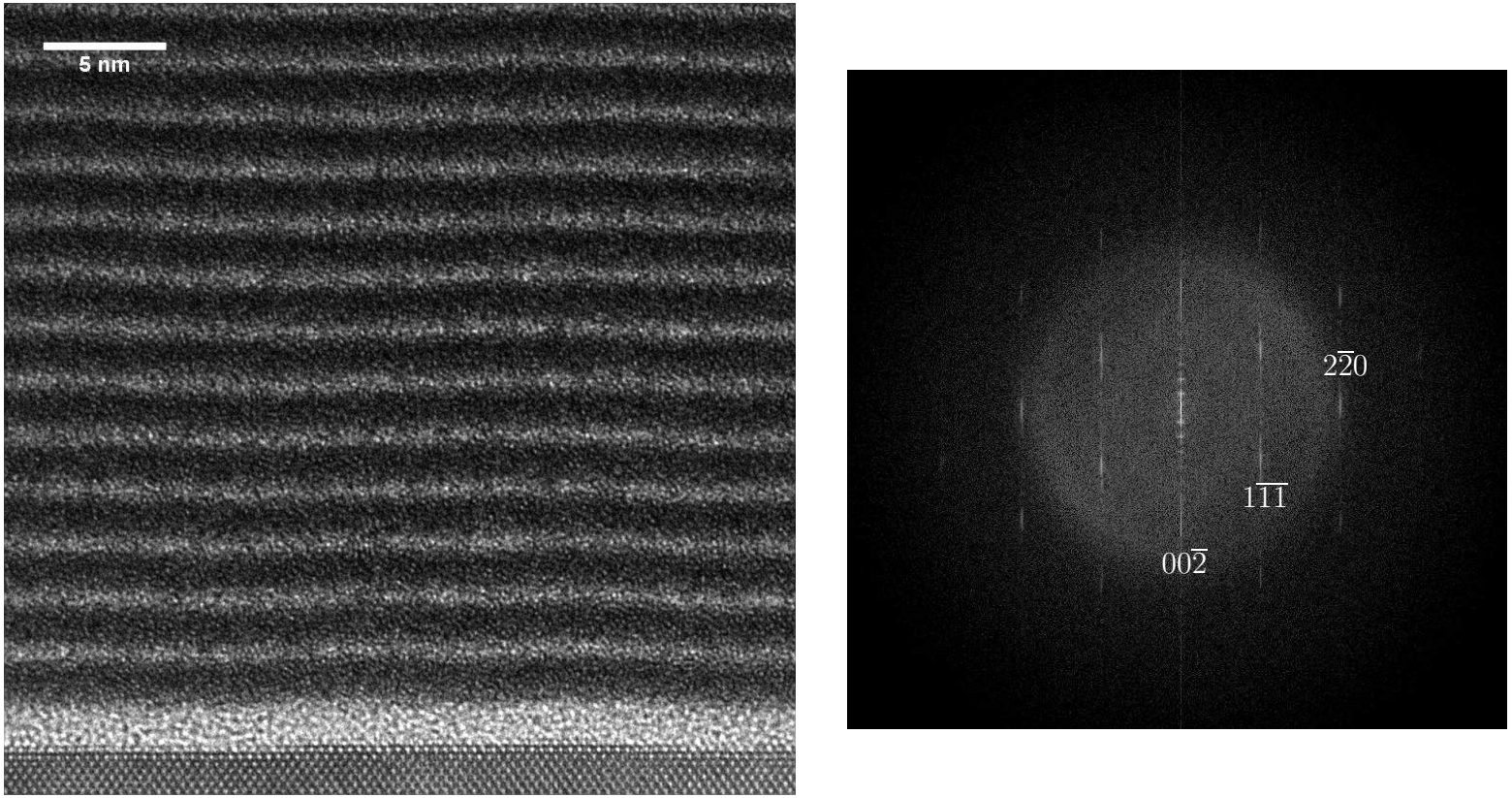

Figure 4.7: A TEM image of Si5355. The bottom of the stack with 500000× magnification is shown. The ordered structure at the bottom of the image represents the Si wafer. An FFT of the image is shown on the right. Lattice planes are indicated. The barely discernible diffuse halo indicates that randomly oriented W crystallites are present in the W layers.

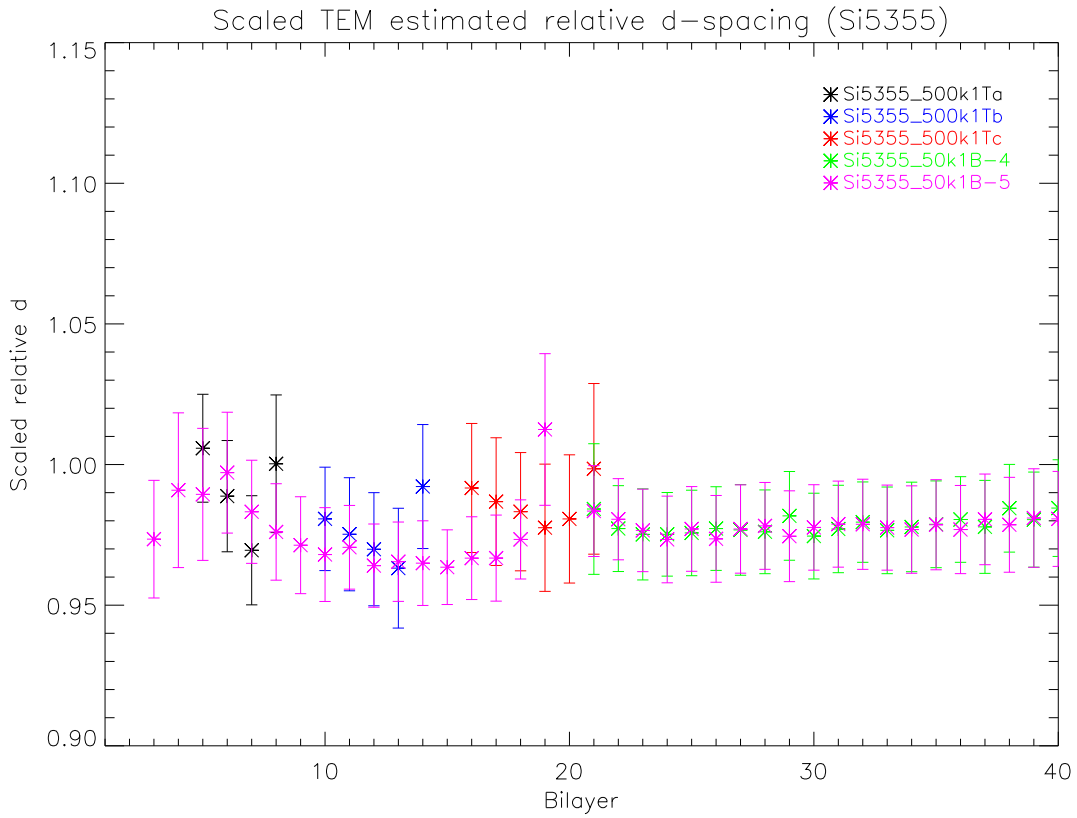

Figure 4.8: Scaled relative d values at 50000× and 500000× magnification. 50000× values have been scaled by M_e from Table 4.2 while 500000× data is scaled by M_{Si} from Table 4.3. There is good agreement between the general shape and size from the two separate data sets, indicating that the scale errors have been correctly compensated for.

4.6 Comparison to RaMCaF data

The TEM determined Si5355 multilayer, scaled as illustrated in Fig. 4.6, was used to produce the reflectivity plots in Fig. 4.9 and Fig. 4.10 at 0.178° and 0.238°, respectively. RaMCaF data and as-coated recipe reflectivity are also shown. Γ_{top} and Γ of the TEM bilayers were established through fitting to the RaMCaF data. An overview of the results can be found in Table 4.4. Eq. 1.9 parameters that approximately fit the TEM multilayer have been estimated to ease comparison. M_{fit} was found through fitting the low energy response to RaMCaF data. Ideally $M_{fit} = M_e$. While this is not the case, M_{fit} is within the uncertainty of M_e for all samples, refer to Table 4.2.

All three samples display improvements in the low energy response fit compared to the as-coated recipes. It is worth noting that while uncertainties for the bottom TEM d-spacings are not necessarily higher than for the top bilayers the impact on reflectivity is greater. This is observable in Fig. 4.10 through the structure variation between 50 keV and 65 keV. The impact is more significant for Si5117 and Si5218 as it causes the TEM multilayer to miss the d_{min} dip (refer to Fig. L.4 and Fig. L.6 in Appendix L). Missing the d_{min} dip dominates the chi-squared values for the high angle data.

It is important to note that M_e, through M_{fit}, essentially reintroduces the degeneracy between Γ_{top} and the d-spacing progression that TEM was employed to break. Improvements are primarily derived from a well-determined c value resulting in linear scaling (M_{fit}) being sufficient to establish the individual bilayer thicknesses. It is further worth noting that the fits were achieved with $\Gamma_i = \Gamma$. In addition to this, Γ and Γ_{top} were fit and found to be near or at nominal values. Si5218 deviates some, but unlike the as-coated values the deviation seems correlated, i.e. both Γ and Γ_{top} are approximately 10% lower than nominal. The implication is that Γ and Γ_{top} are coupled. This was not assumed for the as-coated recipes allowing greater discrepancy between the two parameters.

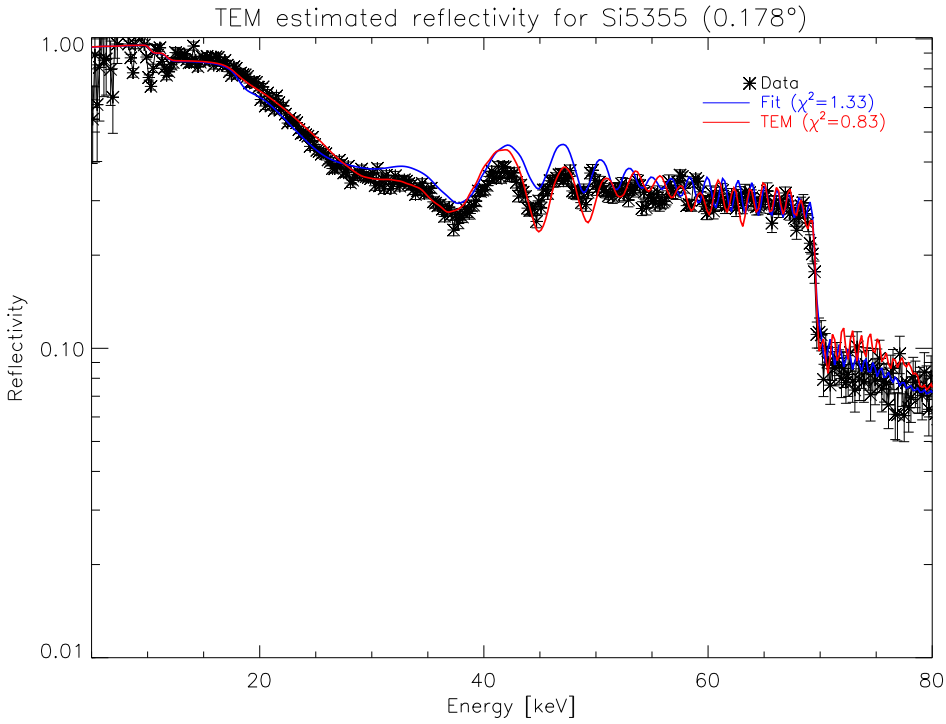

Figure 4.9: Specular reflectivity from Si5355 at RaMCaF compared to reflectivity derived from the as-coated recipe (blue) and TEM d-spacings (red). A significant improvement in the low energy response fit is achieved using the scaled TEM bilayers. Uncertainties in TEM bilayer determination becomes increasingly important as the d-spacing decreases. This is observable above 50 keV.

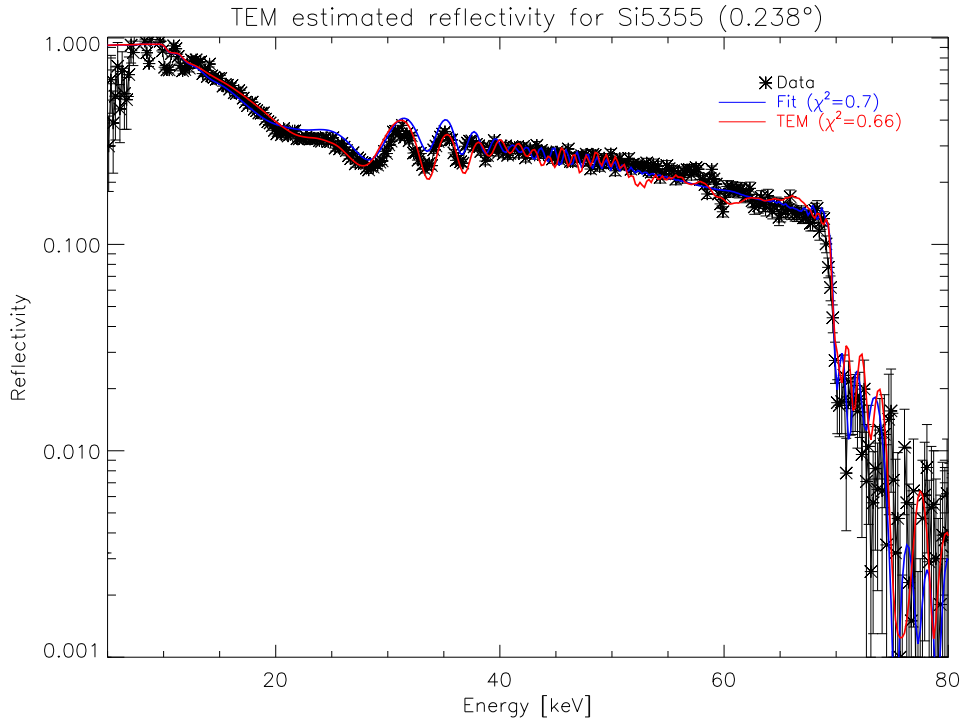

Figure 4.10: Specular reflectivity from Si5355 at RaMCaF compared to reflectivity derived from the as-coated recipe (blue) and TEM d-spacings (red). A significant improvement in the low energy response is achieved using the scaled TEM bilayers. Uncertainties in TEM bilayer determination becomes increasingly important as the d-spacing decreases. This is observable above 50 keV.

Table 4.4: Approximated recipe values for TEM data compared to as-coated recipes. Note that the values were found by favoring the lower energy response which results in both Si5117 and Si5218 missing the d_{min} dip, as $M_{fit} \neq M_e$. Reflectivity plots for these two samples are available in Appendix L. χ^2 values describe the quality of fit for low/high angle data. Missing the d_{min} dip results in the chi-square value being dominated by a poor fit to the high energy response.

Witness	Type	M_{fit}	χ^2	d_{min}[Å]	d_{max}[Å]	c	Γ_{top}	Γ	σ[Å]	d_1	d_2	d_3	d_4	d_5	d_6	Γ_2	Γ_3
Si5117																	
	TEM	1	2.3/4.5	27.5	137.6	0.242	0.71	0.45	4.7	0.98	0.97	1.07	1.05	1.03	1.02	0.45	0.45
	As-coated	N/A	2.18/1.7	27.5	137.6	0.265	0.72	0.44	4.7	0.98	1.01	1	1.01	1	0.98	0.5	0.41
Si5218																	
	TEM	0.945	1.0/142.5	26.4	92.8	0.237	0.63	0.40	5.6	0.97	0.98	1.04	1.02	1	0.99	0.40	0.40
	As-coated	N/A	1.2/0.74	26.4	92.8	0.225	0.67	0.34	4.6	0.98	1	0.99	1	0.98	1	0.49	0.39
Si5355																	
	TEM	0.93	0.83/0.66	20.5	73.5	0.227	0.8	0.38	3.9	1.08	0.98	1.05	1.05	1.02	1.02	0.38	0.38
	As-coated	N/A	1.3/0.73	20.5	73.5	0.239	0.8	0.42	3.9	1.01	0.99	1.05	1.02	1	0.99	0.39	0.39

4.7 Additional work

The time and cost involved in measuring witness samples using TEM discourage investigating the full sample set. However, the preceding chapter has shown that even under non-ideal experimental conditions, a limited TEM data set can contribute to improvements in the as-coated recipe fits. With a more dynamic acquisition process, primarily based on a closer collaboration with the TEM operators, TEM can add a significant amount of confidence to ambiguous specular reflectivity data. To this end, collaboration with the DTU based Center for Electron Nanoscopy (CEN) has been set up. Several interesting images have already been acquired (e.g. Fig. 3.14) and more are planned at the time of writing.

A number of suggested work packages are described in the list below. Several of these are envisioned as a joint venture between CEN and DTU.

- TEM images with a well-calibrated magnification should be acquired from a number of representative witness samples. Three obvious choices are Si5117, Si5218 and Si5355, as a second round would validate the findings discussed in this chapter.

- The individual layer thicknesses have been fit by a simple Gaussian as this was concluded to be adequate based on Si5117 TEM data. In an effort to decrease uncertainty in layer determination this method should be refined with more accurate and material dependent interface profiles. These efforts could be carried out concurrent with the interface improvements suggested in Chapter 3.

- The crystallite structure should be investigated more closely, especially in the context of growing thinner and smoother Pt/C multilayers. The crystallite structure has been shown to dominate micro-roughness in Pt/C coatings [49].

- The method discussed in Sec. 4.4 for determining the as-coated density of amorphous materials should be investigated to validate or replace the bulk density assumed for fitting the as-coated recipes. While W was found to contain randomly oriented crystallites under high magnification (Fig. 4.7) past studies, including [48], have successfully assumed it to be amorphous. The implication is that the as-coated density of Pt/C may also be determinable using the proposed method.

- TEM equipment is capable of carrying out a number of other measurements in addition to contrast imaging. X-ray Energy Dispersive Spectroscopy (EDS) is one such measurement. EDS is used for detailed interface compositional analysis. The main challenge with EDS in the present context derives from the desired details being at the sub-nanometer scale. While EDS can probe such small areas, the stepping resolution may not be sufficient to map out the full interface. At a minimum, EDS is expected to provide coarse information on intermixing at the light-on-heavy and heavy-on-light interfaces.

4.8 Chapter summary

Three NuSTAR flight coated witness samples were measured using TEM with the intention of establishing the top bilayer d-spacings independent of specular reflectivity data and the degeneracies discussed in Chapter 3.

Estimating d-spacings from the TEM images was complicated by magnification scale errors. In-situ calibration of the magnification was carried out using $d_{min,ac}$ and the Si wafer lattice fringes. The corrected d-spacings were used to calculate specular reflectivity, and the result was compared to RaMCaF data. A better fit of the low energy response was achieved. It was further confirmed that d_i represents actual deviations from a power law progression of d.

The improved fit uses near-nominal Γ and Γ_{top} values and has $\Gamma_i = \Gamma$. Two conclusions may be drawn from the improved fit. One, that $\Gamma_i \neq \Gamma$ in the as-coated recipes does not represent the actual multilayer and, two, that Γ and Γ_{top} should be perceived as coupled parameters.

The acquired images were also used to investigate details of the interfaces. It was found that the light-on-heavy and heavy-on-light interfaces have markedly different profiles due to a churning

effect that is most pronounced for the heavy-on-light interface. The interface profile for Pt was further found to be strongly influenced by crystallite growth resulting in a broader interface width compared to W/Si.

Additional work was suggested to improve understanding of interface profiles and reduce uncertainty in bilayer thickness determination.

Chapter 5

Optic response model

Abstract - *In this chapter, the current status of the ORM is established through ray tracing and comparison with NuSTAR calibration data. The impact of including Chapter 2 and Chapter 3 findings is presented. It is found that the uniformity map and as-coated recipes improve the ORM significantly. A thorough quantitative analysis of the current status of the ORM is not possible on account of the immaturity of the ray tracing implementation. Required improvements to the ray tracing implementation are outlined and additional work to improve the ORM summarized.*

In Chapter 2, the coating uniformity map was established for all deposition chamber configurations, while Chapter 3 found the as-coated recipes for the majority of witness samples. In this chapter, these results are combined to describe the as-coated multilayer of mounted flight substrates. The response of the as-coated multilayer is compared to NuSTAR on-ground calibration data through ray tracing. The ray tracing is carried out in a geometry imitating the on-ground calibration setup and the optics. The geometry is loosely referred to as the ORM. While strictly speaking it is merely a part of the ORM, as indicated in Fig. 5.1, the remaining components are implemented in the software environment defined for the optic geometry (refer to Sec. 5.1), blurring the distinction in the present case.

Before proceeding it is relevant to consider the ORM in the proverbial big picture, as is done in Fig. 5.1. The focus of this thesis has been to establish the as-coated multilayer reference database. Through ray tracing the reference database is used to estimate the effective area as a function of energy, A_{eff}. While A_{eff} is a critical part of any observatory, the Point Spread Function (PSF) must also be understood in order to demonstrate the full scientific potential of NuSTAR. The PSF consists of scattering contributions from a range of length scales, and an accurate model is required to span all of these. Length scales from $5\,mm$ up to $200\,mm$ were measured in-situ on all mounted substrates with a Linear Variable Differential Transformer (LVDT) as described in [30]. The LVDT database and additional information regarding LVDT is available from Appendix O. The surface of spare flight substrates was further characterized using Atomic Force Microscopy (AFM) and white-light interferometry (Zygo). The height data obtained through these studies are used to compute the Power Spectral Density (PSD) spanning length scales from nanometers to millimeters. The PSD fits a power-law, and the nature of the surface height errors suggests that a model following the formalism developed in [54, 55] can accurately describe substrate X-ray scattering. This effort is led by LLNL. Verifying the model requires several orders of magnitude higher flux than available at RaMCaF. Four days of beam time at the National Synchrotron Light Source (New York) in February 2012 has been allocated for this purpose. Following verification the scattering model will be implemented in the ORM. Similar to the effort of the current chapter a validation against on-ground calibration PSF data will follow. The NuSTAR calibration data used for this purpose were acquired with a CCD camera and is detailed in [56] and references therein.

Figure 5.1 further indicates that the ORM is merely one of several major inputs to the overall observatory response model. Also included is a detailed flight detector response model [57] and a composition model. The latter accounts for the transmission as a function of energy for the thermal covers and windows over the optic aperture. Both models are being developed at the California Institute of Technology (Caltech). No end-to-end test is carried out prior to launch so validation of the complete observatory response model will be obtained through in-orbit calibration.

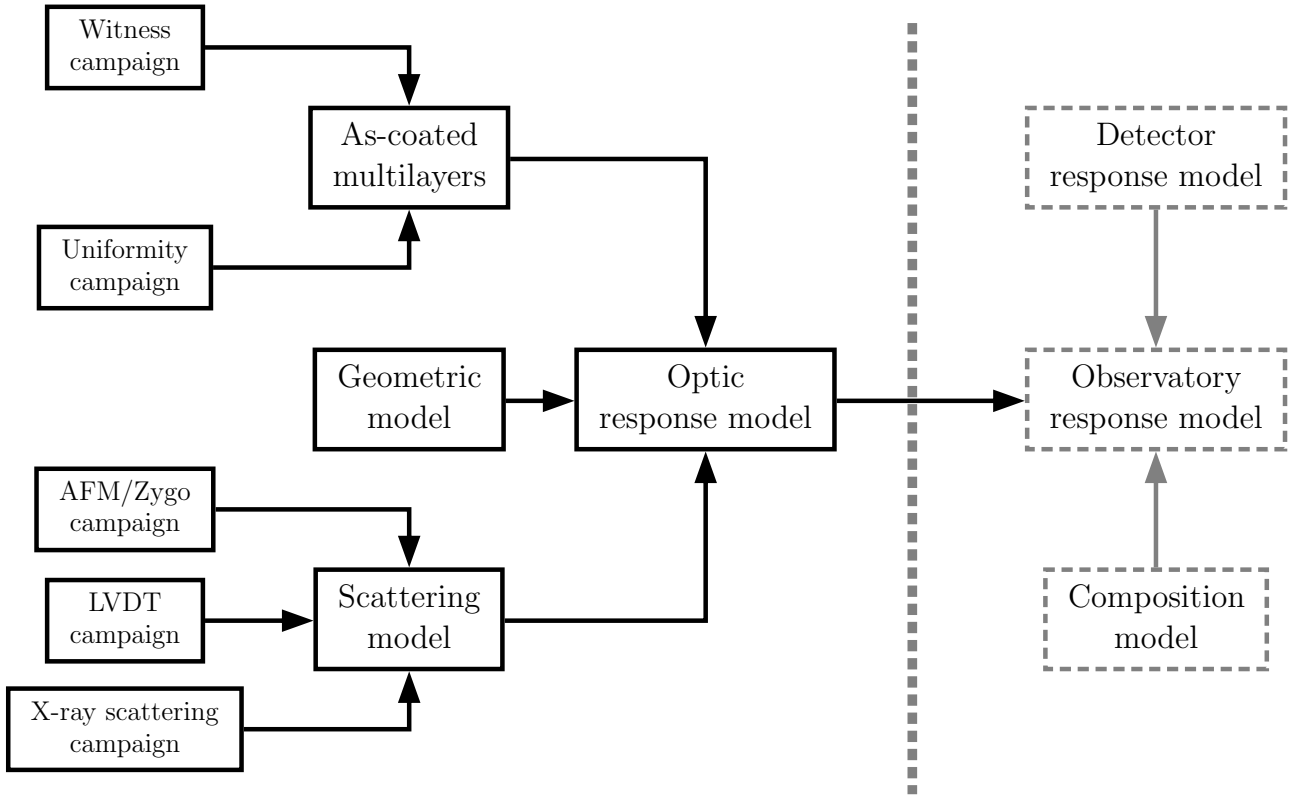

Figure 5.1: Overview of the components that go into the ORM. Right of the dashed line indicates the final stage of integrating the ORM with the detector response and composition models to construct the full NuSTAR observatory response model. Final validation is carried out in-orbit.

5.1 MT_RAYOR

MT_RAYOR is a versatile Monte Carlo ray tracing tool developed at DTU to assist in the design and analysis of X-ray telescopes [58]. It is based on the Yorick interpreted language [59] and the FITS data storage standard [60]. The NuSTAR geometry is implemented as derived from the optic design document (refer to Appendix A). The overall geometry of the RaMCaF setup is also implemented, including the finite source distance, and the resultant extended focal length, and calibration hardware. MT_RAYOR further includes the LVDT data, i.e. large-scale substrate deformation. As a placeholder for the scattering model, X-ray scattering can be approximated with a Gaussian distribution. In this chapter, all ray tracing is carried out with LVDT deformations, but without scattering. Figure legends indicate that only LVDT has been included by having the suffix "Type 3".

Although MT_RAYOR possesses the capability to carry out a complete forward fitting of the NuSTAR response, the RaMCaF X-ray source spectrum is not sufficiently well-understood to allow for this. Instead, monoenergetic photons are thrown at the optic from a point source. Under the assumption that scattering effects do not have an energy dependency, the ray trace can be post-processed to take the energy-dependent reflectivity of the multilayer into account. This approach has the added benefit of speeding up the ray tracing significantly. The energy-independent scatter assumption was validated by calibration results [30] and is supported by an early version of the scattering model from LLNL.

The user manual for MT_RAYOR contains additional information on the implementation and functions available. It can be found from Appendix A. MT_RAYOR is being developed parallel to NuSIM, the official NuSTAR simulator supported by Caltech. A report on the current status of cross-comparisons between the two software packages is available from Appendix A. At the time of writing only minor discrepancies remain. Note that NuSIM implements the same version of the multilayer reference database as discussed in this chapter, but is based on a different approach to ray tracing and does not utilize IMD routines to calculate multilayer reflectivity.

5.1.1 Implementation limitations

The current version of the ORM implemented in MT_RAYOR has two major limitations. For one, only nine of the seventeen uniformity points are used, namely points 1-9. Chapter 2 found that the extreme points of the substrate, as mapped by points A-H, have a relative d significantly different from the central substrate surface. The impact on the estimated reflectivity in a finite source distance geometry is complicated by the illuminated substrate area being heavily dependent on angle of incidence. The implication is that a coarsely defined uniformity map can have more or less of an impact on overall response depending on the angle. Several examples are shown in Sec. 5.3.

Secondly, the relative micro-roughness and Γ values are not implemented in MT_RAYOR. The micro-roughness in particular is important for an accurate estimate of the telescope response. In Chapter 2, it was found that Pt/C coatings on substrates have an on average 16% higher micro-roughness, compared to the value established from witness samples. Similarly, for W/Si the increase is 14%. Section 5.3.2 investigates the approximate influence of the micro-roughness increase through applying the average relative micro-roughness to all substrates.

A third limitation results from the material combination Pt/SiC not being implemented in MT_RAYOR. For this reason the coating on the innermost layer is approximated by design recipe 1 rather than design recipe 0, refer to Table 1.1. Section 5.3.1 demonstrates the influence on the estimated response.

It should also be noted here that an observable offset in spacer location appears in photon site interaction maps, e.g. Fig. 5.5. This artifact is being investigated at the time of writing.

In addition to the limitations inherent to MT_RAYOR a few comments on the LVDT database and the as-coated recipes are relevant. LVDT scans of all mounted substrates exists and are used in the current implementation of the ORM. While the data has been processed to eliminate measurement artifacts, an edge effect remains. The effect is shown in Fig. 5.2. MT_RAYOR currently smoothes over the spikes visible near the front edge ($Z \approx -225\,mm$) before the ray tracing commences, as they may otherwise cause significant, and unrealistic, occlusion of photons. An effort to properly

handle the spikes is being led by CU.

Lastly, at the time of writing, data from fifty-six witness samples, forty-five of which were coated by RXO, have not been analyzed. Consequently the as-coated multilayer cannot be estimated for a number of substrates. Section 5.3.1 demonstrates the influence on reflectivity for the layers in question.

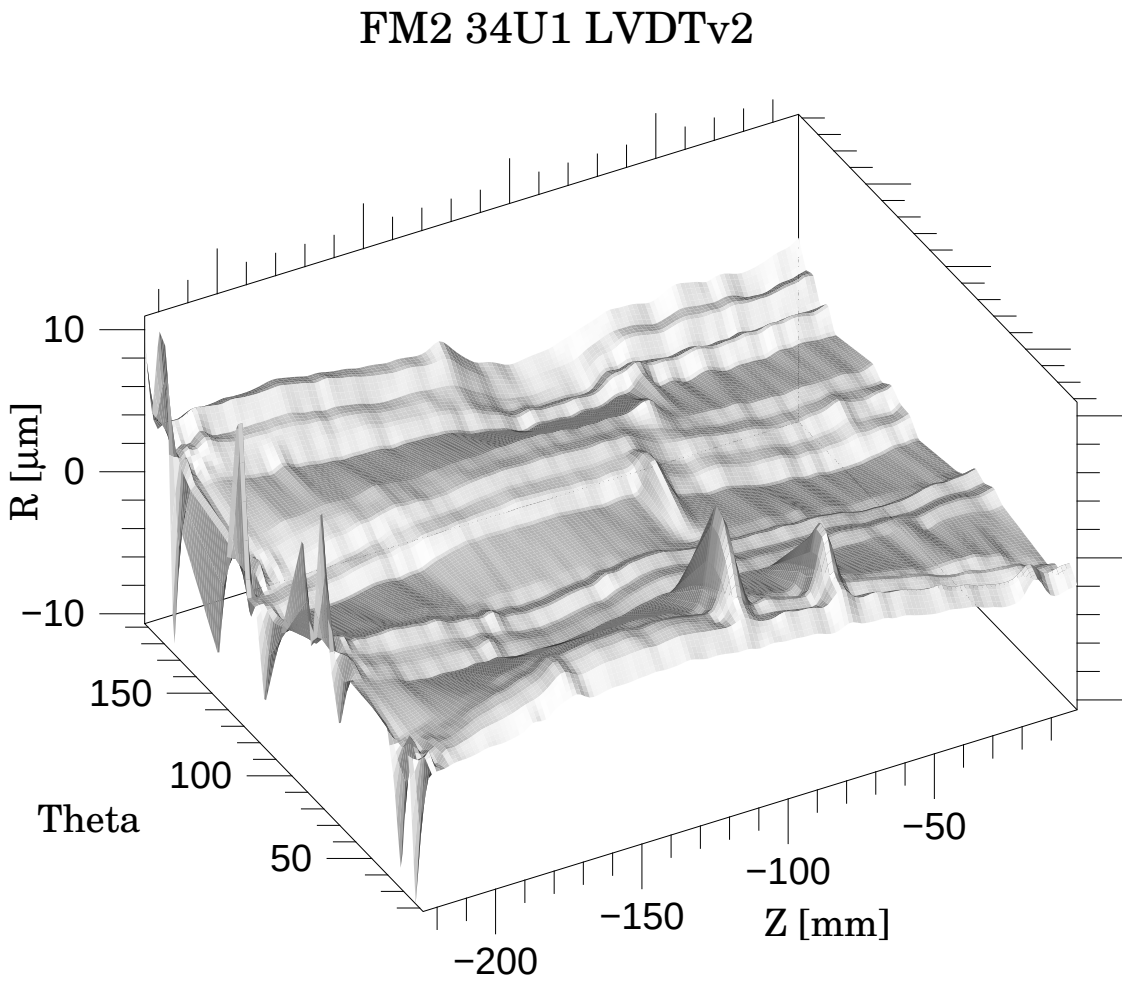

Figure 5.2: LVDT map of layer 34 substrate mounted in FM2. $Z = 0$ corresponds to $x = 112.5\,mm$ in the Fig. 2.8 coordinate system. Similarly, $Theta$ corresponds to ϕ_i. The $Theta$ units are arbitrary, but describes a total span of 49.8°. R describes the height deviation from a flat substrate. The spikes observable at $Z \approx -225\,mm$ cause significant occlusion of photons in the ray trace. The spikes are unrealistic, as they indicate a point-sized height deviation orders of magnitude higher than the average values. For illustrative purposes the spikes have been reduced to $10\,\mu m$ height. In the current implementation of the ORM the spikes are smoothed over to present a more realistic surface. Plot supplied by Niels Jørgen S. Westergaard from DTU.

5.2 On-ground calibration campaign

The on-ground calibration campaign was carried out between March 5 and March 22, 2011. In this time frame, nearly twelve thousand spectra were acquired with either FM1 or FM2 in the beam. Another thousand runs were carried out to obtain the direct beam spectra at regular intervals. The high number of individual measurements was due to measuring subgroups of the optic rather than a straightforward full flood. These subgroups are defined in Table 5.1. The subgroups allow for a more complete optic response to be mapped out in spite of the limitations of finite source distance (refer to Chapter 1). A subgroup is selected by installing an aperture plate on the front of the optic. The aperture is $0.1\,mm$ wider than the inner and outer layer radii for a given subgroup. All other layers are completely obscured. For details on the hardware implementation refer to [2]. Specific subgroups will be referred to as SGx, e.g. SG1 for subgroup 1.

It is not the purpose of this thesis to analyze the vast calibration data set available. For the present work the information of immediate interest is derived from single reflection measurements. In these measurements, the slit unit and detector were moved to collect photons successfully reflected off the upper mirror shell which missed the second substrate, i.e. reflection overshoot in Fig. 1.12c. The as-coated multilayer is more readily evaluated from these spectra as the response consist of summed contributions from a limited number of substrates, rather than summed and convolved contributions from twice as many substrates in the double reflection case. For the subgroups with $\phi_{sub} = 60°$ (SG1-SG11) a total of 6-7 substrates contributes, while the remaining subgroups' single reflections contain the response of 14-16 substrates with ϕ_{sub} spanning 30°.

In the single reflection data set, a sub-selection consisting of a 60° sector of FM2 spanning all subgroups has been investigated. Section 5.3 presents a number of spectra from this sector.

It is important to note that the range of substrates investigated represents 8% of the total number of substrates mounted in FM2. The data presented in Sec. 5.3 is taken at angles where anywhere from $5 - 50\%$ of the substrate surface area, within a single subgroup, contributes to the response. From these numbers it is clear that the single reflection data should only be used as a first order validation of the ORM. For a full validation the model must be checked against the full optic A_{eff} found from the on-ground calibration campaign. A comparison is carried out in Sec. 5.4, but it is stressed that the A_{eff} presented consists of preliminary, conservative values. For this reason conclusions regarding the current status of the ORM are drawn exclusively from the single reflection data, in spite of the limited substrate surface area sampled in these measurements. Work to improve on the A_{eff} estimate is being led by CU and is expected in early 2012.

The calibration data set is currently maintained and distributed by CU. Although the routines required to handle the data directly have been made available, they have not been implemented in MT_RAYOR at the time of writing. For this reason the data discussed in the present chapter consists of normalized reflectivity response values supplied by CU in simple text format. The data is available from Appendix N.

For additional information on the calibration facility, calibration approach and preliminary calibration results, as well as data reduction approach, refer to [1, 2, 30]. As previously mentioned [1, 2] are available from Appendix A.

Table 5.1: Overview of the layers spanned by individual subgroups. The design recipe number is also given.

Subgroup	Recipe	Inner layer	Outer layer
1	1	1	6
2	1	7	12
3	2	13	18
4	2	19	24
5	3	25	30
6	3	31	36
7	4	37	43
8	4	44	49
9	5	50	56
10	5	57	62
11	6	63	69
12	6	70	75
13	7	76	82
14	7	83	89
15	8	90	96
16	8	97	103
17	9	104	111
18	9	112	118
19	10	119	126
20	10	127	133

5.3 Single reflection data

Ray tracing of all subgroups at up to eight incidence angles has been carried out. In the following a representative set of subgroup response spectra are presented and discussed in the context of Chapter 2 and Chapter 3 findings. All simulations were carried out including the substrate figure error derived from LVDT. Note that the chi-squared values quoted in the plot legend text are not comparable between figures.

5.3.1 As-coated multilayer

In Fig. 5.3 the design recipe response is compared to the as-coated recipe for SG18 (W/Si) and RaMCaF data. The as-coated recipe is shown with and without utilizing the uniformity map. From the figure it is clear that the design recipe is not representative of the as-coated flight substrate multilayer and that the uniformity map is essential to the effort of accurately describing the multilayer response. The figure also indicates that the work packages suggested in Chapter 3 are required to improve the fit at low energy. The same overall trend regarding the low energy response is apparent in Fig. 5.4 for SG3 (Pt/C). Keep in mind, however, that the low energy response is influenced by the coarse implementation of the uniformity map. In Fig. 5.5 a map of photon interaction sites from the ray trace is plotted. As the edges of the substrate is shown to contribute it must be expected that utilizing points A-H provides a better representation of the substrate response. This is supported by SG12 data shown in Fig. 5.6. Taking the non-uniformity of the coating into account does little to improve the fit to the data. The poor fit is anticipated to be caused by the substrates predominately being illuminated towards the edges, as illustrated in Fig. 5.7.

The remaining data presented in this chapter have been selected based on the incomplete implementation having minimal effect for the discussed observations. Such data exists for nearly all subgroups and essentially consists of data sets where the photon interaction sites are spread out as in Fig. 5.5. It is however stressed that the limitations of the MT_RAYOR implementation prevents a thorough quantitative study of the current status of the ORM.

It is important to note that at the time of writing a total of fifty-six witness samples are not included in the data set. Among the missing as-coated recipes are witness samples mounted in SG1 and SG20. Without as-coated recipes the subgroups are poorly represented in the current ORM, as shown in Fig. 5.8 and Fig. 5.9. The SG1 response is further influenced by Pt/SiC not being implemented in MT_RAYOR. While some of the substrates in SG20 have known as-coated recipes, the missing recipes dominate the overall response.

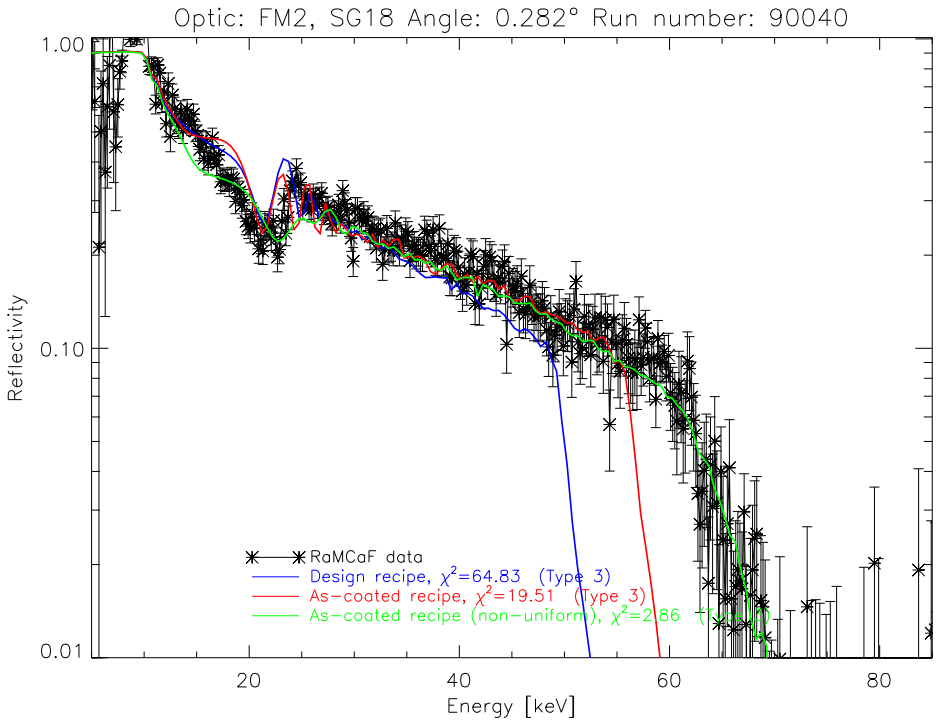

Figure 5.3: Reflectivity response for SG18 on FM2. The RaMCaF data is compared to the design recipe as well as the as-coated with and without utilizing the uniformity map. It is seen that overall the non-uniform as-coated multilayer describes the data well, but at low energy a better fit is desirable.

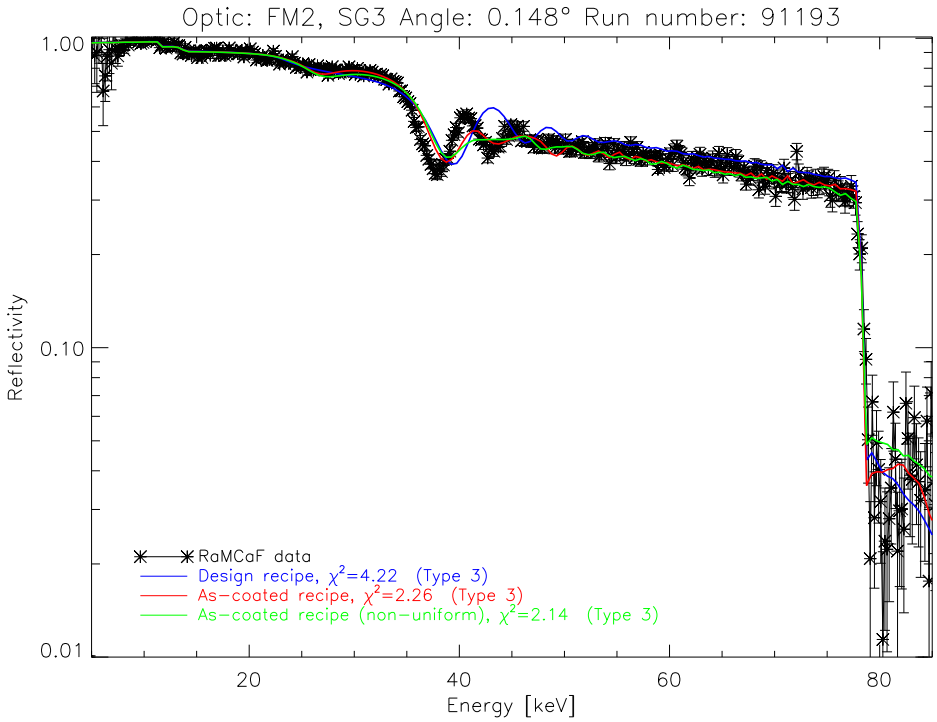

Figure 5.4: Reflectivity response for SG3 on FM2. The RaMCaF data is compared to the design recipe as well as the as-coated with and without utilizing the uniformity map. It is seen that overall the non-uniform as-coated multilayer describes the data well, but at low energy a better fit is desirable. It is not possible to judge whether the poor fit at low energy is caused by the as-coated recipes being off or the uniformity mapping not being descriptive.

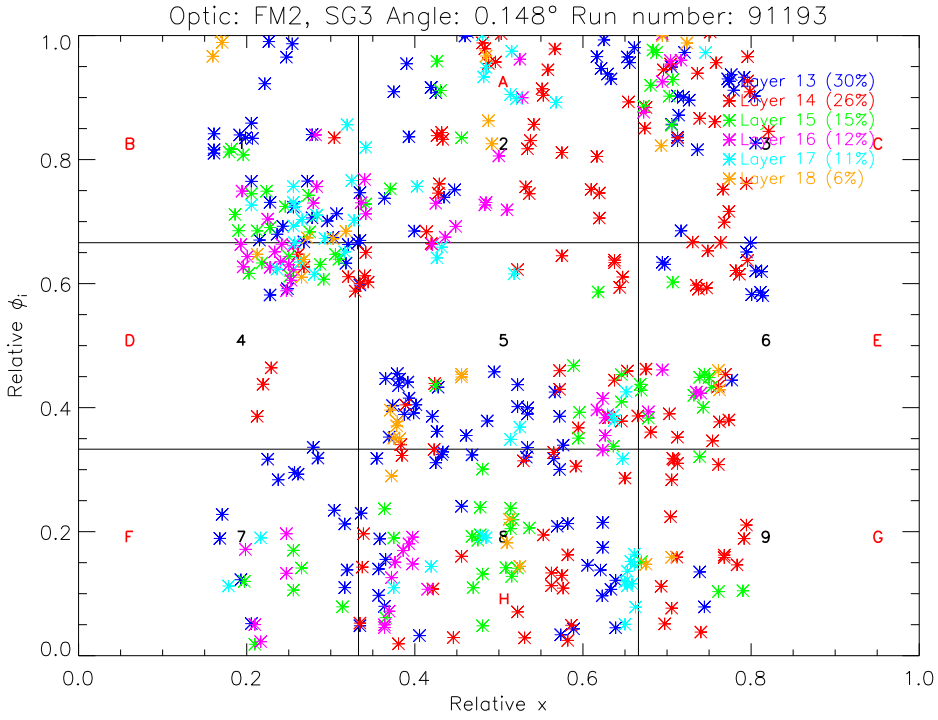

Figure 5.5: Photon interaction site map for SG3 on FM2. The legend indicates the fraction of photons incident on individual layers in the subgroup. The map is segmented into nine areas, indicating which relative thickness value is applied (black numbers). The remaining eight points of the uniformity map not being utilized are also shown (red letters). Note that relative $x = 0.5$ corresponds to $x = 0$ in the substrate coordinate system. Similarly, relative $\phi_i = 0.5$ corresponds to $\phi_i = 0°$. Further note that spacer obscuration is observable along relative $\phi_i \approx 0.3°, 0.55°, 0.8°$. From Fig. 1.11, the obscuration is expected to be centered around relative $\phi_i = 0.25°, 0.5°, 0.75°$. The offset is caused by the optic geometry implementation in MT_RAYOR and is being investigated at the time of writing.

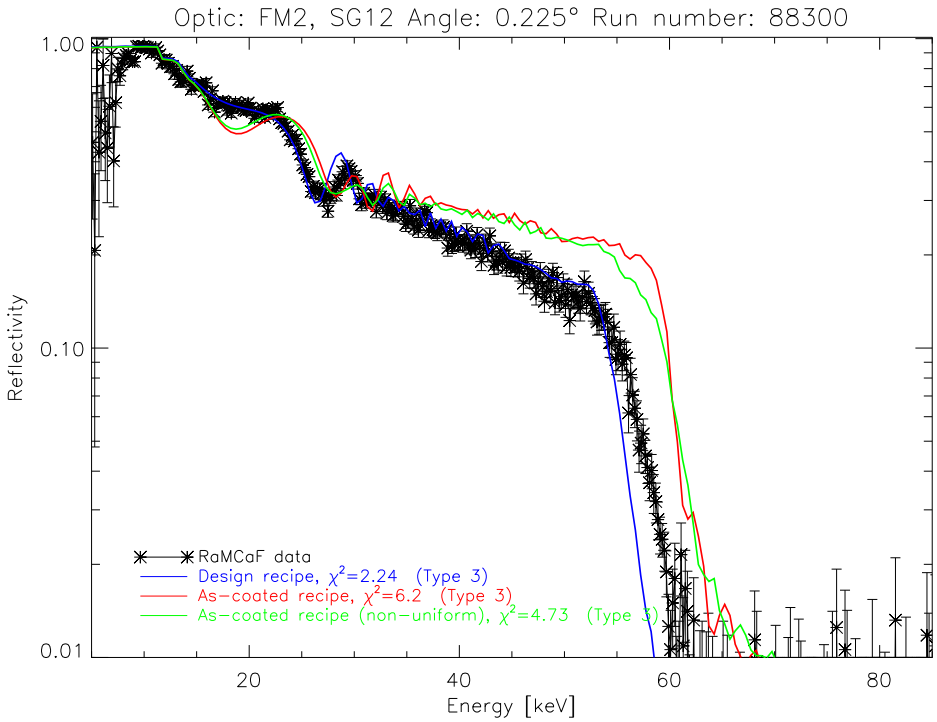

Figure 5.6: Reflectivity response for SG12 on FM2. The RaMCaF data is compared to the design recipe as well as the as-coated with and without utilizing the uniformity map. The as-coated recipes imply too small d-spacings compared to the data. It is anticipated that the too small d-spacings are caused by the incomplete implementation of the uniformity map in MT_RAYOR.

The bulk of the witness sample data that has not been analyzed represents substrates coated at RXO. From Fig. 5.10 it is seen that the RXO coatings are expected to be close to design with a tendency for a slightly lower d_{min}. The lower d_{min} is expected on account of the reflectivity at higher energies demonstrated by the data.

5.3.2 Non-uniform micro-roughness

As discussed in Sec. 5.1.1 micro-roughness and Γ modifications caused by non-uniformity are not supported in the current version of MT_RAYOR. Of these two micro-roughness is expected to impact the reflectivity response significantly. A temporary solution has been implemented in MT_RAYOR allowing the average increase in micro-roughness to be applied to all contributing substrates. The average increase provides a coarse estimation of the effect a full implementation of the uniformity map would have. As is shown in Fig. 5.11 and Fig. 5.12 adding the average value is not descriptive for all subgroups. Substrates in Fig. 5.11 were coated with 100 mm plates while Fig. 5.12 had 120 mm plates installed. The plots imply that 100 mm plates have a significantly lower relative micro-roughness compared to the average. This was not found to be the case in Chapter 2 (refer to Fig. 2.28). The implication is that the micro-roughness uniformity map may not adequately describe the micro-roughness in a flight coating. Proper implementation of the micro-roughness uniformity map is required to investigate the discrepancies in detail.

5.3.3 Cathode drop-outs

From the overview of coating runs affected by cathode drop-outs in Table 3.4 and the master table available from Appendix B, SG7-SG10 layers are suspected of carrying a high fraction of substrates influenced by drop-outs. In SG7, layers 41-43 are from coating runs known to have at least one drop-out. From Fig. 5.13 it is seen that 76% of the photons are illuminating the affected layers, implying the influence on the overall subgroup reflectivity is significant. This is confirmed by Fig.

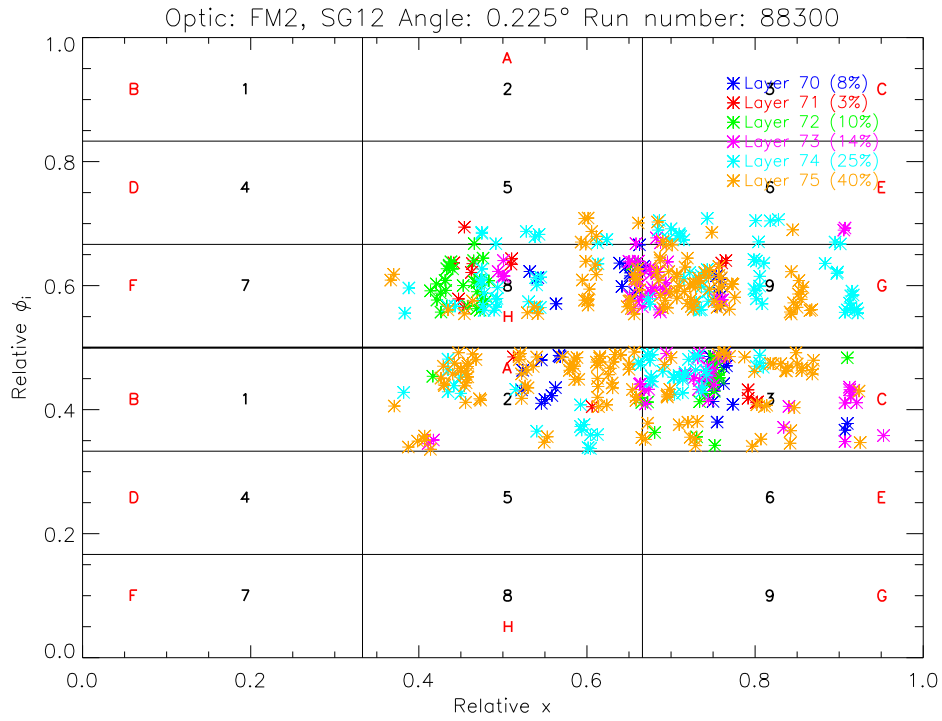

Figure 5.7: Photon interaction site map for SG12 on FM2. The legend indicates the fraction of photons incident on individual layers in the subgroup. The map is segmented into nine areas per substrate, indicating which relative thickness value is applied (black numbers). The remaining eight points per substrate of the uniformity map not being utilized are also shown (red letters). Note that relative $x = 0.5$ corresponds to $x = 0$ in the substrate coordinate system. Similarly, relative $\phi_i = 0.5$ corresponds to $\phi_i = 0°$.

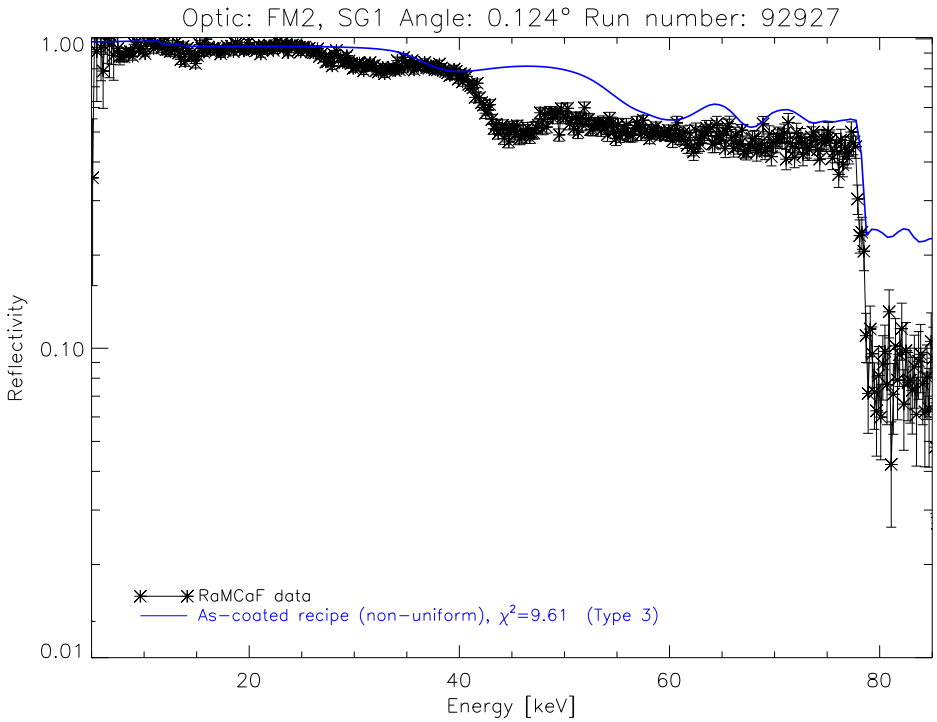

Figure 5.8: Reflectivity response for SG1 on FM2. The poor fit is caused by missing as-coated recipe values for the inner layer. In addition to this, the MT_RAYOR misinterpretation of the uniformity map has a significant influence on the mounted substrates in SG1.

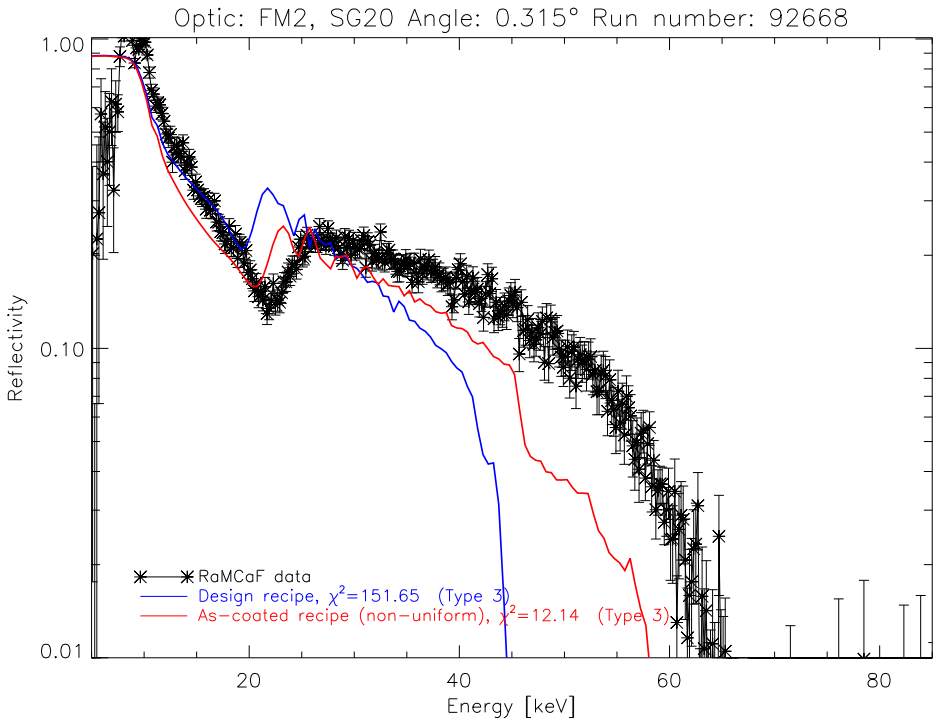

Figure 5.9: Reflectivity response for SG20 on FM2. The poor fit is caused by missing as-coated recipes for three of the contributing five layers in the subgroup.

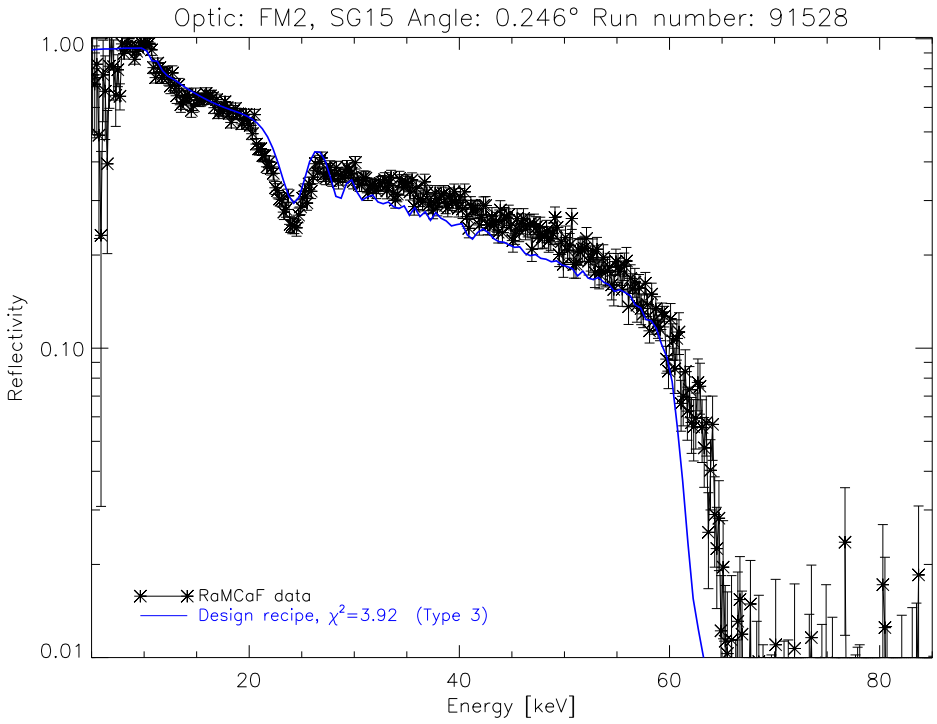

Figure 5.10: Reflectivity response for SG15 on FM2. All layers in SG15 consists of RXO coated substrates with unknown as-coated recipes. The data implies that RXO coatings are close to design, albeit with a lower d_{min}.

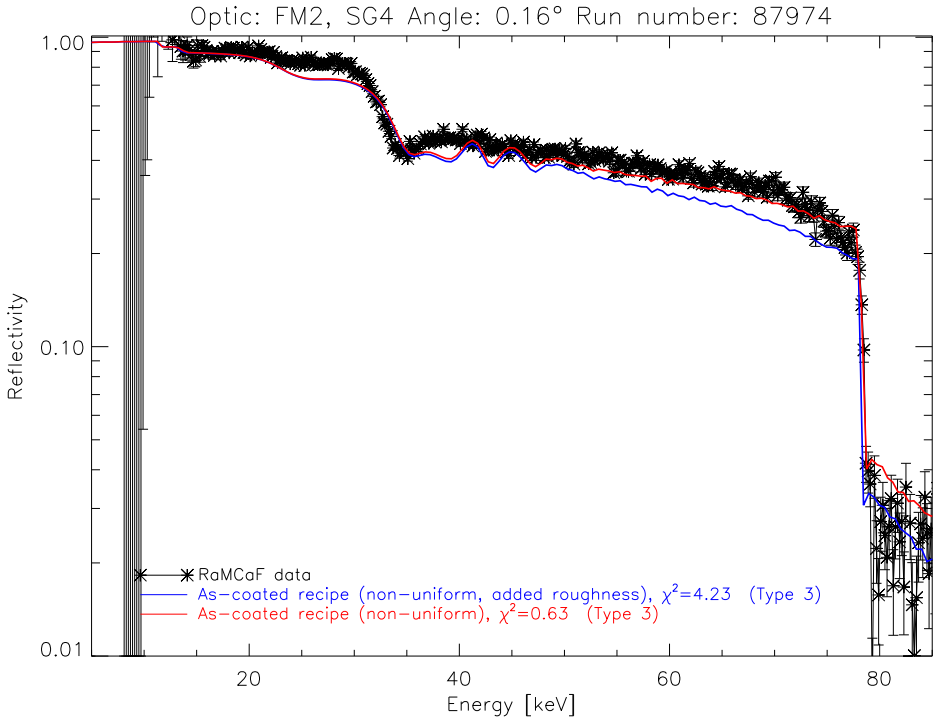

Figure 5.11: Reflectivity response for SG4 on FM2. The RaMCaF data is compared to the non-uniform as-coated recipes with (blue) and without (red) added micro-roughness. All substrates mounted in SG4 are coated with 100 mm separator plates. The underestimated reflectivity response with the added micro-roughness indicates that the substrates are not as rough as the uniformity map implies.

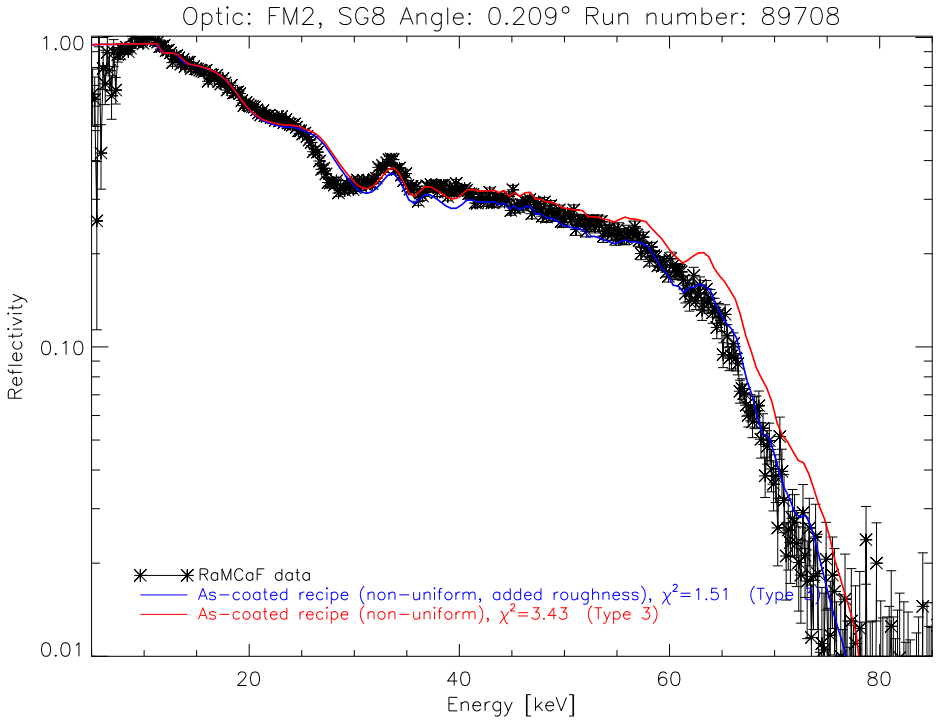

Figure 5.12: Reflectivity response for SG8 on FM2. The RaMCaF data is compared to the non-uniform as-coated recipes with (blue) and without (red) added micro-roughness. All substrates mounted in SG8 are coated with 120 mm separator plates. The added micro-roughness improves the fit significantly.

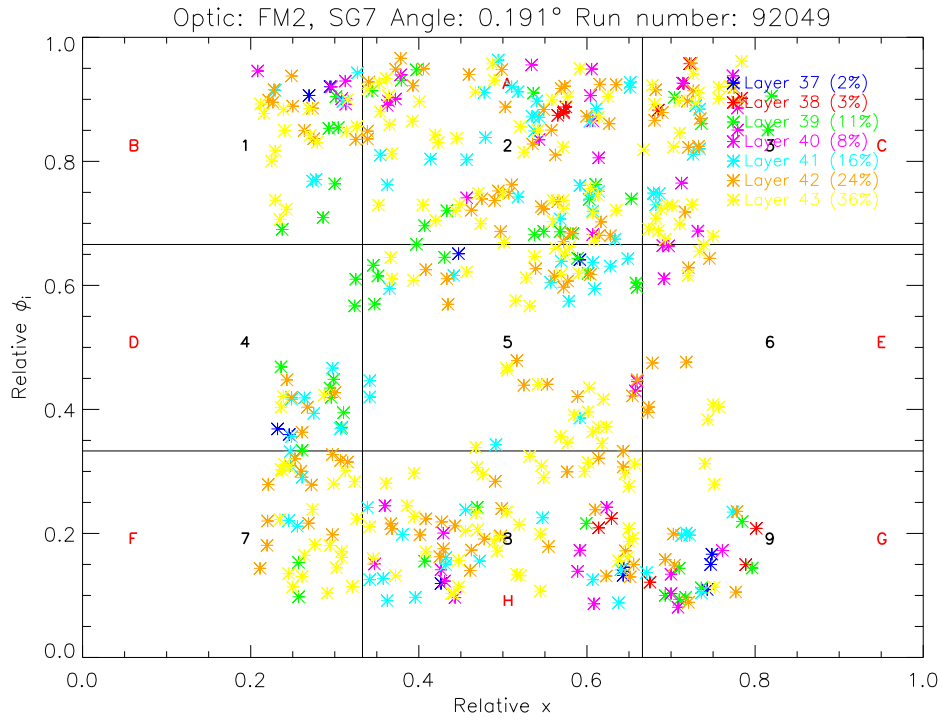

Figure 5.13: Photon interaction site map for SG7 on FM2. Layers 41-43 are suspected of having experienced cathode drop-outs. As 76% of the photons interact with these layers the drop-outs are expected to have a significant impact on the overall subgroup reflectivity.

5.14. Structure is observed in the reflectivity from $35keV$ and up to $60keV$. The irregular structure is characteristic of cathode drop-outs (refer to Fig. 3.15). Drop-outs were observed in both Si5167 and Si5168 witness data, and consequently reflected by the as-coated recipes. It is clear from the figure that some structure is successfully reproduced, but there are strong indications that the witness samples do not carry an accurate description of the influence on the substrate coatings.

It is important to note that while the impact of drop-outs appear limited in the present data, the influence is more pronounced in double reflection, especially if both the upper and lower substrates are affected, as the effect adds in quadrature.

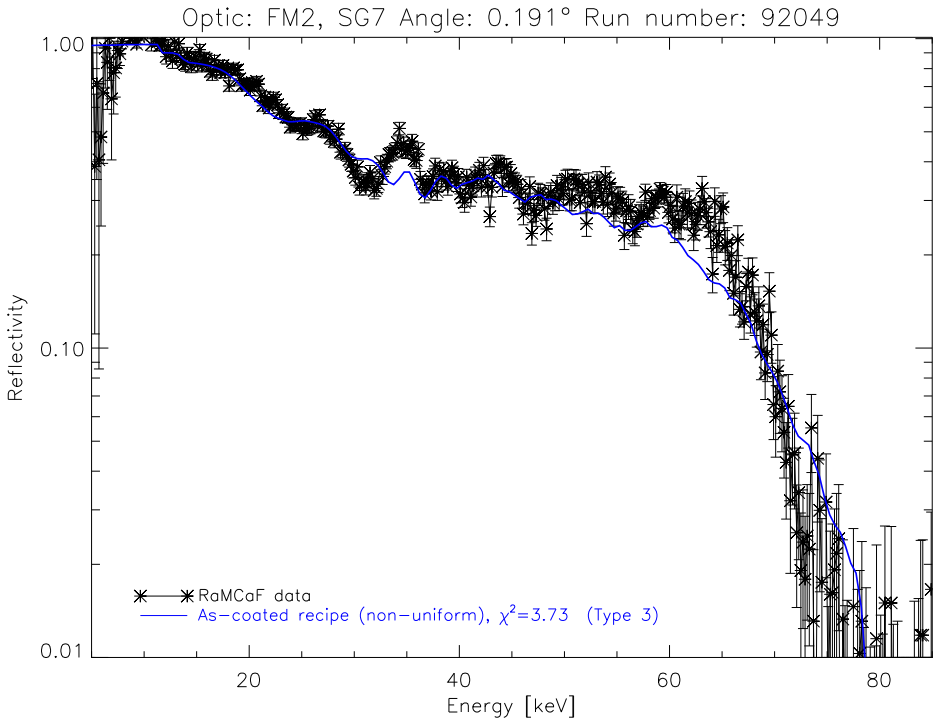

Figure 5.14: Reflectivity response for SG7 on FM2. The bumpy structure observable across the $35-60keV$ plateau is characteristic of cathode drop-outs.

5.4 Current status of the ORM

Although the immaturity of MT_RAYOR prevents a thorough quantitative analysis of the current status of the ORM the overall results imply that the as-coated recipes and the uniformity mapping provide a good representation of the as-coated multilayer. With the exception of SG20, all subgroups either come close to or tend to overestimate the response expected from single reflection data. In the case of SG20, the missing as-coated recipes cause the response to be underestimated, in particular above 45 keV. Regardless, the overall tendency means that the current ORM implementation is expected to provide an optimistic estimate for FM2 A_{eff}. This is confirmed in Fig. 5.15. The RaMCaF data shown consists of summed contributions from individual subgroups measured using pseudo-parallel illumination (refer to Fig. 1.12d). All twenty subgroups were illuminated in turn at an angle befitting their radii. From these the response expected in-orbit is approximated. For comparison MT_RAYOR assumes the source to be at infinity and illuminates all subgroups simultaneously. While a more appropriate comparison would have been to carry out pseudo-parallel ray tracing, the angles required to imitate the data acquisition were not available.

It is stressed that both the conservative A_{eff} estimate and MT_RAYOR limitations prevent final conclusions regarding the NuSTAR effective area at this stage. However, the established values bounds A_{eff} to be above the conservative estimate from calibration data and below the optimistic estimate from the ORM. The estimates are compared to the NuSTAR level 4 requirements in Table 5.2. The level 4 requirements are taken from the NuSTAR calibration plan document available from Appendix A. From Table 5.2, the conservative estimate is on average 19% lower than requirement, while the current implementation of the ORM indicates an average positive margin of 10% with respect to $A_{eff,req}$.

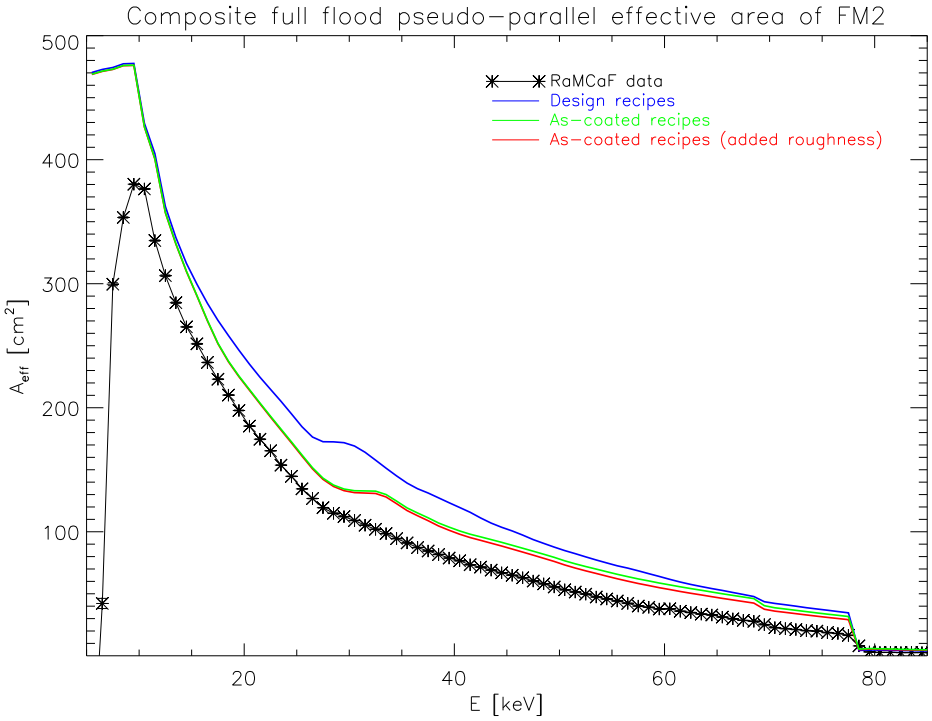

Figure 5.15: NuSTAR effective area estimated from pseudo-parallel measurement of all subgroups. The data is compared to the NuSTAR design recipes response and the current best estimate using as-coated recipes with and without added micro-roughness. Both the design and the as-coated recipes include LVDT, and the as-coated values are modified by the uniformity map. Significant discrepancies remain over the entire energy range. Tracking down the cause of these requires MT_RAYOR to mature further.

Table 5.2: The table compares required effective area ($A_{eff,req}$) at discrete energies for a single optic to the estimated effective area for FM2 given by design ($A_{eff,dsn}$), as-coated recipes ($A_{eff,asc}$) and calibration data ($A_{eff,cal}$). The as-coated recipes include the added micro-roughness.

Energy $[keV]$	6	10	15	20	30	40	50	55	60	70	78
$A_{eff,req}[cm^2]$	402	394	262	201	135	99	71	60	50	34	22
$A_{eff,dsn}[cm^2]$	471	455	307	240	170	121	86	73	63	43	34
$A_{eff,asc}[cm^2]$	470	455	300	220	132	99	75	63	54	36	28
$A_{eff,cal}[cm^2]$	N/A	378	260	192	111	77	54	45	37	24	15

5.5 Additional work

The additional work suggested in this section essentially sums up the most important tasks suggested in the previous chapters for further investigation. The majority of the improvements are expected to come to fruition prior to the NuSTAR launch in early 2012.

It is worth noting that the list below ties into a number of papers under preparation for the summer of 2012. As the papers become available they will be uploaded to the DTU NuSTAR website in the documentation library.

- The remaining eight points of the uniformity map, as well as micro-roughness and Γ non-uniformities, must be implemented in MT_RAYOR.
- The remaining witness sample data must be analyzed. This is expected to occur parallel to the improvements in low energy fitting of the entire data set.
- The calibration database must be implemented in MT_RAYOR in such a way that additional information regarding individual measurements are readily available to improve and ease comparison between calibration data and ray trace results.
- The scattering model must be implemented in MT_RAYOR. This is the first step towards PSF investigations. The second step includes incorporating the calibration data acquired with the CCD to ease comparison with ray trace results. The effort is being led by LLNL.
- The LVDT data must be reprocessed to handle the spike issue properly. The effort is being led by CU.
- A proper representation of the RaMCaF X-ray source must be implemented into MT_RAYOR. Modeling the source is being investigated by NuSTAR collaborators at the University of California, Berkley (UCB). This task primarily ties into the PSF investigations and is not expected to have a significant impact on effective area estimates.

5.6 Chapter summary

The ORM was implemented in the ray tracing tool MT_RAYOR and utilizes the available as-coated recipes and nine of the seventeen points in the uniformity map. Single reflection data from the NuSTAR on-ground calibration was compared to results from the ORM. It was found that the uniformity map is critical for a proper description of the multilayer response. Conclusions on the quality of the as-coated recipes and the uniformity map were derived from data where the influence of the incomplete uniformity map implementation was negligible.

It was confirmed that cathode drop-outs affect the as-coated multilayer in ways that cannot be predicted from the witness campaign.

An optimistic estimate of the NuSTAR effective area was found, effectively bounding the expected effective area through comparison with a conservative estimate derived from calibration data. Both estimates are significantly lower than design, but while calibration data indicates the effective area does not meet requirements, the current implementation of the ORM imply an effective area on average 10% higher than required.

A number of improvements were outlined with emphasis on completing the uniformity map implementation and the analysis of the witness sample data.

Chapter 6

Thesis conclusions

Abstract - *In this chapter, the thesis conclusions and future work are summarized.*

This thesis presents a study of the as-coated multilayers of the NuSTAR hard X-ray focusing optics. To this end, a hard X-ray calibration facility was designed and constructed. The thesis work relating to the facility was presented in [1, 2]. The facility was used to acquire specular reflectivity data from witness samples as well as the NuSTAR optics themselves. Supporting measurements, utilizing an $8\,keV$ beamline at DTU and TEM, were also carried out.

The primary aim of this thesis was to set up a multilayer reference database. The multilayer reference database constitutes a significant part of the NuSTAR ORM, specifically by enabling the effective area as a function of energy, A_{eff}, to be estimated. A_{eff} was expected to differ significantly from design owing to coating non-uniformities and variations in the multilayer deposition. This thesis confirms the expectation to be correct.

To establish the reference database, two main campaigns were carried out. The uniformity campaign, described in Chapter 2, mapped out the uniformity of the coating by acquiring specular reflectivity data from seventeen points evenly distributed over twenty spare flight substrates. The twenty substrates represent all chamber configurations and substrate mounting locations utilized during the flight coating campaign. The substrates were all coated with a cst-d multilayer ($N = 10$). The d-spacings of the deposited multilayers were established and related to the d-spacing of a witness sample included in the individual uniformity coating runs. The uniformity map consists of these relative thicknesses and enables the flight coatings to be estimated by carrying out specular reflectivity measurements on the flight coating witness samples. The results of the uniformity campaign were validated by comparison to a rudimentary model and found to correspond well with expectations. The campaign further found that micro-roughness is expected to be on the order of 15% higher for substrates compared to witness samples.

The witness campaign, described in Chapter 3, acquired and analyzed specular reflectivity data from 183 flight witness samples. The multilayers of the witness samples were described by the as-coated recipes. These were found to differ significantly from the design recipes. It was established that inaccuracies in deposition rate determination from calibration coating runs, as well as target wear, biased the as-coated multilayers towards smaller d-spacings compared to design. While the as-coated recipes fit the data well, improvements to the low energy fit were found to be recommendable. The low energy response is complicated due to degeneracy between fitting parameters. Methods for breaking the degeneracy were outlined. It was further found that at least nineteen coatings were affected by cathode drop-outs. It was shown in Chapter 3 and Chapter 5 that the drop-outs can induce changes to the as-coated multilayer that the as-coated recipes are unable to predict. The available single reflection data implies the effect on the overall response to be limited, however, double reflection data must be analyzed to provide an accurate estimate for the influence.

In addition to the main effort in this thesis of establishing the multilayer reference database, TEM images were acquired and discussed in Chapter 4. The TEM investigations were primarily carried out to establish the validity of Chapter 3 results. TEM showed that improvements to the low energy fit is achieved by determining the top bilayers better and through coupling the Γ parameter

types when fitting the as-coated recipes.

Finally, Chapter 5 assessed the current implementation of the multilayer reference database in the ray tracing tool MT_RAYOR. The assessment was carried out by comparing the simulated reflectivity response of mounted substrates to single reflection data from the on-ground calibration of FM2. It was found that while the as-coated recipes and the uniformity map provide a good description of the as-coated multilayers, a detailed quantitative study is not possible due to limitations in the MT_RAYOR implementation. On account of the limitations, the current ORM provides an optimistic estimate of the expected A_{eff} for NuSTAR. The estimate is on average 10% higher than the NuSTAR level 4 requirement. Along with a conservative estimate based on on-ground calibration data, A_{eff} has been bounded. The conservative estimate is on average 19% lower than the level 4 requirement.

6.1 Future work

There are three aspects to the future work anticipated based on the findings in this thesis. One focuses on refining the multilayer reference database itself, primarily by analyzing data from the remaining fifty-six witness samples and improving the fit at low energy.

The second aspect concerns the implementation of the multilayer reference database in MT_RAYOR. A thorough validation against single reflection calibration data, is already under way at the time of writing. Once coupled with the complete multilayer reference database, double reflection calibration data will be investigated to derive firm conclusions on the overall quality of the ORM and in turn the NuSTAR A_{eff}.

Finally, this thesis has outlined a number of work packages to improve understanding of the coating uniformity, interface details and as-coated material density. The impact from refining these, on the overall accuracy of the estimated A_{eff}, is expected to be limited, but cannot be quantified until the reference database and its implementation into MT_RAYOR have been fully realized. However, as the suggested investigations aim at providing a better general understanding of multilayers, they are not viewed as subjects of interest purely on account of refining the NuSTAR ORM.

Appendix A

Papers and reports

This appendix contains abstracts for the papers published as part of the Ph.D. study and several internal NuSTAR reports. It is noted that a large number of people are included as authors on the published papers to acknowledge their part in the calibration effort and facility construction. The sole contributing author on both articles is Nicolai F. Brejnholt.

A.1 Review paper: The Rainwater Memorial Calibration Facility (RaMCaF) for X-ray optics

Authors: Nicolai F. Brejnholt, Finn E. Christensen, Charles J. Hailey, Nicolas M. Barriére, William W. Craig, Brian Grefenstette, Jason E. Koglin, Kristin K. Madsen, Julia K. Vogel, Hongjun An, Kenneth L. Blaedel, Josh Brown, Todd Decker, Zeshan Haider, Anders C. Jakobsen, Carsten P. Cooper-Jensen, Kaya Mori, Melania Nynka, Michael J. Pivovaroff, Clio Sleator, Dennis Stefanik, Marcela Stern, Gordon Tajiri, Douglas Thornhill and Jeremy S. Cushman

Abstract - *The Nuclear Spectroscopic Telescope ARray (NuSTAR) is a NASA Small Explorer mission that will carry the first focusing hard X-ray ($5 - 80\,keV$) telescope to orbit. The ground calibration of the optics posed a challenge as the need to suppress finite source distance effects over the full optic and the energy range of interest were unique requirements not met by any existing facility. In this paper we present the requirements for the NuSTAR optics ground calibration, and how the Rainwater Memorial Calibration Facility, RaMCaF, is designed to meet the calibration requirements. The nearly $175\,m$ long beamline sports a $48\,cm$ diameter $5 - 100\,keV$ X-ray beam and is capable of carrying out detailed studies of large diameter optic elements, such as the NuSTAR optics, as well as flat multilayer-coated Silicon wafers.*

Paper is available from the papers repository in the documentation library.

A.2 Conference proceeding paper: NuSTAR gr-ound calibration: The Rainwater Memorial Calibration Facility (RaMCaF)

Authors: Nicolai F. Brejnholt, Finn E. Christensen, Anders C. Jakobsen, Charles J. Hailey, Jason E. Koglin, Kenneth L. Blaedel, Marcela Stern, Douglas Thornhill, Clio Sleator, Shuo Zhang, William W. Craig , Kristin K. Madsen, Todd Decker, Michael J. Pivovaroff and Julia K. Vogel

Abstract - *The Nuclear Spectroscopic Telescope Array (NuSTAR) is a NASA Small Explorer mission that will carry the first focusing hard X-ray ($5 - 80\,keV$) telescope to orbit. The ground calibration of the three flight optics was carried out at the Rainwater Memorial Calibration Facility (RaMCaF) built for this purpose. In this article we present the facility and its use for the ground calibration of the three optics.*

Paper is available from the papers repository in the documentation library.

A.3 Conference proceeding paper: NuSTAR as-coated multilayers (working title)

Authors: Nicolai F. Brejnholt (under preparation)

Abstract - *The Nuclear Spectroscopic Telescope Array (NuSTAR) is slated for a 2012 launch carrying the first focusing hard X-ray ($5 - 80\,keV$) telescope to orbit. The multilayer coating was carried out at the Technical University of Denmark (DTU Space). Commercially available flat Silicon wafers were included to witness individual flight coating runs. Specular reflectivity response from the witness multilayer was measured up to $100\,keV$ at the Rainwater Memorial Calibration Facility (RaMCaF) for X-ray optics. These measurements are an integral part of the NuSTAR optic response model. In this article we present updated results from the witness campaign, as well as report on coating uniformity measurements carried out at DTU Space. Implementation of both witness and uniformity results are validated using NuSTAR ground calibration data.*

Paper will be available from the papers repository in the documentation library when published.

A.4 Internal report: Nevis NuSTAR X-ray Calibration Facility

Authors: Nicolai F. Brejnholt, Charles J. Hailey (editor)

Abstract - *This memo describes the NuSTAR X-ray calibration facility with particular emphasis on radiation shielding and operational safety features. The memo provides an overview of the NuSTAR project, the X-ray calibration facility at Nevis Laboratory, the radiation levels and shielding, and source operational details (e.g. operational procedures, radiation interlock system and other safety features).*

Report is available from the reports repository in the documentation library. The repository also contains a number of user and safety manuals authored by Nicolai F. Brejnholt. These are used in the safety training course for operators and users at RaMCaF, and act as guidelines for daily operation.

A.5 Internal report: Optic design document

Authors: Jason E. Koglin, Kristin K. Madsen

Abstract - *Optic design document detailing all optic parameters from individual layer incidence grazing angles to epoxy fillet width.*

Document is available from the reports repository in the documentation library.

A.6 Internal report: MT_RAYOR user manual

Authors: Niels Jørgen S. Westergaard

Abstract - *A Yorick interpreted language based ray tracing tool for the design and analysis of grazing incidence X-ray telescopes.*

Manual is available from the reports repository in the documentation library.

A.7 Internal report: NuSTAR Memo on reflectivity investigations and code verifications

Authors: Niels Jørgen S. Westergaard, Kristin K. Madsen, Finn E. Christensen, Nicolai F. Brejnholt

Abstract - *Memo tracking the effort to develop the two ray tracing tools NuSIM and MT_RAYOR in parallel.*

Memo is available from the reports repository in the documentation library.

A.8 Internal report: NuSTAR calibration plan

Authors: William W. Craig, Brian W. Grefenstette, Fiona A. Harrison, Charles J. Hailey, Jason E. Koglin,

Abstract - *This document describes the calibration plan for the NuSTAR instrument. The main document describes the requirements, overall approach, in-orbit calibration and summarize the plans for the optics modules, focal plane detectors, and detector entrance windows and optics thermal cover. Appendices are included that provide details of the experimental setup, error budgets and specifics of the measurements for both optics and focal plane detectors.*

Memo is available from the reports repository in the documentation library.

Appendix B

Coating campaign: Master table

All glass was tracked from factory roll-out through slumping, cutting and coating. Substrates mounted in an optic are listed in the master table. Table B.1 shows a selection of rows from the master table. The complete master table is available from the data repository located in the coating campaign library.

Table B.1: Selection of rows from the master table. Serial number uniquely identifies the substrate. The substrate naming convention goes: mandrel name (NxxxA or NxxxB), production cycle (yyy), layer (zzz), mirror location (P for hyperbola/upper placement or S for parabola/lower) and span (0 for 60° and 1 or 2 for 30°). It is further worth noting that "xxx" equals D_{sub} in millimeters. Mounting location breaks down into: optic (FMx), layer (yyy), mirror location (U for upper placement, L for lower) and azimuthal position (between 1 and 6 for 60° span and 1 and 12 for 30°). The notes field indicate whether the coating was carried out at DTU or RXO. A number of the RXO substrates had log errors resulting in the serial number being estimated based on shipping logs. Relevant pieces are marked in the notes column. Chamber position breaks down into: separator plates (xxx), mounting plate (yy) and plate position (z).

Serial number	Mounting location	Notes	Coating run	Recipe	Witness sample	Chamber position
N108B199-001P0	FM1_001U1	DTU	33	0	Si4535	100.17.5
⋮	⋮	⋮	⋮	⋮	⋮	⋮
N264B468-092S2	FM1_092L1	RXO	10145	8	A10145	N/A
N264A471-092S2	FM1_092L2	RXO, log error	10145	8	A10145	N/A
⋮	⋮	⋮	⋮	⋮	⋮	⋮
N336B544-117P2	FM2_117U5	DTU	328	9	Si5328	120.05.2

Appendix C

Uniformity campaign: Uniformity data

A total of twenty-five substrates and ten witness samples were measured at the $8\,keV$ beamline to map out coating uniformity. Table C.1 shows a selection of rows from the uniformity data table. The complete data set is available from the data repository located in the uniformity campaign library.

The processed data is available from the input repository located in the ORM library. Processing consists of finding the relative thickness of individual points with respect to the witness sample coating. Relative Γ and micro-roughness values are also found. Separate ORM input files are available for DTU and RXO uniformity. The files are in FITS format [60].

Table C.1: Selection of rows from the uniformity data table. Each sample is identified by substrate name and chamber position. Chamber position is given by separator plates, mounting plate and plate position. Up to seventeen points, 1-9 and A-H, are measured on each substrate (refer to Fig. 2.8, Chapter 2). The point and plate position "0" is used for witness samples only, indicating the same chamber location as plate position 2, point 5 for a substrate. This is a legacy from an early version of the analysis software and may be changed in a future update. Individual witness samples are tied to substrates as given by Table 2.3, Chapter 2. Type indicates whether the data in question is a witness sample, part of the core sample set, used to derive the uniformity mapping for the ORM input, or one of the extra samples coated to validate the model and uniformity mapping. The note on row five indicates that fitting was carried out with an offset to the incidence angle and that fuzzy structure related to poor mounting was observed. These comments flag the data with increased uncertainty in the uniformity map.

Sample	Point	ϕ_i	x	N	d	Γ	σ	Sep. plates	Mount. plate	Plate pos.	Type	Notes
Si5449	0	0	0	10	39.5	0.45	3.5	100	5	0	Witness	0
N136B408-023S0	1	19.4	-70	10	37.1	0.43	3.9	100	1	2	Extra	0
⋮	⋮	⋮	⋮	⋮	⋮	⋮	⋮	⋮	⋮	⋮	⋮	⋮
N140B418-024S0	H	-24.6	0	10	111.1	0.44	4.2	100	1	2	Extra	0
⋮	⋮	⋮	⋮	⋮	⋮	⋮	⋮	⋮	⋮	⋮	⋮	⋮
Si5373	0	0	0	10	55.8	0.45	3.1	90	9	0	Witness	0
⋮	⋮	⋮	⋮	⋮	⋮	⋮	⋮	⋮	⋮	⋮	⋮	⋮
N144B420-027P0	D	0	-100	10	47.8	0.49	3.9	90	7	2	Core	Offset angle 0.1 deg Fuzzy structure

Appendix D

Uniformity campaign: Uniformity data plots

This appendix contains illustrations of the uniformity data set. The plots accurately imitate the mounting plate setup and give relative thicknesses for individual points along with estimated uncertainty values. Note that values colored in red indicate substrate mounting issue at the $8\,keV$ beamline. Teal represents points where data is unavailable. Model values are plotted in place of the missing data, as well as used in the ORM.

The illustrations are also available from the plots repository located in the uniformity campaign library.

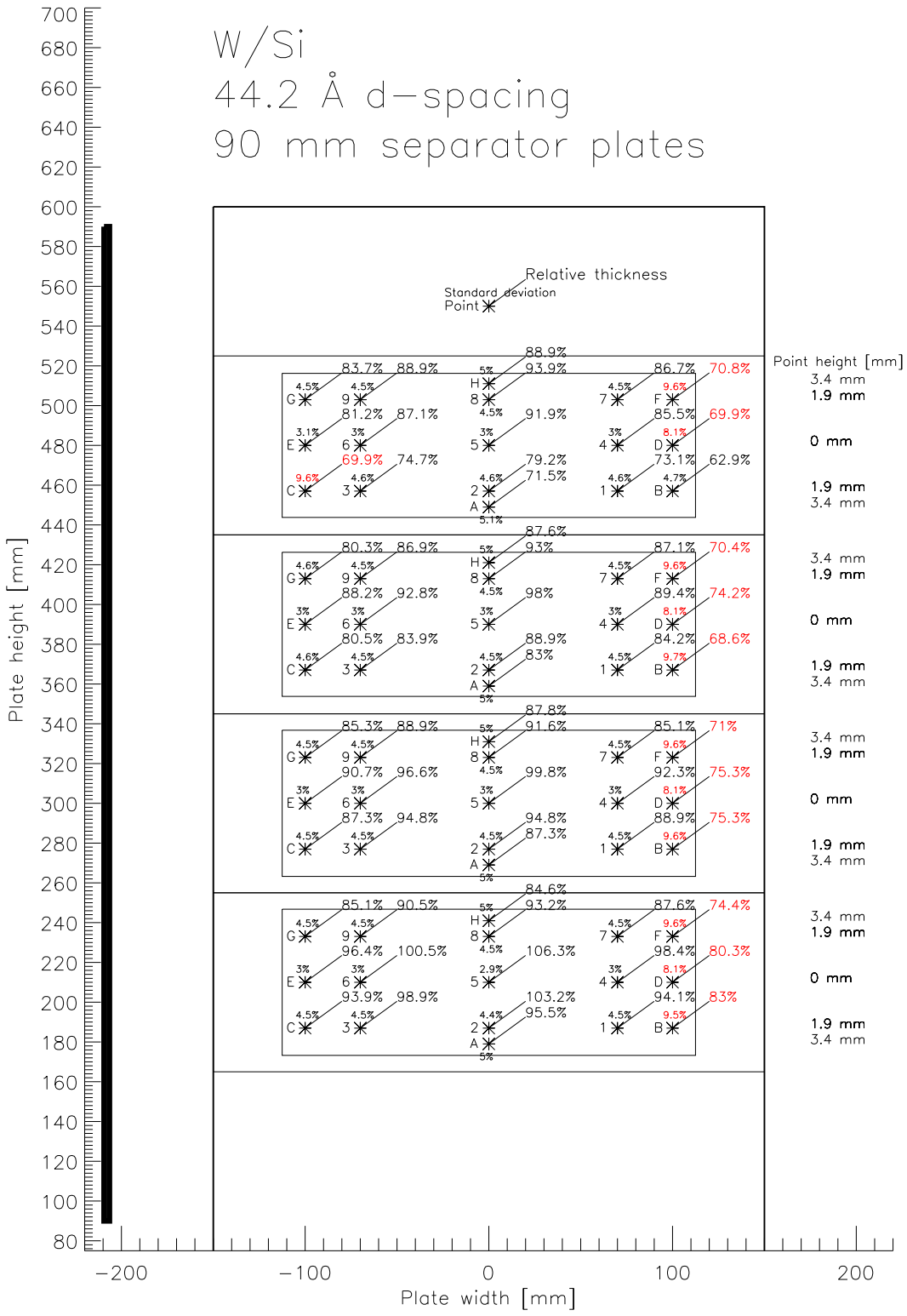

Figure D.1: Uniformity mapping expressed through relative thickness between point and witness sample mounted in PP2P5 on different mounting plate. Estimated standard deviation of each point is indicated. Uncertainty in point location is coarsely given by star. The vertical target extent is indicated by thick black line on left side.

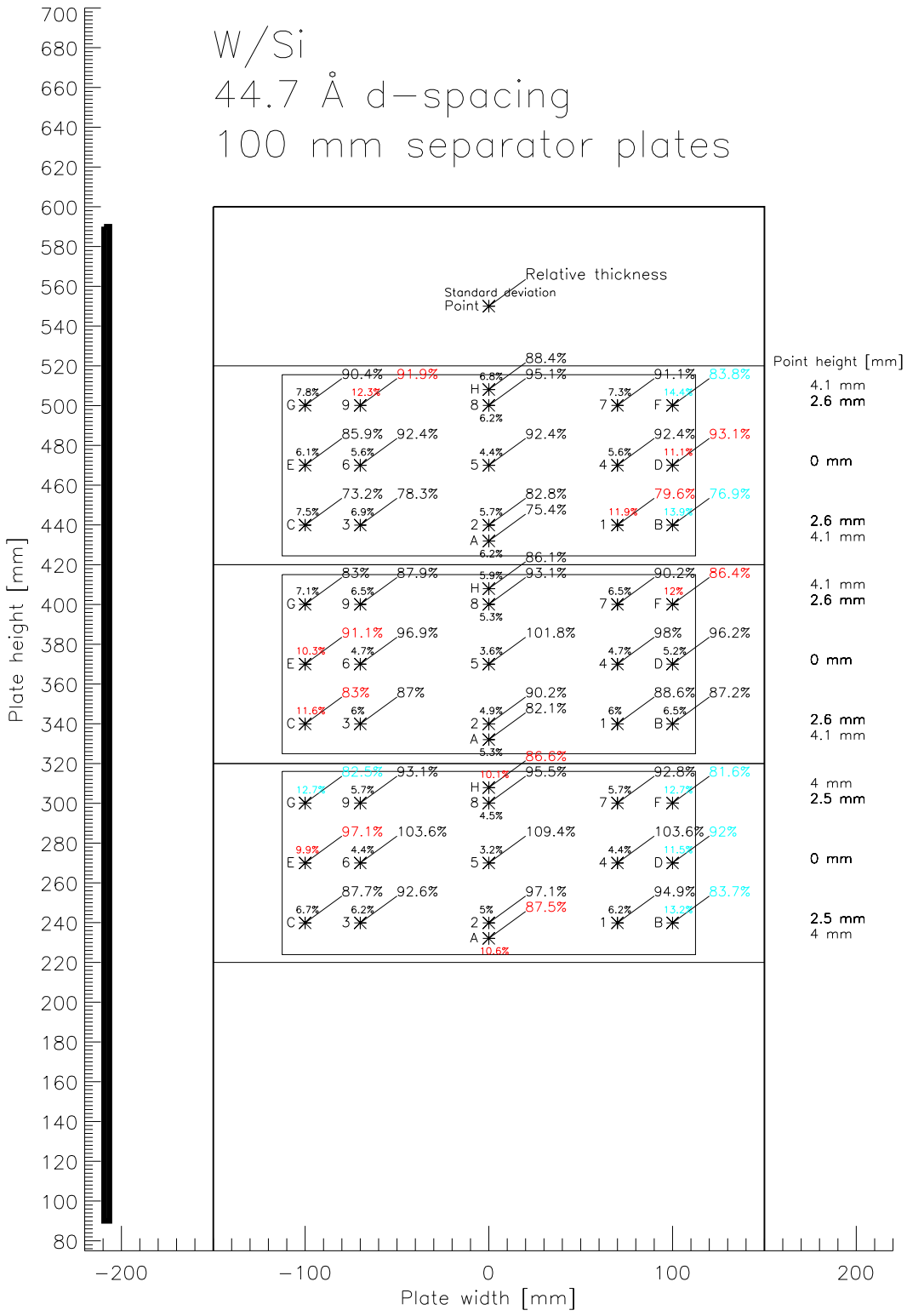

Figure D.2: Uniformity mapping expressed through relative thickness between point and witness sample mounted in PP2P5 on different mounting plate. Estimated standard deviation of each point is indicated. Uncertainty in point location is coarsely given by star. The vertical target extent is indicated by thick black line on left side.

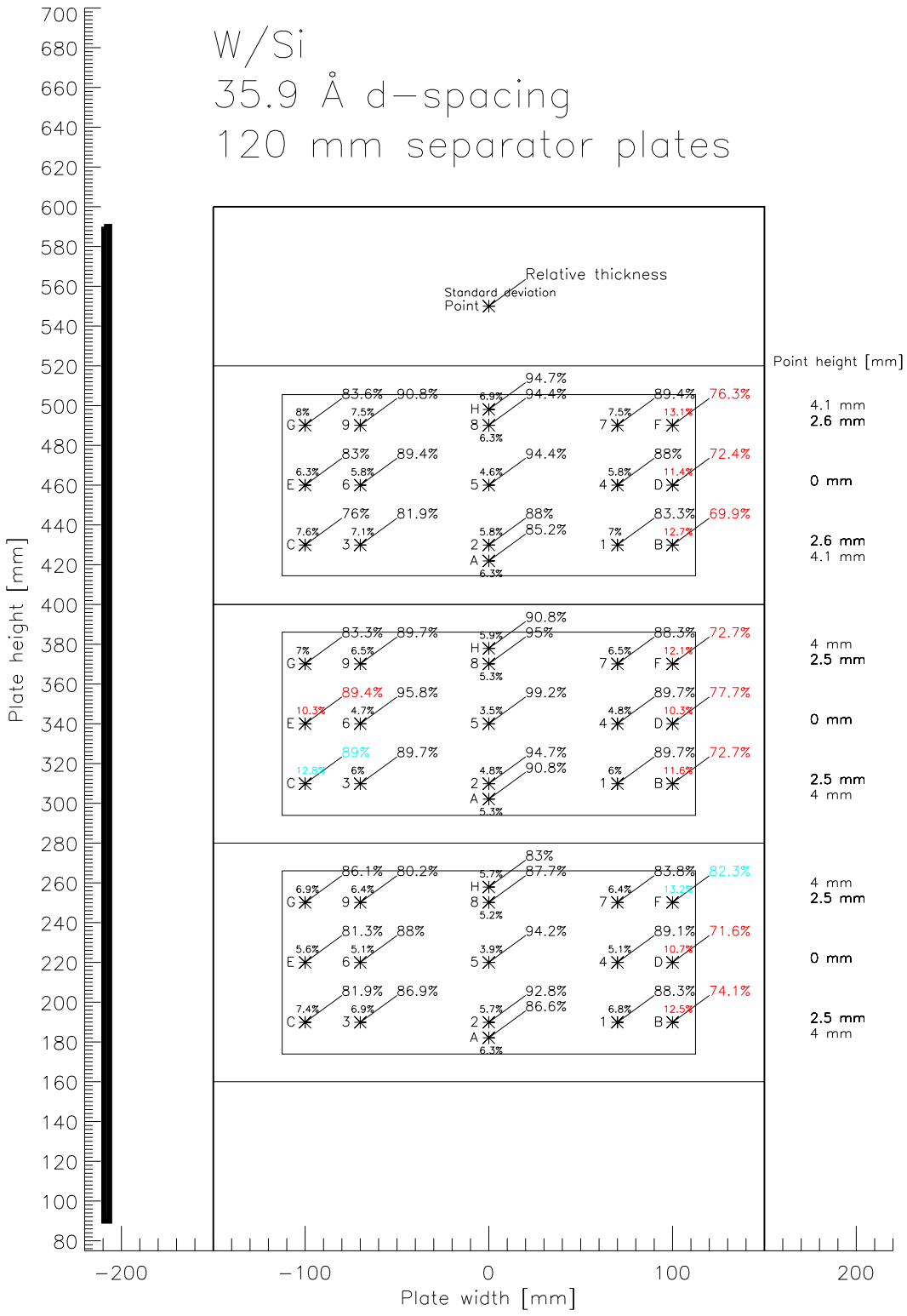

Figure D.3: Uniformity mapping expressed through relative thickness between point and witness sample mounted in PP2P5 on different mounting plate. Estimated standard deviation of each point is indicated. Uncertainty in point location is coarsely given by star. The vertical target extent is indicated by thick black line on left side.

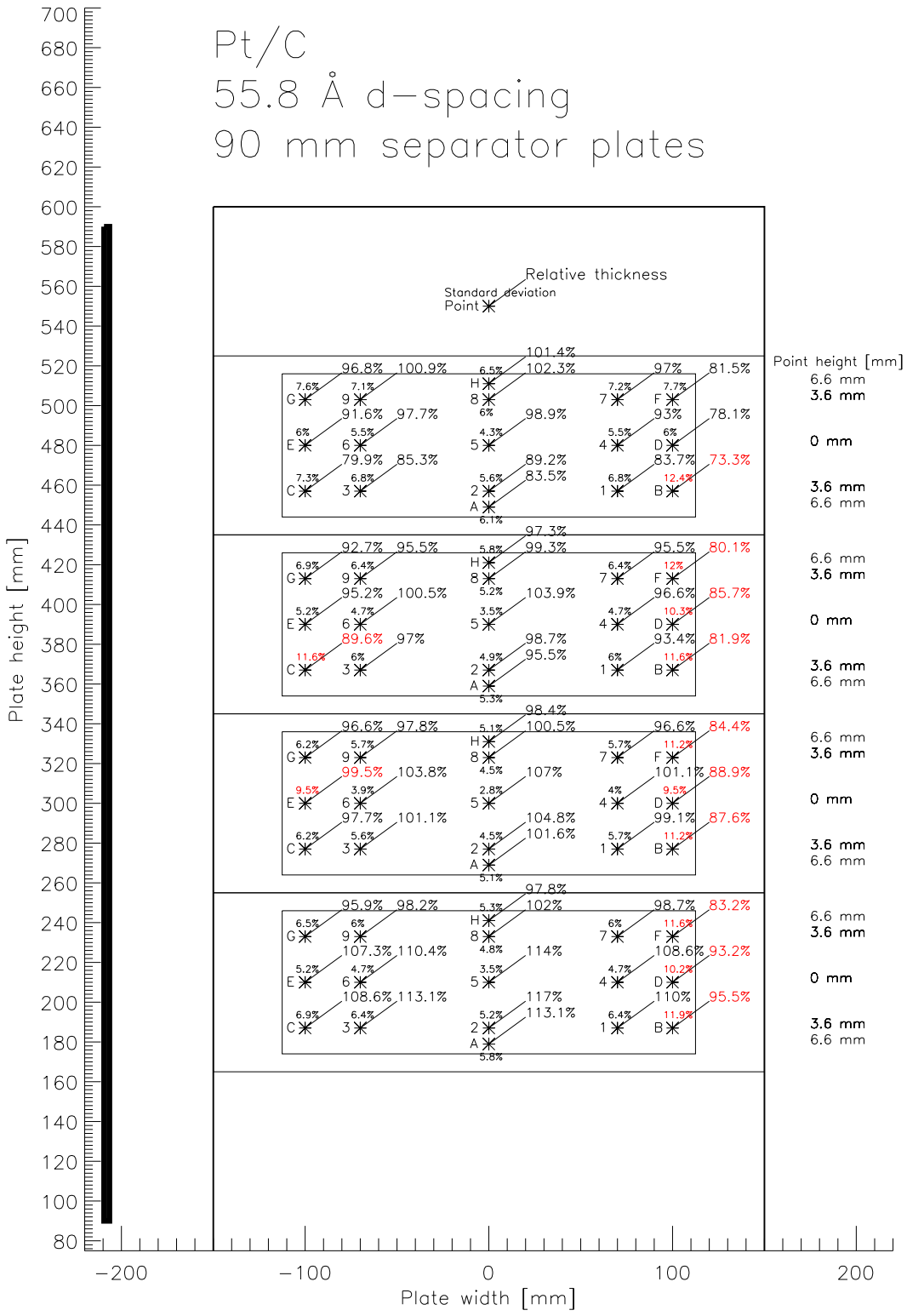

Figure D.4: Uniformity mapping expressed through relative thickness between point and witness sample mounted in PP2P5 on different mounting plate. Estimated standard deviation of each point is indicated. Uncertainty in point location is coarsely given by star. The vertical target extent is indicated by thick black line on left side.

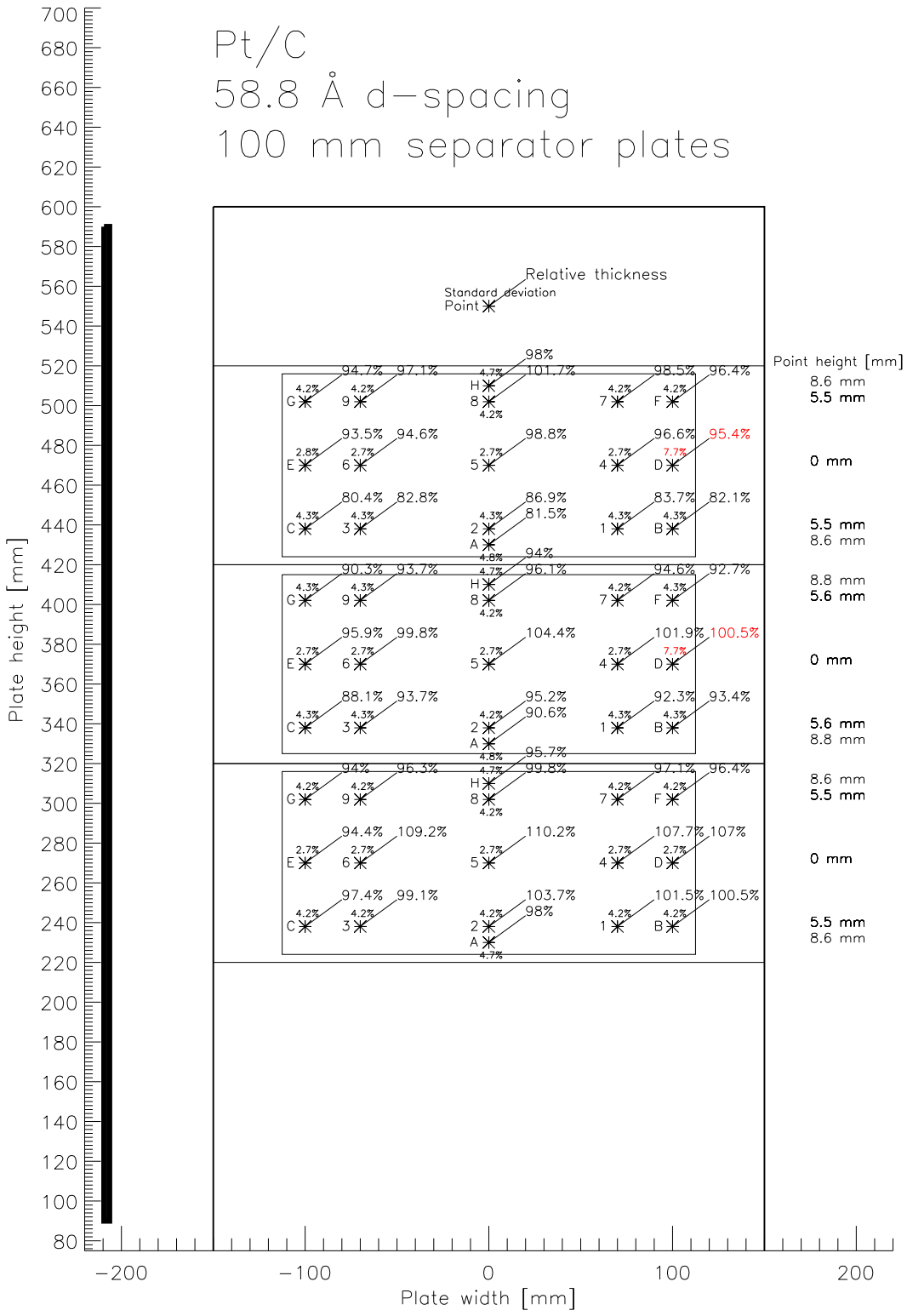

Figure D.5: Uniformity mapping expressed through relative thickness between point and witness sample mounted in PP2P5 on different mounting plate. Estimated standard deviation of each point is indicated. Uncertainty in point location is coarsely given by star. The vertical target extent is indicated by thick black line on left side.

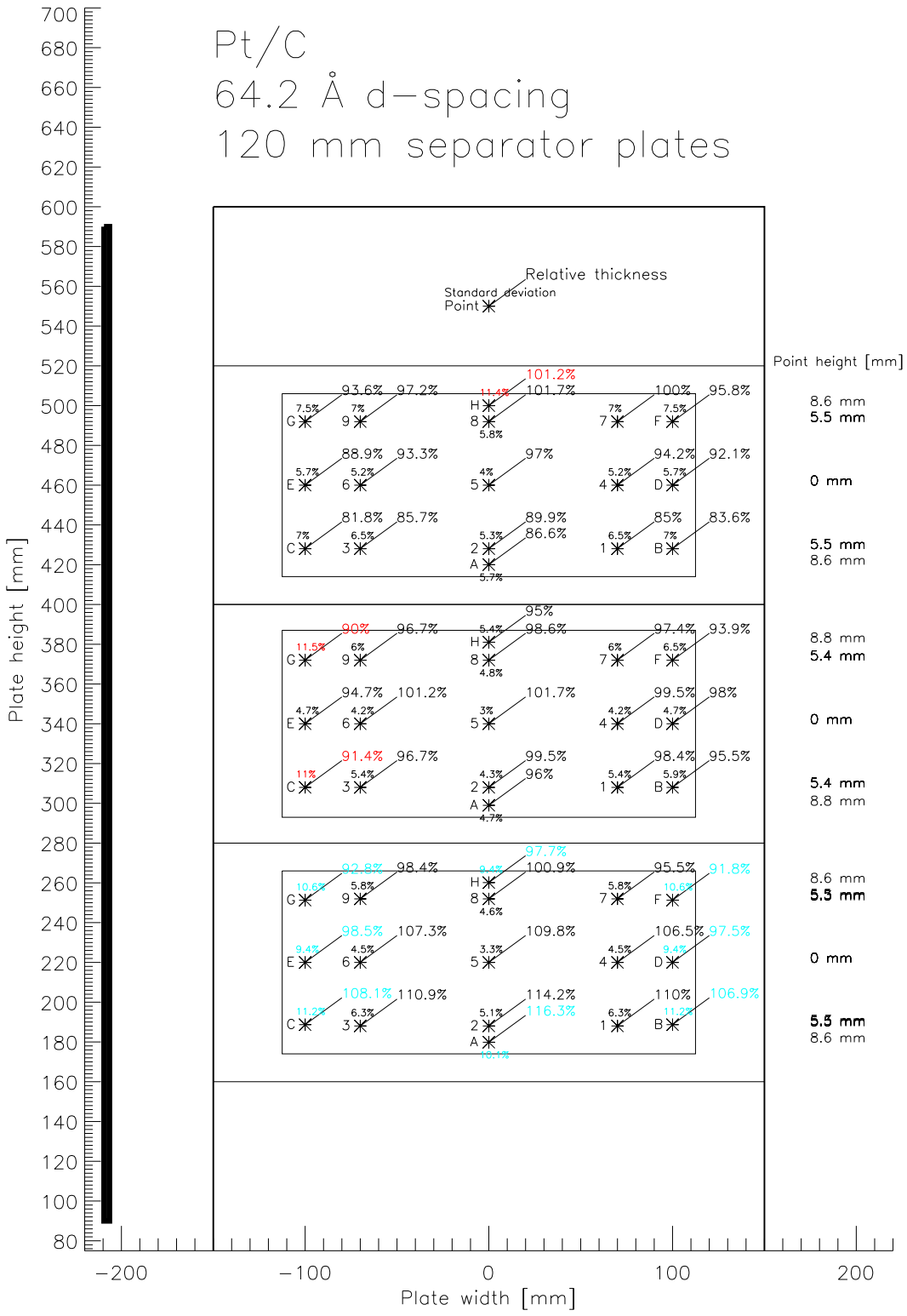

Figure D.6: Uniformity mapping expressed through relative thickness between point and witness sample mounted in PP2P5 on different mounting plate. Estimated standard deviation of each point is indicated. Uncertainty in point location is coarsely given by star. The vertical target extent is indicated by thick black line on left side.

Appendix E

Uniformity campaign: Vertical model versus data

This appendix contains points A, 2, 5, 8 and H data from the entire uniformity data set (core and extra) plotted as a function of plate height. Also plotted are the best vertical model estimates for the relevant substrates.

The plots are also available from the plots repository located in the uniformity campaign library.

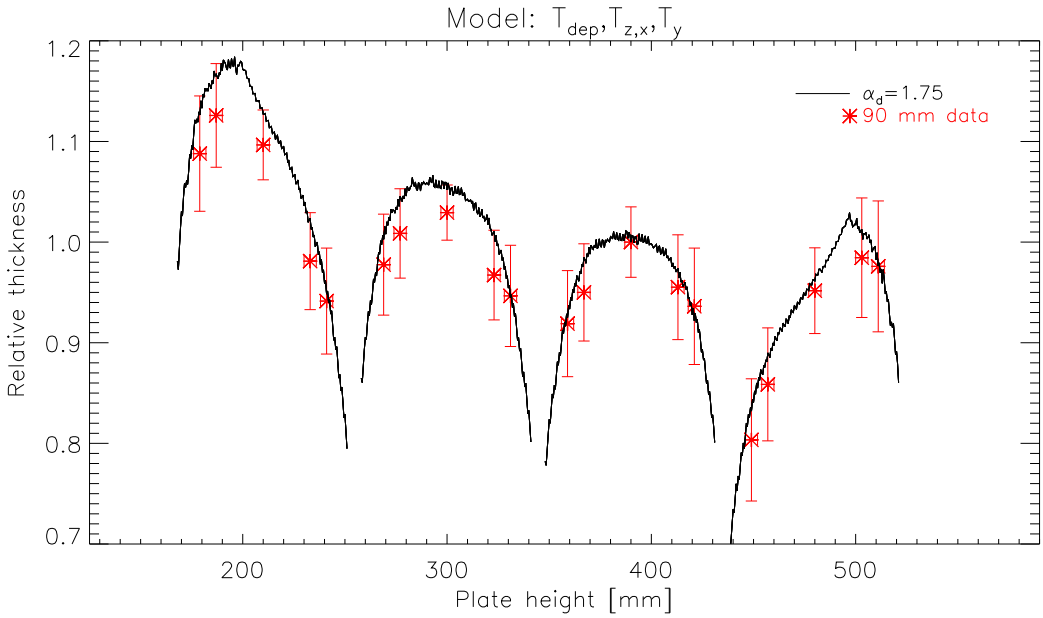

Figure E.1: Data from all uniformity substrates coated with Pt/C and 90mm separator plates compared to model.

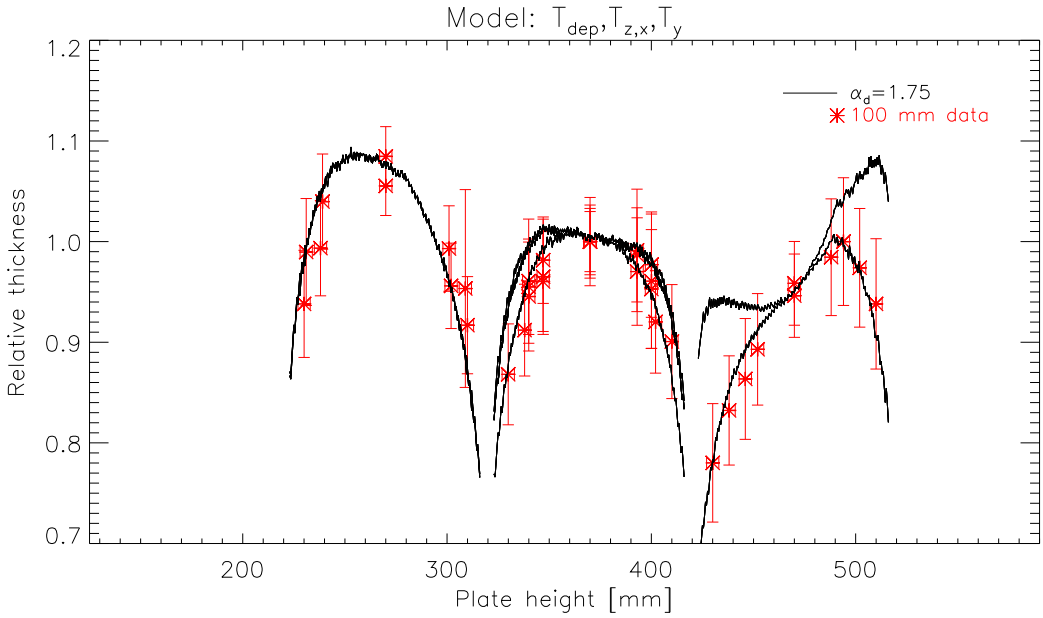

Figure E.2: Data from all uniformity substrates coated with Pt/C and 100mm separator plates compared to model.

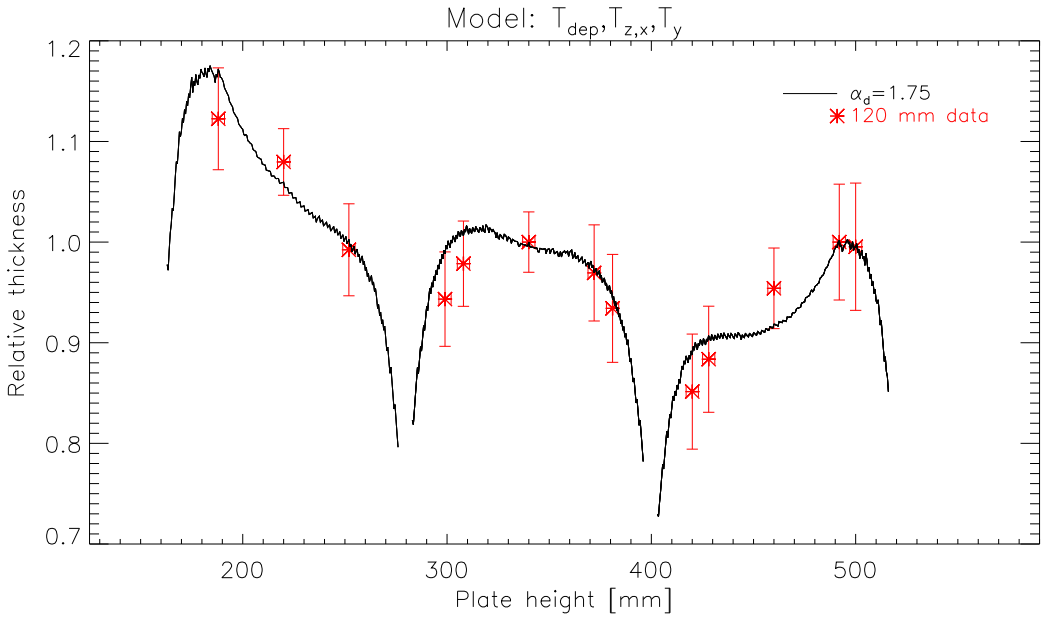

Figure E.3: Data from all uniformity substrates coated with Pt/C and 120mm separator plates compared to model.

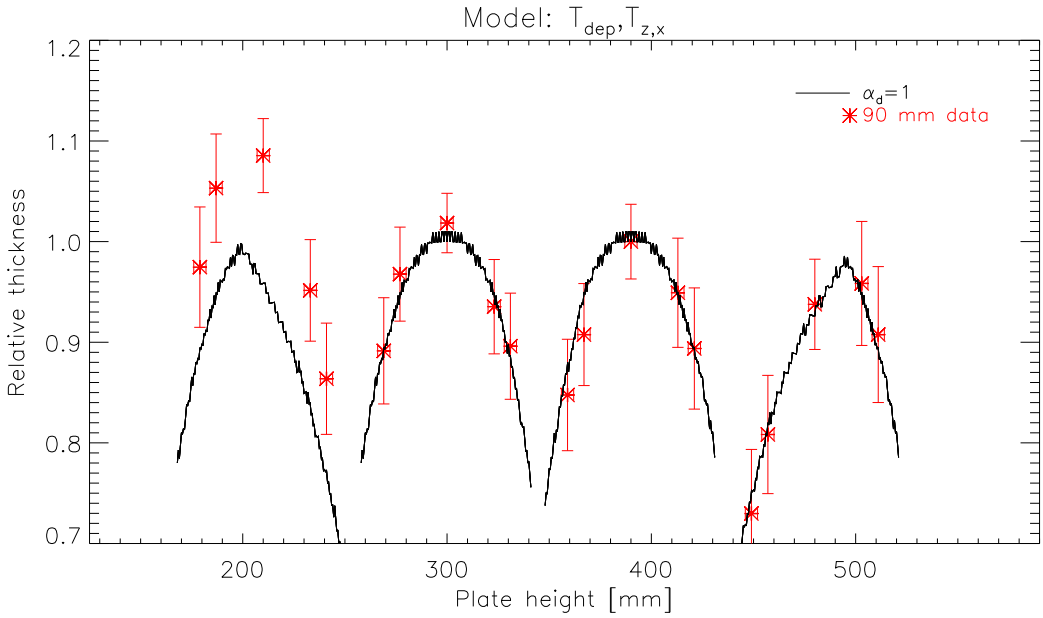

Figure E.4: Data from all uniformity substrates coated with W/Si and 90mm separator plates compared to model. The model is not scaled in relation to T_y as this was not measured for W/Si.

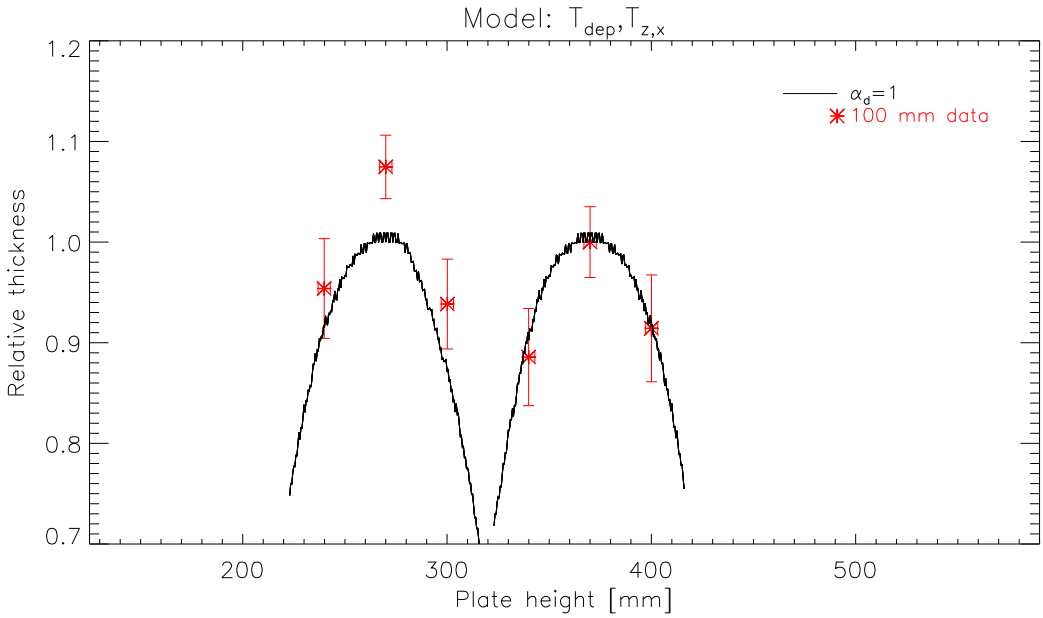

Figure E.5: Data from all uniformity substrates coated with W/Si and 100mm separator plates compared to model. The model is not scaled in relation to T_y as this was not measured for W/Si.

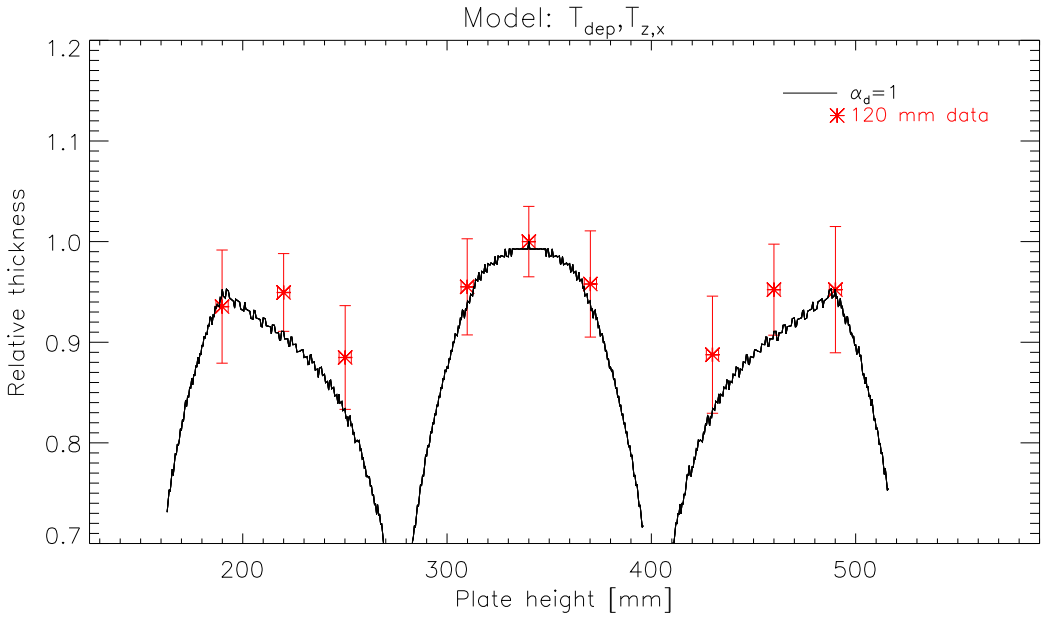

Figure E.6: Data from all uniformity substrates coated with W/Si and 120mm separator plates compared to model. The model is not scaled in relation to T_y as this was not measured for W/Si.

Appendix F

Uniformity campaign: Full model versus data

This appendix contains illustrations of the entire uniformity data set (core and extra). The plots accurately imitate the mounting plate setup and give relative thicknesses for individual points along with estimated relative thickness values based on the full model. Note that values colored in red indicate substrate mounting issues at the 8 keV beamline. Teal represents points where data is unavailable. Model values are plotted in place of the missing data.

The illustrations are also available from the plots repository located in the uniformity campaign library.

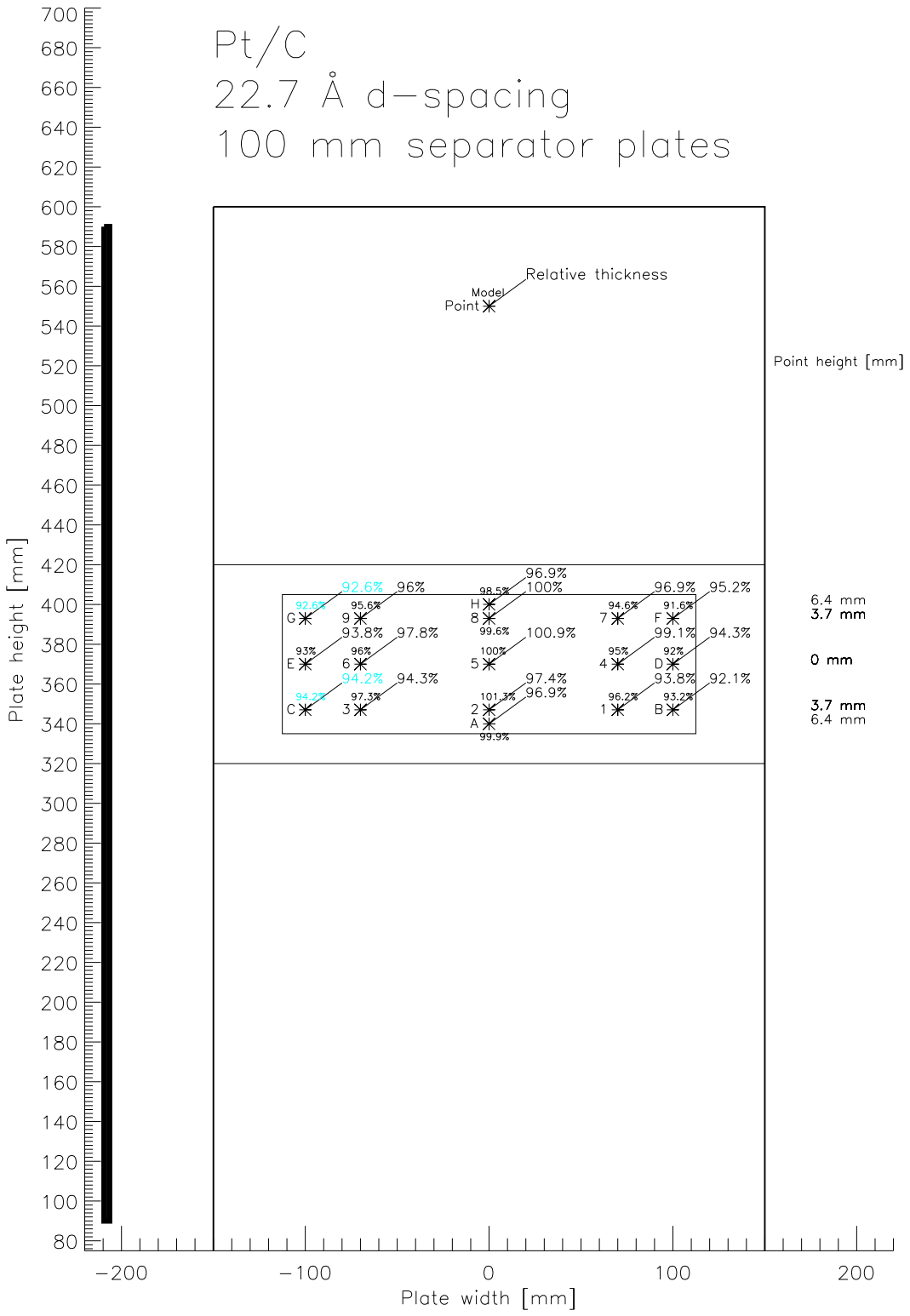

Figure F.1: Uniformity mapping expressed through relative thickness between substrate location and PP2P5 on same mounting plate for Pt/C. Estimated model value of each point is indicated. Model includes T_x, T_y, $T_{z,x}$ and T_{dep}. Uncertainty in point location is coarsely given by star. The vertical target extent is indicated by thick black line on left side.

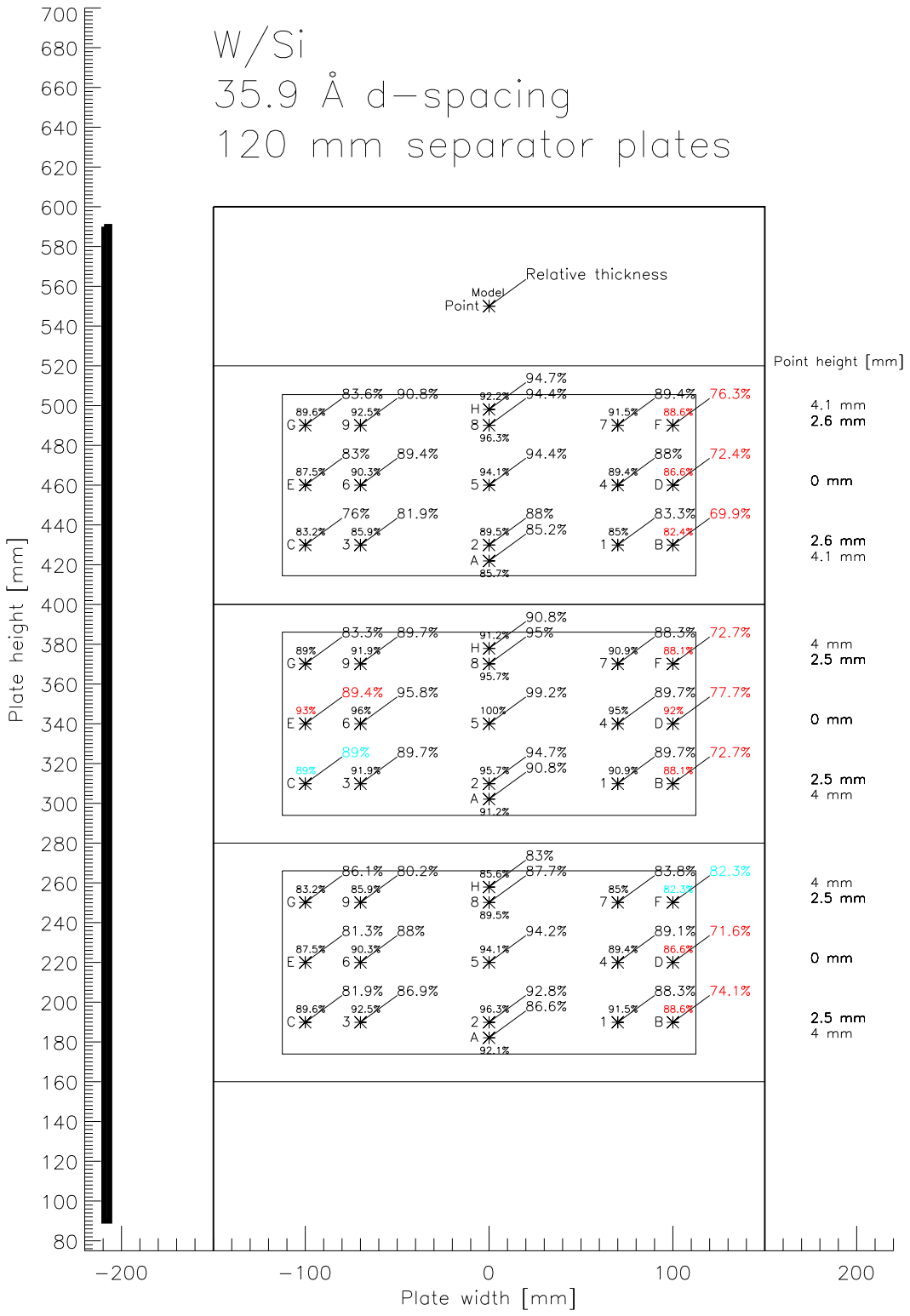

Figure F.2: Uniformity mapping expressed through relative thickness between substrate location and PP2P5 on same mounting plate for W/Si. Estimated model value of each point is indicated. Model includes T_x, $T_{z,x}$ and T_{dep}. Uncertainty in point location is coarsely given by star. The vertical target extent is indicated by thick black line on left side.

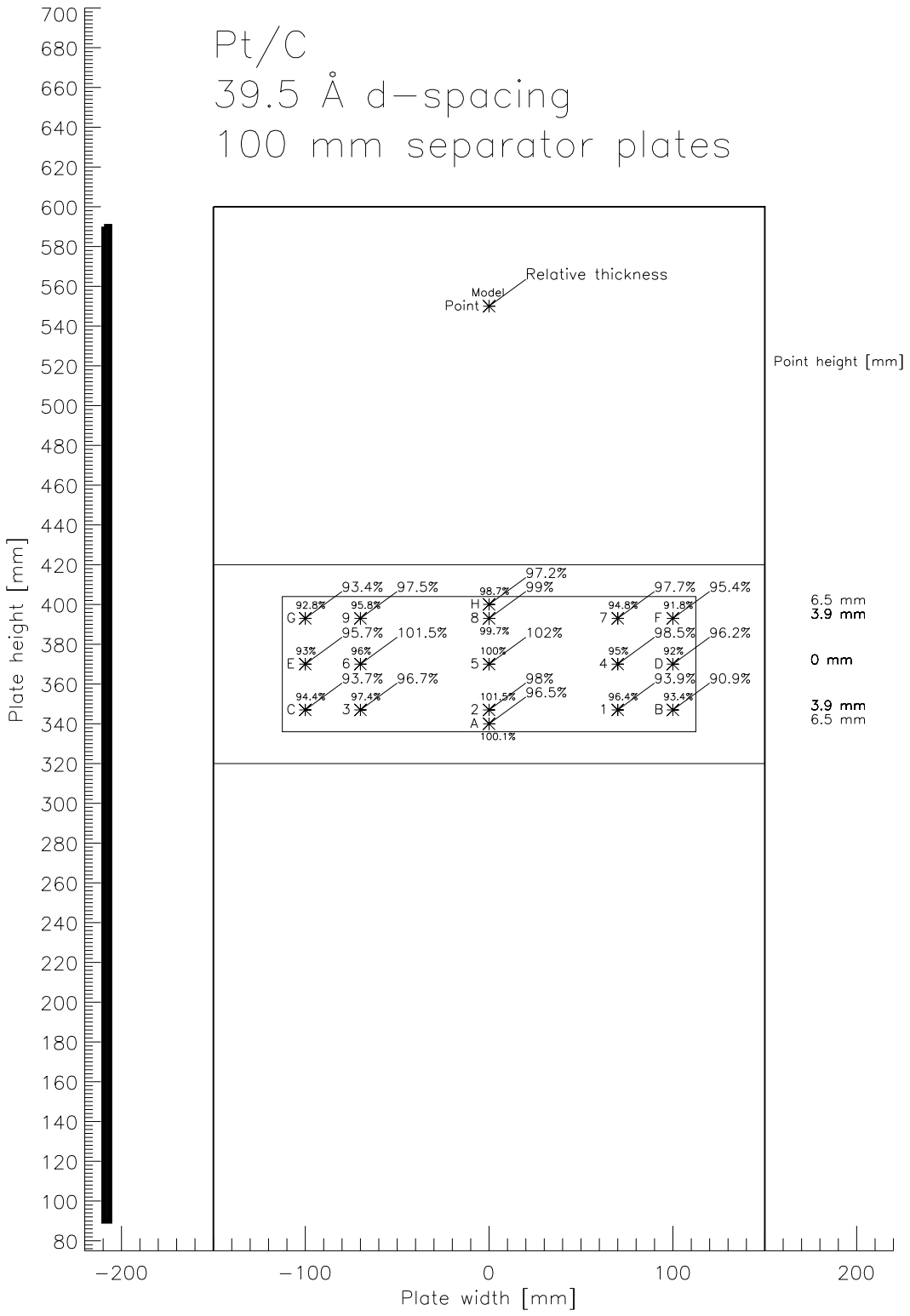

Figure F.3: Uniformity mapping expressed through relative thickness between substrate location and PP2P5 on same mounting plate for Pt/C. Estimated model value of each point is indicated. Model includes T_x, T_y, $T_{z,x}$ and T_{dep}. Uncertainty in point location is coarsely given by star. The vertical target extent is indicated by thick black line on left side.

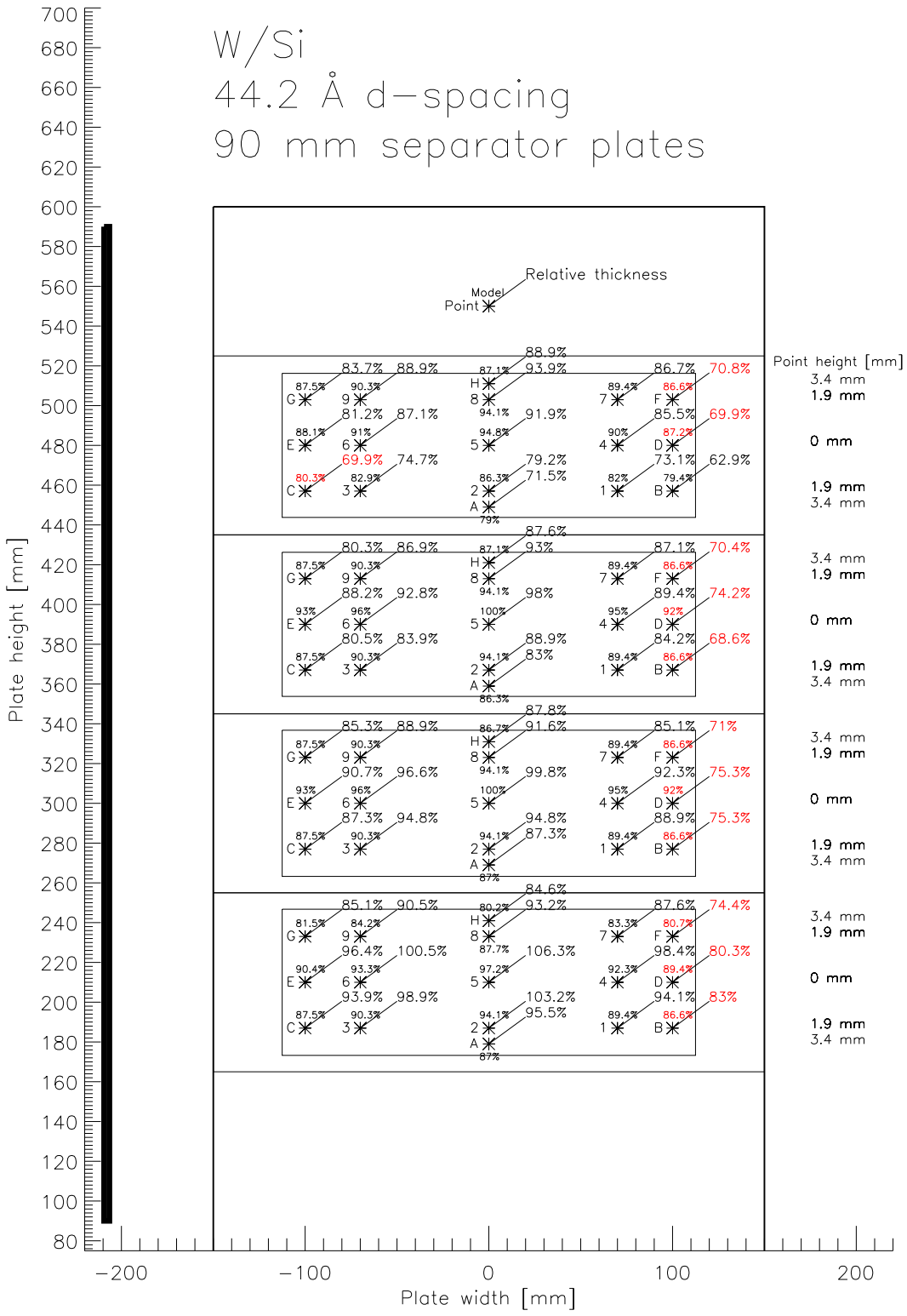

Figure F.4: Uniformity mapping expressed through relative thickness between substrate location and PP2P5 on same mounting plate for W/Si. Estimated model value of each point is indicated. Model includes T_x, $T_{z,x}$ and T_{dep}. Uncertainty in point location is coarsely given by star. The vertical target extent is indicated by thick black line on left side.

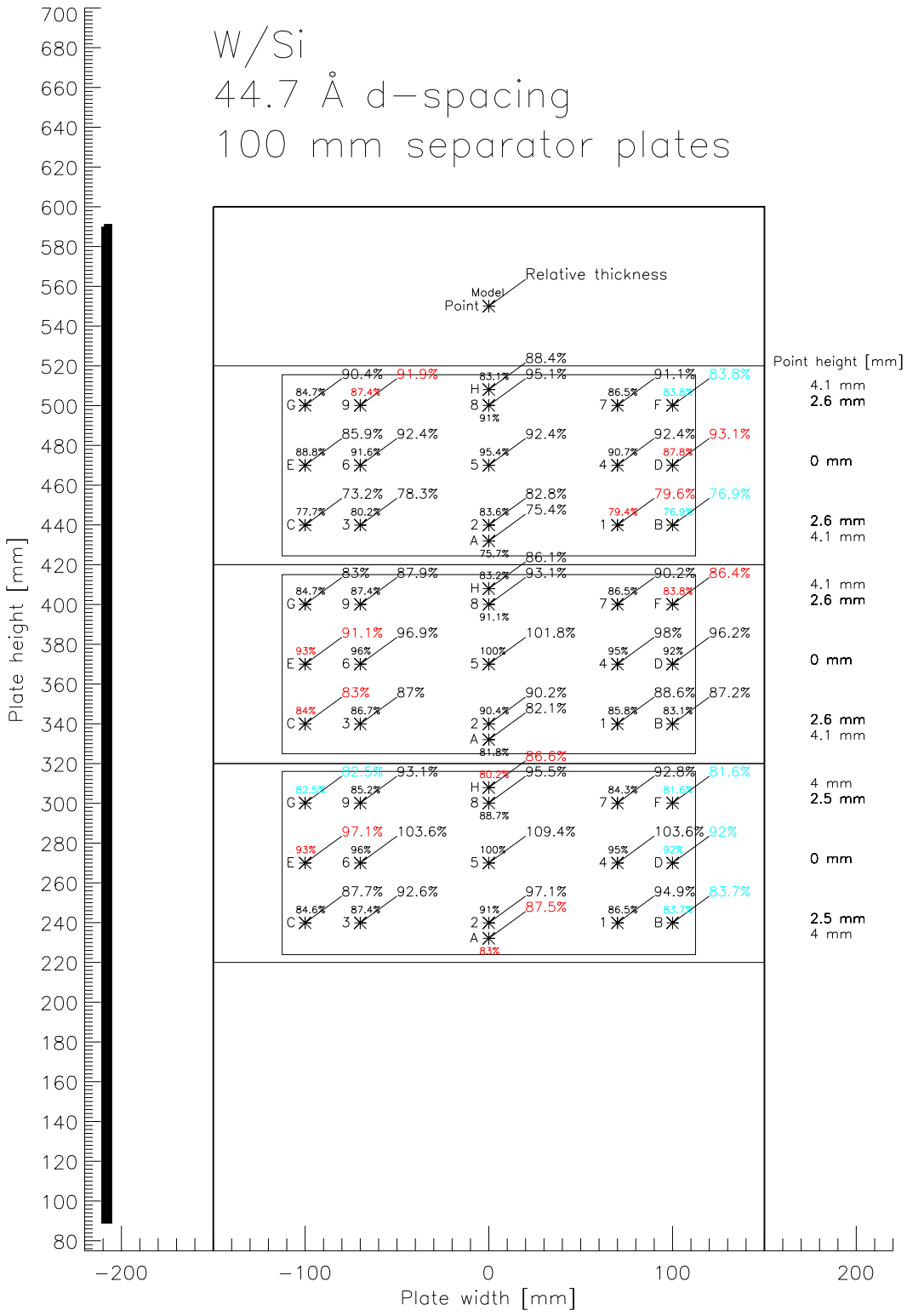

Figure F.5: Uniformity mapping expressed through relative thickness between substrate location and PP2P5 on same mounting plate for W/Si. Estimated model value of each point is indicated. Model includes T_x, $T_{z,x}$ and T_{dep}. Uncertainty in point location is coarsely given by star. The vertical target extent is indicated by thick black line on left side.

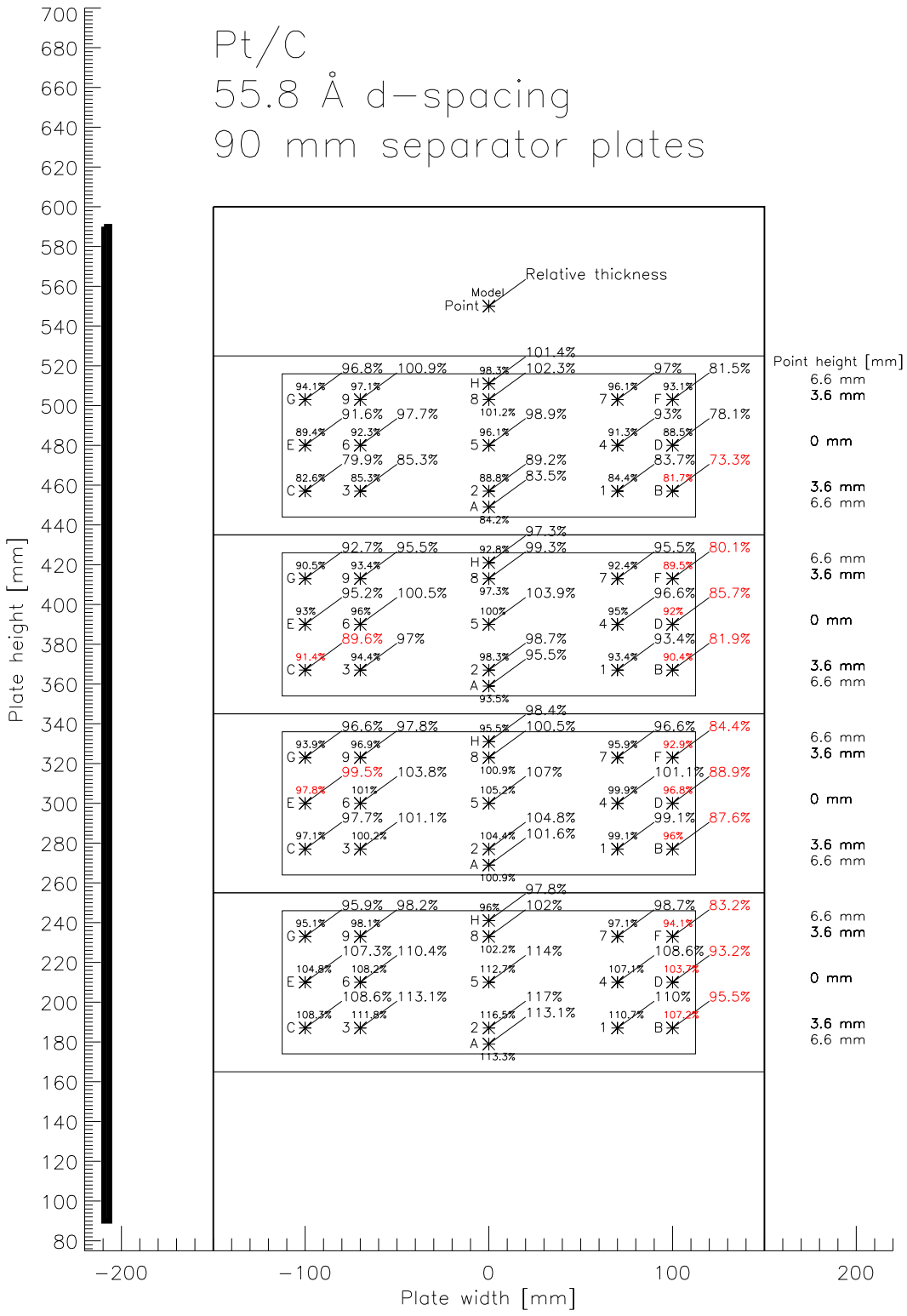

Figure F.6: Uniformity mapping expressed through relative thickness between substrate location and PP2P5 on same mounting plate for Pt/C. Estimated model value of each point is indicated. Model includes T_x, T_y, $T_{z,x}$ and T_{dep}. Uncertainty in point location is coarsely given by star. The vertical target extent is indicated by thick black line on left side.

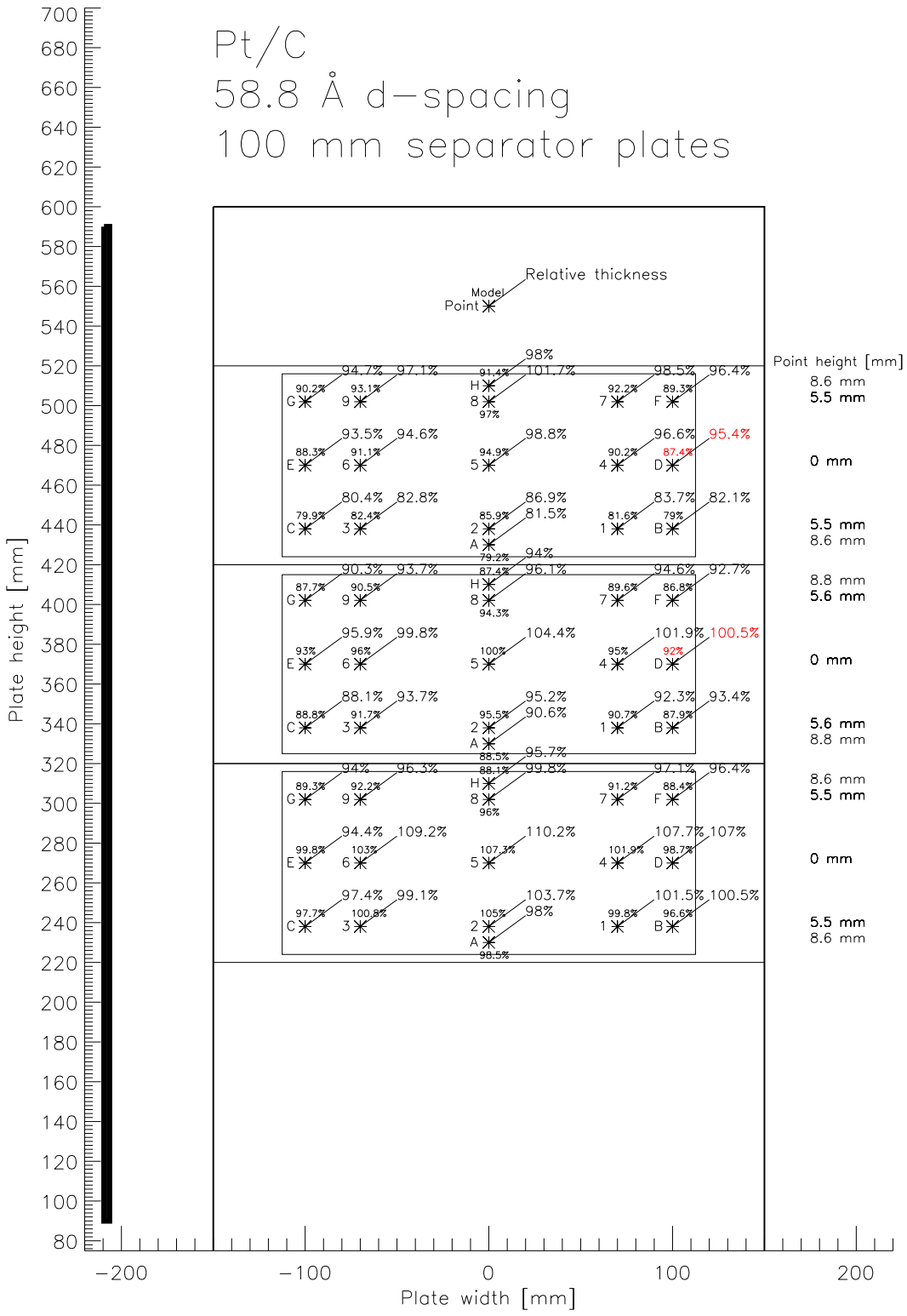

Figure F.7: Uniformity mapping expressed through relative thickness between substrate location and PP2P5 on same mounting plate for Pt/C. Estimated model value of each point is indicated. Model includes T_x, T_y, $T_{z,x}$ and T_{dep}. Uncertainty in point location is coarsely given by star. The vertical target extent is indicated by thick black line on left side.

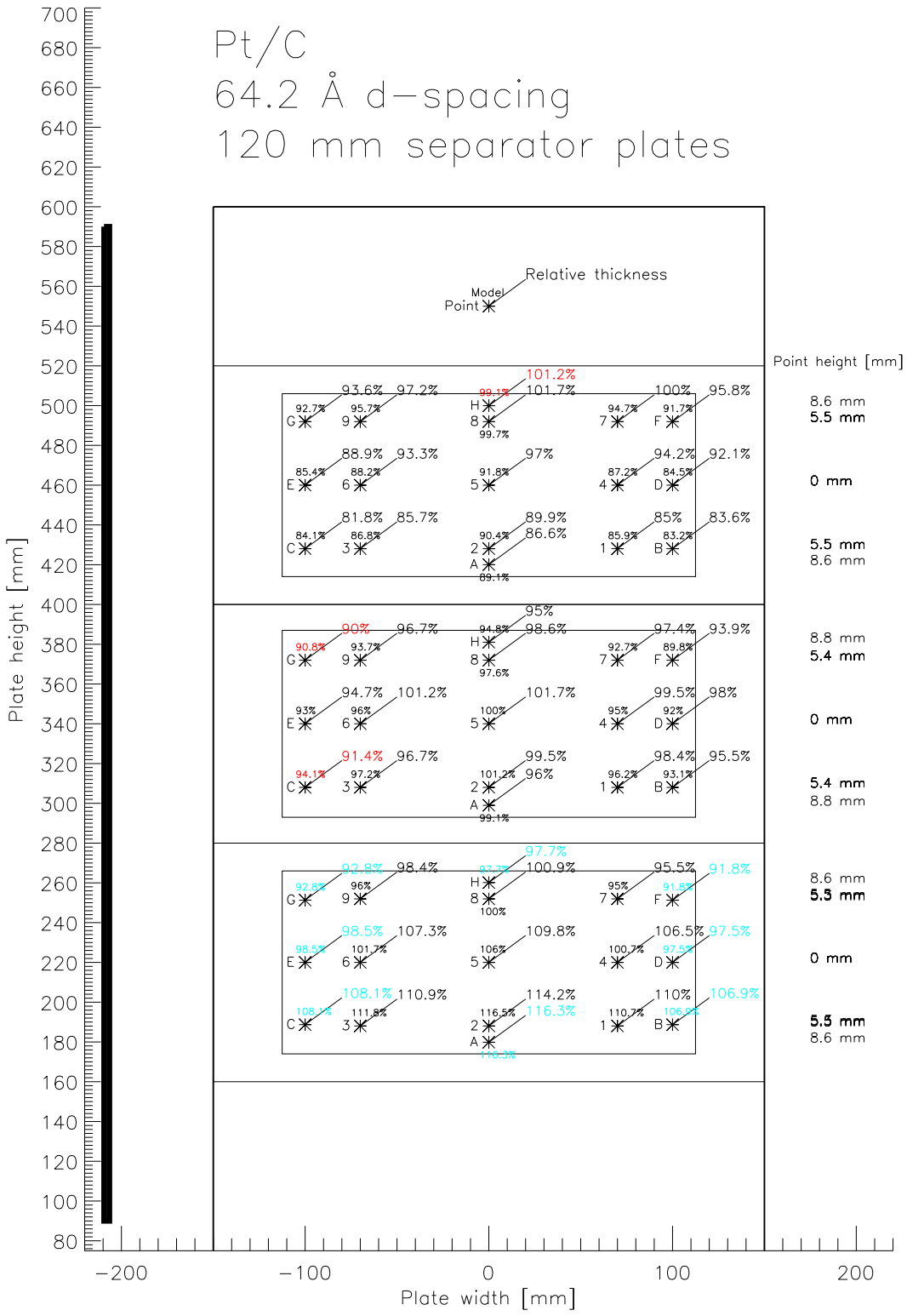

Figure F.8: Uniformity mapping expressed through relative thickness between substrate location and PP2P5 on same mounting plate for Pt/C. Estimated model value of each point is indicated. Model includes T_x, T_y, $T_{z,x}$ and T_{dep}. Uncertainty in point location is coarsely given by star. The vertical target extent is indicated by thick black line on left side.

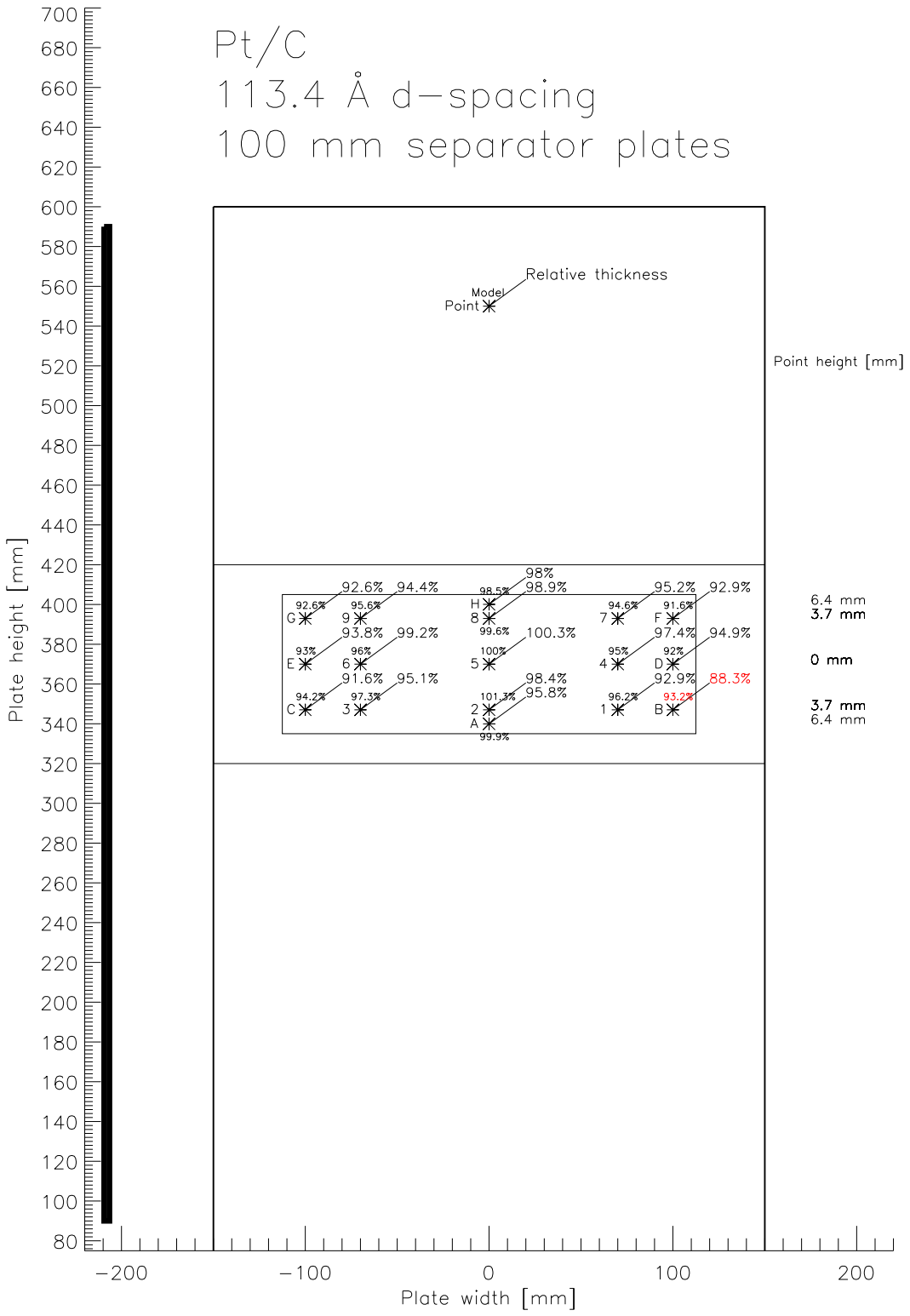

Figure F.9: Uniformity mapping expressed through relative thickness between substrate location and PP2P5 on same mounting plate for Pt/C. Estimated model value of each point is indicated. Model includes T_x, T_y, $T_{z,x}$ and T_{dep}. Uncertainty in point location is coarsely given by star. The vertical target extent is indicated by thick black line on left side.

Appendix G

Uniformity campaign: Full model versus data overview

This appendix presents an overview of the point by point comparison between the measured relative thickness and the modeled value for the entire uniformity data set (core and extra).

The plots are also available from the plots repository located in the uniformity campaign library.

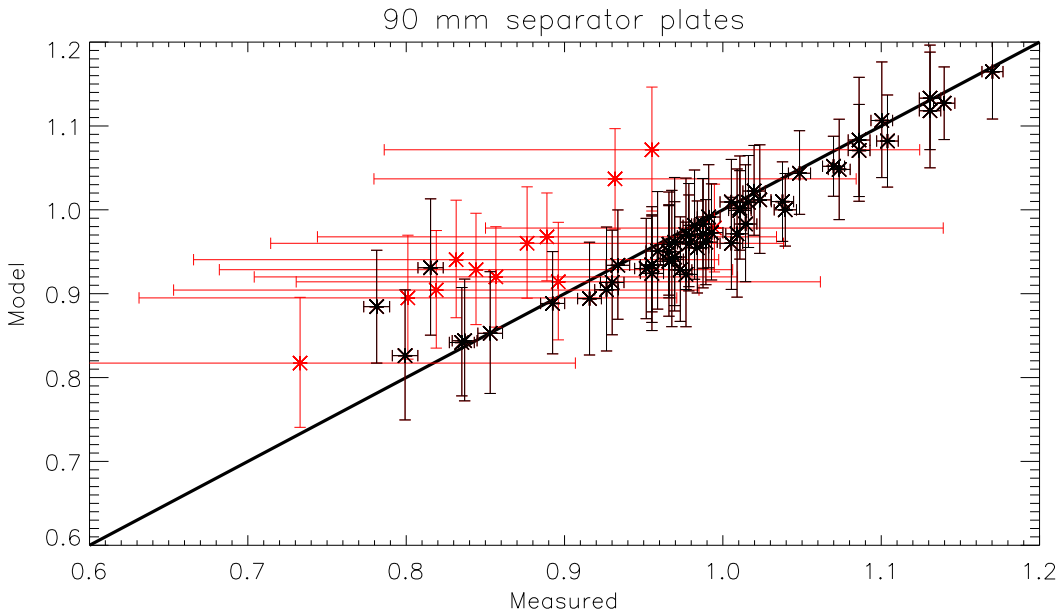

Figure G.1: Overview of the model fit to points 123456789ABCDEFGH for all Pt/C uniformity substrates coated with 90 mm separator plates. Ideal fit indicated by heavy black line. Points colored red indicate substrate mounting issues at the 8 keV beamline.

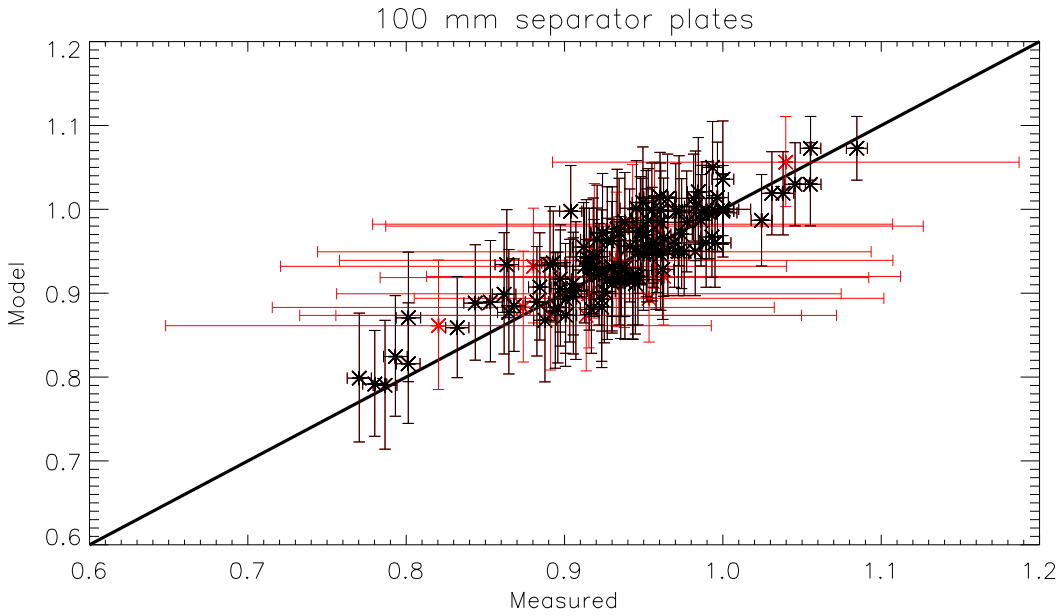

Figure G.2: Overview of the model fit to points 123456789ABCDEFGH for all Pt/C uniformity substrates coated with 100 mm separator plates. Ideal fit indicated by heavy black line. Points colored red indicate substrate mounting issues at the 8 keV beamline.

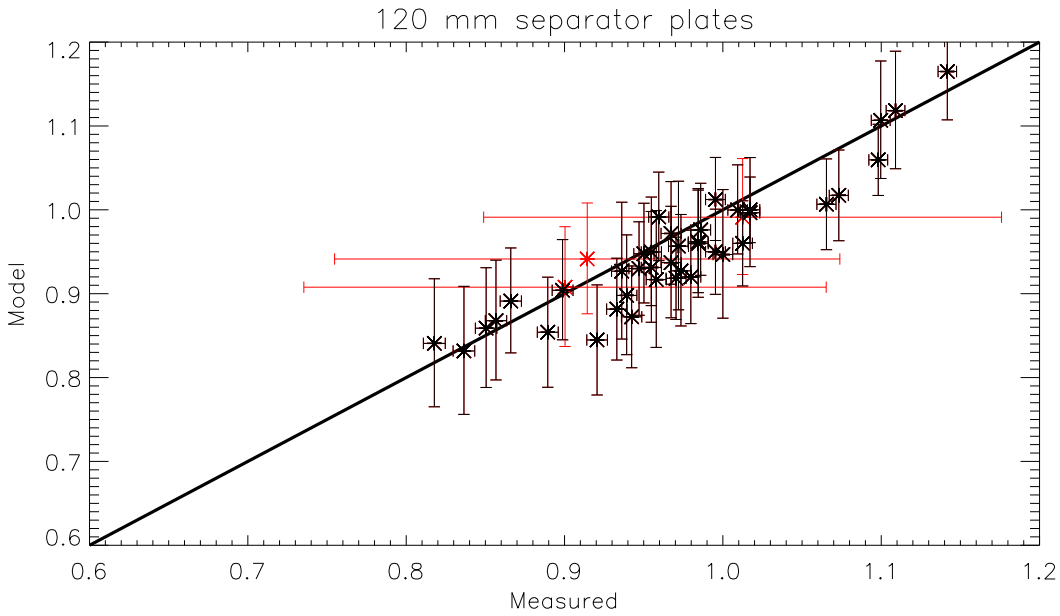

Figure G.3: Overview of the model fit to points 123456789ABCDEFGH for all Pt/C uniformity substrates coated with 120 mm separator plates. Ideal fit indicated by heavy black line. Points colored red indicate substrate mounting issues at the 8 keV beamline.

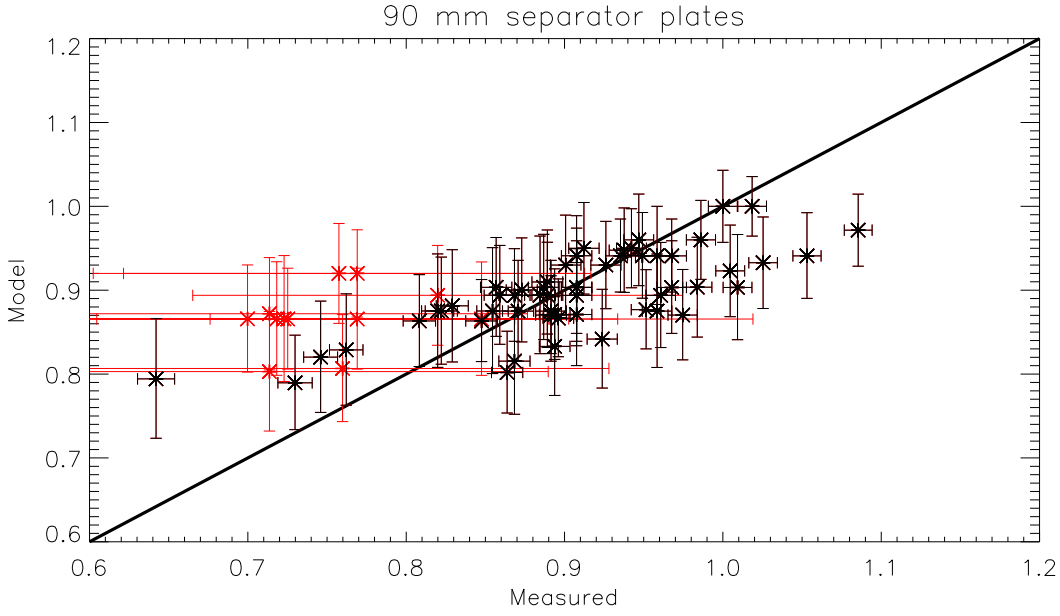

Figure G.4: Overview of the model fit to points 123456789ABCDEFGH for all W/Si uniformity substrates coated with 90 mm separator plates. Ideal fit indicated by heavy black line. Points colored red indicate substrate mounting issues at the 8 keV beamline.

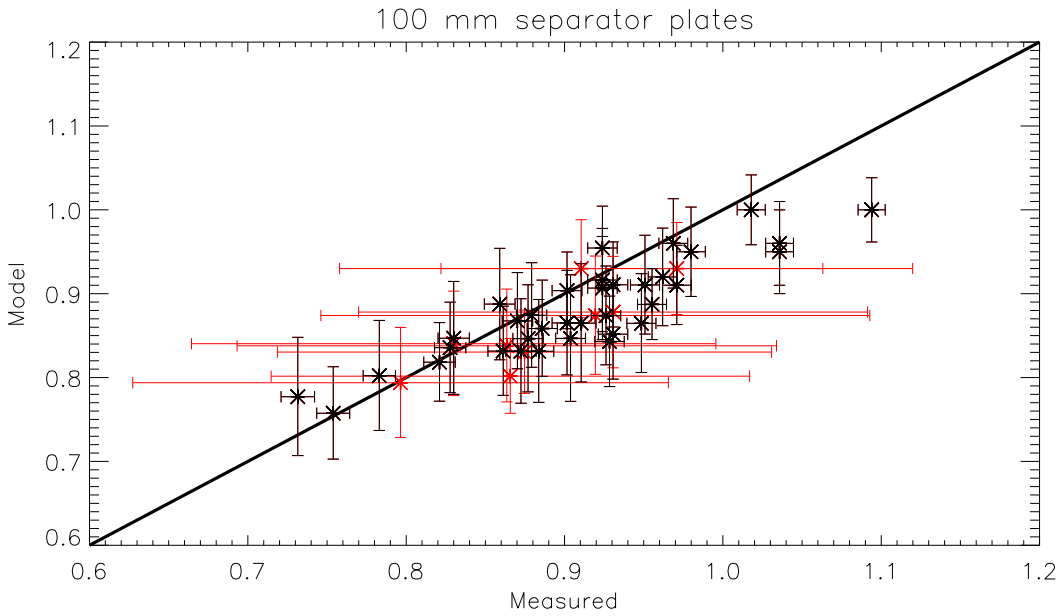

Figure G.5: Overview of the model fit to points 123456789ABCDEFGH for all W/Si uniformity substrates coated with 100 mm separator plates. Ideal fit indicated by heavy black line. Points colored red indicate substrate mounting issues at the 8 keV beamline.

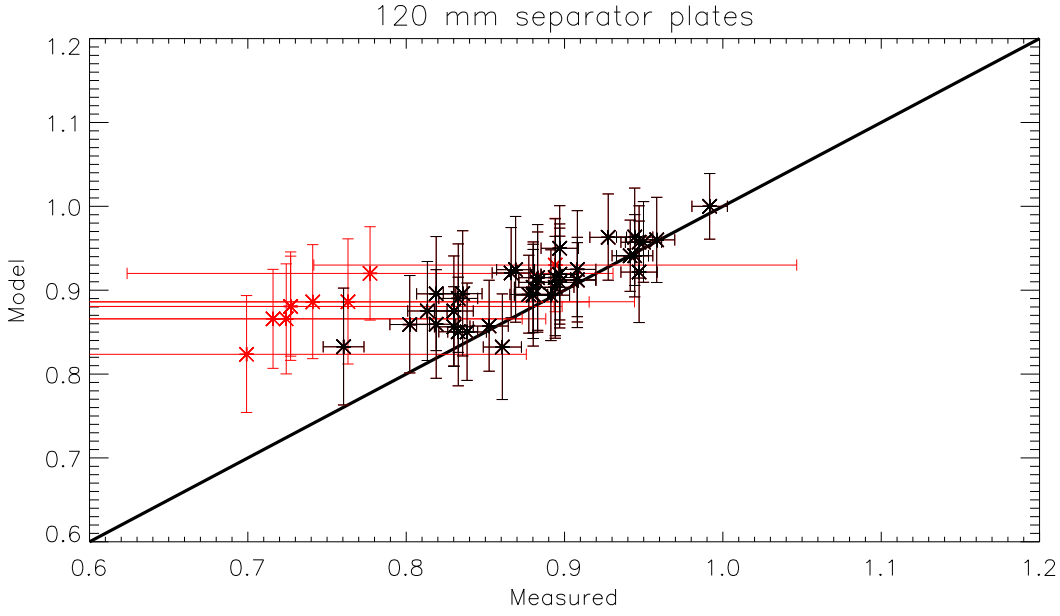

Figure G.6: Overview of the model fit to points 123456789ABCDEFGH for all W/Si uniformity substrates coated with 120 mm separator plates. Ideal fit indicated by heavy black line. Points colored red indicate substrate mounting issues at the 8 keV beamline.

Appendix H

Witness campaign: Witness data

More than four hundred individual spectra were acquired from the witness samples in the RaMCaF campaign. A standard witness sample was measured at a high and a low angle. In addition to this, all DTU coated samples were measured at the $8\,keV$ beamline.

The complete data set is available from the data repository located in the witness campaign library. Note that several RXO samples were not measured at RaMCaF before the witness sample campaign concluded. Presently no $8\,keV$ data exists from these samples either. Alternative means are being investigated for acquiring data on the remaining samples and as it is acquired the data will be added to the repository.

Appendix I

Witness campaign: As-coated recipes

Data from each of the multilayer coated witness samples have been analyzed using IMD to establish the as-coated recipe parameters. In addition to the recipe parameters given by the design, several other parameters were defined to improve the fit to RaMCaF data. A selection of rows from the as-coated recipe table are shown in Table I.1 and Table I.2.

The as-coated recipes are available from the input repository located in the ORM library. Both a comma-separated text file and FITS format [60] files are available. The comma-separated text file contains the full as-coated recipe list partially represented by Table I.1 and Table I.2. One FITS file per witness sample is available. The FITS files contain the as-coated recipe in addition to other relevant information regarding the witness sample and fit. The additional information includes an array describing any cathode drop-outs and the fitted reduction in bilayer thickness resulting from the drop-out. Only the FITS files are used directly in the ORM.

Table I.1: Part one of a selection of rows from the as-coated recipe table. Part two is found in Table I.2. Each row represents the as-coated recipe found for a given coating run. The number of substrates from said coating run mounted in a flight optic is given by n_m. Recipe values were established based on specular reflectivity data acquired with a grazing incidence angle of θ_i at RaMCaF. If data has yet to be analyzed fields read "N/A". At the time of writing this is the case for all RXO (Axxxxx) and recipe 0 witness samples.

Coating run	n_m	Witness sample	Recipe	θ_i[°]	χ^2	c	N	d_{min}[Å]	d_{max}[Å]	Γ_{top}	Γ	σ[Å]
11012	15	A11012	8	N/A	N/A	N/A	N/A	N/A	N/A	N/A	N/A	N/A
28	9	Si4402	0	N/A	N/A	N/A	N/A	N/A	N/A	N/A	N/A	N/A
⋮	⋮	⋮	⋮	⋮	⋮	⋮	⋮	⋮	⋮	⋮	⋮	⋮
167	20	Si5089	1	0.219	0.69	0.261	145	27.1	121.7	0.71	0.39	4.7
⋮	⋮	⋮	⋮	⋮	⋮	⋮	⋮	⋮	⋮	⋮	⋮	⋮
196	20	Si5122	3	0.218	0.59	0.242	145	28.5	124.6	0.7	0.42	4.6
⋮	⋮	⋮	⋮	⋮	⋮	⋮	⋮	⋮	⋮	⋮	⋮	⋮
279	30	Si5230	6	0.223	0.85	0.244	145	25.9	90.5	0.72	0.35	4.1

Table I.2: Part two of a selection of rows from the as-coated recipe table. Part one is found in Table I.1. Each row represents the as-coated recipe found for a given coating run. If data has yet to be analyzed fields read "N/A". d_i, with $i = 1..6$, and Γ_i, with $i = 1, 2$, represents modifications of the top bilayers. d_i is a relative modification of the relevant bilayer d while Γ_i replaces the Γ value for the bilayer in question. σ_{sub} is the estimated micro-roughness of the Si wafer substrate. C1-C3 values are "1" if a cathode drop-out has been logged or identified from data and "0" if not. Similarly, T1-T3 values are "1" if the target was changed just prior to the coating run and "0" if not. C3/T3 always mounts the heavy material target. Finally, the calibration column indicates whether or not the deposition rate was calibrated before coating commenced.

Coating run	d_1	d_2	d_3	d_4	d_5	d_6	Γ_2	Γ_3	σ_{sub}[Å]	C1	C2	C3	T1	T2	T3	Calibration
11012	N/A	N/A	N/A	N/A	N/A	N/A	N/A	N/A	N/A	N/A	N/A	N/A	N/A	N/A	N/A	N/A
28	N/A	N/A	N/A	N/A	N/A	N/A	N/A	N/A	N/A	N/A	N/A	N/A	N/A	N/A	N/A	N/A
⋮	⋮	⋮	⋮	⋮	⋮	⋮	⋮	⋮	⋮	⋮	⋮	⋮	⋮	⋮	⋮	⋮
167	0.99	1.01	0.99	1.00	0.98	1.00	0.49	0.41	3.9	0	0	0	0	0	0	0
⋮	⋮	⋮	⋮	⋮	⋮	⋮	⋮	⋮	⋮	⋮	⋮	⋮	⋮	⋮	⋮	⋮
196	0.98	1.00	1.01	1.00	1.01	1.00	0.49	0.40	3.9	0	0	0	1	1	1	1
⋮	⋮	⋮	⋮	⋮	⋮	⋮	⋮	⋮	⋮	⋮	⋮	⋮	⋮	⋮	⋮	⋮
279	0.96	1.01	0.99	1.01	1.00	1.00	0.47	0.39	3.9	0	1	0	0	0	0	0

Appendix J

Witness campaign: Witness plots

Plots of all witness data are available from the plots repository located in the witness campaign library. There are two types of plots in the repository. One compares all three specular reflectivity data sets (low angle, high angle and 8 keV) to the as-coated recipe fit, while the other shows only the high angle data and the fit. The former was used for a visual check of the fit quality across the three data sets.

Appendix K

TEM campaign: TEM images

Two separate TEM campaigns were carried out with EAG in February and August 2011, while the budding collaboration between CEN and DTU resulted in several TEM images being acquired between August and December 2011.

All acquired images are available from the data repository located in the TEM campaign library. The images used for Chapter 4 are located in the EAG folder, while the CEN folder contains images acquired from witness samples Si5157 and Si5169, including the cathode drop-out example shown in Chapter 3.

Appendix L

TEM campaign: TEM multilayer

The multilayer applied to witness samples Si5117, Si5218 and Si5355 was determined from specular reflectivity measurements at RaMCaF and from TEM images. The TEM images are available from Appendix K. Each image consists of a two-dimensional intensity map. Summing the map horizontally (parallel to the multilayer interfaces) gives contrast intensity curves. Through fitting a simple Gaussian to these curves the d-spacing of the multilayer can be found.

The plots repository in the TEM campaign library contains simple text files with estimated d-spacing values. The values are plotted against the as-coated recipes in Fig. 4.3-4.5. The figures imply an error in the nominal magnification value. Figure 4.6 shows a plot where the scale error for Si5355 has been corrected by assuming the minimum d-spacing determined from TEM is equal to the minimum d-spacing determined from RaMCaF data. Similar plots for Si5117 and Si5218 are shown in Fig. L.1 and Fig. L.2

The scaled d-spacings have been used to calculate specular reflectivity in Fig. 4.10 and Fig. 4.9 for Si5355. Similar plots for Si5117 and Si5218 are shown in Fig. L.3-L.6. The uncertainty in the minimum d-spacing determination and, for Si5218, measurement artifacts, means that only the low energy response can be fit for a given scale error correction. Although a generally better fit to the low energy response is achieved, compared to the as-coated recipes, the chi-square values for Si5117 and Si5218 are dominated by missing the d_{min} dip at high energies.

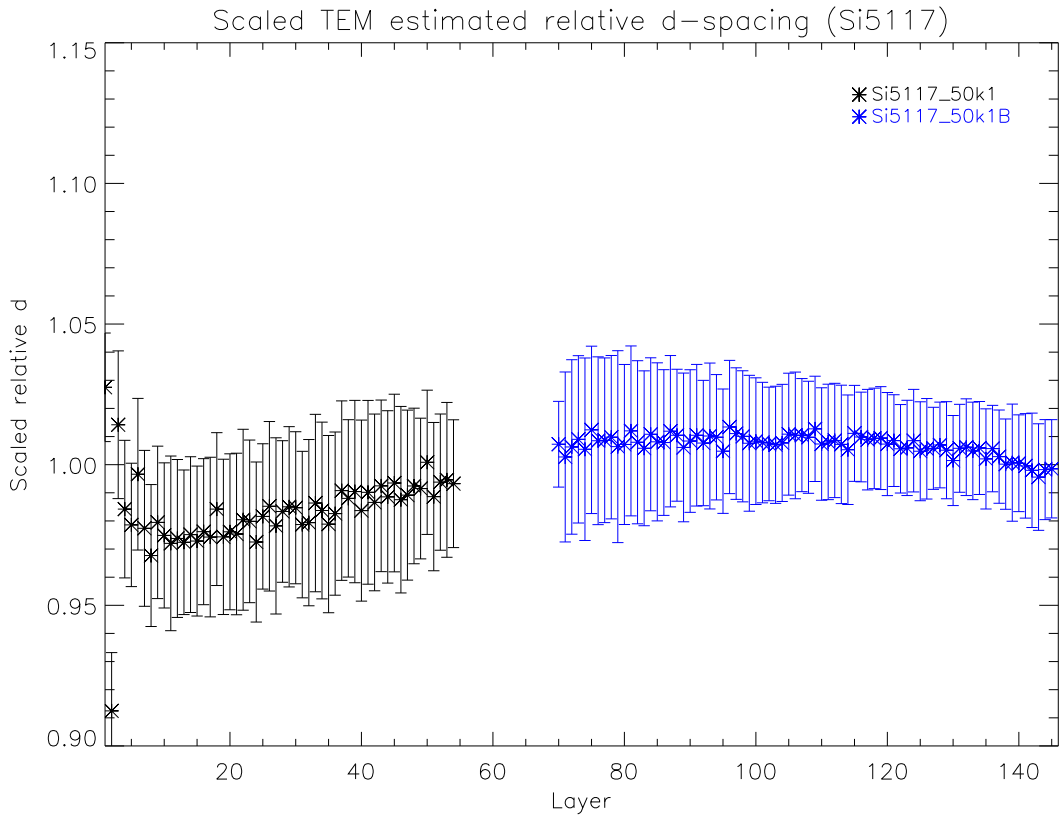

Figure L.1: The shape of relative d values for the top bilayers indicates disagreement on c and d_i values between the two types of measurements.

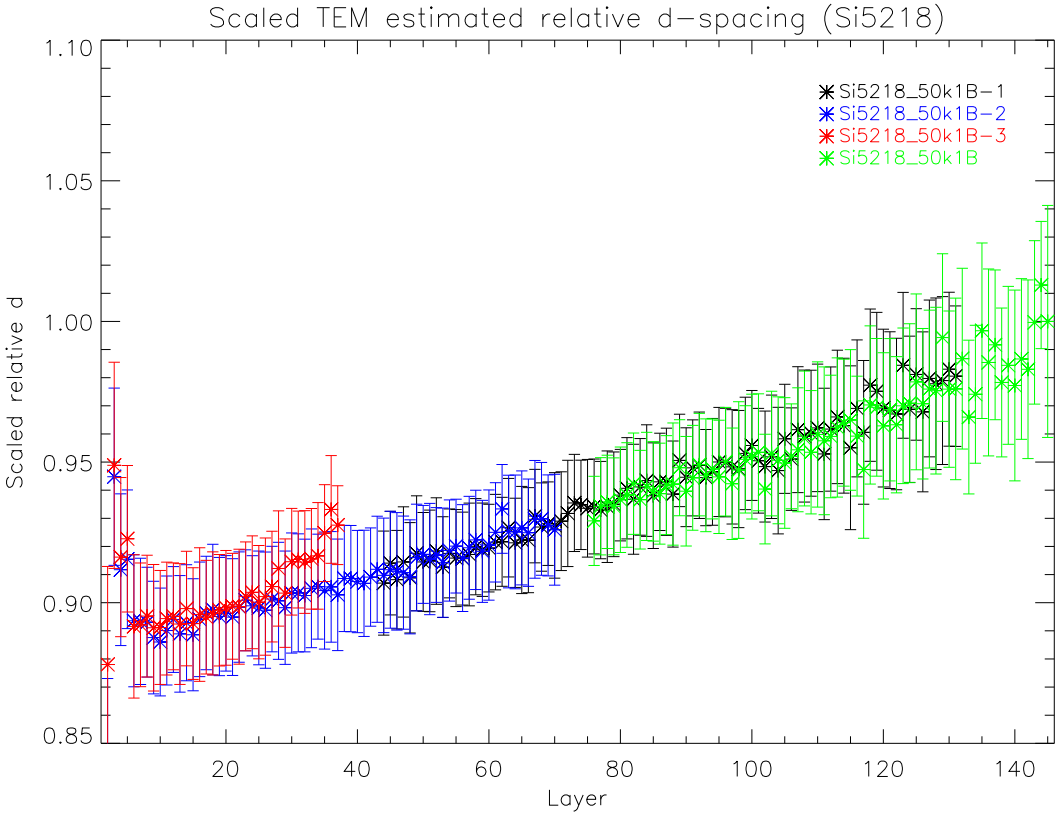

Figure L.2: The nearly linearly decreasing relative d is indicative of an unknown measurement artifact. The artifact makes it impossible to fit both the top and bottom bilayers even remotely correct.

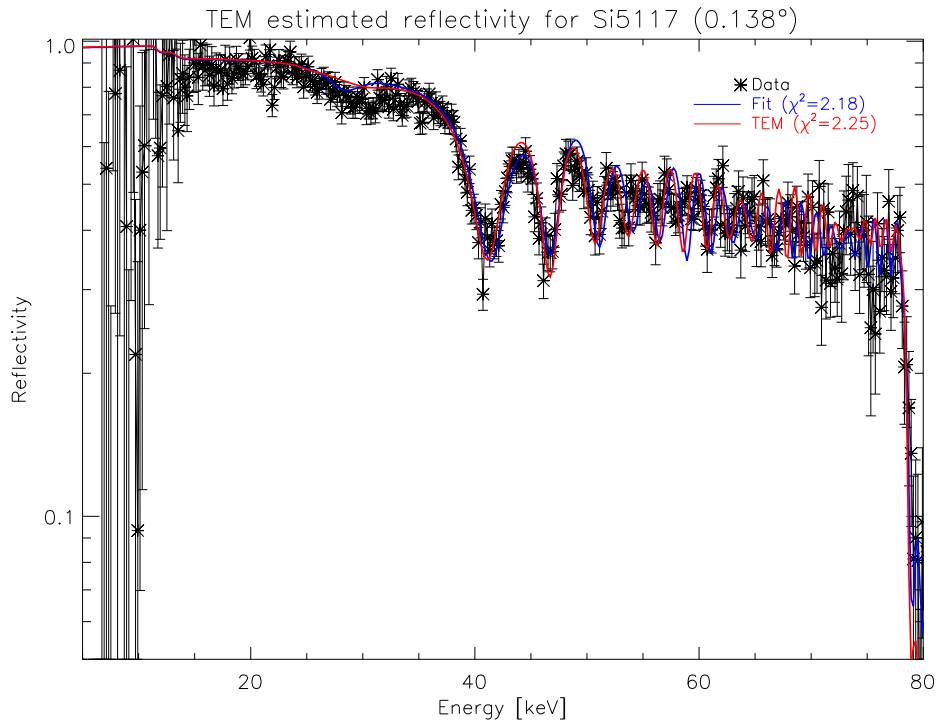

Figure L.3: Specular reflectivity from Si5117 at RaMCaF compared to reflectivity derived from the as-coated recipe (blue) and TEM d-spacings (red).

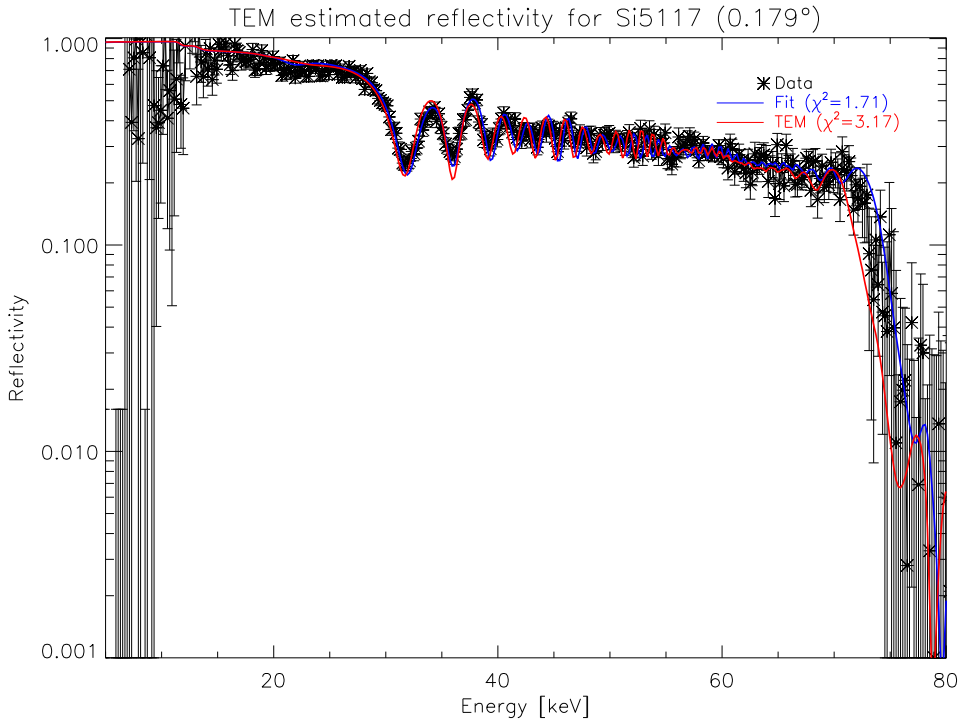

Figure L.4: Specular reflectivity from Si5117 at RaMCaF compared to reflectivity derived from the as-coated recipe (blue) and TEM d-spacings (red).

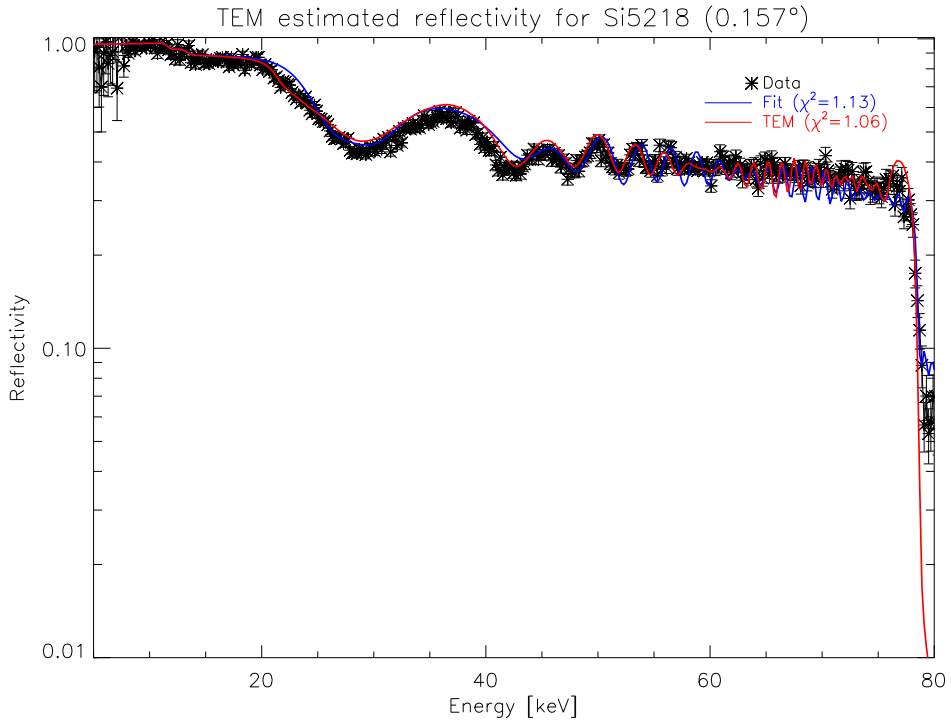

Figure L.5: Specular reflectivity from Si5218 at RaMCaF compared to reflectivity derived from the as-coated recipe (blue) and TEM d-spacings (red).

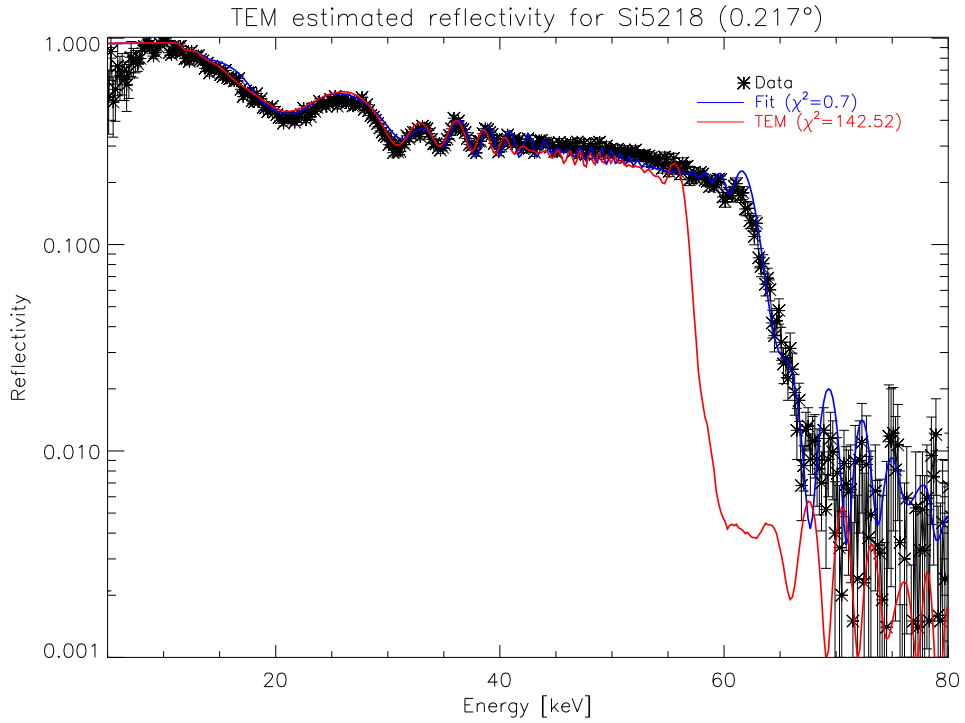

Figure L.6: Specular reflectivity from Si5218 at RaMCaF compared to reflectivity derived from the as-coated recipe (blue) and TEM d-spacings (red).

Appendix M

TEM campaign: EAG communication

Communication with EAG was initially done through LLNL collaborators, but as the images were analyzed a number of questions arose that befitted more direct contact. The below represents the correspondence with EAG on image discrepancies and general method. The person answering from EAG is Research Fellow Harry Kawayoshi. The text has been edited for typos and to remove a number of abbreviations.

Question: *What was the spot size on the specimen at f.ex. 100k magnification? At 300k? At 600k?* **Answer:** *Spot size would be variable depending on the condenser lens setting.*

Question: *What is the depth of focus of this device at given magnifications?* **Answer:** *Samples are generally imaged near a fixed height (Z) objective lens setting for calibration purposes. JEOL says magnification should fall within* 5% *if imaged at this position.*

Question: *You mention that JEOL claim a* 5% *accuracy on magnification at a given specimen height. Can you estimate errors deriving from not being at this designated height? I.e. order of magnitude of magnification inaccuracies from being off by some (realistic) amount?* **Answer:** *Cannot estimate as we normally always try and stay close to the designated focusing position.*

Question: *Can you give me any details on your NIST calibration standard and your general calibration approach?* **Answer:** *This is a MAG*I*CAL calibration standard serial* #270 *said to be accurate to* 2% *(see Ted Pella Inc. catalogue). Sample has several sets of multiple layers for low magnification to high resolution mode calibration.*

Question: *What thickness were the individual specimens thinned to?* **Answer:** *We would estimate the thickness as less than 100 nm*

Question: *Why would FIB give a wedge as opposed to mechanical grinding/polishing? Literature indicates that FIB is what enabled accurate ¡100 nm specimen preparation.* **Answer:** *FIB can sometimes produce a wedge or ridges on the sample depending on the preparation conditions.*

Question: *From knowledge of the FIB and mechanical grinding/polishing method, can you give an estimate of possible wedge error?* **Answer:** *This may not be easily determined*

Question: *Was there a dedicated effort to aligning the samples to the Si wafer planes or is it coincidental (f.ex. 5355-500k1Ba.dm3)?* **Answer:** *Si cleaves along the (110) faces, so for TEM samples on Si substrates the samples are aligned along the (110) zone axis in diffraction mode. The electron beam should then pass closely parallel to the (100) wafer surface.*

Question: *What plane was aligned to?* **Answer:** *Two sets of (111) planes should be imageable at approximately 55 degrees to the surface along the (110) zone.*

Question: *Is it your professional opinion that planes may be used for in-situ calibration of the magnification given that the orientation is known?* **Answer:** *Yes, the lattice planes can be used as in-situ calibration. For Si(111)* 3.1 *Å.*

Question: *I have attached a .pdf* (Fig. M.1) *of the relative thicknesses of the layers imaged by TEM compared to the values determined with X-ray reflectrometry. Reflectrometry determines these values to better than* $0.05nm$*. Each layer is* $3.1nm$ *thick. As you can see from the attachment TEM overestimates this value by anywhere from* $5-35\%$*. Note that even from TEM image to TEM image this may vary with as much as* 30%*. In your professional opinion, what might cause this?*

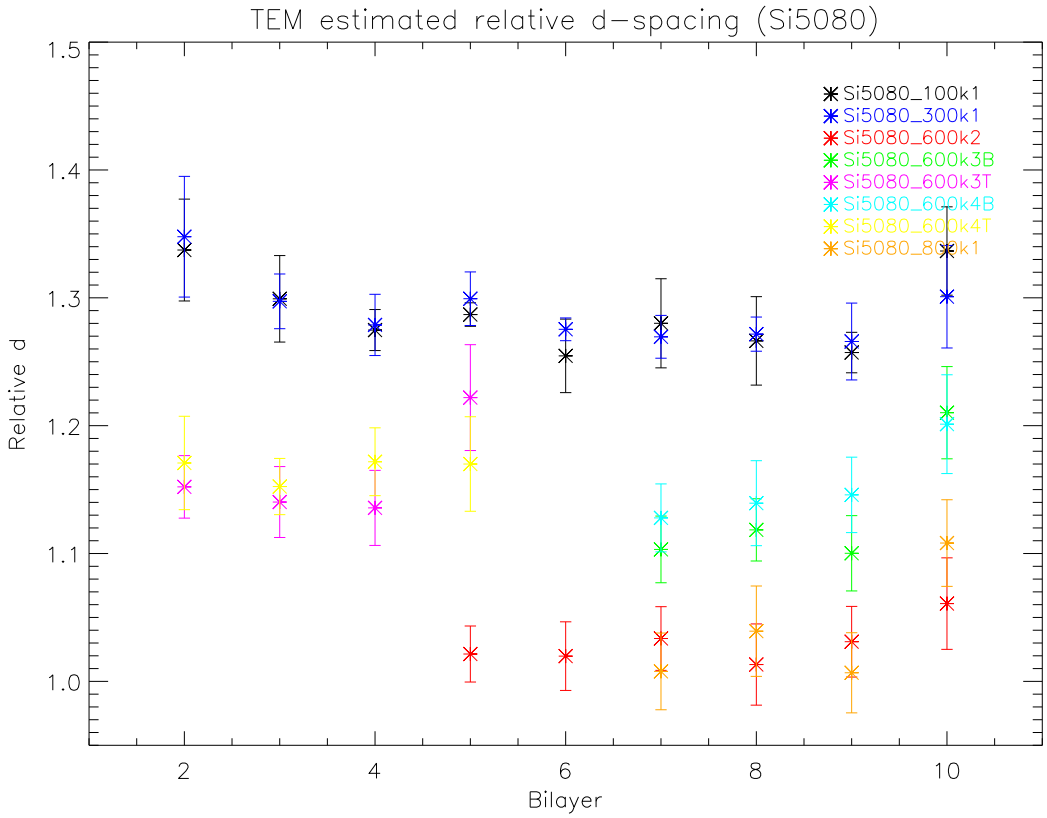

Figure M.1: Relative d for Si5080, a cst-d coated sample ($N = 10$, $d = 31.2$ Å, $\Gamma = 0.45$) imaged with TEM.

Answer: *I have examined the 600k images, I notice this difference between 600k2 and other 600k images? I believe the 600k images were acquired in the same session not sure what caused these differences other than location? I could check sample but I believe all TEM samples have been given to LLNL.*

Question: *Please see attached plot* (Fig. 4.4). *Note that it describes several shots taken over the same range and specimen. All of them describe an (unrealistic) increase in the difference between our X-ray determination of the layer thickness and the one estimated from TEM. What leads me to believe this is not real, but a measurement artifact, is in particular the overlap between two separate images at layers* $30 - 40$. *Any take on what could cause this? I should also note that Si5218 is the only sample of the lot where the Silicon wafer lattice fringes were not resolved at 500k magnification and that these measurements were done for the explicit reason of having overlaps between images (so it should be imaging the same horizontal area of the sample as well as vertical).*
Answer: *A camera error can occur if the TEM magnification is changed while the camera is in acquisition (viewing) mode. The camera will maintain the previous magnification until the image acquisition is stopped and restarted, it then will refresh with the new magnification. The only thing we can suggest is to reexamine the sample to see if there is any variation. However I believe all samples have been returned to LLNL.*

Electron Microscopy Sciences's company website contains additional information on the MAG*I*CAL calibration standard.

Appendix N

Optic response model: Single reflection data

The complete single reflection data set is available from the data repository located in the calibration campaign library. The data is provided in simple text files with the reflectivity as a function of energy and 1σ error bars.

Appendix O

Optic response model: LVDT data

The LVDT scanner used was supplied by Colorado Precision Products. Additional information on the unit may be found from their website.

The complete data set is available from the input repository located in the ORM library.

Bibliography

[1] Nicolai F. Brejnholt, Finn E. Christensen, Charles J. Hailey, Nicolas M. Barriere, William W. Craig, Brian Grefenstette, Jason Koglin, Kristin Kruse Madsen, Julia K. Vogel, Hongjun An, Kenneth Blaedel, Josh Brown, Todd Decker, Zeshan Haider, Anders Clemen Jakobsen, Carsten P. Cooper-Jensen, Kaya Mori, Melania Nynka, Michael J. Pivovaroff, Clio Sleator, Dennis Stefanik, Marcela Stern, Gordon Tajiri, Douglas Thornhill, and Jeremy S. Cushman. The Rainwater Memorial Calibration Facility for X-Ray Optics. *X-ray Optics and Instrumentation*, 2011:15, 2011.

[2] Nicolai F. Brejnholt, Finn E. Christensen, Anders C. Jakobsen, Charles J. Hailey, Jason E. Koglin, Kenneth L. Blaedel, Marcela Stern, Doug Thornhill, Clio Sleator, Shuo Zhang, William W. Craig, Kristin K. Madsen, Todd Decker, Michael J. Pivovaroff, and Julia K. Vogel. NuSTAR ground calibration: The Rainwater Memorial Calibration Facility (RaMCaF). *Proceedings of SPIE–the international society for optical engineering*, 8147(1):81470I–9, 2011.

[3] S Agostinelli, J Allison, K Amako, John Apostolakis, H M Araao, P Arce, M Asai, D A Axen, S Banerjee, G Barrand, F Behner, L Bellagamba, J Boudreau, L Broglia, A Brunengo, S Chauvie, J Chuma, R Chytracek, G Cooperman, G Cosmo, P V Degtyarenko, A Dell'Acqua, G O De Paola, D D Dietrich, R Enami, A Feliciello, C Ferguson, H S Fesefeldt, G Folger, F Foppiano, A C Forti, S Garelli, S Giani, R Giannitrapani, D Gibin, J J Gomez-Cadenas, I Gonzalez, G Gracabral, L G Greeniaus, W Greiner, V M Grichine, A Grossheim, P Gumplinger, R Hamatsu, K Hashimoto, H Hasui, A M Heikkinen, A Howard, A M Hutton, V N Ivanchenko, A Johnson, F W Jones, Jeff Kallenbach, N Kanaya, M Kawabata, Y Kawabata, M Kawaguti, S Kelner, P Kent, T Kodama, R P Kokoulin, M Kossov, H Kurashige, E Lamanna, T Lampen, V Lara, V Lefebure, F Lei, M Liendl, W Lockman, F Longo, S Magni, M Maire, B A Mecking, E Medernach, K Minamimoto, P Mora de Freitas, Y Morita, K Murakami, M Nagamatu, R Nartallo, P Nieminen, T Nishimura, K Ohtsubo, M Okamura, S W O'Neale, Y O'Ohata, J Perl, A Pfeiffer, M G Pia, F Ranjard, A Rybin, S Sadilov, E Di Salvo, G Santin, T Sasaki, N Savvas, Y Sawada, S Scherer, S Sei, V I Sirotenko, D Smith, N Starkov, H Stacker, J Sulkimo, M Takahata, S Tanaka, E Chernyaev, F Safai-Tehrani, M Tropeano, P R Truscott, H Uno, L Urban, P Urban, M Verderi, A Walkden, W Wander, H Weber, J P Wellisch, T Wenaus, D C Williams, D Wright, T Yamada, H Yoshida, and D Zschiesche. GEANT4: A Simulation toolkit. *Nuclear Instruments and Methods in Physics Research Section A: Accelerators, Spectrometers, Detectors and Associated Equipment*, 506:250–303, 2003.

[4] S. Elliott. *The Physics and Chemistry of Solids*. John Wiley & Sons, N.Y., 1997.

[5] J. Als-Nielsen and D. McMorrow. *Elements of modern x-ray physics*. Wiley, New York,NY, 2001.

[6] E. Hecht. *Optics*. Addison Wesley, San Francisco, Calif., 2002.

[7] Ludwig Reimer. *Transmission electron microscopy : physics of image formation*. Springer, New York, NY, 2008.

[8] Windt. IMD-Software for modeling the optical properties of multilayer films. *Comput. Phys. (USA)*, 12(4):360–370, 1998.

[9] WL Bragg and JJ Thomson. The diffraction of short electromagnetic waves by a crystal. *P CAMB PHIL P CAMB PHILOS SOC PROC CAMBRIDGE PHIL SOC*, 17:43–57, 1914.

[10] M. Born and E. Wolf. *Principles of optics / Electromagnetic theory of propagation, interference and diffraction of light.* Pergamon Press, Oxford, 1965.

[11] Parratt. Surface studies of solids by total reflection of X-rays. *Phys. Rev. (USA)*, 95:359–369, 1954.

[12] Stearns. The scattering of X-rays from nonideal multilayer structures. *J. Appl. Phys. (USA)*, 65(2):491–506, 1989.

[13] Nevot and Croce. Characterisation of surfaces by grazing X-ray reflection. Application to the study of polishing some silicate glasses. *Rev. Phys. Appl. (France) Revue de physique appliquee*, 15(3):761–779, 1980.

[14] Kiessig. Interference of X-rays in thin films. *Ann. Phys. (Germany)*, 10(7):769–788, 1931.

[15] Peter M. Martin and Inc. Books24x7. *Handbook of deposition technologies for films and coatings : science, applications and technology, third edition.* Books24x7.com, Norwood Mass, 2010.

[16] David M. Broadway, Yuri Ya. Platonov, and Luis A. Gomez. Achieving desired thickness gradients on flat and curved substrates. *Proc SPIE Int Soc Opt Eng*, 3766:262–274, 1999.

[17] David B. Williams and C. Barry. Carter. *Transmission electron microscopy : a textbook for materials science.* Springer, New York London, 2009.

[18] Giacconi, Brandaurdi, Briel, Epstein, Fabricant, Feigelson, Forman, Gorenstein, Grindlay, Gursky, Jr. Harnden, Henry, Jones, Kellogg, Koch, Murray, Schreier, Seward, Tananbaum, Topka, van Speybroeck, Holt, Becker, Boldt, Serlemitsos, Clark, Canizares, Markert, Novick, Helfand, and Long. The Einstein (HEAO 2) X-ray Observatory. *Astrophys. J. (USA) The Astrophysical Journal*, 230(2):540–550, 1979.

[19] P. A. J. de Korte, J. A. M. Bleeker, A. J. F. den Boggende, G. Branduardi-Raymont, A. C. Brinkman, J. L. Culhane, E. H. B. M. Gronenschild, I. Mason, and S. P. McKechnie. The X-ray imaging telescopes on Exosat. *Space Sci Rev*, 30(1-4):495–511, 1981.

[20] Jansen, Lumb, Altieri, Clavel, Ehle, Erd, Gabriel, Guainazzi, Gondoin, Much, Munoz, Santos, Schartel, Texier, and Vacanti. XMM-Newton Observatory. I. The spacecraft and operations. *Astron. Astrophys. (France) Astronomy and astrophysics*, 365(1):L1–6, 2001.

[21] M.C. Weisskopf, H.D. Tananbaum, L.P. Van Speybroeck, and S.L. O'Dell. Chandra X-Ray Observatory (CXO): Overview. *Proc SPIE Int Soc Opt Eng*, 4012:2–16, 2000.

[22] David N. Burrows, J.E. Hill, J.A. Nousek, A. Wells, A. Short, R. Willingale, O. Citterio, G. Chincarini, and G. Tagliaferri. Swift X-ray telescope. *Proc SPIE Int Soc Opt Eng*, 4140:64–75, 2000.

[23] Christensen, Hornstrup, and Schnopper. Surface correlation function analysis of high resolution scattering data from mirrored surfaces obtained using a triple-axis X-ray diffractometer. *Appl. Opt. (USA)*, 27(8):1548–1557, 1988.

[24] Jason E. Koglin, HongJun An, Kenneth L. Blaedel, Nicolai F. Brejnholt, Finn E. Christensen, William W. Craig, Todd A. Decker, Charles J. Hailey, Layton C. Hale, Fiona A. Harrison, Carsten P. Jensen, Kristin K. Madsen, Kaya Mori, Michael J. Pivovaroff, Gordon Tajiri, and William W. Zhang. NuSTAR hard x-ray optics design and performance. *Proceedings of SPIE–the international society for optical engineering*, 7437(1):74370C–8, 2009.

[25] K. K. Madsen, F. A. Harrison, P. H. Mao, Finn Erland Christensen, Carsten P. Cooper-Jensen, Nicolai Brejnholt, J. Koglin, and M. J. Pivovaroff. Optimizations of Pt/SiC and W/Si multilayers for the Nuclear Spectroscopic Telescope Array. *Proceedings of SPIE, the International Society for Optical Engineering*, 7437(743716):–, 2009.

[26] Fiona A. Harrison, Steve Boggs, Finn Christensen, William Craig, Charles Hailey, Daniel Stern, William Zhang, Lorella Angelini, Hongjun An, Varun Bhalerao, Nicolai Brejnholt, Lynn Cominsky, W. Rick Cook, Melania Doll, Paolo Giommi, Brian Grefenstette, Allan Hornstrup, Vicky Kaspi, Yunjin Kim, Takeo Kitaguchi, Jason Koglin, Carl Christian Liebe, Greg Madejski, Kristin Kruse Madsen, Peter Mao, David Meier, Hiromasa Miyasaka, Kaya Mori, Matteo Perri, Michael Pivovaroff, Simonetta Puccetti, Vikram Rana, and Andreas Zoglauer. The Nuclear Spectroscopic Telescope Array (NuSTAR). *Proceedings of SPIE–the international society for optical engineering*, 7732(1):77320S–8, 2010.

[27] Charles J. Hailey, HongJun An, Kenneth L. Blaedel, Nicolai F. Brejnholt, Finn E. Christensen, William W. Craig, Todd A. Decker, Melanie Doll, Jeff Gum, Jason E. Koglin, Carsten P. Jensen, Layton Hale, Kaya Mori, Michael J. Pivovaroff, Marton Sharpe, Marcela Stern, Gordon Tajiri, and William W. Zhang. The Nuclear Spectroscopic Telescope Array (NuSTAR): optics overview and current status. *Proceedings of SPIE–the international society for optical engineering*, 7732(1):77320T–13, 2010.

[28] Finn E. Christensen, Anders C. Jakobsen, Nicolai F. Brejnholt, Kristin K. Madsen, Allan Hornstrup, Niels J. Westergaard, Joan Momberg, Jason Koglin, Anne M. Fabricant, Marcela Stern, William W. Craig, Michael J. Pivovaroff, and David Windt. Coatings for the NuSTAR mission. *Proceedings of SPIE–the international society for optical engineering*, 8147(1):81470U–19, 2011.

[29] William W. Craig, HongJun An, Kenneth L. Blaedel, Finn E. Christensen, Todd A. Decker, Anne Fabricant, Jeff Gum, Charles J. Hailey, Layton Hale, Carsten B. Jensen, Jason E. Koglin, Kaya Mori, Melanie Nynka, Michael J. Pivovaroff, Marton V. Sharpe, Marcela Stern, Gordon Tajiri, and William W. Zhang. Fabrication of the NuSTAR flight optics. *Proceedings of SPIE–the international society for optical engineering*, 8147(1):81470H–14, 2011.

[30] Jason E. Koglin, HongJun An, Nicolas Barriere, Nicolai F. Brejnholt, Finn E. Christensen, William W. Craig, Charles J. Hailey, Anders Clemen Jakobsen, Kristin K. Madsen, Kaya Mori, Melania Nynka, Monica Fernandez-Perea, Michael J. Pivovaroff, Andrew Ptak, Clio Sleator, Doug Thornhill, Julia K. Vogel, Daniel R. Wik, and William W. Zhang. First results from the ground calibration of the NuSTAR flight optics. *Proceedings of SPIE–the international society for optical engineering*, 8147(1):81470J–16, 2011.

[31] Holy and Baumbach. Nonspecular X-ray reflection from rough multilayers. *Phys. Rev. B, Condens. Matter (USA)*, 49(15):10668–10676, 1994.

[32] Carsten P. Cooper-Jensen, Finn Erland Christensen, Hubert Chen, E.B.W. Smitt, and E. Ziegler. Multilayer coating facility for the HEFT hard x-ray telescope. *SPIE proceedings : X-Ray Optics for Astronomy: Telescopes, Multilayers, Spectrometers, and Missions*, 4496:104–108, 2002.

[33] Jensen, Madsen, Chen, Christensen, and Ziegler. Coating of the HEFT telescope mirrors: method and results. *Proc. SPIE - Int. Soc. Opt. Eng. (USA) Proceedings of SPIE–the international society for optical engineering*, 4851:724–733, 2003.

[34] A. Vickery, Carsten P. Cooper-Jensen, Finn Erland Christensen, M.P. Steenstrup, and T. Schoenfeldt. Collimated Magnetron Sputter Deposition for Mirror Coatings. *X-Ray Optics and Instrumentation*, 2008:9, 2008.

[35] K.K. Madsen, F.E. Christensen, C.P. Jensen, E. Ziegler, W.W. Craig, K. Gunderson, J.E. Koglin, and K. Pedersen. X-ray study of W/Si multilayers for the HEFT hard x-ray telescope. *Proc SPIE Int Soc Opt Eng*, 5168:41–52, 2004.

[36] Windt and Waskiewicz. Multilayer facilities required for extreme-ultraviolet lithography. *J. Vac. Sci. Technol. B, Microelectron. Nanometer Struct. (USA)*, 12(6):3826–3832, 1994.

[37] Andre Anders. Physics of arcing, and implications to sputter deposition. *Thin Solid Films*, 502(1-2):22–28, 2006.

[38] Toshinari Yamazaki, Takayuki Kida, Toshio Kikuta, Atsuhiro Sakaya, and Yukichi Takayasu. Thickness Distribution of Films Formed by Magnetron Sputtering. In *The Eleventh International Symposium on Sputtering and Plasma Processes (ISSP 2011)*, 2011.

[39] Koglin, Christensen, Chonko, Craig, Decker, Jimenez-Garate, Gunderson, Hailey, Harrison, Jensen, Sileo, Windt, and Haitao Yu. Development and production of hard X-ray multilayer optics for HEFT. *Proc. SPIE - Int. Soc. Opt. Eng. (USA) Proceedings of SPIE–the international society for optical engineering*, 4851:607–618, 2003.

[40] Fiona A. Harrison, Finn E. Christensen, William Craig, Charles Hailey, Wayne Baumgartner, C. M. H. Chen, James Chonko, W. Rick Cook, Jason Koglin, Kristin-Kruse Madsen, Michael Pivavoroff, Steven Boggs, and David Smith. Development of the HEFT and NuSTAR focusing telescopes. *Exp Astron*, 20(1-3):131–137, 2005.

[41] Adrian Ivan, Ricardo J. Bruni, Paul Gorenstein, and Suzanne E. Romaine. Influence of deposition parameters on the reflectivity of multilayer hard x-ray mirrors. *Proc SPIE Int Soc Opt Eng*, 4501:142–151, 2001.

[42] R.P. Lin, G. Hurford, D.M. Smith, B. Dennis, and A. Zehnder. The Reuven Ramaty High Energy Solar Spectroscopic Imager (RHESSI) Mission. *Proc SPIE Int Soc Opt Eng*, 5171:38–52, 2004.

[43] V. Ambarzumian. Uber eine Frage der Eigenwerttheorie. *Z. Physik*, 53(9-10):690–695, 1929.

[44] Yuji Nonomura, Naoyuki Ohnishi, Yoshiharu Namba, and Koujun Yamashita. Fabrication and microstructure analysis of Pt/C multilayers for hard X-ray optics. In *American Society for Precision Engineering*, 2004.

[45] B.K. Gan, B.A. Latella, and R.W. Cheary. Fabrication and characterisation of ultra-thin tungsten-carbon (W/C) and platinum-carbon (Pt/C) multilayers for X-ray mirrors. *Applied Surface Science*, 239(2):237–245, 2005.

[46] Regina Soufli, Michael J. Pivovaroff, Sherry L. Baker, Jeff C. Robinson, Eric M. Gullikson, Tom J. McCarville, Peter M. Stefan, Andrew L. Aquila, Jay Ayers, Mark A. McKernan, and Richard M. Bionta. Development, characterization and experimental performance of x-ray optics for the LCLS free-electron laser. *P SPIE P SOC PHOTO-OPT INS P SOC PHOTO-OPT INSTRUM ENG*, 7077:–, 2008.

[47] A. Aschentrup, W. Hachmann, T. Westerwalbesloh, Y.C. Lim, U. Kleineberg, and U. Heinzmann. Determination of layer-thickness fluctuations in Mo/Si multilayers by cross-sectional HR-TEM and X-ray diffraction. *Appl Phys A*, 77(5):607–611, 2003.

[48] M.J.H. Kessels, F. Bijkerk, F.D. Tichelaar, and J. Verhoeven. Determination of in-depth density profiles of multilayer structures. *J Appl Phys*, 97(9):1–8, 2005.

[49] Ohnishi, Nonomura, Ogasaka, Tawara, Namba, and Yamashita. HRTEM analysis of Pt/C multilayers. *Proc. SPIE - Int. Soc. Opt. Eng. (USA) Proceedings of SPIE–the international society for optical engineering*, 5168(1):508–517, 2004.

[50] M.D. Abramoff, P.J. Magalhaes, and S.J. Ram. Image Processing with ImageJ. *Biophotonics International*, 11:36–42, 2004.

[51] W.C. Shih and W.M. Stoobs. The measurement of the roughness of W/Si multilayers using the Fresnel method. *Ultramicroscopy*, 32(3):219–239, 1990.

[52] MM Hasan, RJ Highmore, and RE Somekh. The uhv deposition of short-period multilayers for X-ray mirror applications. *Vacuum*, 43(1-2):55–59, 1992.

[53] DL Windt, FE Christensen, WW Craig, C Hailey, FA Harrison, M Jimenez-Garate, R Kalyanaraman, and PH Mao. Growth, structure, and performance of depth-graded W/Si multilayers for hard x-ray optics. *J. Appl. Phys. J APPL PHYS J APPL PHYS J APPL PHYS*, 88(1):460–470, 2000.

[54] Church and Takacs. Specification of the surface figure and finish of optical elements in terms of system performance. *Proc. SPIE - Int. Soc. Opt. Eng. (USA) Proceedings of SPIE–the international society for optical engineering*, 1781:118–130, 1993.

[55] Church and Takacs. Specification of glancing- and normal-incidence X-ray mirrors. *Opt. Eng., Bellingham (USA)*, 34(2):353–360, 1995.

[56] Julia K. Vogel, Michael J. Pivovaroff, Vivek V. Nagarkar, Haris Kudrolli, Kristin K. Madsen, Jason E Koglin, Finn E. Christensen, and Nicolai F. Brejnholt. Application of an EMCCD Camera for Calibration of Hard X-ray Telescopes. In *IEEE Proceedings Draft for Transactions on Nuclear Science*, 2012.

[57] Takao Kitaguchi, Brian W. Grefenstette, Fiona A. Harrison, Hiromasa Miyasaka, Varun B. Bhalerao, Walter R. Cook III, Peter H. Mao, Vikram R. Rana, Steven E. Boggs, and Andreas C. Zoglauer. Spectral calibration and modeling of the NuSTAR CdZnTe pixel detectors. *Proceedings of SPIE–the international society for optical engineering*, 8145(1):814507–11, 2011.

[58] Niels J. Westergaard. MT_RAYOR: a versatile raytracing tool for x-ray telescopes. *Proceedings of SPIE–the international society for optical engineering*, 8147(1):81470Y–6, 2011.

[59] David H. Munro and Paul F. Dubois. Using the Yorick interpreted language. *Comput Phys*, 9(6):–, 1995.

[60] Wells, Griesen, and Harten. FITS: a Flexible Image Transport System. *Astron. Astrophys. Suppl. Ser. (France)*, 44(3):363–370, 1981.